

Université de Montréal

Modèles d'atmosphères hors-ETL avec métaux : applications aux étoiles sous-naines chaudes

par

Marilyn Latour

Département de physique

Faculté des arts et des sciences

Thèse présentée à la Faculté des études supérieures

en vue de l'obtention du grade de

Philosophiae Doctor (Ph.D.)

en physique

Avril, 2014

©Marilyn Latour, 2014

Université de Montréal
Faculté des études supérieures

Cette thèse intitulée:

Modèles d'atmosphères hors-ETL avec métaux : applications aux étoiles sous-naines chaudes

présentée par:

Marilyn Latour

a été évaluée par un jury composé des personnes suivantes:

Nicole St-Louis, Président-rapporteur
Gilles Fontaine, Directeur de recherche
Patrick Dufour, Membre du jury
Ulrich Heber, Examineur externe
Nicole St-Louis, Représentant du Doyen de la FES

Thèse acceptée le: _____

Sommaire

Avec la mise en place dans les dernières années d'une grappe d'ordinateurs (CALYS) dédiés aux calculs de modèles stellaires pour notre groupe de recherche, il nous est désormais possible d'exploiter à leur plein potentiel les modèles d'atmosphères hors équilibre thermodynamique local (HETL) en y incluant des éléments métalliques. Ce type de modèles, plutôt exigeant en temps de calcul, est toutefois essentiel pour analyser correctement les spectres d'étoiles chaudes comme les sous-naines de type O (sdO). Les travaux effectués dans le cadre de cette thèse ont comme point commun l'utilisation de tels modèles d'atmosphères pour faire l'analyse spectroscopique d'étoiles sous-naines chaudes dans des contextes variés.

Le coeur de cette thèse porte sur BD+28°4211, une étoile standard de type sdO très chaude, dans laquelle le problème des raies de Balmer, qui empêche de reproduire ces dernières avec une unique, et réaliste, combinaison de paramètres atmosphériques, est bien présent. Cette étoile a d'ailleurs servi à définir ce problème, commun aux étoiles très chaudes, dans les années 90. Dans un premier temps nous présentons une analyse approfondie de son spectre ultraviolet (UV). Cette analyse nous permet de déterminer les abondances de métaux dans l'atmosphère de l'étoile et de contraindre sa température effective et sa gravité de surface. Par la suite, ces résultats servent de point de départ à l'analyse du spectre optique de l'étoile, dans lequel le problème des raies de Balmer se fait sentir. L'analyse de différents spectres optiques de BD+28°4211 nous permet de conclure que l'inclusion des abondances métalliques propres à l'étoile dans les modèles d'atmosphères HETL n'est pas suffisant pour surmonter le problème des raies de Balmer. Toutefois, en y incluant des abondances dix fois solaires, nous arrivons à reproduire correctement les raies de Balmer et d'hélium présentes dans les spectres visibles lors d'un ajustement de paramètres. De plus, les paramètres résultants concordent avec ceux

indiqués par le spectre UV. Nous concluons que des sources d'opacité encore inconnues ou mal modélisées sont à la source de ce problème endémique aux étoiles chaudes.

Par la suite nous faisons une étude spectroscopique de Feige 48, une étoile sous-naine de type B (sdB) pulsante particulièrement importante, ayant une température effective beaucoup plus froide que BD+28°4211. Nous arrivons à reproduire très bien le spectre visible de cette étoile, ainsi que les nombreuses raies métalliques qui s'y trouvent. Les paramètres fondamentaux obtenus pour Feige 48 corroborent ceux déjà présents dans la littérature, qui ont été obtenus avec des types de modèles d'atmosphères moins sophistiqués, ce qui implique que les effets HETL couplés à la présence de métaux ne sont pas importants dans l'atmosphère de cette étoile particulière. C'est un résultat particulièrement encourageant dans un contexte sismique. Nous pouvons donc affirmer que les paramètres déterminés pour cette étoile sont fiables et peuvent servir de base à une future étude astérosismologique quantitative.

Finalement, 38 étoiles sous-naines chaudes appartenant à l'amas globulaire ω Centauri ont été analysées afin de déterminer, outre leur température et gravité de surface, leurs abondances d'hélium et de carbone. Nous montrons qu'il existe une corrélation entre les abondances photosphériques de ces deux éléments. Contre toute attente, nous trouvons aussi des différences de températures significatives entre les étoiles riches en hélium de l'amas et celles du champ. Dans leur ensemble, nos résultats remettent en question notre compréhension du mécanisme de formation des sous-naines riches en hélium.

Mots clés : étoiles : sous-naines chaudes - atmosphères - paramètres fondamentaux - spectroscopie - abondances - étoiles : individuelles : Feige 48 - BD+28°4211- amas globulaires : individuel : ω Centauri

Abstract

With the availability of CALYS, a cluster of computers dedicated to stellar modeling for our group, we can now compute large grids of line-blanketed non local thermodynamic equilibrium (NLTE) model atmospheres. The computation of such models is very time consuming but essential in order to analyze properly the spectra of hot subdwarf O stars (sdO). The work done for this thesis made use of these state-of-the-art model atmospheres to perform spectroscopic analyses of hot subdwarf stars in various contexts.

The main part of this thesis is about BD+28°4211, a very hot sdO star. The optical spectrum of this star suffers from the so-called Balmer line problem. That means the observed lines cannot be simultaneously matched with a unique model spectrum. This star was moreover used to define this problem, generally affecting very hot stars, in the 90's. The first part of our study is dedicated to the analysis of the UV spectra of BD+28°4211 in order to determine the chemical composition of its atmosphere. We also constrain its effective temperature and surface gravity. In the second part of the study, we use the abundances determined with the UV spectra to build a grid of model atmospheres especially suited for the star. We next use that grid to perform spectroscopic fits of three high sensitivity optical spectra of BD+28°4211. We find that these models do not allow for a good reproduction of the optical lines of the star, a failure compounded by the fact that the derived effective temperature resulting from our fitting procedure is $\sim 10,000$ K cooler than expected. However, when increasing the metal abundances to ten times their solar values we can achieve a very good fit of the observed spectra and, at the same time, obtaining fundamental parameters consistent with those indicated by the UV spectrum. We infer that opacity sources are still missing or modeled poorly in the atmospheres of very hot stars.

We then made a spectroscopic study of Feige 48, a very important pulsating hot subdwarf B star, much cooler than BD+28°4211. We are able to reproduce very well its optical spectrum, including a lot of weak metallic lines. The fundamental parameters we get for the star are coherent with what is found in the literature, even if those analysis were made with much less sophisticated types of atmospheres. This implies that NLTE effects coupled to metal line blanketing are not very important in the atmosphere of this particular star. This is a good thing, particularly from a seismic point of view. The parameters determined for Feige 48 are thus very reliable and should be useful to constrain a future quantitative seismic analysis of the star.

At last, we analyze the spectra of 38 hot subdwarfs in the globular cluster ω Centauri in order to determine, besides their effective temperature and surface gravity, their helium and carbon abundances. We find that there is a positive correlation between the abundances of these two elements. Against expectations, we also notice a significant difference in the temperatures at which are found the helium rich stars of the cluster versus those in the field. Our results raise important questions about the formation scenario usually invoked to explain the existence of helium rich subdwarfs.

Subject headings : stars : hot subdwarf - atmosphere - fundamental parameters - spectroscopy - abundances - stars : individual : Feige 48 - BD+28°4211- globular clusters : individual : ω Centauri

Table des matières

Sommaire	i
Abstract	iii
Table des matières	v
Liste des figures	viii
Liste des tableaux	xi
Remerciements	xii
1 Introduction	1
1.1 Les sous-naines chaudes	1
1.1.1 Astérosismologie	4
1.2 Évolution	6
1.2.1 Évolution canonique et flash d'hélium tardif	6
1.2.2 Évolution à l'intérieur de systèmes binaires	8
1.2.3 Évolution post-EHB, post-AGB et sous-naines de faible masse	10
1.3 Spectroscopie et modèles d'atmosphères	11
1.3.1 Principe de base de la spectroscopie quantitative	11
1.3.2 Les modèles d'atmosphères	13
1.3.3 Spectroscopie quantitative des sous-naines chaudes	14
1.4 Format de cette thèse	18

2	A NLTE Analysis of the SdO Star BD+28°4211: I	20
2.1	Abstract	21
2.2	Introduction	21
2.3	Model Atmospheres	24
2.3.1	Characteristics of Our Model Atmospheres	24
2.3.2	A Word on the Inclusion of Metallic Elements	28
2.4	Abundance Analysis	30
2.4.1	Observational Material	30
2.4.2	Fitting Technique and Resulting Abundances	35
2.4.3	Evaluation of the Abundance Uncertainties	41
2.5	Constraining the Atmospheric Parameters	43
2.5.1	With the Metal Lines	43
2.5.2	With the Parallax Distance	44
2.6	Discussion	49
2.7	References	54
2.8	Supplementary Figures	57
3	A NLTE Analysis of the SdO Star BD+28°4211: II	63
3.1	Abstract	64
3.2	Introduction	65
3.3	Observational Material	69
3.4	Spectroscopic Analysis	71
3.4.1	Model Atmosphere Grids	71
3.4.2	Derived Atmospheric parameters	74
3.4.3	Additional Verifications	82
3.5	Discussion	90
3.6	References	98
4	Atmospheric Parameters of Feige 48	100
4.1	Abstract	101

4.2	Introduction	101
4.3	Some Background	104
4.4	Spectral Analysis of Feige 48	106
4.4.1	Previous Studies	106
4.4.2	Observational Material	108
4.4.3	Model Atmospheres	110
4.4.4	Derived Atmospheric Parameters	115
4.4.5	Fine Tuning of the Metal Abundances	120
4.5	Conclusion	125
4.6	References	128
5	Analysis of EHB stars in ω Centauri	131
5.1	Abstract	132
5.2	Astrophysical Context	133
5.3	Observational Material	136
5.4	Spectroscopic Analysis	141
5.4.1	Fundamental Parameters	141
5.4.2	Carbon Abundances	153
5.4.3	Spectroscopic masses	159
5.5	Discussion	162
5.6	References	166
6	Conclusion	170
6.1	BD+28°4211 et le problème des raies de Balmer	170
6.2	Feige 48, sdB pulsante	173
6.3	Les sous-naines chaudes de ω Centauri et le puzzle des étoiles riches en hélium	174
	Bibliographie	176

Liste des figures

1.1	Schéma du diagramme Hertzsprung-Russel.	2
1.2	Séquences évolutives de flash tardifs.	8
1.3	Séquences évolutives post-EHB et pour des étoiles de faible masse.	10
2.1	Temperature stratification and monochromatic optical depth $\tau_\nu = 2/3$ as functions of depth.	26
2.2	Ionization fractions as functions of the depth.	28
2.3	Comparison between nickel lines in the observed STIS spectrum of BD+28°4211 and in synthetic spectra.	30
2.4	Sample of fitted spectral intervals from the STIS spectrum.	36
2.5	Sample of fitted spectral intervals from the FUSE spectrum.	37
2.6	Comparison of iron lines with models having different temperatures.	45
2.7	Comparisons of iron lines with models at different $\log g$	46
2.8	Summary of the determined chemical composition of BD+28°4211.	50
3.1	Temperature stratification and monochromatic optical depth $\tau_\nu = 2/3$ as functions of depth.	72
3.2	Balmer and helium lines profiles for models having different metallicity.	73
3.3	Best fit obtained with the NLTE H, He model grid.	75
3.3	Continued	76
3.4	Best fit obtained with the model grid having a metallicity suited for BD+28°4211.	77
3.4	Continued	78
3.5	Best fit obtained with the model grid having ten times solar abundances.	79

3.5	Continued	80
3.6	Comparisons with the HIRES He II 4686 Å line.	83
3.7	Comparisons with the HIRES H β line.	84
3.8	Comparison with the HIRES H α line.	84
3.9	Comparison with the HIRES H γ line.	85
3.10	Comparison with the HIRES He II 5412 Å line.	86
3.11	Comparisons with the HIRES spectrum in the He I 5876 Å region.	87
3.12	Comparisons with the He II 1640 Å line from the STIS spectrum.	88
3.13	Comparison with the He II 1085 Å line from the FUSE spectrum.	89
3.14	Model optical lines for various T_{eff} and metallicity (H α , H β and H γ).	95
3.15	Model optical lines for various T_{eff} and metallicity (H γ , He II $\lambda\lambda$ 4686, 5412).	96
4.1	NLTE effects in the log g - T_{eff} plane.	105
4.2	Metal blanketing effects in the log g - T_{eff} plane.	106
4.3	Temperature stratification and monochromatic optical depth $\tau_{\nu} = 2/3$ as functions of depth.	113
4.4	Effects of metal line blanketing on the inferred atmospheric parameters.	114
4.5	Best fit obtained with our optical spectra of Feige 48. Panels a - b	116
4.5	Continued, panels c - d	117
4.6	Best fit of the He II λ 1640 line in the STIS spectrum.	120
4.7	Detailed comparison of the observed MMT spectrum with a synthetic spectrum having the abundances fine tuned. Panel a	122
4.7	Continued. Panels b - c	123
4.7	Continued. Panels d - e	124
4.7	Continued. Panel f	125
5.1	Observed spectra of the 38 stars that make up our sample of ω Cen's EHB stars. Panel a)	137
5.1	Continued. Panels b - c	138
5.1	Continued. Panels d - e	139

5.1	Continued. Panels f- g	140
5.1	Continued. Panel h	141
5.2	Correlation between the He abundance and the equivalent width of the CIII 4650 complex.	142
5.3	Resulting fits for four stars of the sample. Panels a - b	145
5.3	Continued. Panels c - d	146
5.4	Helium abundance versus effective temperature for the 38 stars of our sample .	147
5.5	Helium abundance versus surface gravity for the 38 stars of our sample	148
5.6	Distribution of our sample of ω Cen EHB stars in the $\log g-T_{\text{eff}}$ plane	149
5.7	Distribution of field hot subdwarfs in the $\log g-T_{\text{eff}}$ plane	150
5.8	Comparison of the $\log g-T_{\text{eff}}$ distribution of the He-rich subdwarfs of our sample with that of similar He-rich stars from Moehler et al. (2011)	151
5.9	Distribution of field hot subdwarfs in the $\log g-T_{\text{eff}}$ plane	154
5.10	Fits of the carbon lines for the four stars presented in Fig. 5.3	158
5.11	Helium abundance versus the mean carbon abundance	159
5.12	Mass distribution of our sample of ω Cen EHB stars	161

Liste des tableaux

2.1	STIS Datasets Retrieved From StarCAT	33
2.2	BD+28°4211 Chemical Composition — Results of our abundance analysis. . .	38
2.3	Chromium, manganese and cobalt estimated abundances (LTE).	40
2.4	Determined abundances of nitrogen, silicon and iron.	43
2.5	Spectroscopic distances.	48
3.1	Results of our fitting procedures for BD+28°4211	81
4.1	Abundances of Metals Detected in the Atmosphere of Feige 48	111
4.2	Results of our fitting procedure for Feige 48	118
5.1	Atmospheric and Other Parameters for the 38 Stars of our Sample	144
5.2	Inferred Carbon Abundances ($\log N(\text{C})/N(\text{H})$)	157

Remerciements

Je dois remercier tout d'abord Gilles, mon directeur de recherche. Trouver un superviseur pour nos études graduées lorsqu'on n'en est qu'à sa troisième année de baccalauréat, c'est un peu comme aller à la pêche, on ne sait pas trop ce que ça va donner. Je dois dire que j'ai pêché le meilleur poisson ! Plusieurs éléments entrent en ligne de compte dans le succès d'une thèse de doctorat, je pense que le "match" entre l'étudiant et le superviseur y compte pour beaucoup. Je ne crois pas que j'y serais arrivée avec quelqu'un d'autre, à tout le moins pas de la même façon, pour moi ce fût un match plutôt parfait. Je lui en suis infiniment reconnaissante pour avoir vu en moi dès le début quelque chose que je n'y voyais pas moi-même, mais que je commence à entrevoir après toutes ces années.

Ce projet n'aurait pas été possible sans le travail de Pierre Brassard, qui a construit CALYS et y a adapté TLUSTY et SYNSPEC. Tout cet arsenal constitue vraiment la base de mon projet. Mon travail n'aurait pas été le même non plus sans la collaboration de Betsy Green, qui nous fournit des spectres à faire pâlir d'envie n'importe quel observateur. Ses observations fantastiques nous facilitent vraiment la tâche. Les conseils et l'optimisme de Pierre Chayer ont aussi été forts utiles.

J'ai passé plus de 5 ans à travailler dans le "bureau de filles", c'est pratiquement devenu mon deuxième chez-moi, ma deuxième famille. Leur soutien, leur complicité et leur présence ont ensoleillé chacune de mes journées de travail. Elles ont contribué à leur façon à l'accomplissement de cette thèse.

Je dois aussi remercier tous les chercheurs qui *n'ont pas* étudié BD+28°4211, ils m'ont laissé des données d'une qualité exceptionnelle à analyser et ce fût un vrai plaisir !

Chapitre 1

Introduction

1.1 Les sous-naines chaudes

Les sous-naines chaudes sont des étoiles évoluées dont l'existence est plutôt méconnue, même parmi les astrophysiciens. Peut-être est-ce parce qu'elles sont rarement mentionnées dans les manuels d'astrophysique et qu'elles résultent d'une évolution atypique après leur période de brûlage d'hydrogène sur la séquence principale. Les progéniteurs des sous-naines chaudes, pour des raisons qui ne sont pas toujours bien comprises, perdent la majorité de leur enveloppe d'hydrogène lors de la phase géante rouge. Ainsi lorsque l'étoile entame sa phase de brûlage d'hélium, sa couche superficielle d'hydrogène est trop ténue pour qu'il y ait de la fusion nucléaire à sa base. Cette évolution particulière les amène dans une région du diagramme Hertzsprung-Russel (H-R) située à l'extrémité chaude de la branche horizontale (HB) qu'on identifie comme la branche horizontale extrême (EHB), visible à la figure 1.1. Les sous-naines chaudes ont donc peu à voir avec les sous-naines traditionnelles qui sont beaucoup plus froides et qui se trouvent à droite de la séquence principale. Ces sous-naines traditionnelles diffèrent des étoiles de la séquence principale uniquement par leur abondance en métaux plus faible¹.

Bien que peu connues, les sous-naines n'en sont pas pour autant sans importance. Par exemple, l'excès de luminosité dans l'ultraviolet (UV) des galaxies elliptiques est connu depuis

¹Maintenant que cette distinction est faite et afin d'alléger le texte, le terme sous-naine sera dorénavant employé pour désigner les sous-naines chaudes

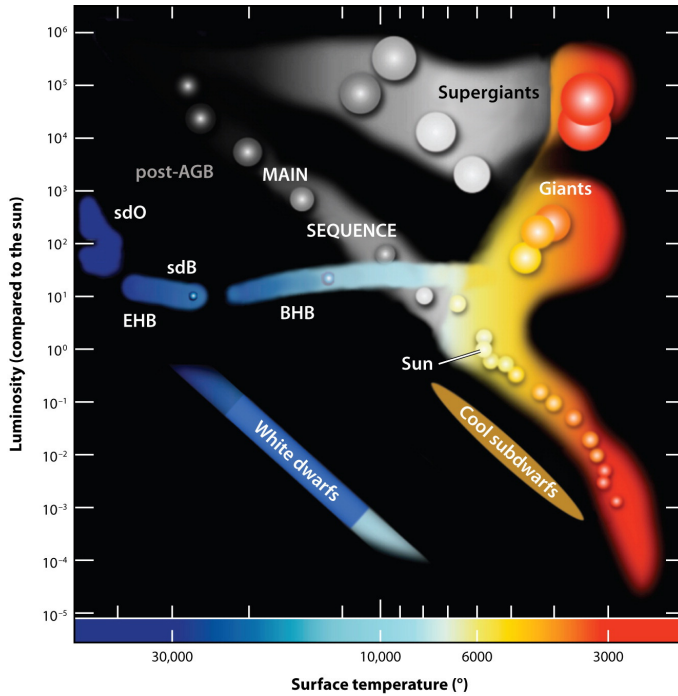



FIGURE 1.1 – Représentation schématique du diagramme H-R où est indiquée la position des sous-naines chaudes (sdO et sdB) qui forment la branche horizontale extrême. La position des sous-naines traditionnelles, qui forment une classe distincte des sous-naines chaudes, se trouve à droite de la séquence principale entre les types spectraux F et K. Figure tirée de Heber (2009).

 Heber U. 2009.
Annu. Rev. Astron. Astrophys. 47:211–51

les années 70, mais n’a pu être expliqué qu’en 1997 par la présence d’une population d’étoiles de la EHB à l’intérieur de ces galaxies (Brown et al. 1997). Non seulement présentes dans notre environnement local et dans les galaxies elliptiques, les sous-naines sont aussi observées dans les amas globulaires de notre galaxie. Elles sont présentes aussi bien dans de vieux amas globulaires pauvres en métaux comme ω Centauri (Whitney et al. 1994) et NGC 6752 (Heber et al. 1986) que parmi des populations d’étoiles plus riches en métaux comme à l’intérieur de l’amas ouvert NGC 6791 (Liebert et al. 1994). Leur présence dans les amas s’avère être un excellent outil pour tester les modèles de formation des sous-naines. Puisque les étoiles d’un amas se forment généralement lors de l’effondrement d’un même nuage moléculaire, elles partagent certaines caractéristiques communes comme leur âge et leur métallicité. Certains amas ont toutefois des populations stellaires plus complexes, comme ω Centauri dont il sera question au Chapitre 5.

Ces étoiles se divisent en 2 classes spectrales, les sous-naines de type B (sdB) et de type O (sdO). Ces types spectraux sont analogues à ceux des étoiles B et O de la séquence principale: les sdB, plus froides, montrent de fortes raies de Balmer parfois accompagnées de faibles raies

d’He I, alors que les sdO, plus chaudes, présentent des raies de Balmer moins fortes ainsi que des raies d’He II. Les sdB ont des températures effectives entre 22 000 et 38 000 K. La limite supérieure en température des sdB n’est pas nettement définie, elle dépend de la température d’ionisation de l’hélium (qui elle-même est influencée par la densité) et la transition se fait donc graduellement entre les types spectraux B et O aux alentours de 35 000 - 38 000 K. On appelle parfois les sous-naines ayant de telles températures des sdOB.

Les sdB forment un ensemble d’étoiles plutôt homogène. Bien installées sur la EHB, elles brûlent de l’hélium en leur coeur tout comme les étoiles de la HB. Toutefois, contrairement à ces dernières, les sous-naines ne brûlent pas d’hydrogène en couche puisque celle-ci est beaucoup trop mince. Cette couche d’hydrogène qui entoure le coeur d’hélium agit comme un isolant, c’est pourquoi les sous-naines, avec leur mince couche ($\lesssim 0.02 M_{\odot}$) sont plus chaudes que les étoiles “normales” de la HB. La grande majorité des sdB sont pauvres en hélium, mais environ 5% d’entre elles font exception à la règle et ont une atmosphère plutôt riche en hélium (Ahmad & Jeffery 2006).

Les sdO quant à elles forment un ensemble plutôt hétérogène, surtout en terme de leur composition chimique. Elles sont séparées en deux “sous-classes”: les sdO riches en hélium lorsque l’abondance d’hélium est plus grande que l’abondance solaire ($\log N(\text{He})/N(\text{H}) \geq -1.0$) et les sdO pauvres en hélium (lorsque l’abondance est sous-solaire). Stroeer et al. (2007) ont montré que ces deux sous-classes semblent avoir des caractéristiques bien distinctes. Dans leur échantillon comprenant 58 sdO, ils ont observé des raies de carbone et/ou d’azote dans la portion visible des spectres de toutes leurs sdO riches en hélium alors qu’aucune raie de ces éléments n’a été observée dans les étoiles pauvres en hélium. De plus, ces deux sous-classes tendent à se distribuer de façon différente dans le plan $T_{\text{eff}} - \log g$: les étoiles riches en hélium se retrouvent majoritairement entre des températures de 40 000 K et 50 000 K et des gravités ($\log g$) de 5.5 et 6.3 dex, bien que quelques-unes soient en dehors de ces limites (Hirsch et al. 2008). Quant aux sdO pauvres en hélium, elles sont répandues de façon beaucoup plus uniforme à travers les gammes de températures et de gravités des sdO.

La figure 7 présentée au Chapitre 5 illustre bien la diversité des sous-naines et on y voit distinctement la population plus homogène des sdB qui forment la EHB.

1.1.1 Astérosismologie

C'est en 1996 que des variations de luminosité dans des étoiles sdB ont été observées pour la première fois (Kilkenny et al. 1997). Par une heureuse coïncidence, à la même époque des études théoriques ont été menées conduisant à la prédiction de ces variations rapides de luminosité dans des sdB (Charpinet et al. 1996). Avec des outils théoriques déjà en place, un nouveau sous-domaine d'étude s'est rapidement développé, soit l'astérosismologie des sous-naines chaudes. Deux types de modes de pulsations sont présents dans les sous-naines: les modes p et les modes g . Les modes p sont associés à des ondes de pression et leur périodes d'oscillations sont assez courtes (entre 80 et 500 secondes). Ces modes sont présents dans certaines sdB qui forment la partie chaude de la EHB ($T_{\text{eff}} \gtrsim 30\,000$ K). Ces étoiles sont généralement désignées comme étant des pulsateurs rapides. Les sdB montrant des modes g , associés à des ondes de gravité, ont été découvertes quelques années plus tard par Green et al. (2003). Ces modes ont des périodes caractéristiques plus longues (2000 à 9000 s) ainsi que des amplitudes beaucoup plus faibles. C'est surtout dans des sous-naines froides de la EHB ($T_{\text{eff}} \lesssim 30\,000$ K) que ce type de pulsations "lentes" est observé. Comme la quasi totalité des sdB pulsantes connues sont sur la EHB, ce sont aussi des sdB dont l'atmosphère est pauvre en hélium, la seule exception étant LS IV-14°116 avec une abondance d'hélium de $N(\text{He})/N(\text{H}) = -0.6$ (Green et al. 2011). Cette étoile est d'autant plus mystérieuse que ses longues périodes d'oscillations sont associées aux modes g mais sa température élevée (près de 35 000 K) la place à l'extrémité chaude de la zone d'instabilité des pulsateurs rapides, alors qu'aucun mode p n'est observé dans son spectre de pulsation.

Mentionnons aussi que certaines sous-naines ont un spectre de pulsation qui montrent à la fois des modes de pression et de gravité, en faisant des pulsateurs hybrides. Les premiers cas découverts étaient des étoiles ayant une température effective près de la zone de transition entre les deux types de modes ($\sim 30\,000$ K). Toutefois les courbes de lumière exceptionnelles obtenues par le satellite Kepler ont permis d'identifier de faibles modes p dans certains pulsateurs lents, ce qui suggère une transition plutôt graduelle entre un spectre de pulsation dominé par les modes de gravité/pression avec la température (Baran et al. 2011). Feige 48, l'étoile dont il sera question au Chapitre 4 a récemment été classifiée comme hybride, avec la

découverte de 15 modes g parmi un spectre dominé par des modes p , grâce à une très longue campagne d'observations menée au sol (Fontaine et al. 2013).

Il n'a été question jusqu'à maintenant que de sous-naines pulsantes de type B. Les sdO pulsantes connues sont beaucoup moins nombreuses et ce n'est pas faute de recherches (Rodríguez-López et al. 2007; Johnson et al. 2013). La seule candidate confirmée parmi les étoiles du champ est SDSS J1600+0748, une sdO à près de 70 000 K (Woudt et al. 2006; Fontaine et al. 2008; Latour et al. 2011). Plusieurs étoiles appartenant à la EHB de l'amas globulaire ω Cen, ont été suivies photométriquement afin de détecter des variabilités périodiques (Randall et al. 2010). Quatre étoiles pulsantes ont ainsi été découvertes, ayant des périodes compatibles avec celles des pulsateurs rapides du champ. La spectroscopie des candidates obtenue par la suite a révélé qu'il ne s'agissait pas de sdB appartenant à la EHB mais plutôt de sdO nettement plus chaudes, ayant des températures effectives aux environs de 50 000 K (Randall et al. 2011). Ces étoiles ayant des températures qui se situent entre les deux régions d'instabilité précédemment connues, et prédites, il n'est pas clair encore s'il s'agit d'une nouvelle classe ou si elles sont reliées à SDSS J1600+0748 bien qu'elle soit nettement plus chaude. Un élément additionnel qui rend cette découverte d'autant plus intrigante est qu'il n'y pas d'analogues aux pulsateurs de ω Cen dans le champ, et ce malgré des observations plutôt exhaustives d'étoiles du champ ayant des paramètres atmosphériques similaires (Johnson et al. 2013). Le Chapitre 5 de cette thèse portera d'ailleurs sur l'étude spectroscopique d'un échantillon de sous-naines ayant été observées dans le cadre de la recherche de pulsateurs dans cet amas globulaire.

L'intérêt porté aux sous-naines pulsantes n'est pas sans raison, l'astérosismologie est un outil sans pareil pour sonder les propriétés internes d'une étoile. Un modèle sismique théorique permet de prédire des périodes d'oscillations bien précises selon la gravité, la température, la masse totale de l'étoile et l'épaisseur de sa couche d'hydrogène. S'il est possible de bien faire concorder des périodes théoriques avec les périodes observées, on obtient alors de précieuses informations sur l'étoile en question. De plus, puisque les modes g sondent le coeur de l'étoile (alors que les modes p sont plutôt actifs dans l'enveloppe), l'analyse sismique d'une étoile présentant des modes de gravité permet d'obtenir des informations supplémentaires sur la composition du coeur, la zone de brûlage nucléaire ainsi que sur le temps que l'étoile a déjà

passé sur la EHB à brûler de l'hélium (Van Grootel et al. 2010). Une analyse astérosismologique reste cependant une tâche complexe qui demande un temps considérable, c'est pourquoi seulement une quinzaine de sdB pulsantes ont ainsi été analysées. Il est néanmoins possible d'en tirer des conclusions très intéressantes. En combinant les masses obtenues par astérosismologie avec celles de sous-naines faisant partie de systèmes binaires, une distribution de masse incluant 22 sdB a récemment été obtenue (Fontaine et al. 2012). Cette distribution de masse concorde très bien avec les prédictions théoriques émises par Dorman et al. (1993) et fourni une masse moyenne de $0.47 M_{\odot}$, avec 68% des étoiles de l'échantillon ayant une masse entre 0.44 et $0.5 M_{\odot}$. De plus, il n'y a pas de différences systématiques entre les masses obtenues par astérosismologie et celles obtenues pour les étoiles en systèmes binaires. Deux petites planètes ont aussi été détectées autour de KPD 1943+4058, une sdB observée par le satellite Kepler. Les extraordinaires courbes de lumières obtenues par le satellite ont permis la détection de signaux à des périodes de 5.76 et 8.23 heures. Ceux-ci ne pouvant s'expliquer par des variations intrinsèques à l'étoile, ils ont finalement été associés à un effet de réflexion sur deux planètes orbitant autour de la sous-naine (Charpinet et al. 2011).

1.2 Évolution

Les étoiles sous-naines chaudes forment dans leur ensemble un groupe d'étoiles plutôt hétéroclite; deux types spectraux différents, une plage de températures couvrant plus de 60 000 K, des gravités de surface variant sur plus d'un ordre de grandeur et des abondances d'hélium variant sur six ordres de grandeurs. Leur diversité est en partie due aux différents scénarios évolutifs produisant des étoiles qui passeront, à un certain moment de leur évolution, dans cette région du diagramme H-R.

1.2.1 Évolution canonique et flash d'hélium tardif

La phase cruciale du destin des sous-naines se joue sur la branche des géantes rouges (RGB), c'est là que survient une perte de masse si importante que l'étoile se retrouve presque dépourvue de tout son hydrogène. Les raisons physiques de cette importante perte de masse demeurent obscures, à tout le moins pour une étoile isolée, mais il est tout de même possible de

caractériser la perte de masse de façon empirique. Habituellement c’est la formule de Reimers qui est utilisée :

$$\dot{M} = -4 * 10^{-13} \eta \frac{L}{gR} M_{\odot} / \text{année},$$

où la luminosité (L), la gravité de surface (g) et le rayon (R) sont exprimés en unités solaires. Le paramètre d’efficacité η peut être varié afin d’augmenter ou de diminuer le taux de perte de masse. Cette méthode a été utilisée avec succès par Dorman et al. (1993) et D’Cruz et al. (1996) pour calculer des séquences évolutives qui produisent assez naturellement des sous-naines. Depuis, c’est la technique standard utilisée pour produire des sous-naines chaudes via l’évolution canonique. En expérimentant avec diverses combinaisons de masses, métallicités et efficacité de perte de masse (η), un phénomène particulier a été découvert dans certaines séquences évolutives: le flash d’hélium survenait parfois après que l’étoile ait quitté la RGB (Castellani & Castellani 1993; D’Cruz et al. 1996). Il peut même survenir lorsque l’étoile a déjà entamé sa phase de refroidissement sur la séquence des naines blanches. Ce phénomène de “flash tardif” a par la suite été examiné plus en détails par Brown et al. (2001) et Lanz et al. (2004) et ils ont noté différentes variantes de flash tardif. Si le flash survient quand l’étoile est une jeune naine blanche (séquence $\eta = 0.60$ à la Figure 1.2), la zone de convection produite lors de l’allumage de l’hélium s’étend jusqu’à atteindre la mince couche d’hydrogène superficielle. L’hydrogène est alors amené vers le coeur de l’étoile où il sera consumé par les réactions nucléaires alors que de l’hélium est transporté en surface. Une sous-naine ainsi formée aurait une composition de surface riche en hélium et aussi enrichie en carbone. Le flash d’hélium peut aussi se produire lorsque l’étoile est encore lumineuse (séquence $\eta = 0.58$, Figure 1.2), dans ce cas la zone de convection n’atteint pas la surface et l’atmosphère ne sera pas perturbée. Ce scénario de flash tardif est particulièrement important pour expliquer l’existence des sdB et sdO riches en hélium. Il s’agit aussi du mécanisme de formation le plus prometteur pour expliquer la présence des étoiles du “blue hook” présentes dans certains amas globulaires comme ω Cen et NGC 2808 (D’Cruz et al. 2000; Brown et al. 2001). Il s’agit d’étoiles sous-lumineuses par rapport à la EHB dont la position dans le diagramme couleur-magnitude ne s’explique pas par le scénario canonique.

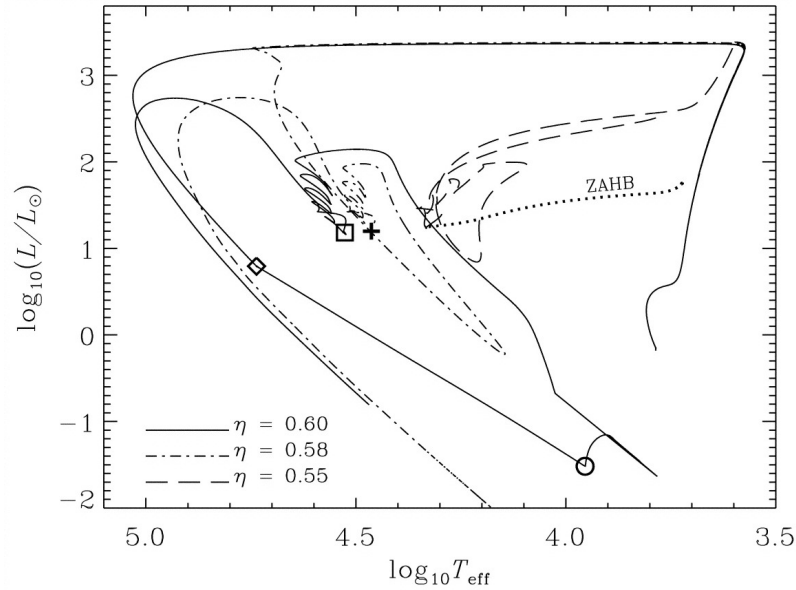


FIGURE 1.2 – Séquences évolutives pour différentes valeurs du paramètres d’efficacité η , le modèle canonique est représenté par la séquence en tiret, où le flash d’hélium a lieu en haut de la RGB. Une valeur de $\eta = 0.58$ produit un flash d’hélium lorsque l’étoile est encore lumineuse. La position subséquente de l’étoile sur la branche horizontale d’âge zéro (ZAHB) est indiquée par le +. La séquence ayant le paramètre d’efficacité le plus élevé (trait plein) produit un flash d’hélium (losange) alors que l’étoile est sur la séquence de refroidissement des naines blanches. Dans ce dernier cas, la zone de convection qui se développe dans le coeur lors du flash d’hélium atteint la surface de l’étoile (cercle) et l’étoile se pose ensuite sur la ZAHB (carré). Figure tirée de Cassisi et al. (2003).

1.2.2 Évolution à l’intérieur de systèmes binaires

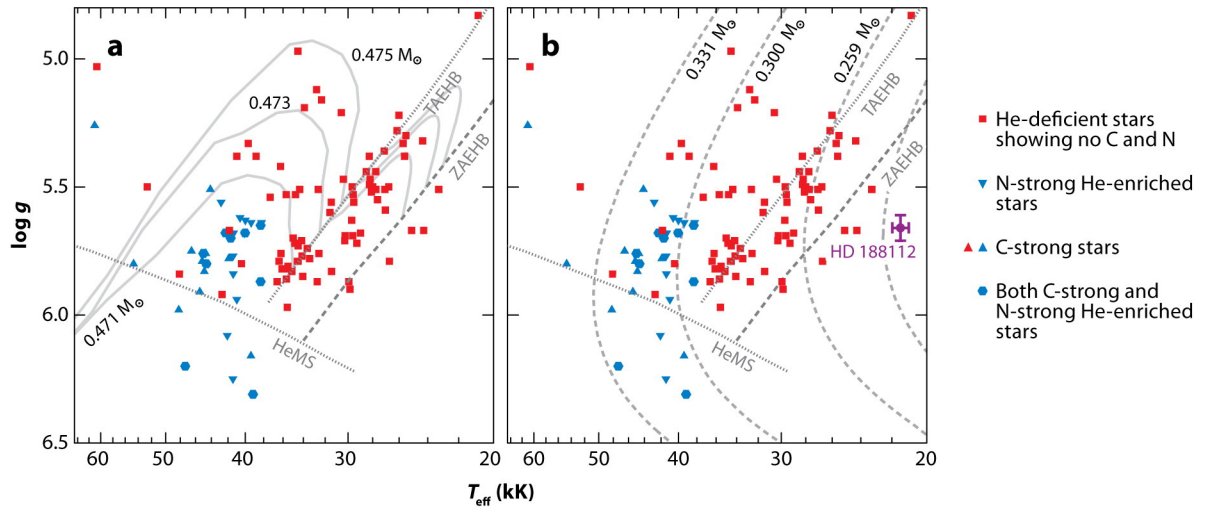
Une fraction importante des sdB réside dans des systèmes binaires. Selon les différents échantillons analysés, cette proportion varie entre 30 % pour l’échantillon 2MASS de Stark & Wade (2003) à 60 % dans le cas de l’échantillon de Maxted et al. (2001) en passant par 40 % pour l’échantillon SPY de Napiwotzki et al. (2004). Ces études ne ciblaient pas nécessairement le même type de systèmes binaires, mais elles démontrent hors de tout doute qu’une fraction importante des sdB a évolué avec la présence d’un compagnon. Comme le démontre d’ailleurs les travaux de Han et al. (2002; 2003), l’importante perte de masse que doit subir le progéniteur d’une sous-naine sur la RGB s’explique plus naturellement par des scénarios d’évolution à l’intérieur de systèmes binaires que par les scénarios impliquant une étoile isolée. Les mécanismes possibles menant à la perte de l’enveloppe d’hydrogène d’une géante rouge dans un

système binaire ont été examinés par Han et al. (2002; 2003) et trois scénarios principaux en sont ressortis.

1. La formation par phase d'enveloppe commune (CE) a lieu lorsque qu'un transfert de masse instable s'établit entre le progéniteur de la sdB, une géante rouge, et son compagnon, une étoile de la séquence principale (MS) ou une naine blanche (WD). Dans cette situation, le compagnon ne peut accréter toute la matière perdue par l'étoile géante, ce qui occasionne la formation d'une enveloppe de gaz englobant les deux étoiles. La friction entre le gaz et les étoiles occasionne une perte d'énergie orbitale. Ceci a pour effet de faire diminuer la période orbitale du système et de mener à l'éjection de l'enveloppe de gaz. Il en résulte un système binaire rapproché (incluant une sdB et une étoile de la MS ou une WD) dont la période se situe entre 0.1 et 10 jours.
2. Un transfert de masse stable (sans formation de CE) peut avoir lieu entre une géante rouge et un compagnon de la MS. Il en résultera une sdB avec une étoile de la MS dans un système binaire à longue période (10 - 500 jours).
3. Il serait aussi possible qu'un système binaire de naines blanches (à coeur d'hélium) rapprochées perde suffisamment d'énergie par ondes gravitationnelles pour que les deux composantes fusionnent.

C'est le rapport de masse initiale entre les deux étoiles du système qui détermine le type de transfert (stable ou instable) qui aura lieu entre les étoiles. Le troisième cas, bien que possible, ne semble pas être responsable de la formation d'une fraction importante des sous-naines; il prédit une vitesse de rotation plutôt rapide pour l'étoile résultante, ce qui n'est pas observé (Geier & Heber 2012).

La découverte récente de petites planètes autour d'une sdB grâce aux données du satellite Kepler ouvre la possibilité à un nouveau mécanisme de formation. Les planètes observées autour de KPD 1943+4058 sont possiblement les coeurs rocheux de planètes joviennes qui se seraient retrouvées dans l'enveloppe de leur étoile hôte lors de sa phase géante rouge (Bear & Soker 2012; Passy et al. 2012). Un phénomène similaire à celui de la phase d'enveloppe commune dans un système binaire pourrait alors avoir lieu, amenant les planètes très proche du coeur de l'étoile et occasionnant l'éjection d'une partie de l'enveloppe de celle-ci. Les




 Heber U. 2009.
Annu. Rev. Astron. Astrophys. 47:211–51

FIGURE 1.3 – Figure tirée de Heber (2009).

résidus planétaires dans un scénario comme celui-ci étant extrêmement difficiles à détecter, s'ils survivent, il est possible que ce phénomène soit à l'origine de la formation de sous-naines apparemment isolées.

1.2.3 Évolution post-EHB, post-AGB et sous-naines de faible masse

Qu'arrive-t-il par la suite à ces étoiles de la EHB avec leur quantité infime d'hydrogène? Sans brûlage d'hydrogène en couche, elles ne produisent pas assez d'énergie pour entreprendre l'ascension de la branche asymptotique des géantes (AGB) comme le ferait une étoile de la HB. Elles vont plutôt suivre un chemin évolutif bien à elles sur des séquences appelées post-EHB (voir la Figure 1.3, panneau *a*). Essentiellement, l'étoile devient un peu plus lumineuse puis sa température augmente alors qu'elle se contracte vers la séquence de refroidissement des naines blanches en passant dans la région des sdO. Strictement parlant, ces sdO ne font pas partie de la EHB, elles sont plutôt associées à la phase post-EHB de brûlage en couche de l'hélium. Une partie des sdO pauvres en hélium sont donc des descendantes des étoiles sdB. Les sous-naines qui ont subi un flash d'hélium tardif vont éventuellement évoluer d'une façon similaire, comme il est possible de constater à la Figure 1.2, et devenir elles aussi des naines blanches.

Deux autres types d'étoiles traversent la région des sous-naines dans le diagramme H-R. Tout d'abord certaines étoiles post-AGB et post-Early AGB de faible masse ($0.5-0.6 M_{\odot}$) vont traverser le diagramme $\log g - T_{\text{eff}}$ à des gravités plus faibles et des températures plus élevées que celles des séquences post-EHB (coin supérieur gauche du diagramme *a* à la figure 1.3). Ces étoiles se dirigent elles aussi vers la région des naines blanches. Certaines sdO parmi les plus chaudes et les plus lumineuses peuvent donc être des post-AGB.

À l'autre extrême, certaines étoiles vont quitter la RGB en ayant perdu tellement de masse qu'elles ne pourront tout simplement pas brûler d'hélium. Elles vont donc devenir directement des naines blanches de faible masse à coeur d'hélium. De telles séquences évolutives sont illustrées au panneau *b* de la Figure 1.3. Les temps évolutifs de telles séquences sont beaucoup plus rapides que ceux des étoiles de la EHB, et donc seulement une infime fraction des sous-naines ont une masse trop faible pour brûler de l'hélium.

1.3 Spectroscopie et modèles d'atmosphères

1.3.1 Principe de base de la spectroscopie quantitative

Au-delà de l'indication du type spectral d'une étoile, il est possible d'extraire d'un simple spectre, ou de plusieurs spectres de la même étoile, plusieurs informations supplémentaires. La spectroscopie peut ainsi fournir de précieuses informations comme la vitesse radiale d'une étoile, sa vitesse de rotation, la présence d'un champ magnétique, la composition chimique de l'atmosphère, etc. Dans le cas des sous-naines pulsantes, les analyses astérosismologiques donnent parfois plus d'une solution possible en terme de température effective et de gravité, souvent ce sont les valeurs de ces paramètres obtenues par analyse spectroscopique qui permettent de trouver un unique modèle stellaire. Déterminer les paramètres atmosphériques de Feige 48, une sdB pulsante, pour mieux en contraindre les modèles sismiques est d'ailleurs l'un des buts de l'article présenté au Chapitre 4. Il n'est cependant pas toujours simple d'extraire les informations voulues de données spectroscopiques. Parfois, cela requiert des observations très minutieuses et parfois il faut des modèles sophistiqués avec lesquels comparer nos observations.

Dans le cas des sous-naines chaudes, les trois paramètres fondamentaux qui déterminent l'allure du spectre de l'étoile sont la température effective (T_{eff}), la gravité de surface ($\log g$) et l'abondance d'hélium ($\log N(\text{He})/N(\text{H})$). Déterminer ces paramètres permet de placer les étoiles dans des diagrammes $\log g - T_{\text{eff}}$ comme ceux montrés à la Figure 1.3. Ces diagrammes fournissent entre autre de l'information en ce qui a trait au statut évolutif des sous-naines. De plus, les relations qui existent parfois entre ces différents paramètres sont autant d'indices qui aident à comprendre les phénomènes physiques à l'oeuvre dans l'atmosphère de ces étoiles et qui servent à améliorer les modèles évolutifs. Ces trois paramètres fondamentaux influencent le spectre visible des sous-naines de différentes façons. Dans l'intervalle de température auquel se trouvent les sous-naines (22 000 K à $\sim 90\,000$ K), les raies de Balmer se comportent de façon monotone par rapport à la température; la force des raies décroît lorsque la température augmente. Les raies d'hélium sont elles aussi influencées dans une certaine mesure par la température, cette dernière détermine en partie les abondances relatives de l'hélium I et II. Pour ce qui est de la gravité de surface, elle est reliée à la densité du gaz. De façon générale, lorsque la valeur de $\log g$ augmente, la densité dans l'atmosphère de l'étoile augmente aussi. Une forte densité occasionne un élargissement des raies atomiques qu'on appelle l'élargissement par pression (ou collisionnel). L'abondance d'hélium quant à elle se détermine bien évidemment avec la force des raies d'hélium présentes dans le spectre.

Il existe différentes techniques pour déterminer ces paramètres à partir des spectres. Toutefois, la plus répandue dans le domaine et celle qui sera utilisée dans les différents chapitres de cette thèse consiste à déterminer simultanément les trois paramètres à l'aide d'une procédure de minimisation du khi-carré (χ^2). Pour ce faire, il faut une grille de spectres synthétiques, obtenue à l'aide de modèles d'atmosphères, qui représentent le mieux possible l'atmosphère de l'étoile qu'on cherche à modéliser. Des modèles sont calculés pour différentes combinaisons de T_{eff} , $\log g$ et $\log N(\text{He})/N(\text{H})$ de façon à obtenir une grille en trois dimensions, puis les spectres synthétiques obtenus sont comparés au spectre observé à l'aide de la procédure de minimisation. De cette façon, il est possible de trouver la combinaison de paramètres qui reproduit le mieux les raies d'hydrogène et d'hélium présentes dans le spectre optique de l'étoile.

1.3.2 Les modèles d'atmosphères

L'un des éléments essentiels de la spectroscopie quantitative est la construction de modèles d'atmosphères; ce sont ces modèles qui permettent de produire les spectres synthétiques. Un modèle d'atmosphère ne comprend que les couches superficielles d'une étoile, là où la radiation s'y échappe; c'est ce qu'on appelle la photosphère. Il s'agit de modéliser la distribution spectrale du flux de l'étoile à partir d'une profondeur où cette distribution est essentiellement celle d'un corps noir jusqu'à la surface où le flux émergent a bien peu en commun avec la fonction de Planck. Pour déterminer la distribution du flux émergent, il faut connaître les propriétés du gaz qui compose l'atmosphère tels que son équation d'état et son opacité. Ces propriétés permettent de définir la structure en pression de l'atmosphère, qui est gouvernée par les contraintes de l'équilibre hydrostatique. La structure thermodynamique ainsi obtenue pour les couches superficielles de l'étoile permet de résoudre l'équation de transfert radiatif qui détermine la distribution du flux aux différentes fréquences du spectre. La résolution de cette équation se fait de façon itérative jusqu'à satisfaire la contrainte d'équilibre radiatif, c'est-à-dire que le flux radiatif doit être conservé; il demeure le même à chaque couche de l'atmosphère.

On fera une distinction entre deux types de modèles d'atmosphères selon la façon dont sont calculés les populations des niveaux d'ionisation et d'énergie atomiques. Les modèles dit ETL utilisent l'approximation de l'équilibre thermodynamique local où les populations atomiques dépendent uniquement des conditions locales de température et de pression. Cependant cette approximation n'est pas toujours valide. Dans les étoiles chaudes, par exemple, le rayonnement émergent des couches chaudes (et profondes) de l'atmosphère affecte les populations atomiques. Dans ce cas, chaque processus microscopique susceptible de peupler ou dépeupler un niveau doit être individuellement pris en compte dans les modèles dit hors-ETL (HETL). Ce traitement plus complexe est nécessaire pour modéliser de façon réaliste l'atmosphère des sdO, dont les températures sont assez élevées pour que les effets HETL y soit présent. Le traitement HETL étant beaucoup plus complexe que l'approximation ETL; il demande plus de temps de calcul ainsi que des méthodes astucieuses pour solutionner l'équation de transfert radiatif. C'est dans les années 70 que les premiers traitements HETL ont été effectués,

principalement grâce aux travaux de Mihalas (Mihalas 1978).

Par la suite, le défi a été d'intégrer des éléments métalliques, comme le carbone, l'azote et l'oxygène dans les modèles d'atmosphères. Ajouter de tels éléments en HETL implique de devoir calculer les populations d'un très grand nombre de niveaux atomiques en considérant un nombre encore plus grand de transitions possibles entre ces niveaux. D'importants développements sur ce front ont eu lieu dans les années 90 (Dreizler & Werner 1993; Hubeny & Lanz 1995) et deux codes de modèles d'atmosphères distincts sont utilisés depuis pour traiter les effets des métaux en HETL dans un contexte d'étoiles compactes (sous-naines et naines blanches). Les modèles d'atmosphères utilisés pour les analyses présentées dans les prochains chapitres sont faits avec l'un de ces codes, TLUSTY, développé par I. Hubeny et T. Lanz (Hubeny & Lanz 1992).

1.3.3 Spectroscopie quantitative des sous-naines chaudes

La spectroscopie quantitative est la technique utilisée dans les chapitres de cette thèse afin d'étudier des étoiles sous-naines chaudes dans différents contextes. Il peut donc s'avérer pertinent de présenter tout d'abord certains aspects particuliers de la spectroscopie des sous-naines.

1.3.3.1 Effets hors-ETL et ceux des métaux

Le principal effet HETL dans les modèles sans métaux a été noté dès les premiers calculs de ce genre effectués par Auer & Mihalas (1969). On y observe une augmentation de la température à la surface de l'étoile alors qu'un traitement ETL produit une structure en température qui décroît de façon monotone. Cette différence de structure en température provoque généralement un élargissement des raies de Balmer (Mihalas & Auer 1970, Napiwotzki 1997) qui deviennent aussi plus profondes. Une inversion de température dans les couches atmosphériques d'une étoile peut aussi produire de l'émission dans le coeur des raies si celles-ci sont formées suffisamment haut dans la photosphère. Ce phénomène est le plus souvent observé dans $H\alpha$, la raie de Balmer formée le plus près de la surface, mais peut aussi être présent dans $H\beta$ ainsi que dans les raies d'hélium II les plus fortes. Dans les sous-naines, ce

type d'émission apparaît dans les spectres de sdO très chaudes comme BD+28°4211 (Herbig 1999). Il est impossible d'obtenir une telle émission avec des modèles d'atmosphères ETL.

L'ajout des éléments métalliques (comme le carbone, l'azote, l'oxygène et le fer) dans les modèles va quant à lui refroidir les couches externes de l'atmosphère alors que les couches internes vont se réchauffer. L'émission centrale dans le coeur de certaines raies est aussi accrue par la présence de métaux. De plus, les raies de Balmer et d'hélium ont tendance à devenir plus profondes. Évidemment, ces effets vont dépendre des paramètres du modèle comme sa température et sa gravité, mais Latour et al. (2011) ont aussi montré que l'abondance d'hélium influence les effets des métaux. Finalement, Dreizler & Werner (1993), ainsi que Lanz & Hubeny (1995), ont souligné l'importance d'inclure les métaux de façon cohérente dans les modèles d'atmosphères. Il faut savoir ici que les modèles HETL avec métaux, surtout lorsqu'on y inclut du fer, demandent beaucoup de temps de calculs. Une solution économique parfois utilisée est donc de construire un modèle d'atmosphère HETL sans métaux et d'y ajouter ensuite, par exemple, du fer en calculant les populations de façon ETL avec la structure atmosphérique obtenue sans métaux. De cette façon, on peut avoir des raies de fer dans les spectres synthétiques sans toutefois que cet élément ait influencé la structure de l'atmosphère. Cette méthode économique peut cependant donner des résultats erronés. Dreizler & Werner (1993) ont montré que dans un modèle cohérent, où les métaux sont utilisés pour déterminer la structure en température, les effets HETL ont tendance à favoriser les plus hauts degrés d'ionisation. Si l'équilibre d'ionisation est différent selon le type d'approche utilisée, lors d'une analyse d'abondance les résultats dépendront aussi du type de modèle. Il n'est pas toujours facile de savoir à l'avance si les effets HETL vont influencer de façon importante l'équilibre d'ionisation et les raies d'un élément donné, c'est pourquoi l'approche cohérente est préférable.

1.3.3.2 Le problème des raies de Balmer

L'un des problèmes bien connu depuis Napiwotzki (1992) est le *problème des raies de Balmer*, qui se manifeste dans les étoiles chaudes ($T_{\text{eff}} \gtrsim 50\,000$ K) pour lesquelles il n'est pas possible de trouver des paramètres ($T_{\text{eff}} - \log g$) qui reproduisent simultanément les raies de Balmer. Plus précisément, les modèles prédisent des raies de Balmer trop peu profondes

par rapport à celles observées dans les spectres. De plus, si chaque raie de Balmer est ajustée individuellement, il en résulte d'importantes différences entre les températures indiquées par chacune d'entre elle. De façon générale, l'ajustement de $H\alpha$ donne une température beaucoup plus faible que celle indiquée par $H\delta$ alors que $H\beta$ et $H\gamma$ donnent des résultats intermédiaires.

Napiwotzki (1993) s'est penché sur le cas de BD+28°4211 et a estimé une température effective d'environ 82 000 K à l'aide de l'équilibre d'ionisation des raies d'He I et II. Puisque la température ainsi obtenue correspondait à celle indiquée par la raie $H\epsilon$, il en conclut que l'utilisation de $H\epsilon$ ou encore $H\delta$ est susceptible de donner des résultats fiables pour l'estimation de la température effective des étoiles affectées par le problème des raies de Balmer.

Différentes pistes ont été explorées pour solutionner ce problème comme les effets d'un vent stellaire ou d'un champ magnétique, ainsi que la remise en question des calculs de profils de raies pour l'hydrogène. Ces hypothèses n'ont cependant pas donné les résultats escomptés et ont rapidement été rejetées (Napiwotzki & Rauch 1994). La solution la plus prometteuse s'est avérée être l'ajout d'éléments métalliques dans les modèles d'atmosphères de ces étoiles.

Il a été démontré par la suite (Haas et al. 1996; Lanz et al. 1997), que l'ajout des métaux peut influencer significativement la forme des raies de Balmer et d'hélium dans le domaine optique, et par le fait même, les paramètres atmosphériques qu'on obtient lors d'un ajustement. Lanz et al. (1997), en faisant l'analyse de BD+75°325 (une sdO), ont montré qu'avec des modèles sans métaux, ils reproduisent le spectre de l'étoile avec une température de 58 000 K alors qu'il faut plutôt une température de 52 000 K lorsque du C, N, O, Si, Fe et Ni sont inclus dans les modèles d'atmosphères. Selon Haas et al. (1996), les métaux n'ont toutefois pas un effet suffisamment important pour résoudre entièrement le problème des raies de Balmer. C'est finalement Werner (1996) qui propose une meilleure solution en incluant dans ses modèles des profils de raies détaillés tenant compte de l'élargissement Stark pour le C, N, O. Ces profils ont permis de mieux reproduire les raies de BD+28°4211 et de LS V +46°21 (une naine blanche très chaude au centre d'une nébuleuse planétaire). Par contre, Werner (1996) utilise des paramètres atmosphériques déterminés par d'autres méthodes lors d'études précédentes; aucun ajustement formel des raies n'a été effectué. Même dans la récente analyse détaillée de LS V +46°21 par Rauch et al. (2007), les auteurs ne font pas d'ajustement simultané

des raies présentes dans le spectre optique. Ils déterminent plutôt la meilleure température à l'aide de l'équilibre d'ionisation de quelques espèces métalliques présentes dans le spectre UV qu'ils confirment avec la raie d'He II à 4686 Å. Pour ce qui est de la gravité de surface, ils l'obtiennent à l'aide de la raie d'He II 1640 Å dans l'UV et de $H\beta$ dans le visible.

Bien qu'étant moins dramatique que dans les années 90, le problème des raies de Balmer demeure présent dans les étoiles très chaudes et la détermination de températures effectives basées sur leur spectre visible demeure un exercice délicat. Par exemple, il est possible d'obtenir un ajustement acceptable du spectre visible mais de se retrouver malgré tout avec des paramètres atmosphériques erronés. Ce fut le cas avec l'étoile post-AGB GD 605, dont le spectre visible indiquait une température effective de 58 400 K alors que cette température était incompatible avec le spectre UV qui nécessitait plutôt 85 000 K. Pour ces étoiles chaudes, la prudence est donc de mise et c'est pourquoi un spectre UV s'avère presque essentiel pour s'assurer de la validité des paramètres atmosphériques, surtout la température.

Le domaine UV est riche en raies métalliques des différentes espèces atomiques présentes dans l'atmosphère. L'analyse de ces raies est un excellent moyen pour déterminer l'abondance des métaux présents dans l'atmosphère de l'étoile mais permet aussi de contraindre la température de l'étoile via l'équilibre d'ionisation. Souvent on retrouve dans le spectre d'une étoile des raies provenant de différents ions d'un même élément, par exemple, à la Section 2.5.1, il sera question de raies de Fe V, VI et VII. Puisque la température influence les populations ioniques d'un élément, et donc l'intensité des raies émises par ces ions, il est très difficile de reproduire simultanément (avec une abondance unique) ces raies spectrales avec une température erronée. Une température trop basse favorisera l'état d'ionisation le plus faible alors qu'une température trop chaude produira des raies trop fortes pour l'état d'ionisation plus élevé. Voilà pourquoi cette méthode peut permettre de bien cerner la température effective d'une étoile. Elle possède tout de même ses propres inconvénients: les spectres UV sont plus difficiles à obtenir (ils requièrent des observations faites de l'espace), les raies métalliques sont nombreuses et peuvent se superposer, et finalement les raies d'absorption du milieu interstellaire sont bien présentes dans ce domaine de longueur d'onde. C'est pourquoi le principal but du Chapitre 3 sera de trouver une méthode pour déterminer les paramètres atmosphériques

de sdO chaudes à l'aide de spectres optiques seulement.

1.4 Format de cette thèse

Cette thèse comprend quatre articles destinés à la revue *The Astrophysical Journal*: un publié, un soumis et deux en préparation. Ces articles ont comme point commun l'utilisation de modèles d'atmosphères HETL avec métaux qui servent de base à l'analyse spectroscopique de différentes étoiles sous-naines chaudes dans des contextes variés.

Les Chapitres 2 et 3 portent sur une étoile sdO particulièrement chaude: BD+28°4211. Puisqu'il s'agit d'une étoile relativement brillante, elle est souvent utilisée comme étoile de référence dans le domaine visible. Sa température élevée en a aussi fait une étoile de calibration pour les télescopes spatiaux observant dans l'UV. Elle a déjà été mentionnée à quelques reprises dans ce document puisque c'est une des étoiles qui a servi à caractériser le problème des raies de Balmer. Ayant en main des données observationnelles d'une qualité exceptionnelle, nous avons décidé d'utiliser BD+28°4211 comme sujet de notre étude de ce problème particulier. Dans un premier temps les observations UV de l'étoile seront utilisées pour déterminer la composition chimique de son atmosphère. Nous examinerons aussi comment ces données peuvent aider à contraindre la température effective et la gravité de l'étoile. Après avoir exploité la portion UV du spectre de BD+28°4211 et déterminé les abondances métalliques de son atmosphère, nous nous attaquerons à la partie visible, et plus problématique, de son spectre dans le Chapitre 3. Notre objectif pour ce chapitre sera de trouver une façon d'obtenir les paramètres atmosphériques de l'étoile en utilisant uniquement des spectres visibles de celle-ci.

Le Chapitre 4 porte sur une étoile différente, Feige 48, une sdB pulsante ayant une température aux environs de 30 000 K. Nous utiliserons donc cette fois-ci nos modèles d'atmosphères dans un régime de température différent. Nous verrons que pour une étoile aussi "froide" que Feige 48, les effets des métaux en HETL sont relativement faibles et les paramètres fondamentaux déterminés avec ce type de modèles se rapprochent de ceux trouvés dans la littérature.

Le Chapitre 5 est consacré à l'analyse spectroscopique d'un échantillon d'étoiles faisant partie de la EHB de l'amas globulaire ω Cen. Rappelons que c'est dans cet amas que les

premières sous-naines pulsantes “hors champ” ont été découvertes. Notre travail a découlé d’un projet cherchant à caractériser la zone d’instabilité des sous-naines pulsantes de cette amas. Pour ce faire de la spectroscopie de bonne qualité a été obtenue pour un échantillon d’une cinquantaine d’étoiles et nous avons exploité celle-ci dans le but de quantifier les abondances d’hélium et de carbone présentes dans ces étoiles. Nous verrons que nos résultats soulèvent plusieurs interrogations quant à l’évolution des sous-naines riches en hélium de l’amas.

Finalement, cette thèse se terminera par une conclusion au Chapitre 6.

Chapitre 2

A NLTE ANALYSIS OF THE HOT SUBDWARF O STAR BD+28°4211. I. THE UV SPECTRUM

M. Latour¹, G. Fontaine¹, P. Chayer², and P. Brassard¹

¹ *Département de Physique, Université de Montréal, Succ. Centre-Ville, C.P. 6128,
Montréal, QC H3C 3J7, Canada*

² *Space Telescope Science Institute, 3700 San Martin Drive, Baltimore, MD 21218, USA*

Received 2013 April 18; accepted 2013 June 12; published 2013 July 29

Published in *The Astrophysical Journal*

August 2013, Volume 773:84

Reproduced by permission of the AAS

2.1 Abstract

We present a detailed analysis of the UV spectrum of the calibration star BD+28°4211 using high-quality spectra obtained with the *Hubble Space Telescope* and *Far-Ultraviolet Spectroscopic Explorer* satellites. To this aim, we compare quantitatively the observed data with model spectra obtained from state-of-the-art non-LTE metal line-blanketed model atmospheres and synthetic spectra calculated with TLUSTY and SYNSPEC. We thus determine in a self-consistent way the abundances of eleven elements with well-defined lines in the UV, namely those of C, N, O, F, Mg, Si, P, S, Ar, Fe, and Ni. The derived abundances range from about solar to 1/10 solar. We find that the overall quality of the derived spectral fits is very satisfying. Our spectral analysis can be used to constrain rather tightly the effective temperature of BD+28°4211 to a value of $T_{\text{eff}} = 82,000 \pm 5000$ K. We also estimate conservatively that its surface gravity falls in the range $\log g = 6.2_{-0.1}^{+0.3}$. Assuming that the *Hipparcos* measurement for BD+28°4211 is fully reliable and that our model atmospheres are reasonably realistic, we can reconcile our spectroscopic constraints with the available parallax measurement only if the mass of BD+28°4211 is significantly less than the canonical value of $0.5 M_{\odot}$ for a representative post-extended horizontal branch star.

2.2 Introduction

BD+28°4211 is a hot subdwarf O (sdO) star whose brightness, high effective temperature, and relatively simple spectrum have made it a standard star in the optical domain as well as a calibration star for UV space missions such as *IUE*, *HST*, and *FUSE*. Its status of standard star implies that some of its observational properties are very well known. For example, high precision *UBVRI* magnitudes have been presented by Landolt & Uomoto (2007). In addition, its parallax measurement in the *Hipparcos* catalog places the star at 92_{-11}^{+14} pc. While studying BD+28°4211 as a spectrophotometric standard, Massey & Gronwall (1990) found it to have a faint red companion at a separation of $2''.8$. Moreover, BD+28°4211 has been extensively observed in the UV range by the missions mentioned above and there are highly valuable data available on that star. Ultraviolet spectra are precious tools for studying the chemical

composition via the numerous metallic lines present in this wavelength range. It could be thought that with this privileged status, BD+28°4211 would have been thoroughly studied and its physical parameters would be accurately known, but this is not exactly the case. In this connection, it has to be mentioned that because of its high effective temperature (around 80,000 K), the local thermodynamic equilibrium (LTE) approximation is inappropriate for model atmospheres intended to represent the star. Instead, the more sophisticated and realistic approach of non-LTE (NLTE) has to be used. Given the physical and technical difficulties associated with that approach, however, more efforts remain to be made along that avenue in order to characterize better the atmosphere of this star.

The first determination of the effective temperature of BD+28°4211, using quantitative spectroscopy, has been made by Napiwotzki (1993) who estimated it to be around 82,000 K. He determined this value by comparing the Balmer lines of the star with those of NLTE model atmospheres with a variable H/He ratio (but with no metals) for different effective temperatures and surface gravities. This method is now largely used and its ability to give reliable fundamental parameters (T_{eff} , $\log g$, and sometimes also $N(\text{He})/N(\text{H})$) for white dwarfs and hot subdwarf B stars has already been demonstrated (Bergeron et al. 1992; Saffer et al. 1994). However, this method is rather tricky in the case of BD+28°4211 because, like others sdO stars and white dwarfs that have high temperatures, the model spectra used generally suffer from the so-called Balmer line problem. That is, the observed lines cannot be simultaneously matched with a unique model spectrum. In other words, each line needs a model of different effective temperature in order to be well reproduced. Usually, the lowest lines in the series (like $\text{H}\alpha$ and $\text{H}\beta$) need a lower temperature, while the highest ones are better reproduced at higher temperatures. In the case of BD+28°4211, to give the “extreme” values, $\text{H}\alpha$ was best reproduced at $T_{\text{eff}} \simeq 50,000$ K and $\text{H}\epsilon$ at around 85,000 K (Napiwotzki 1993). The author also found a $\log g$ value of 6.2 and a solar helium abundance to be appropriate values for BD+28°4211. His best estimate of the effective temperature of $\sim 82,000$ K was subsequently confirmed by Dreizler & Werner (1993) who checked that parts of the *IUE* UV spectrum of BD+28°4211, showing Fe VI and Fe VII lines, are properly reproduced at around 82,000 K. This time, the NLTE model atmospheres they used included metals, namely carbon,

oxygen, nitrogen, and iron group elements that were grouped together into six model atoms (one for each ionization stages between III and VIII). With similar models, and on the basis of the same *IUE* spectrum, Haas et al. (1996) estimated the abundance of iron to be about ten times subsolar while nickel was found to be nearly solar. According to them, oxygen and nitrogen also have abundances near the solar value. The improved UV spectra taken with the Space Telescope Imaging Spectrograph *STIS* onboard the HST allowed to derived a solar abundance of manganese, while a sole line of chromium indicated an abundance between two and four times the solar value (Ramspeck et al. 2003).

The inclusion of metallic elements in NLTE model atmospheres, though costly in terms of computation time and complexity, allows not only for more realistic models, but also permits to solve, at least in part, the Balmer line problem (Werner 1996). We will address this issue in more details in the second paper of this series (M. Latour et al. 2013, in preparation). The optical spectrum of BD+28°4211 is rather featureless in comparison to its rich UV spectrum. Except for the Balmer and He II lines, nothing else is seen at medium resolution in the optical range. Because of this, BD+28°4211 was chosen to be part of an investigation of diffuse interstellar bands in OB stars given its uncomplicated spectrum. However, the high resolution HIRES spectra of the star obtained for this investigation at the Keck I telescope show a lot of narrow absorption lines as well as a handful of emission lines (Herbig 1999). The sharpness of the absorption lines allowed to set an upper limit on the star’s rotational velocity, $v \sin i \lesssim 4 \text{ km s}^{-1}$, which is quite slow.

As for the high-quality *FUSE* spectrum of BD+28°4211, it has only been used to study interstellar abundances in the line of sight of the star (Sonneborn et al. 2002). To our knowledge, this data set has not been exploited so far to better characterize the star. Although we have a general idea of its atmospheric chemical composition, no comprehensive or systematic studies were made on that star. With high-quality data available from *HST* and *FUSE* in particular, we felt we should exploit them in order to reexamine the chemical composition of BD+28°4211 and also try to constrain better its effective temperature and surface gravity by studying the ionization equilibrium of some metallic elements. Getting a portrait of the chemical composition of BD+28°4211 should also be a first step in studying the optical spectrum

of the star, with appropriate model atmospheres, for the Balmer line problem.

In the second section of this paper we describe our model atmospheres. This is followed by a short description of the observational material we used and of our abundance analysis in Section 2.3. We then discuss our attempts at constraining the effective temperature and the surface gravity by using the ionization equilibrium of metals in the UV range as well as the parallax distance in Section 2.4. Finally, we present a discussion and conclusion in Section 2.5.

2.3 Model Atmospheres

2.3.1 Characteristics of Our Model Atmospheres

We have developed the capacity to compute large grids of NLTE metal line-blanketed model atmospheres over reasonable timescales (days to weeks) with our parallel versions of TLUSTY and SYNSPEC that run on a dedicated cluster of computers (currently containing 320 processors). Our setup is described in more details in Latour et al. (2011) and has not changed since, apart from the increase in the number of processors we have available. Our final fully-blanketed model atmospheres for BD+28°4211 include the following ions (besides those of H and He): C II to C V, N II to N VI, O II to O VII, Si III to Si V, P IV to P VI, S III to S VII, Fe IV to Fe VIII and Ni III to Ni VII. The highest ionization stage of each element is taken as a one-level atom. More information on the model atoms we used can be found on TLUSTY's Web site¹ and in Lanz & Hubeny (2003, 2007). Since our thorough examination of BD+28°4211's UV spectrum revealed also lines of argon, magnesium and fluorine, we needed to construct additional model atoms in order to study the abundance of these extra elements. This was done with the MODION program² which uses the TOPBASE data (Lanz et al. 1996). This program allows the user to choose the explicit energy levels and also build superlevels that are included in the model atom. We thus constructed in this way model atoms for the following ions : F III with 9 levels and 5 superlevels, F IV with 11 levels and 5 superlevels, F V with 19 levels and 3 superlevels, F VI with 12 levels and 5 superlevels, Mg III with 37 levels and 3 superlevels, Mg IV with 29 levels and 5 superlevels, Mg V with 18 levels and 2

¹<http://nova.astro.umd.edu/Tlusty2002/tlusty-frames-data.html>

²<http://idlastro.gsfc.nasa.gov/ftp/contrib/varosi/modion/README>

superlevels, Ar IV with 39 levels, Ar V with 25 levels, Ar VI with 20 levels, and Ar VII with 18 levels. All transitions (bound-bound and bound-free) between these levels are thus considered when the ions are included in a model atmosphere.

Since Werner (1996) underlined the importance of using Stark profiles for CNO lines when modeling atmospheres of hot stars such as BD+28°4211, we inspected our different model atoms to check what kinds of profiles were used. We found that the strongest transitions (often resonance lines) of each ion are treated with Stark profiles while the weaker ones are represented by Doppler profiles. We then examined a synthetic spectrum that could represent BD+28°4211 and identified its most prominent lines and made sure they were described with a Stark profile in the corresponding atomic model. This way we added a classic Stark profile to a few more lines of some elements, namely C IV, N IV, O IV and O V, Si IV and P V. A striking effect that Werner (1996) noticed when including Stark profiles was the disappearance of a high-temperature bump around $\log m$ of -3 g cm^{-2} which was present when using Doppler profiles only (see his Figure 1). Since this bump is not seen either in our models (see our Figure 2.1), we believe our atomic data are appropriate for the study of BD+28°4211 or other hot stars. Note that, even without modifying the original model atoms used by Lanz & Hubeny (2003, 2007), our temperature structures do not present this bump (see Figure 4 of Latour et al. 2011).

The inclusion of our metallic elements must be done “step by step” if we want to assure the convergence of our models. Too drastic changes in the physical parameters of the model atmosphere used as input and the one we want to compute will prevent the latter from converging. Thus, when constructing a grid of these line-blanketed models, we end up with a number of “subgrids” including only some of the elements mentioned above. In the case of BD+28°4211, we built five “subgrids” in order to end up with our final fully-blanketed one. For example, we have a grid including only C, N, and O in solar abundances, from which comes one of the models plotted in Figure 2.1.

In Figure 2.1, we show the temperature stratification for models with $T_{\text{eff}} = 82,000 \text{ K}$, $\log g = 6.2$, and having a solar helium abundance culled from three of our grids. These estimates of the atmospheric parameters come from the work of Napiwotzki (1993). The first model is a

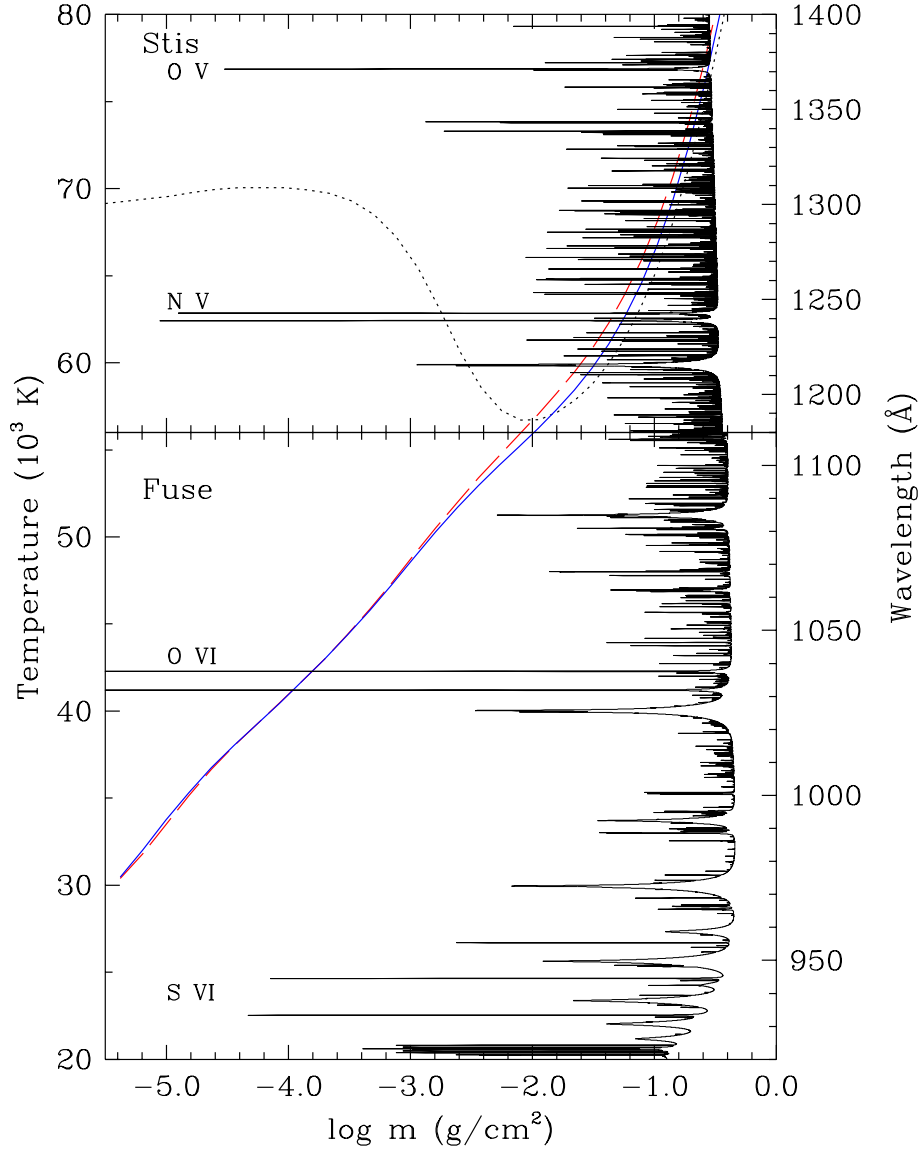


FIGURE 2.1 – Temperature stratification and monochromatic optical depth $\tau_\nu = 2/3$ as functions of depth, where m is the column density, for NLTE models defined by $T_{\text{eff}} = 82,000 \text{ K}$, $\log g = 6.2$, and $\log N(\text{He})/N(\text{H}) = -1.0$. The temperature structure is shown for models including H and He only (dotted curve), H, He, and CNO in solar abundances (solid curve), and H, He, and CNOSiPSFe in solar abundances (dashed curve). The $\tau_\nu = 2/3$ curve is from the latter model and shows part of the FUSE and STIS wavelength range in the UV.

“classical” pure H+He NLTE model that shows the well known outwardly rise of temperature near the surface (dotted curve). The second one includes C, N, and O (solid curve), while the third one includes all the elements of our final model (see above) besides nickel (dashed curve). At this point, all our elements have a solar abundance (Grevesse & Sauval 1998). Though we plotted only three models in the figure, we examined the ones (having the same parameters) from our other grids and concluded that adding S, P and Si to the C, N, O, only induces a minor drop of the temperature in the outer layers ($\log m < -2$). When we add nickel to models already including C, N, O, Si, P, S, and Fe, the changes in the temperature structure are unnoticeable on a graph like Figure 2.1. The cooling of the outer layers is thus mostly done by the inclusion of C, N, O elements; adding more metals does not cool anymore the surface. As for the inner layers, their heating comes essentially from the presence of C, N, O, as well as Fe that was included afterward in the third model depicted in the figure.

It is easy to see from the temperature stratification that metallic elements, though they are not the dominant ones in the atmosphere, have an important effect on the thermodynamic structure at the surface of the star. Via their important opacity, they block a non-negligible part of the flux in the UV range, thus rising the continuum in the optical range. The presence of metals also causes a heating of the inner layers of the atmosphere, while it cools the outer layers. These changes in the atmospheric structure influence the emergent spectrum of the star, and thus the Balmer lines themselves. This is why their presence is an essential ingredient in the solution of the Balmer line problem (Werner 1996).

The other curve featured in Figure 2.1 shows the optical depth $\tau_\nu = 2/3$ as a function of the column density m . It allows us to locate where the continuum and different lines are formed. The most opaque features, formed very near the surface, are the core of the resonance doublets of S VI, O VI and N V as well as the O V line at 1371 Å. As for the broadest lines, they are either hydrogen or helium II ones. Depending on where a line is formed in the atmosphere, it might be affected differently by a change of the temperature structure.

In a model atmosphere with fundamental parameters like those of BD+28°4211, some of the atomic species have a sole ion which dominates the atmosphere while the other ionization degrees have populations that are lower by orders of magnitude. This is the case for carbon,

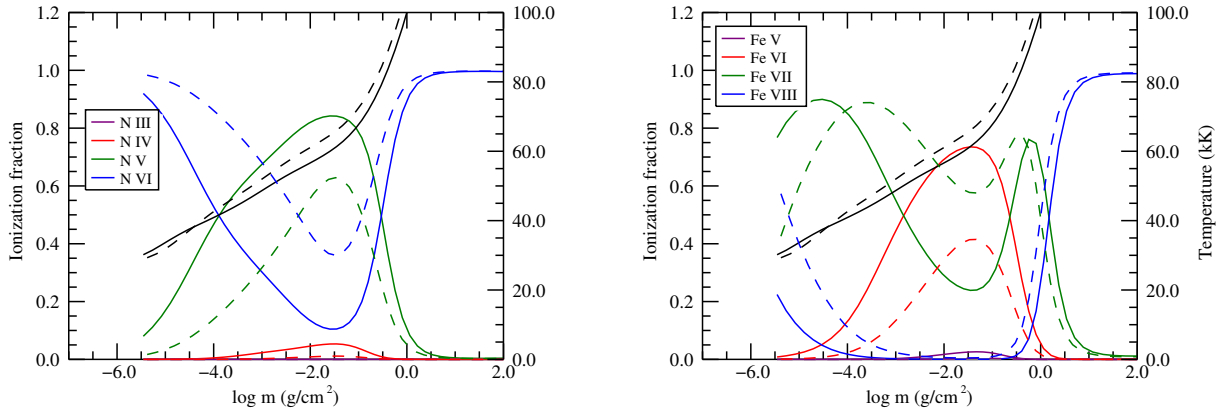


FIGURE 2.2 – a) (left) Ionization fractions of nitrogen as functions of depth in models with $T_{\text{eff}} = 82,000$ K (solid lines) and $92,000$ K (dashed lines), $\log g = 6.2$, and $\log N(\text{He})/N(\text{H}) = -1.0$. The black curves show the temperature profiles of the two models. b) (right) Similar to Fig. 2.2a, but this time showing the ionization structure of iron.

silicon and phosphorus, where ions in a noble gas configuration (C v, Si v and P vi) are the ones that contribute the most to the thermodynamic structure of the atmosphere. The population of the other elements is dominated by ions of different ionization degrees depending on the depth in the atmosphere. We show the ionization equilibria of nitrogen and iron in Figure 2.2 for models including all the elements mentioned at the beginning of this section and having an effective temperature of $T_{\text{eff}} = 82,000$ K (solid lines) and $T_{\text{eff}} = 92,000$ K (dashed lines), a surface gravity $\log g = 6.2$, and a solar helium content. The temperature is also shown in black for each model. Though the equilibrium changes as function of depth, N v is dominant in the line forming region (around $\log m = -1$) while Fe vi and vii are in comparable proportions in this region for the model at $82,000$ K. However, when the temperature is raised to $92,000$ K, Fe vii become more dominant.

2.3.2 A Word on the Inclusion of Metallic Elements

By self-consistently including each element we want to study in our models, we allow it to influence the thermodynamical structure of the atmosphere. This is crucial if we want to get the right ionization equilibria and populations for our different ions. Dreizler & Werner (1993) show that large discrepancies can arise in the strength of iron lines in a synthetic

spectrum, depending on whether iron is included in a NLTE and self-consistent way or not. The inconsistent approach uses LTE statistics to obtain iron populations and ignore the back-reaction of the element on the atmospheric structure. The discrepancies increase between the two methods as the NLTE effects increase (as well as the abundance of the element in question), which means in our case, when the effective temperature increases. For BD+28°4211, it is essential that the elements we want to fit be consistently included in the models.

The TLUSTY package allows to add new elements afterward in the synthetic spectrum computed by SYNSPEC. Even though it is an inconsistent approach, we tried it just to take a look at some lines of additional elements we did not plan to include in our models because of their expected low abundances, the lack of model atoms, as well as the limit on the number of atomic levels and transitions the code can handle without becoming unstable. Even though for some atomic species we could easily make model atoms with the TOPBASE data, it is not the case for the iron-peak elements. They are not present in TOPBASE (except for iron) and their data (for iron and nickel) come from the Kurucz atomic data sets. Building model atoms for other elements of the iron peak would be a far more complex task than what was done for magnesium, fluorine, and argon. That being said, we added a solar amount of manganese, cobalt, and chromium in SYNSPEC to an already line-blanketed model atmosphere computed without these elements. When the resulting spectrum was compared with observations, it immediately appeared that there was a problem with the ionization equilibrium. Both Mn and Cr show lines of two different ions (v and vi); lines corresponding to the higher ionization degree were well reproduced by our model while the ones from the lower degree were not correctly matched. In order to illustrate this, we included nickel in our synthetic spectrum with the determined abundance of this element (see Section 2.4.1) and compared the result with our final model, which included nickel in the model atmosphere. We show in Figure 2.3 two regions of the STIS spectrum featuring some Ni v and vi lines. The two upper panels show the comparison between the observed spectrum of BD+28°4211 and the synthetic one obtained by adding nickel ($\log N(\text{Ni})/N(\text{H}) = -6.0$) in SYNSPEC only. The lower ones show the result of adding the same amount of nickel this time directly in the model atmosphere. In the case of nickel, Ni vi lines are definitely not strong enough in the upper panels, which

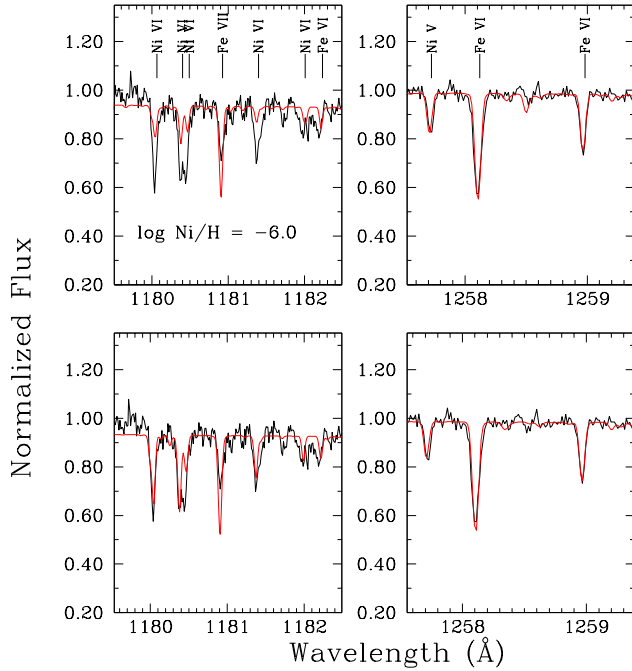


FIGURE 2.3 – Comparison between portions of the observed STIS spectrum of BD+28°4211 and synthetic spectra. The two upper panels show the synthetic spectra obtained when nickel is included in the spectrum only, thus in an inconsistent manner. In the lower panels, nickel was included from the beginning in the model atmosphere. It is possible to see the differences arising from the two ways of treating the presence of nickel in the models.

is consistent with the observations of Lanz & Hubeny (2003) that NLTE effects favor higher ionization degree due to the strong radiation field coming from the hotter and deeper layers that causes overionization. In the other hand, the Ni v line shows in the second portion of the spectrum, as well as the few other we examined, remain quite unaffected by the difference in the inclusion method.

2.4 Abundance Analysis

2.4.1 Observational Material

2.4.1.1 FUV and UV Observations

A wealth of FUV and UV observations of BD+28°4211 has been gathered over the years. As we have mentioned earlier, BD+28°4211 has been used as a calibration star by several space observatories. In order to find all the FUV and UV observations of BD+28°4211, we

carefully searched the Mikulski Archive for Space Telescopes (MAST)³. Spectroscopic observations of BD+28°4211 have been obtained not only with space observatories such as *IUE*, *FUSE*, and *HST*, but also with instruments such as the Orbiting Retrievable Far and Extreme Ultraviolet Spectrometers and the Hopkins Ultraviolet Telescope that flew on space shuttle missions. Moreover, the *HST* spectroscopic observations include observations obtained with the Goddard High-Resolution Spectrograph and STIS. After retrieving the BD+28°4211 data from MAST and looking at the available data, we selected the *FUSE* and STIS observations in order to carry out our spectroscopic analysis. The choice of these spectroscopic data is based on the wide wavelength range covered by both instruments, and on their higher resolution and higher signal-to-noise ratio (S/N) than the data obtained by other instruments. The next two sections describe in detail the *FUSE* and STIS data that we selected for our analysis.

2.4.1.2 *FUSE* Observations

FUSE covers a wavelength range of 905 Å to 1187 Å with a resolution of about $R = \lambda/\Delta\lambda = 20,000$. For more information about the design of the instrument and the spectroscopic data products, see Moos et al. (2000), Sahnou et al. (2000), and Dixon et al. (2007). During the lifetime of the *FUSE* mission, several observations of BD+28°4211 have been carried out under three calibration programs. The first *FUSE* observation of BD+28°4211 was obtained through the program M108 in order to establish the suitability of the star to the calibration program, given that its FUV flux was close to the bright limit of the *FUSE* detectors. Subsequently, BD+28°4211 was observed under the program M104 to test the use of the focal plane splits (FP splits) in order to mitigate the fixed-pattern noise, and therefore to increase the S/N of the final spectrum. This technique consisted in taking a series of exposures at different focal plane assembly positions. In this way, the corresponding spectra were shifted along the dispersion direction and exposed on different portions of the detectors. The fixed-pattern noise was therefore reduced by co-aligning and co-adding all the spectra. The M104 observations consisted of exposures using the LWRS and MDRS apertures. Finally, two series of short observations taken through the LWRS, MDRS, HIRES apertures were carried out under the

³<http://archive.stsci.edu/index.html>

M103 program, which monitored the photometric stability of the *FUSE* instrument.

We selected the M1080901, M1040101, M104105, M1031201, and M1031204 observations. All these observations were taken through the LWRS aperture and recorded in spectral image mode, or histogram (HIST) mode. We considered 66 exposures with an average exposure time of about 485 s, such that the total exposure time amounts to about 32,000 s. The eight *FUSE* segments, LiF1A, LiF1B, LiF2A, LiF2B, SiC1A, SiC1B, SiC2A, and SiC2B were cross-correlated and co-added. All LiF1B exposures show a depression in flux between 1130 Å and 1170 Å. This depression in flux is caused by a electron repeller wire grid that can cast shadows on the detectors. The LiF1B data in this wavelength range were not considered. A final co-added *FUSE* spectrum was obtained by considering and merging the following spectral regions: SiC1B(905–990 Å), LiF1A (990–1080 Å), SiC2B (1080–1090 Å), LiF2A (1090–1180 Å), and LiF1B (1180–1187 Å). The final spectrum has a signal-to-noise ratio $S/N \sim 68$ at 950 Å, $S/N \sim 130$ at 1050 Å, and $S/N \sim 89$ at 1150 Å.

The *FUSE* spectrum displays many interstellar and stellar absorption lines. The most prominent stellar lines are the Lyman series of hydrogen starting from Ly β up to Ly-8. There are followed by the He II lines that involve transitions between energy levels $n_l = 2 \rightarrow n_u = 4$ up to 13. Transitions with upper even numbers produce, however, lines that are blended with the hydrogen Lyman lines. The strongest metal lines are the O VI $\lambda\lambda$ 1031.91 and 1037.61 resonance lines that have equivalent widths of about 400 mÅ each. It is interesting to note that the O VI doublet does not display any P Cygni profile characteristic, which suggests that no stellar wind expanding away from BD+28°4211 is detected. In addition to the O VI lines, many metal lines of highly ionized species are observed. For instance, the following ions are observed in the *FUSE* spectrum: C IV, N IV, O IV, O V, F IV, F VI, Si IV, P V, S IV, S V, S VI, Ar VII, Fe VI, Fe VII, Co VI, and Ni VI. The equivalent widths of the metal lines range from a few mÅ to ~ 150 mÅ. Although a large number of metal lines have been identified, there are still about 150 absorption features with no identification. This state of affairs is also observed in FUV and UV spectra of many hot stars, and reflects the lack of atomic data for highly ionized species. Finally, the *FUSE* spectrum of BD+28°4211 contains a large number of strong absorption lines from interstellar H₂, and also several absorption lines from species

TABLE 2.1 – STIS Datasets Retrieved From StarCAT

Dataset	Grating	λ_{cen} (Å)	Range (Å)	Exp. Time (s)
E140M-1425_020X020_50710-53135	E140M	1425	1140.5–1730.0	20607
E140H-1416_020X020_50812-53135	E140H	1416	1325.1–1505.8	15311
E230M-1978_020X020_50710-53135	E230M	1978	1611.1–2150.1	9510
E230H-2263_020X020_50812-53135	E230H	2263	2139.5–2394.0	22962
E230H-2513_020X020_52461	E230H	2513	2386.5–2639.6	2674
E230M-2707_020X020_50678-53135	E230M	2707	2629.6–3118.2	22547

such as H I, D I, C I, C II, N I, O I, P II, Ar I, and Fe II. Sonneborn et al. (2002) analyzed the line of sight toward BD+28°4211 by using *FUSE* and STIS data, and measured interstellar D I, H I, N I, O I, Fe II and H₂ column densities.

2.4.1.3 STIS Observations

Since the installation of STIS on board *HST* in 1997, BD+28°4211 has been observed to monitor the sensitivity of each Multi-Anode Microchannel Array (MAMA) echelle grating mode. Although STIS suffered a major failure in 2004 August, it returned to science operations after being repaired during the fourth *HST* servicing mission in 2009 May. To this date about 206 observations of BD+28°4211 have been carried out with the echelle gratings E140M and E140H FUV-MAMA, and the E230M and E230H NUV-MAMA. Specifically, BD+28°4211 has been observed with the following echelle grating setups: E140M (central wavelength of spectrum $\lambda_{\text{cen}} = 1425$ Å; wavelength range 1140–1729 Å), E140H (1416 Å; 1316–1517 Å), E230M (1978 Å; 1607–2365 Å), E230H (2263 Å; 2128–2396 Å), E230H (2514 Å; 2385–2650 Å), and E230M (2707 Å; 2275–3118 Å). Therefore the spectroscopic coverage ranges from 1140 Å to 3118 Å. The resolution $R = \lambda/\Delta\lambda$ for the E140M and E230M is $\sim 45,800$, and it is $\sim 114,000$ for the E140H and E230H. All the observations were carried out by using the $0''.2 \times 0''.2$ aperture. The exposure times for the individual observations are on average ~ 360 s and ~ 500 s for the E140M and E230M observations, and they are ~ 1000 s and ~ 1500 s for the E140H and E230H observations.

Instead of using all the STIS observations of BD+28°4211 that are available at MAST, we opted to retrieve the observations from StarCAT⁴, which is a STIS echelle spectral catalog

⁴<http://archive.stsci.edu/prepds/starcat/>

of stars that Ayres (2010) created based on observations of high-resolution spectra. StarCAT contains all the echelle high-resolution spectra of BD+28°4211 that were collected from 1997 to the failure of STIS in 2004. Given that BD+28°4211 has been observed frequently, Ayres (2010) cross-correlated and co-added all the BD+28°4211 spectra in order to achieve a high S/N. We retrieved six datasets from Ayres (2010)’s StarCAT. The properties of the datasets are summarized in Table 2.1. The table gives the name of the dataset, the grating that was used with its setting λ_{cen} , the wavelength range, and the total exposure time in seconds that is the sum of all the exposures. The resulting S/N for the observations taken with the E140M at $\lambda_{\text{cen}} = 1425 \text{ \AA}$ is S/N ~ 180 at 1250 \AA and S/N ~ 145 at 1500 \AA . The observations performed with the E230H at $\lambda_{\text{cen}} = 2513 \text{ \AA}$ has the shortest exposure time and consequently has the lowest signal-to-noise ratio with S/N ~ 30 at 2500 \AA . The remaining observations have S/N greater than 100. The resulting STIS spectra of BD+28°4211 with their high S/N and large spectral coverage are FUV and UV data of outstanding quality.

As in the case of the *FUSE* data, the STIS data show a large number of absorption lines. The greatest number of lines are observed between 1140 \AA and $\sim 1475 \text{ \AA}$. Beyond 1475 \AA , the intensity and the number of lines decrease dramatically. On the short wavelength side, absorption lines of high-ionization species such as Fe V, Fe VI, Fe VII, Co VI, Ni V, and Ni VI are the most numerous. The equivalent widths of these absorption lines vary from a few m \AA to $\sim 75 \text{ m\AA}$. The strongest line observed in the STIS spectrum is Ly α . In fact, most of the absorption at Ly α comes from the interstellar H I along the line of sight of BD+28°4211. Sonneborn et al. (2002) measured a H I column density of $\log N(\text{H I}) = 19.842$ in the direction of BD+28°4211, and showed that the stellar H I component is much fainter than the interstellar absorption. The second strongest observed line is the He II $\lambda 1640$ line ($n_l = 2 \rightarrow n_u = 3$) that has an equivalent width of about 1200 m\AA . The line shows broad wings that extend to about 4.5 \AA from the center of the line, and it shows a shallow core. Interestingly, the He II line series $n_l = 3 \rightarrow n_u = 6$ up to 11 is observed at longer wavelengths. The wings of these He II lines are also broad, but the lines show a much shallower core than the He II $\lambda 1640$ line. The N V $\lambda\lambda 1238, 1242$ lines and O V $\lambda 1371$ line are the strongest metal lines observed in the STIS spectrum. The lines have equivalent widths of about 770 m\AA , 482

mÅ, and 574 mÅ. The total equivalent widths of the Si IV $\lambda\lambda$ 1393, 1402 lines and C IV $\lambda\lambda$ 1548 and 1550 lines have equivalent widths of about 125 mÅ and 340 mÅ.

Even though we have identified most stellar and interstellar absorption lines in the STIS spectrum of BD+28°4211, there are still about 260 lines that do not have any identification. The equivalent widths of these lines range from a few mÅ to a few ten of mÅ. The total approximate number of lines with no identification in both *FUSE* and STIS spectra is around 410 lines. We extended our search of metal lines to elements beyond Zn. For instance, O’Toole & Heber (2006) and Chayer et al. (2006) observed strong absorption lines of heavy elements such as Ga, Ge, Zr, Sn, and Pb in *FUSE* and STIS spectra of sdB stars, while Vennes et al. (2005) and Chayer et al. (2005) observed Ge and Sn in a handful of hot DA white dwarfs, and Ge, As, Se, Br, Sn, Te, and I in two cool DO white dwarfs. Werner et al. (2012) added the discovery of Kr and Xe in the atmosphere of the DO white dwarf RE 0503–289 to the list of heavy elements detected in the atmospheres of compact stars. We looked for these heavy elements in both *FUSE* and STIS spectra by using the wavelengths of the high-ionization species. We also added Mo to our search. Unfortunately, no lines from heavy elements are observed. There is an absorption feature around 987.6 Å that could correspond to the As V λ 987 line, but no absorption feature matches the second component of the As V doublet at 1029.48 Å adequately. As we have concluded in the previous section, the non-identification of many absorption features in the *FUSE* and STIS spectra of BD+28°4211 illustrates the lack of atomic data of high-ionization species.

2.4.2 Fitting Technique and Resulting Abundances

Our fitting technique consists in minimizing a χ^2 -type value defined as the sum of the squared difference between the model and observed fluxes over a given range of wavelength. Our free parameters are the solid angle and, obviously, the abundance of the fitted element. It is also possible to add a trend (linear or quadratic) if the continuum in the range of interest needs one, which was sometimes useful since the normalized UV spectra are not always as flat as they should.

The method used to determine the abundance is a partial iterative one. First of all, from

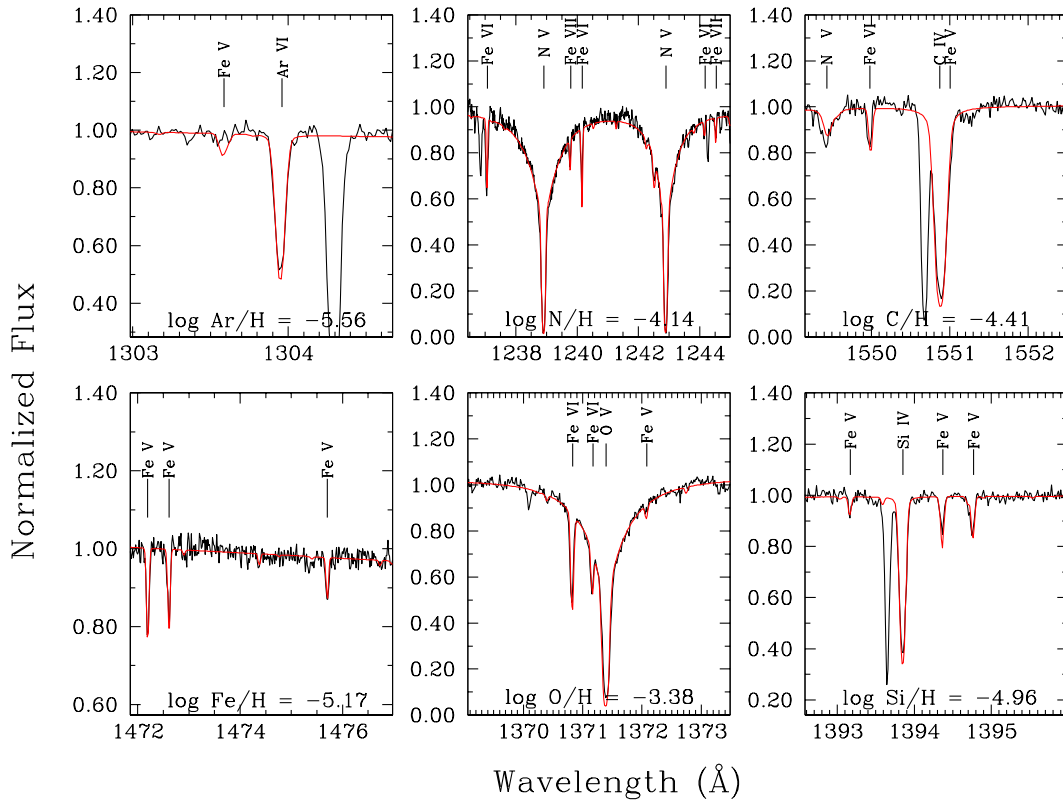


FIGURE 2.4 – Sample of our fitted spectral intervals from the STIS spectrum. The red curve shows the result of the fitting procedure for the element mentioned at the bottom of each panel, where the resulting abundance for the interval is expressed as $\log N(X)/N(H)$. All our models have $T_{\text{eff}} = 82,000$ K, $\log g = 6.2$, and $\log N(\text{He})/N(H) = -1.0$. Interstellar features are visible in some spectral chunks, such as a strong Si II line beside Ar VI $\lambda 1303$ and shortward-shifted C IV and Si IV lines.

the work of Napiwotzki (1993), the temperature and gravity of our models are held fixed at $T_{\text{eff}} = 82,000$ K and $\log g = 6.2$, and the helium abundance is fixed at the solar value. Most of our metal grids consist of six or seven different abundances centered around the solar one and varying in steps of 0.5 dex. For example, in the case of oxygen (whose solar abundance is $\log N(\text{O})/N(\text{H}) = -3.3$), its grid covers a range from $\log N(\text{O})/N(\text{H}) = -2.0$ to -4.5 in steps of 0.5 dex. Since we have a better idea of the iron and nickel abundances (thanks primarily to the work of Ramspeck et al. (2003)), their grid meshes are narrower; between one tenth and one time solar for iron, and centered around the solar value for nickel, but this time varying only in steps of 0.2 dex. In the first step of the procedure, we used models including C, N, O,

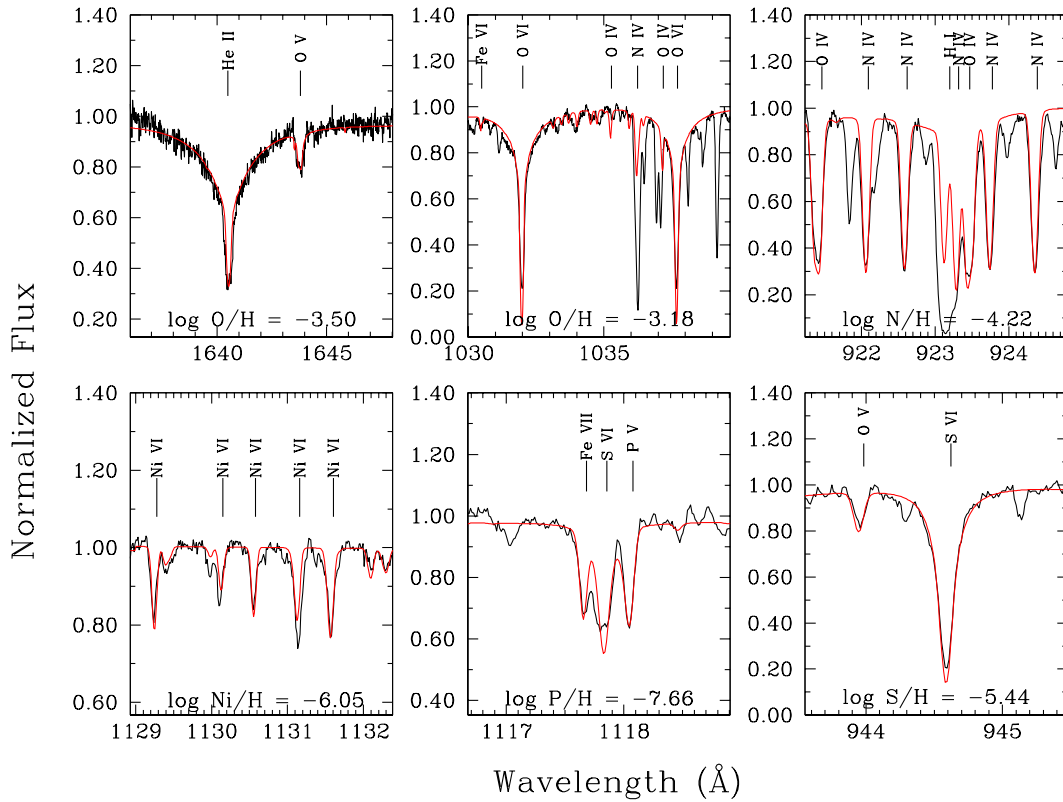


FIGURE 2.5 – Same as Figure 2.4 but for parts of the FUSE spectrum, except for the first interval, showing He II $\lambda 1640$, which comes from the STIS spectrum. Note the He II line which is particularly well reproduced with the assumed fundamental parameters. There is a lot more interstellar lines in the FUSE wavelength range. We notice in this figure, among others, C II $\lambda 1036.3$, O I $\lambda\lambda 1039.19$, 921.82 and C I $\lambda 945.15$.

and Fe in solar abundances initially and then varied the abundances of these four elements, one at a time. We then used these improved models to build the grids for silicon, sulfur, and phosphorus. We were then able to obtain a first estimate of the abundances for these seven elements. The number of lines fitted for each element is given in Table 2.2. We carefully chose lines that are reasonably well isolated in regions of the spectrum not too crowded with blends or interstellar lines. Our second step was to redo our grids for each element, this time including the previously found abundances for the other elements. At this point, when redoing our fitting procedure, the values found for individual lines sometimes changed a little, but the mean abundances stayed roughly the same. Once we got the abundances of C, N, O,

TABLE 2.2 – BD+28°4211 Chemical Composition — Results of our abundance analysis

Element (Ions)	No. of Intervals (No. of Lines)	Mean Abundance $\log N(X)/N(H)$	Standard Deviation (dex)	Total Uncertainty (dex)
C (IV)	3 (3)	-4.48	0.16	0.46
N (IV, V)	4 (8)	-4.23	0.19	0.78
O (IV, V, VI)	10 (15)	-3.48	0.15	0.46
F (IV, V, VI) ^a	1 (1)	-8.00	–	0.50
Mg (IV)	7 (7)	-4.57	0.12	0.45
Si (IV)	3 (3)	-4.95	0.06	0.30
P (V)	2 (2)	-7.45	0.29	0.52
S (V, VI)	8 (8)	-5.53	0.18	0.47
Ar (VI, VII)	2 (2)	-5.53	0.04	0.43
Fe (V, VI, VII)	11 (33)	-5.08	0.12	0.32
Ni (V, VI)	7 (17)	-6.04	0.21	0.48

^a Fluorine was not formally fitted, we visually examined some lines in order to estimate an abundance. See the text for more details.

Si, P, S, and Fe fixed, we made new grids in order to obtain, this time, a value for nickel, fluorine, magnesium, and argon. The new grids for these four elements only included, besides the element of interest, C, N, O and Fe, which are the atomic species playing the major role in setting up the atmospheric structure. We took a particular interest in argon because the spectrum of BD+28°4211 features two strong lines of this element, coming from two ionization states : Ar VI at 1303.86 Å and Ar VII at 1063.63 Å.

After these three steps, we were able to draw up a good portrait of the chemical composition of BD+28°4211, with quite satisfactory fits. Our final results are summarized in Table 2.2. The first column shows the different elements as well as the ionic species present in our sample of fitted lines. We then give the number of fitted intervals (like the six ones presented in Figure 2.4) and the total number of lines (from the element of interest) included in those intervals. The third column presents the mean abundance of the analyzed ranges while the fourth one gives the standard deviation associated with the previous column. Finally, the last one gives the total uncertainty of our abundances, which will be discussed in the next subsection.

We tentatively tried to formally fit some fluorine lines, but since they were either too faint, or blended the results were not conclusive. Our result is thus based on a sole isolated line, F IV λ 1059.719, for which we visually estimated an abundance of $\log N(F)/N(H) = -8.0$ to

be appropriate. The resulting comparison can be found in the last panel of Figure 2.9. This result is compatible with the other lines we checked ($\lambda\lambda$ 1082.345, 1088.400 and 1139.523), although these lines are either blended or in a noisy region of the spectrum for which their faintness does not help.

For the sake of completeness, we also examined the chromium, manganese and cobalt lines visible in our spectra and estimated their abundances. This time we had to add these elements afterward in the synthetic spectrum (as explained in Section 2.2.2) where their populations were computed assuming LTE. The model atmosphere used as input for the spectra computation included our main metallic elements (C, N, O, Si, P, S, Fe, and Ni). The abundances of the three studied elements were in turn varied in the synthetic spectra and then fitted the same way we did for the other elements. In order to avoid the ionization problem discussed in Section 2.2.2, we fitted only lines coming from the dominant ionization stage, which is VI for these three iron-peak elements. As for the previously fitted elements, the uncertainties include the standard deviation as well as effects from a change of temperature and surface gravity in the input model atmosphere. Despite the fact that our resulting abundances presented in Table 2.3 are only rough estimates, obtained with an approximate method, our values for Cr and Mn are in good agreement with the ones found by Ramspeck et al. (2003), which were around -5.88 for Cr and -6.62 for Mn.

Figures 2.4 and 2.5 show a sample of our fitted intervals taken from the STIS (Figure 2.4) and *FUSE* (Figure 2.5, except the top left panel) spectra. The abundance resulting from the fitting procedure of the featured region is given as $\log N(X)/N(H)$. We show here the final step of our fitting method, so the elements included, besides the fitted one, have abundances corresponding to the ones presented in Table 2.2. The totality of our fitted spectral chunks are available as supplementary material.

Some of our intervals include important interstellar lines, such as O I, N I, C I, H I and H₂. Interstellar shortward-shifted C IV and Si IV components are also seen for both doublets lines (one of which is shown in Figure 2.4). These features are thought to originate from a circumstellar cloud or shell near the star (Bruhweiler & Dean 1983). Since BD+28°4211 has some similarities with central stars of old planetary nebulae in its spectrum as well as in

TABLE 2.3 – Chromium, manganese and cobalt estimated abundances (LTE)

Element (Ions)	No. of Intervals (No. of Lines)	Mean Abundance $\log N(X)/N(H)$	Standard Deviation (dex)	Total Uncertainty (dex)
Cr (VI)	4 (4)	-6.17	0.31	0.41
Mn (VI)	5 (6)	-6.71	0.21	0.32
Co (VI)	5 (11)	-6.71	0.12	0.25

its fundamental parameters, this could be some sort of old planetary nebula remnant. When strong ISM lines are present in our fitted intervals, we exclude them from our minimization procedure by iteratively rejecting wavelength points of the observed spectrum too far from the model's ones.

We carefully inspected each fitted range to make sure the resulting model was appropriate, the continuum was at a satisfactory level, and to notice any discrepant lines. Our checkup highlighted some points we found worth mentioning.

First of all, if we consider the most prominent features (i.e., resonance and strong lines), they are all well reproduced. The only exception is the O VI doublet ($\lambda\lambda 1032, 1038$), for which the cores happen to be too opaque in our models. This phenomenon can also be seen, at a smaller amplitude, in the cores of the resonance doublet of S VI ($\lambda\lambda 933, 944$), in S VI $\lambda 1117.76$ and in O V $\lambda 1371.3$. We have to mention here that the analysis of Rauch et al. (2007) has been a useful reference to us on this particular account. They analyzed STIS and *FUSE* spectra of a star (LS V +46°21) whose fundamental parameters ($T_{\text{eff}} = 95,000$ K and $\log g = 6.9$) give it a spectrum quite similar to that of BD+28°4211, in the sense that both star show lots of common lines. It allows us to compare some of our fits with theirs. This way, we noticed that they reported the same effect of too strong cores in resonance lines of their star, letting us know the issue is not only about our own model atmospheres.

Secondly, when choosing our sample of lines to be fitted, a few lines gave inconsistent results or could not be matched in any way whatsoever. For instance, our attempt to fit the O IV structure around 1081 \AA was not conclusive enough to be included in our final sample because the core of the central component at 1080.97 \AA was too strong in our models. The N IV triplet between 1225 and 1226 \AA required a much higher abundance ($\log N(N)/N(H) =$

−3.2) than our other lines of nitrogen, so we did not include it our sample. The same thing happened for O v λ 968.9, but this time we suspect this line to be blended with interstellar H₂ lines at 968.997 and/or 969.07 Å. This possibility is supported by the few H₂ lines present in the vicinity of the oxygen line.

Finally, some odd lines of oxygen appear in our models, whereas there is no sign of them in the observed spectrum. We noticed O III λ 1153.775 and two O IV lines at 1076.06 and 1294.065 Å. A too strong oscillator strength value might be the cause of their presence. We should also mention four other lines, among which three of them appear also too strong in our final model, namely Fe v λ 1393.072 and Fe VII $\lambda\lambda$ 1154.990, 1180.827. As for the last one, Ni VI at 1204.078 Å is too faint in our models and was excluded from our fitted nickel sample. However, these lines also appear too strong (or too faint for the nickel one) in the final model of Rauch et al. (2007), so there is a strong chance that the oscillator strengths of the lines are involved here.

2.4.3 Evaluation of the Abundance Uncertainties

Hot stars sometimes “become” hotter with time, in the sense that their estimated effective temperature tend to be revised upwards. For example, the DAO white dwarf LS V +46°21, has seen its estimated effective temperature go from 83,000 K in Napiwotzki (1999) to 95,000 K in the thorough study of Rauch et al. (2007). In a most extreme case, the white dwarf KPD 0005+5106 was shown to be the hottest known DO in Werner et al. (1994) with an estimated value of $T_{\text{eff}} = 120,000$ K, but a subsequent analysis of better spectroscopic data found lines of highly ionized metals (Ne VIII and Ca X), thus needing the star to have an effective temperature of at least 180,000 K (Wassermann et al. 2010). With these rather extreme cases in mind, we wanted to have an idea of how our abundances would change if the effective temperature or the surface gravity of BD+28°4211 end up being different from our assumed values.

Therefore, we redid a part of our abundance analysis, using in a first step models with an effective temperature of 92,000 K, and then models at $\log g = 6.6$. To do this for all the atomic species studied in the previous section would require computing twice as many grids as we did for determining the abundances themselves. We therefore decided to do this exercise for three

elements only, namely nitrogen, silicon, and iron. The resulting abundances are presented in Table 2.4 which gives, for each model considered, the abundance and standard deviation obtained for the indicated element. The first column specifies the model used in our fitting procedure by indicating the parameter that has been changed with respect to the ones used in the previous section. The first quoted model is our reference model at $T_{\text{eff}} = 82,000$ K and $\log g = 6.2$. One thing to note here is that a change in the effective temperature of the models of the magnitude considered here induces a larger change in the determined abundance than a change in $\log g$. Another interesting thing to look at is the value of σ , the standard deviation of the different spectral chunks we fitted. In the case of iron and nitrogen, this value is larger for $T_{\text{eff}} = 92,000$ K and $72,000$ K, meaning the abundances obtained from each interval agree less with each other than in the reference case. The results for silicon are somewhat different because there is only three fitted lines, produced by a sole ion (Si IV), whereas nitrogen and iron have lines produced by two and three ions. Silicon is thus less expected to show larger discrepancies between its fitted lines at different atmospheric parameters. The behavior of the standard deviation (for nitrogen and iron) with the temperature can be taken as a reassuring sign pointing towards $82,000$ K to be a good value for the star's effective temperature. About the two additional $\log g$ values, their standard deviation for iron is a bit larger than the one found in the previous section but as a whole, they are nevertheless quite similar to the ones obtained with models at $\log g$ of 6.2.

We used the abundance differences between different models in the calculations of the uncertainties reported in Table 2.2. We wanted our chemical composition, within the given uncertainties, to be able to stand a potential change in the fundamental parameters of BD+28°4211. By using the abundances found at $T_{\text{eff}} = 92,000$ K and $\log g = 6.6$, our determined values should remain appropriate for changes of $\pm 10,000$ K and ± 0.4 dex, assuming the errors should be symmetrical in T_{eff} and $\log g$. Although we also have abundances for $72,000$ K and $\log g$ of 5.8 we prefer not to include them in our uncertainty calculations because they are less likely to be realistic values for BD+28°4211. This will be discussed in the next section.

TABLE 2.4 – Determined abundances of nitrogen, silicon and iron

Models	Nitrogen		Silicon		Iron	
	Abundance	σ	Abundance	σ	Abundance	σ
T_{eff} 82 kK	-4.23	0.19	-4.95	0.06	-5.07	0.12
T_{eff} 92 kK	-3.47	0.32	-4.66	0.05	-4.83	0.58
T_{eff} 72 kK	-4.64	0.33	-5.32	0.13	-5.03 ^a	0.35 ^a
$\log g$ 6.6	-4.24	0.16	-4.95	0.02	-4.89	0.20
$\log g$ 5.8	-4.15	0.18	-4.94	0.13	-5.23	0.14

^aThe quality of the iron fits with these models is rather poor.

That being said, our final uncertainties are the sum of three components :

$$\sigma = \sqrt{(\sigma_{\text{fit}})^2 + (\sigma_{T_{\text{eff}}})^2 + (\sigma_{\log g})^2}, \quad (2.1)$$

where σ_{fit} is the standard deviation of the fitted chunks, $\sigma_{T_{\text{eff}}}$ is the difference between the abundances at $T_{\text{eff}} = 92,000$ K and $82,000$ K while $\sigma_{\log g}$ is the difference between the results at $\log g$ of 6.6 and 6.2. For the elements besides nitrogen, silicon and iron, $\sigma_{T_{\text{eff}}}$ and $\sigma_{\log g}$ were taken as the mean values of the three determined ones.

2.5 Constraining the Atmospheric Parameters

2.5.1 With the Metal Lines

As mentioned in the Introduction, finding out the effective temperatures and surface gravities of hot stars is not straightforward and standard methods used on cooler stars do not work very well. A more reliable approach in this case is to look at the metal lines visible in the UV spectrum of the star. A change of temperature will modify the ionization equilibrium of the atomic species present in the photosphere, as shown previously in Figure 2.2, and this will result in changes of the spectral lines strength. The exercise done in the last subsection, when fitting iron and nitrogen with models having different parameters, favors the models at $T_{\text{eff}} = 82,000$ K. The standard deviations of the fitted intervals are smaller with this temperature and moreover, the ionization equilibrium of iron lines cannot be correctly reproduced neither with the hotter or cooler models. This is what is shown in Figure 2.6, where the two left

panels feature an interval of the STIS spectrum including three ionization stages of iron and three model spectra having different temperatures. Fe VI lines do not change much with the effective temperature, but Fe V and VII lines are more sensitive and become quite stronger with, respectively, a lower and higher temperature. The changes are easily seen, even with a difference of 5,000 K between models. Thus, when trying to do a fit of the iron lines, at hotter or cooler temperatures, it is impossible to simultaneously match the lines coming from the three ionization degrees. Indeed, the four fits shown in Figure 2.6 (middle and right panels) are rather poor. Therefore, when looking at iron lines as a temperature indicator, it appears clearly that the temperature of the star must be quite close to 82,000 K.

Figure 2.7 shows the same kind of plots than Figure 2.6, except that this time we changed the value of the surface gravity between $\log g$ of 6.6 and 5.8 while the temperature was fixed at $T_{\text{eff}} = 82,000$ K. Like the temperature, the gravity also affects the iron lines, but to a lesser extend, at least in the ranges investigated. With a higher $\log g$ it is still possible to represent correctly the lines shown in the two right panels, but the fits lead to abundances that are different by 0.45 dex, which is larger than the difference of 0.12 dex obtained with our models at $\log g = 6.2$ (see the Figure 2.6, panel g). When fitting our principal range of interest, 1330-1333 Å, with models having different $\log g$, we do not obtain a match as good as with our reference grid. Indeed, when looking at the standard deviations for the iron fits found in Table 2.4 for the various $\log g$, the agreement is better with the reference model, but σ is not much higher in the two other cases. In the case of nitrogen, the standard deviations of the various $\log g$ do not obviously support a specific gravity. That being said, when considering iron lines, the surface gravity we assumed for our analyses ($\log g = 6.2$) seems to be right.

2.5.2 With the Parallax Distance

Another method that can be used to place constraints on the parameters of BD+28°4211 is to compare its spectroscopic distance with the one determined by parallax measurements, which is between 81 and 106 pc according to the latest reduction of the *Hipparcos* catalog (van Leeuwen 2007). The idea here is to compute the absolute magnitude of a model atmosphere and combine it with the apparent magnitude of the star (recently measured by Landolt &

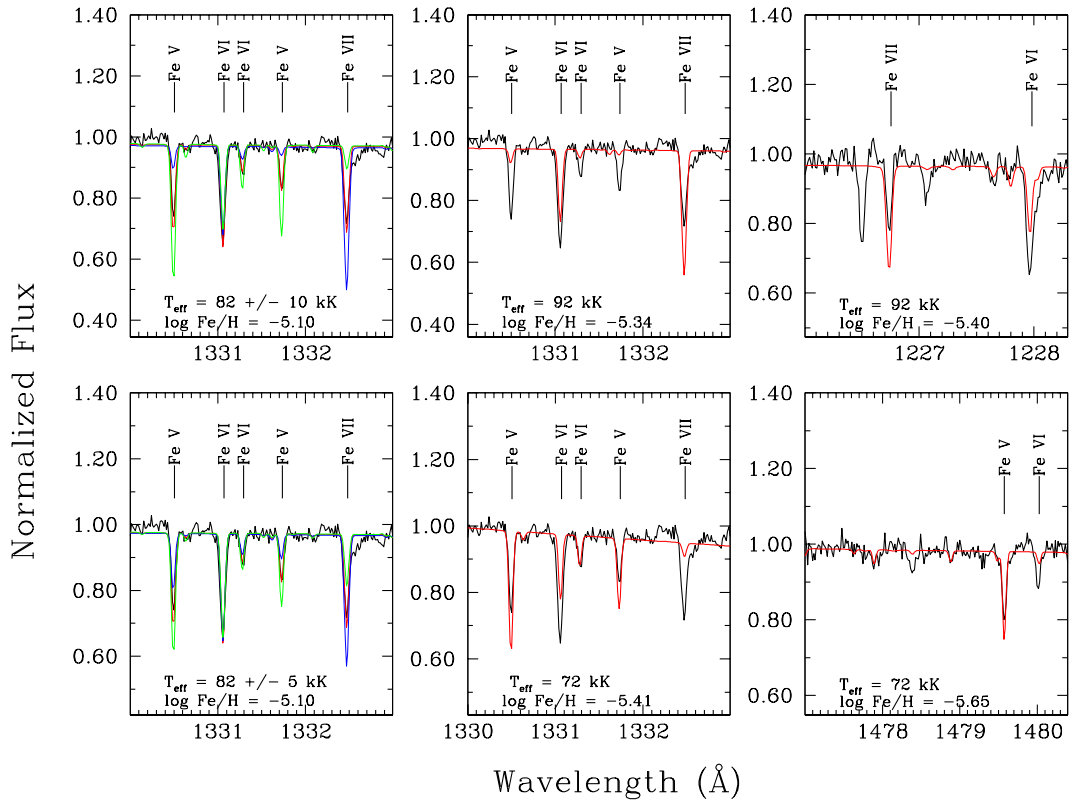


FIGURE 2.6 – Comparison of iron lines with models having different temperatures. The temperature and the abundance of iron are indicated on each panel. The two left panels present a comparison of three model spectra with the spectrum of BD+28°4211 over a range featuring lines from three ionization stages of iron. The standard model at $T_{\text{eff}} = 82,000$ K and $\log g = 6.2$ is represented by the red line, the hotter ones (92,000 K in the top panel and 87,000 K in the bottom one) are in blue, while the cooler models (72,000 K in the top panel and 77,000 K in the bottom one) are in green. It can be seen that with a fixed abundance, a change in the temperature, even of only 5,000 K, leads to a poorer agreement between the observed lines and the modeled ones. The two middle panels show the result of a fitting procedure, over the same wavelength range, with hotter and cooler models, while the right panels also show a fit of iron lines, but over two other spectral ranges.

Uomoto (2007)) to get the distance. In order to do that, some other quantities are required.

First of all, at these distances, reddening must be considered, and we thus computed theoretical, unreddened $(B - V)_o$ color indices for several relevant model spectra. We used the flux calibration of Holberg & Bergeron (2006) to find the absolute B and V magnitudes. By considering six models (with $T_{\text{eff}} = 82,000$ K and 87,000 K, and $\log g = 6.2, 6.4,$ and 6.6), we derived an average representative color index $(B - V)_o = -0.3831 \pm 0.0018$ showing a

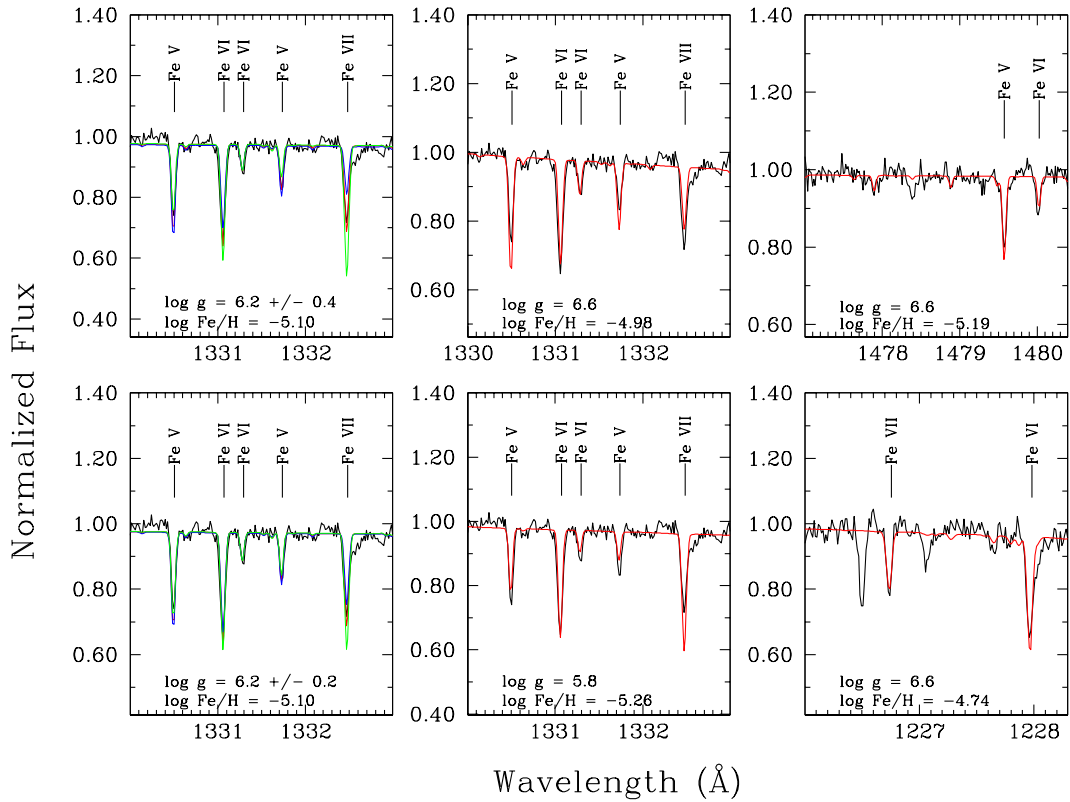


FIGURE 2.7 – Comparisons of iron lines with models at different $\log g$. This figure is very similar to Figure 2.6, but for different values of $\log g$ while the temperature is kept at 82,000 K. The two left panels show the observed spectrum and three models with different surface gravity, having a fixed iron abundance. Models in the upper panel have gravities that change by 0.4 dex with $\log g = 6.2$ as a middle value, while the changes are of 0.2 dex in the lower panel. The spectrum with the highest value is in blue, the middle one in red, and the lowest one in green. The two middle panels show the results of the fits with the two extreme values of $\log g$, while the right panels show different ranges, fitted with models at $\log g$ of 6.6.

very small dispersion (which is, of course, not surprising for a star as hot as BD+28°4211). This is to be compared with the accurate observed value of $(B - V) = -0.3410 \pm 0.0018$ obtained by Landolt & Uomoto (2007), leading immediately to a rather precise reddening index of $E(B - V) = 0.042 \pm 0.003$ for BD+28°4211. Combined with the extinction law proposed by Seaton (1979), this leads to an absorption coefficient in the V band of $A_V = 3.20E(B - V) = 0.135 \pm 0.008$. We note that this value is quite compatible with the overall absorption coefficient of $A_V = 0.3$ along the line-of-sight in the direction of BD+28°4211 as

obtained from the Infrared Science Archive⁵ using data from Schlegel et al. (1998).

Another parameter needed in the computation of the spectroscopic distance is the mass of the star, which allows to find its radius given the surface gravity. Unfortunately, that parameter is largely unknown, except to say that BD+28°4211 must be either a post-asymptotic giant branch (AGB), a post-extended horizontal branch (EHB), or maybe a post-red giant branch (RGB; though this is less likely because of the relatively short timescale of this evolutionary path). Constraints on the mass can then be derived from model calculations of these late evolutionary phases. For instance, according to the evolutionary tracks of Schoenberner (1983) (post-AGB), Dorman et al. (1993) (post-EHB), and Driebe et al. (1998) (post-RGB) and the approximate position of BD+28°4211 in the $\log g - T_{\text{eff}}$ plane, it would appear that its mass should be around $0.5 M_{\odot}$ and could hardly be higher than $0.6 M_{\odot}$ or lower than $0.4 M_{\odot}$. Plots of post-AGB and post-EHB tracks can be found in Figure 1 of Haas et al. (1996), while post-RGB tracks are shown in Figure 10 of Stroeer et al. (2007). However, this is probably not the full story because we know of post-EHB stars with masses less than $0.4 M_{\odot}$, one of which not known to be part of a close binary system (Heber et al. 2005; Randall et al. 2007; For et al. 2010; Fontaine et al. 2012). We cannot therefore exclude a mass for BD+28°4211 less than $0.4 M_{\odot}$ and, as an extreme limit, we will also consider a value as low as $0.3 M_{\odot}$.

Finally, the surface gravity and the effective temperature of a given model atmosphere influence directly the absolute magnitude determined in a given bandpass and, thus, the inferred distance. Since the effective temperature of BD+28°4211 appears to be well constrained by the pattern of iron lines, this parameter was initially fixed at $T_{\text{eff}} = 82,000$ K and we computed the spectroscopic distance of the star for different combinations of mass and surface gravity. This was done by comparing the computed absolute visual magnitude M_V with the well-measured reddened apparent magnitude of $V = 10.509 \pm 0.0027$ provided by Landolt & Uomoto (2007)

Our results are presented in Table 2.5, where, for each combination of mass and gravity, we computed two distances, with and without the reddening. The comparison of our computed spectroscopic distances and the measured one favors a surface gravity higher than 6.2

⁵<http://irsa.ipac.caltech.edu/applications/DUST/>

TABLE 2.5 – Spectroscopic distances (pc) obtained with models having $T_{\text{eff}} = 82,000$ K in V-band with $A_v = 0$ and 0.135

Mass / $\log g$	$0.3 M_{\odot}$	$0.4 M_{\odot}$	$0.5 M_{\odot}$	$0.6 M_{\odot}$
$\log g = 6.2$	129 / 122	150 / 140	167 / 157	183 / 172
$\log g = 6.4$	103 / 97	119 / 111	133 / 125	145 / 136
$\log g = 6.6$	81 / 77	94 / 88	105 / 99	115 / 108

and/or a low mass for BD+28°4211. If we were to insist that the mass of BD+28°4211 is a representative post-EHB star value, $0.5 M_{\odot}$ say, then our optimal spectroscopic model – characterized by $T_{\text{eff}} = 82,000$ K and $\log g = 6.2$ – would lead to a distance of 157 pc, in apparent conflict with the parallax measurement of 81-106 pc. This is very reminiscent of the situation encountered by Rauch et al. (2007) in the case of the hot DAO white dwarf LS V +46°21 where the authors estimated the unknown mass by interpolating in a given set of evolutionary tracks. With a fixed value of $0.55 M_{\odot}$, they found a discrepant spectroscopic distance of 224_{-58}^{+46} pc compared to a ground-based parallax measurement giving 129_{-5}^{+6} pc.

If we take the parallax measurement of BD+28°4211 at face value, then the surface gravity has to be pushed above $\log g \sim 6.5$ for our spectroscopic distance to become compatible with that measurement, again assuming that the mass of the star is $0.5 M_{\odot}$. However, such large values of the surface gravity are now in conflict with the iron line profiles depicted in Figure 2.7. It may thus be preferable to think in terms of a low mass for BD+28°4211 for the time being. This may also be an option in the case of LS V +46°21 (Rauch et al. 2007).

Finally, we also checked what would be the effect of a change in the temperature of our model spectra and we thus computed a table similar to Table 2.5, except that all models were characterized by $T_{\text{eff}} = 87,000$ K instead of 82,000 K. We found that the spectroscopic distance increases by only 2 to 6 pc, depending on the parameters mass and gravity, compared to the entries of Table 2.5. Hence, within an uncertainty of 5000 K (which seems to be a reasonable range according to the result of the previous section), the conclusions of this subsection are practically not dependent on the effective temperature.

2.6 Discussion

In spite of the huge progress made in the model atmosphere modeling field in the last two decades, the analysis of hot stars still remains a challenge. In this paper, we have presented the first part of our analysis of BD+28°4211, which consists in the study of its UV spectrum. Our work made use of high-quality spectra from the *HST* and *FUSE* satellites combined with state-of-the-art NLTE line-blanketed model atmospheres and synthetic spectra computed with TLUSTY and SYNSPEC. To our knowledge, the *FUSE* data available on that star have not been exploited previously in the context of an atmospheric abundance analysis. The abundances of eleven elements have been determined, namely those of C, N, O, F, Mg, Si, P, S, Ar, Fe, and Ni. Our abundance analysis was made in a self-consistent way, meaning that the element analyzed contributed to the thermodynamical structure of the model and its populations were explicitly calculated in NLTE during the computation of the model atmosphere. We also made sure that the models used for fitting elements always included, besides the fitted element, at least the atomic species that most contribute to the thermodynamical structure, that is to say helium, carbon, nitrogen, oxygen, and iron. For a star as hot as BD+28°4211, we stress that it is crucial to compute NLTE populations of the studied elements in order to get realistic abundances. Even with the thermodynamical structure of a NLTE line-blanketed model atmosphere, the LTE ionization equilibrium is likely to be wrong, thus preventing a simultaneous fit of absorption lines originating from different ionization stages of a given atomic species. We illustrated this effect in Figure 2.3, with an example of nickel lines computed in both the NLTE self-consistent way and with LTE populations. In addition to the elements mentioned above, the UV spectrum of BD+28°4211 shows lines of chromium, manganese, and cobalt (and probably those of other species as well). We tentatively tried to fit these three elements by using the LTE approximation, because of the lack of proper model atoms that could be used in our NLTE models. We analyzed only lines originating from the dominant ionization stage (VI) and we got abundances surprisingly similar to the ones Ramspeck et al. (2003) derived (for Cr and Mn) using the “generic ion” approach in NLTE model atmosphere.

Our resulting chemical composition is summed up in Figure 2.8 and the entire sample of our NLTE fitted lines is shown in the supplementary Figure 2.9. We found the overall quality

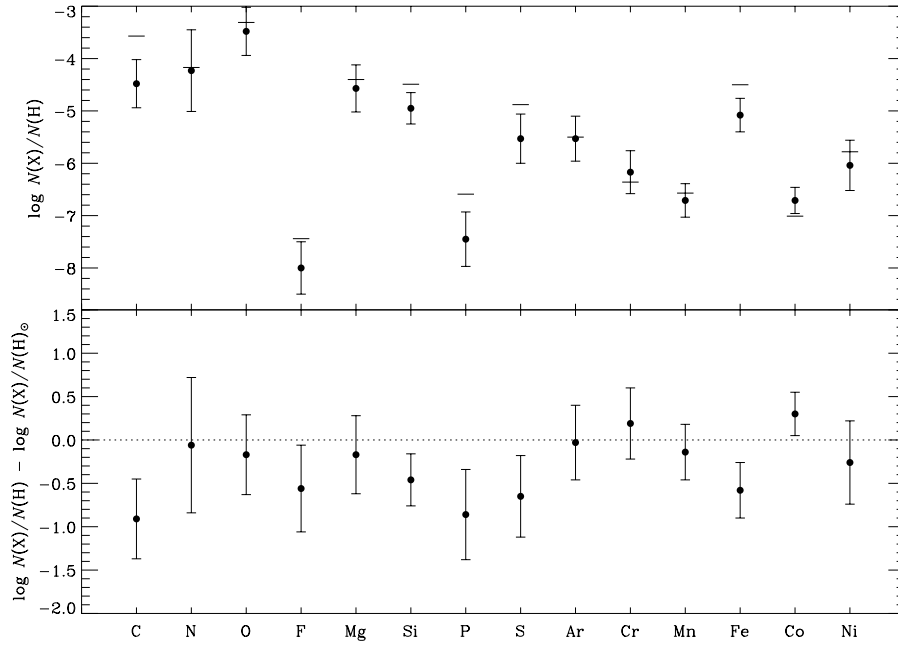


FIGURE 2.8 – Summary of the determined chemical composition of BD+28°4211. The top panel shows the absolute abundances relative to hydrogen ($\log N(X)/N(H)$) and the horizontal lines indicate the solar one for each element (Asplund et al. 2009). The bottom panel shows this time the abundances relative to the solar value.

of our fits very satisfying. When comparing the abundances of BD+28°4211 with those of the Sun, it appears that none of the elements studied with self-consistent NLTE models has an abundance higher than solar (the only exceptions being the LTE estimated abundances of chromium and cobalt). Instead, our derived abundances are all between one and 1/10 of the solar ones (Asplund et al. 2009). The most depleted species is carbon with $\log N(C)/N(C_\odot) = -0.91 \pm 0.46$, followed by phosphorus with $\log N(P)/N(P_\odot) = -0.86 \pm 0.52$. It turns out that these two elements, as mentioned in Section 2.2.2, are present in the photosphere mainly as C v and P vi, which are in a noble gas configuration. This kind of ion usually has its resonance lines in the extreme UV (EUV) or even in the X-ray domain because of the large energy gap between their ground and first excited levels. Therefore, they are less sensitive to radiative levitation, since the EUV and X-ray fluxes of stars are usually lower than the flux at larger wavelengths. This might explain why carbon and phosphorus are the most depleted elements,

since their resonance lines are respectively around 40 Å and 90 Å. Even if BD+28°4211 is a hot star, its flux at these extreme wavelengths remains quite low. For its part, even though our abundance of fluorine is at best an estimation based on a sole line, its value around $\log N(\text{F})/N(\text{F}_\odot) = -0.56 \pm 0.50$ still suggests that this element is not enriched in BD+28°4211. This is in line with the findings of Werner et al. (2005) who found an important enrichment of fluorine in a number of PG1159 stars, while its abundance remains around or slightly lower than solar in their sample of H-rich central stars of planetary nebulae, the latter being a family of stars having similar evolutionary paths than BD+28°4211. As for iron, our results indicate that $\log N(\text{Fe})/N(\text{Fe}_\odot) = -0.58 \pm 0.32$, while they indicate $\log N(\text{Ni})/N(\text{Ni}_\odot) = -0.26 \pm 0.48$ for nickel. Both results are compatible with the findings of Ramspeck et al. (2003) which suggest a depleted value of iron by about an order of magnitude (formally, from their Table 1, $\log N(\text{Fe})/N(\text{Fe}_\odot) = -0.82 \pm 0.15$), and a solar abundance for nickel⁶. We thus find a ratio $N(\text{Fe})/N(\text{Ni}) \simeq 9.1$, which is about half of the solar value. An even more depleted ratio was first suggested by Haas et al. (1996) in BD+28°4211 and is particularly interesting because it connects well with the work of Werner & Dreizler (1994) who found a similar trend in four hot DA white dwarfs. This trend may possibly be explained through the combined effects of radiative levitation and residual stellar winds (see, e.g., the work of Chayer et al. 1994). It must be kept in mind that with an effective temperature of 82,000 K, the abundance pattern of BD+28°4211 is strongly affected by radiative levitation. We made sure that the uncertainties on our determined abundances were computed in a way that includes the effects of a change in the temperature and the gravity of our model atmospheres. Therefore, our abundances should remain fairly reliable even if the effective temperature or the surface gravity are revised upward or downward by some 10,000 K or 0.4 dex, respectively⁷.

Even if we took the fundamental parameters of BD+28°4211 from the literature (Napiwotzki 1993), we nevertheless checked the validity of the assumed effective temperature and surface gravity. To carry out that task, we first redid our fits for nitrogen, silicon, and iron (used as proxy elements) by constructing additional model atmospheres having different pa-

⁶Our derived abundances $\log N(\text{N})/N(\text{N}_\odot) = -0.06 \pm 0.78$ and $\log N(\text{O})/N(\text{O}_\odot) = -0.17 \pm 0.46$ are equally compatible with the work of Haas et al. (1996) who deduced about solar abundances for those two elements.

⁷After our complete analysis, it appears that a $\pm 10,000$ K margin of error on the effective temperature is twice our adopted value. Thus, the uncertainties on our abundances are a bit generous.

rameters. The standard deviation of the sample of fitted intervals for an element gives us an idea of how well the different abundances agree internally with each other. A small value of σ indicates that all intervals lead to similar abundances, which is a good thing in our case. By examining the standard deviations obtained when the temperature of the models is changed, we found the results to be in better agreement when the effective temperature of our models is near 82,000 K, which is the assumed one. As for the standard deviations obtained with various $\log g$ values, they do not point toward a favored value of the surface gravity. Instead, we have to look at a comparison of observed and synthetic spectra over a wavelength range featuring iron lines originating from three ionization stages, namely Fe V, VI, and VII to have an indication of the better value for the surface gravity (see Figure 2.7). This figure suggests the assumed value of 6.2 dex to be the one giving the best simultaneous match of the iron lines over the selected range. The differences between our model spectra at different $\log g$ are not as striking as the one we obtained with different T_{eff} (see Figure 2.6), but they are nevertheless significant.

We also exploited the availability of an *Hipparcos* parallax measurement for BD+28°4211 and compared the inferred distance with spectroscopic distances estimated from several model spectra. In a first step, we were able to derive an accurate determination of the reddening between Earth and BD+28°4211, $E(B - V) = 0.042 \pm 0.003$, thanks to the high-precision optical photometry of Landolt & Uomoto (2007). Several spectroscopic distances (with and without reddening correction) were derived as indicated in Table 2.5. A comparison with the parallax distance implies a relatively large value of the surface gravity and/or a small mass for BD+28°4211. We can reconcile our spectroscopic constraints with the available parallax measurement only if the mass of BD+28°4211 is significantly less than the canonical value of $0.5 M_{\odot}$ for a representative post-EHB star. Assuming that the *Hipparcos* measurement for BD+28°4211 is fully reliable and that our model atmospheres are reasonably realistic, we must conclude that BD+28°4211 is likely less massive than could have been expected on the basis of standard evolutionary tracks.

Our analysis has allowed us to get a good idea of the atmospheric chemical composition of BD+28°4211. Its main constituents, in terms of atomic species, have been analyzed and we

were able to get abundances for eleven elements, including the ones that influence the most the thermodynamical structure, i.e., carbon, nitrogen, oxygen, and iron. This now allows us to compute more realistic NLTE model atmospheres including the appropriate line blanketing for BD+28°4211. The value of 82,000 K for the effective temperature of the star now seems quite robust and realistic uncertainties are likely less than ± 5000 K. The case of the surface gravity is somewhat more difficult, but we estimate conservatively that $\log g = 6.2_{-0.1}^{+0.3}$ for BD+28°4211. These informations should be a good starting point for the study of the optical spectrum of the star. This will follow in an upcoming paper.

This work was supported in part by the NSERC of Canada. G.F. also acknowledges the contribution of the Canada Research Chair Program. M.L. wishes to thank Patrick Dufour for help with the fitting routines.

2.7 References

- Asplund, M., Grevesse, N., Sauval, A. J., & Scott, P. 2009, *ARA&A*, 47, 481
- Ayres, T. R. 2010, *ApJS*, 187, 149
- Bergeron, P., Saffer, R. A., & Liebert, J. 1992, *ApJ*, 394, 228
- Bruhweiler, F. C. & Dean, C. A. 1983, *ApJ*, 274, L87
- Chayer, P., Fontaine, M., Fontaine, G., Wesemael, F., & Dupuis, J. 2006, *Baltic Astronomy*, 15, 131
- Chayer, P., LeBlanc, F., Fontaine, G., Wesemael, F., & Vennes, S. 1994, *ApJ*, 436, L161
- Chayer, P., Vennes, S., Dupuis, J., & Kruk, J. W. 2005, *ApJ*, 630, L169
- Dixon, W. V., Sahnou, D. J., Barrett, P. E., Civeit, T., Dupuis, J., Fullerton, A. W., Godard, B., Hsu, J.-C., Kaiser, M. E., Kruk, J. W., Lacour, S., Lindler, D. J., Massa, D., Robinson, R. D., Romelfanger, M. L., & Sonnentrucker, P. 2007, *PASP*, 119, 527
- Dorman, B., Rood, R. T., & O'Connell, R. W. 1993, *ApJ*, 419, 596
- Dreizler, S. & Werner, K. 1993, *A&A*, 278, 199
- Driebe, T., Schoenberner, D., Bloeker, T., & Herwig, F. 1998, *A&A*, 339, 123
- Fontaine, G., Brassard, P., Charpinet, S., & et al. 2012, *A&A*, 539, A12
- For, B.-Q., Green, E. M., Fontaine, G., & et al. 2010, *ApJ*, 708, 253
- Grevesse, N. & Sauval, A. J. 1998, *Space Sci. Rev.*, 85, 161
- Haas, S., Dreizler, S., Heber, U., Jeffery, S., & Werner, K. 1996, *A&A*, 311, 669
- Heber, U., Drechsel, H., Karl, C., Østensen, R., B., & Koester, D. 2005, in *Astronomical Society of the Pacific Conference Series*, Vol. 334, 14th European Workshop on White Dwarfs, ed. D. Koester & S. Moehler, 357
- Herbig, G. H. 1999, *PASP*, 111, 1144
- Holberg, J. B. & Bergeron, P. 2006, *AJ*, 132, 1221
- Landolt, A. U. & Uomoto, A. K. 2007, *AJ*, 133, 768
- Lanz, T. & Hubeny, I. 2003, *ApJS*, 146, 417

- . 2007, *ApJS*, 169, 83
- Lanz, T., Hubeny, I., & de Koter, A. 1996, *Physica Scripta Volume T*, 65, 144
- Latour, M., Fontaine, G., Brassard, P., Green, E. M., Chayer, P., & Randall, S. K. 2011, *ApJ*, 733, 100
- Massey, P. & Gronwall, C. 1990, *ApJ*, 358, 344
- Moos, H. W., Cash, W. C., Cowie, L. L., et al. 2000, *ApJ*, 538, L1
- Napiwotzki, R. 1993, *Acta Astronomica*, 43, 343
- . 1999, *A&A*, 350, 101
- O’Toole, S. J. & Heber, U. 2006, *A&A*, 452, 579
- Ramspeck, M., Haas, S., Napiwotzki, R., Heber, U., Deetjen, J., & Dreizler, S. 2003, in *Astronomical Society of the Pacific Conference Series*, Vol. 288, *Stellar Atmosphere Modeling*, ed. I. Hubeny, D. Mihalas, & K. Werner, 161
- Randall, S. K., Green, E. M., Van Grootel, V., Fontaine, G., Charpinet, S., Lesser, M., Brassard, P., Sugimoto, T., Chayer, P., Fay, A., Wroblewski, P., Daniel, M., Story, S., & Fitzgerald, T. 2007, *A&A*, 476, 1317
- Rauch, T., Ziegler, M., Werner, K., Kruk, J. W., Oliveira, C. M., Vande Putte, D., Mignani, R. P., & Kerber, F. 2007, *A&A*, 470, 317
- Saffer, R. A., Bergeron, P., Koester, D., & Liebert, J. 1994, *ApJ*, 432, 351
- Sahnow, D. J., Moos, H. W., Ake, T. B., et al. 2000, *ApJ*, 538, L7
- Schlegel, D. J., Finkbeiner, D. P., & Davis, M. 1998, *ApJ*, 500, 525
- Schoenberner, D. 1983, *ApJ*, 272, 708
- Seaton, M. J. 1979, *MNRAS*, 187, 73P
- Sonneborn, G., André, M., Oliveira, C., Hébrard, G., Howk, J. C., Tripp, T. M., Chayer, P., Friedman, S. D., Kruk, J. W., Jenkins, E. B., Lemoine, M., Moos, H. W., Oegerle, W. R., Sembach, K. R., & Vidal-Madjar, A. 2002, *ApJS*, 140, 51
- Stroeer, A., Heber, U., Lisker, T., Napiwotzki, R., Dreizler, S., Christlieb, N., & Reimers, D. 2007, *A&A*, 462, 269

van Leeuwen, F. 2007, *A&A*, 474, 653

Vennes, S., Chayer, P., & Dupuis, J. 2005, *ApJ*, 622, L121

Wassermann, D., Werner, K., Rauch, T., & Kruk, J. W. 2010, *A&A*, 524, A9

Werner, K. 1996, *ApJ*, 457, L39

Werner, K. & Dreizler, S. 1994, *A&A*, 286, L31

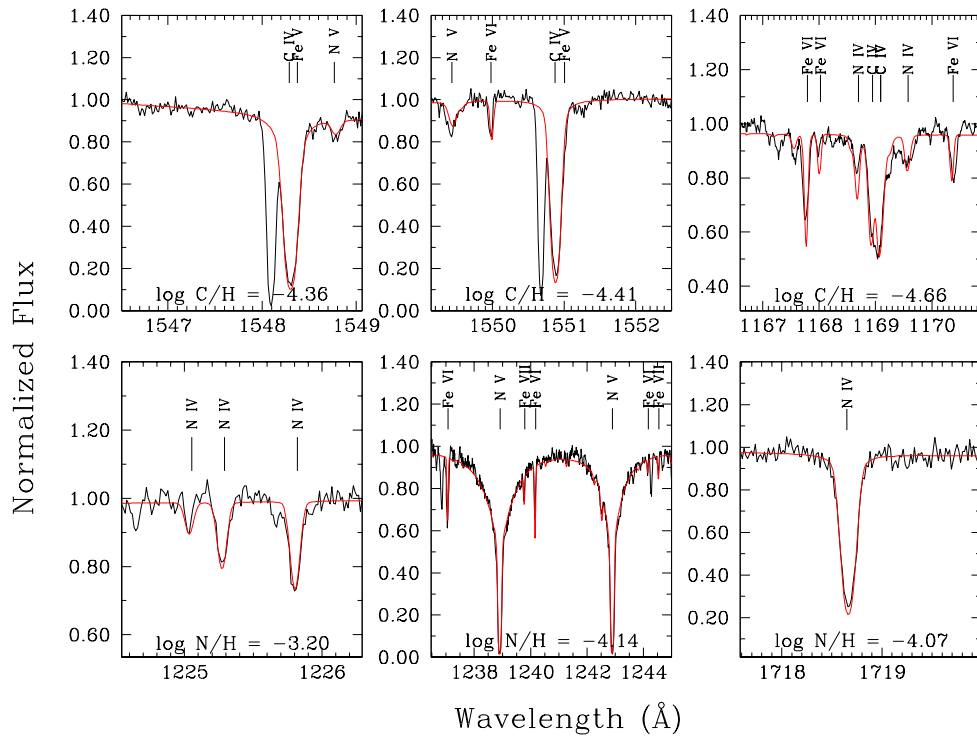
Werner, K., Heber, U., & Fleming, T. 1994, *A&A*, 284, 907

Werner, K., Rauch, T., & Kruk, J. W. 2005, *A&A*, 433, 641

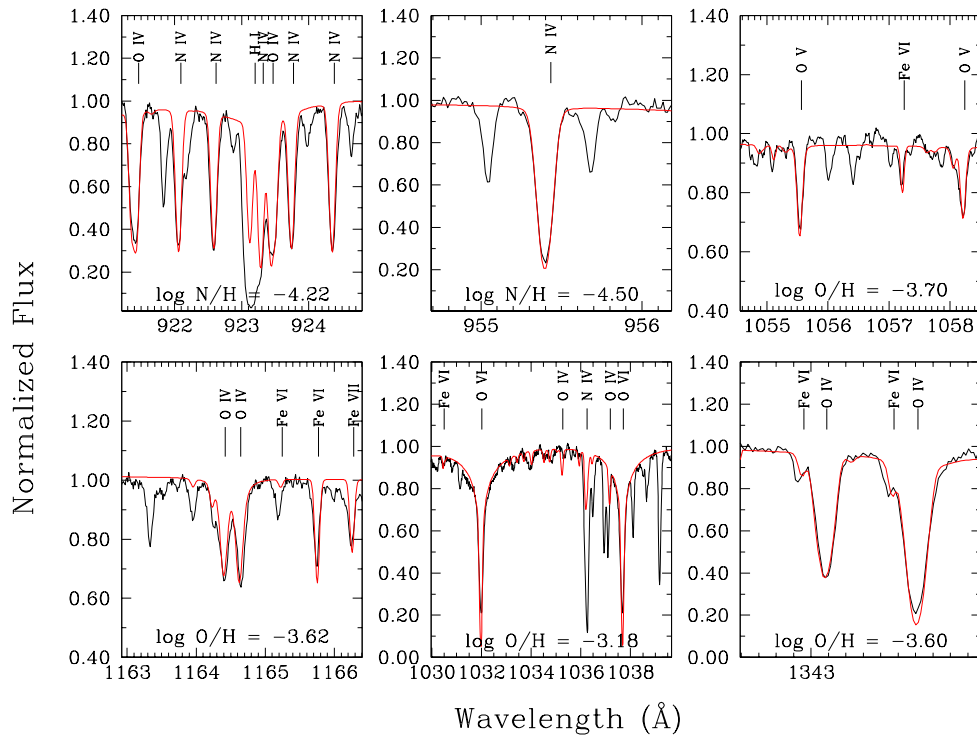
Werner, K., Rauch, T., Ringat, E., & Kruk, J. W. 2012, *ApJ*, 753, L7

2.8 Supplementary Figures

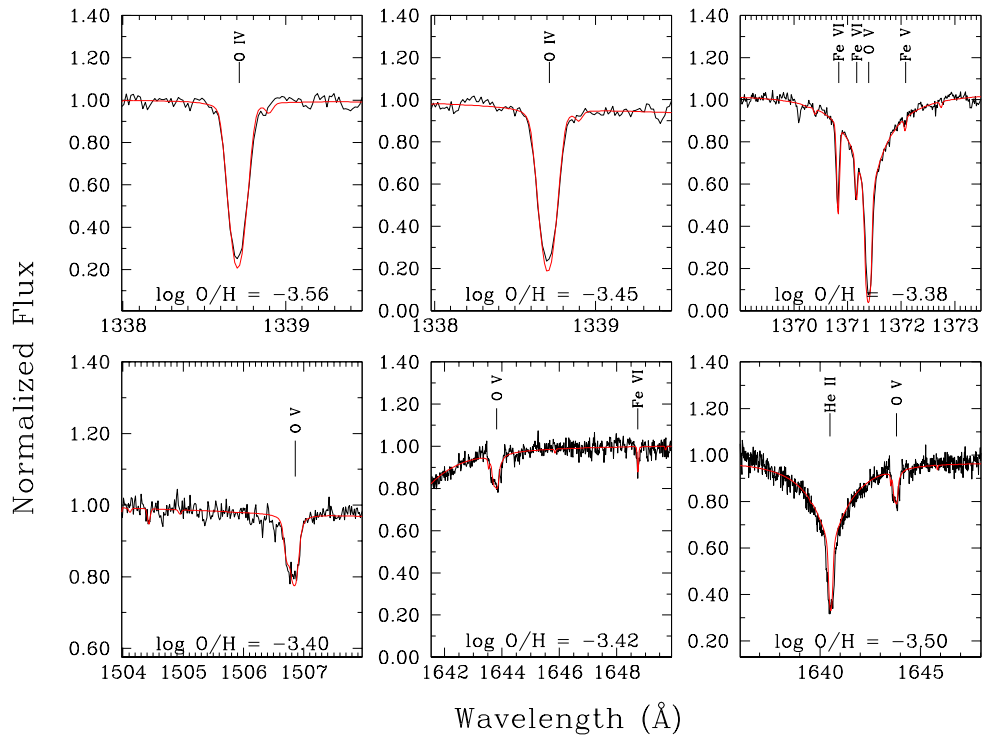
The supplementary Figure 2.9 present the totality of our fitted spectral intervals for all the atomic species. The fits were done with models having $T_{\text{eff}} = 82,000$ K, $\log g = 6.2$, and $\log N(\text{He})/N(\text{H}) = -1.0$. The red curve shows the result of the fitting procedure for the element mentioned on each panel and the abundance obtained is expressed as $\log N(\text{X})/N(\text{H})$. a) The fit showed in the lower left panel was not included in our mean abundance for nitrogen. c) The O IV line at 1338.6 \AA is fitted twice because each line comes from two different STIS orders. They were both included in the mean abundance. The lower right panel shows a view of He II $\lambda 1640$, with the oxygen abundance fixed to its determined value. g) In the middle top panel, the line at the left is Co VI $\lambda 1226.4$, an element not included in our model atmospheres.



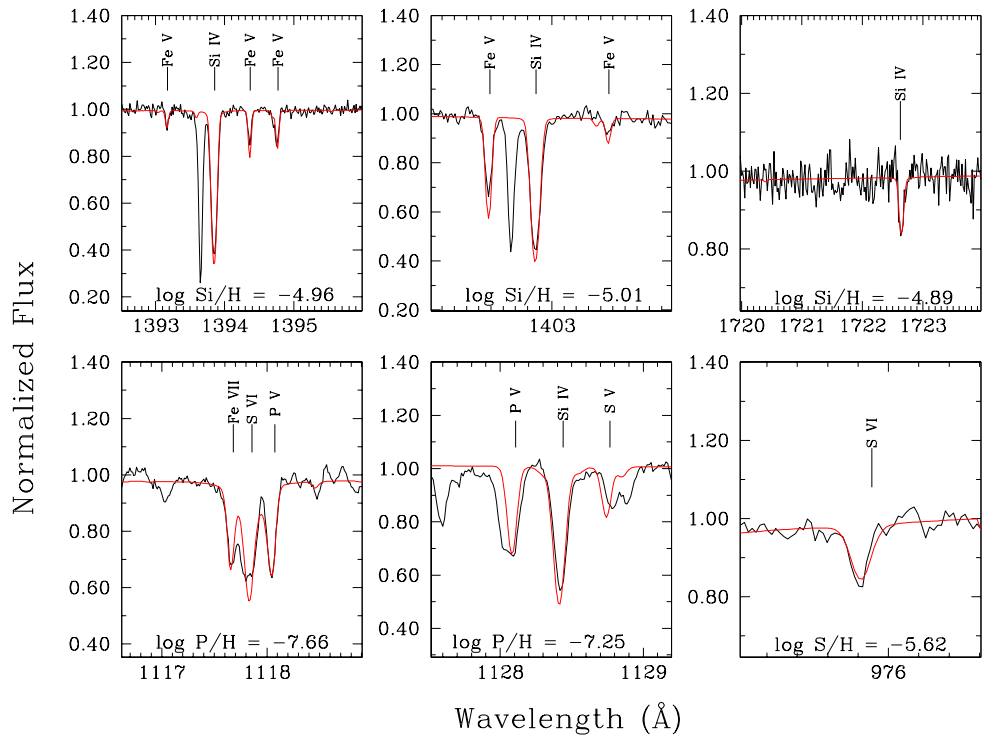
Supplementary Figure panel a



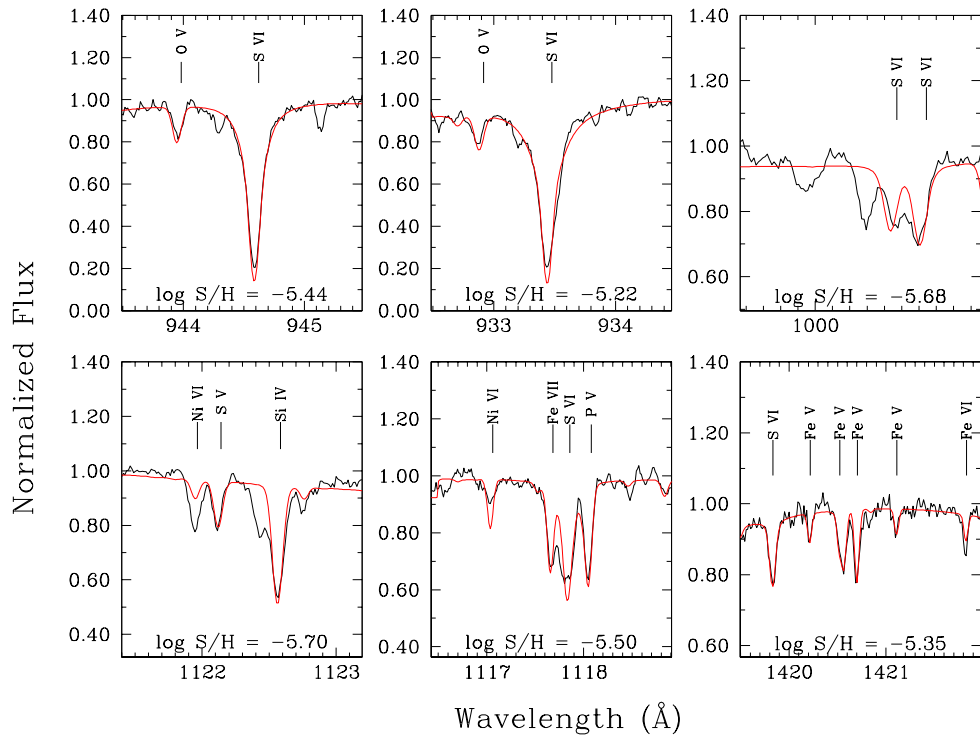
Supplementary Figure panel b



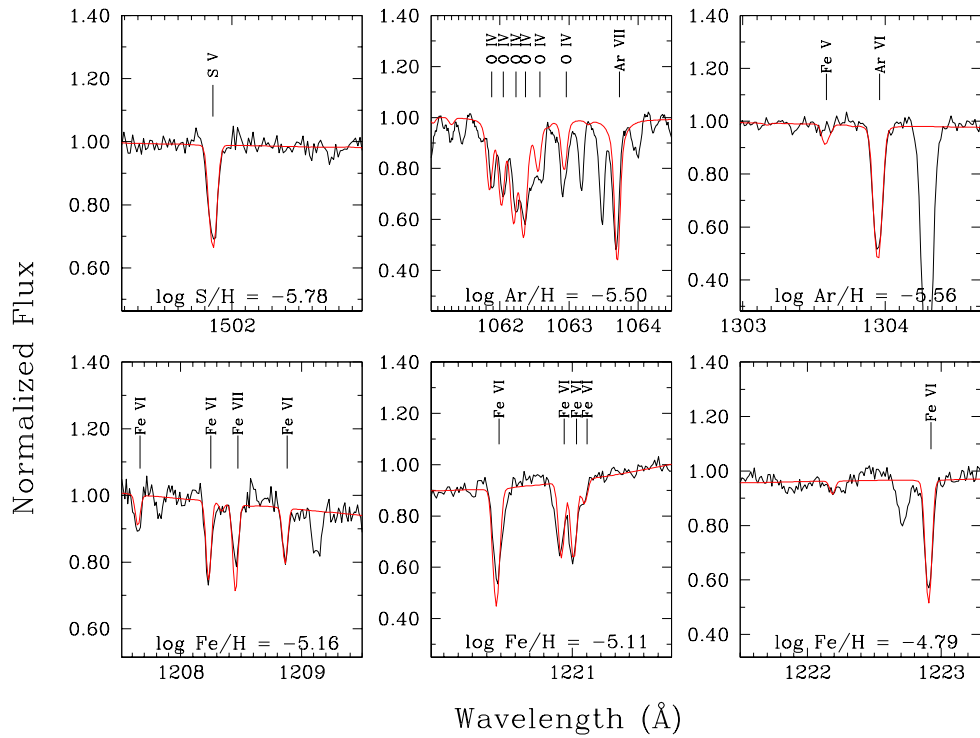
Supplementary Figure panel c



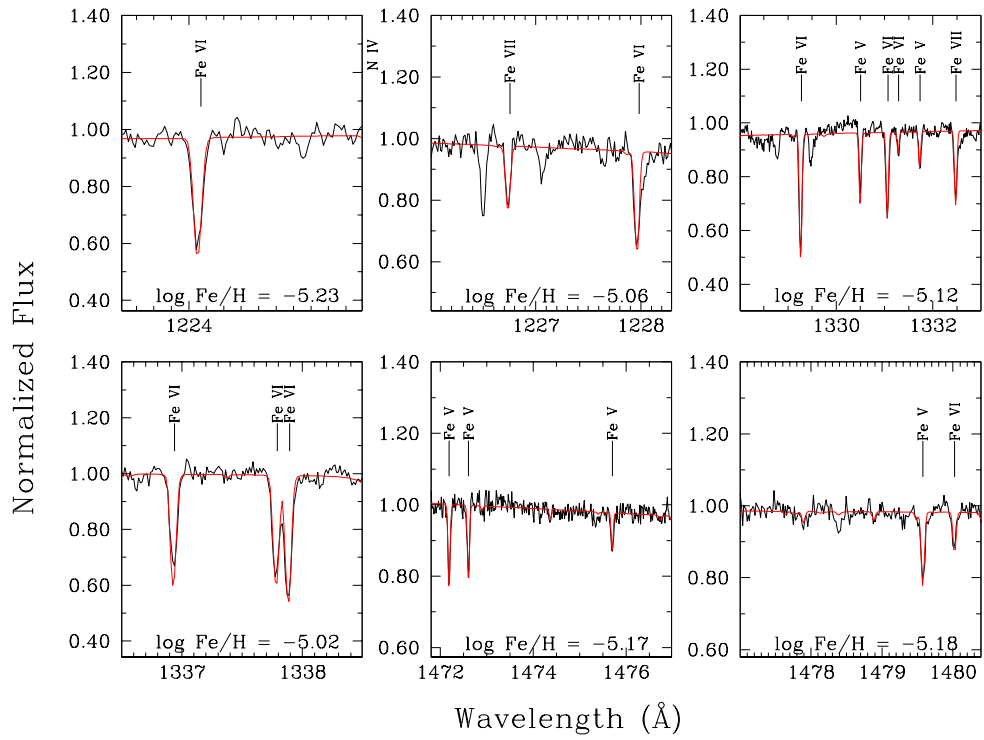
Supplementary Figure panel d



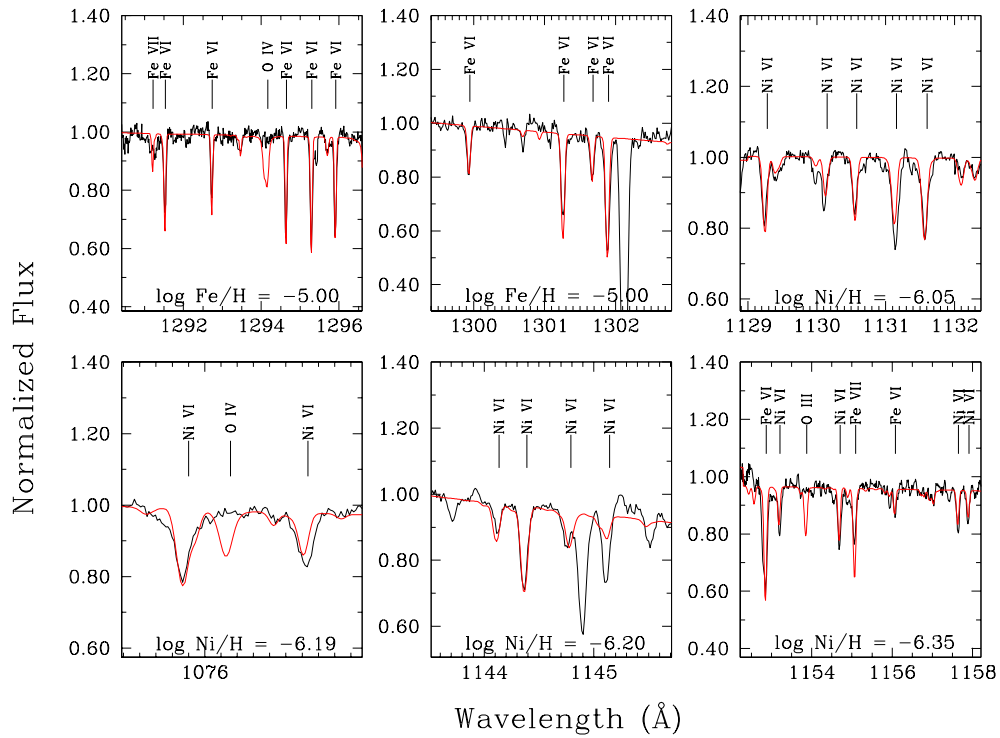
Supplementary Figure panel e



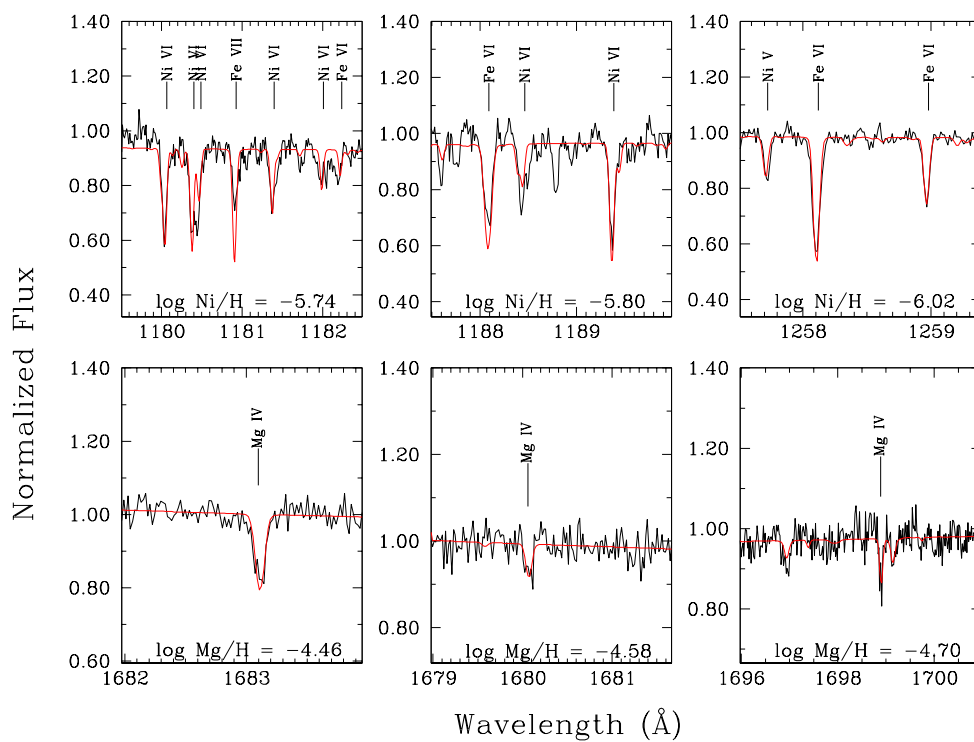
Supplementary Figure panel f



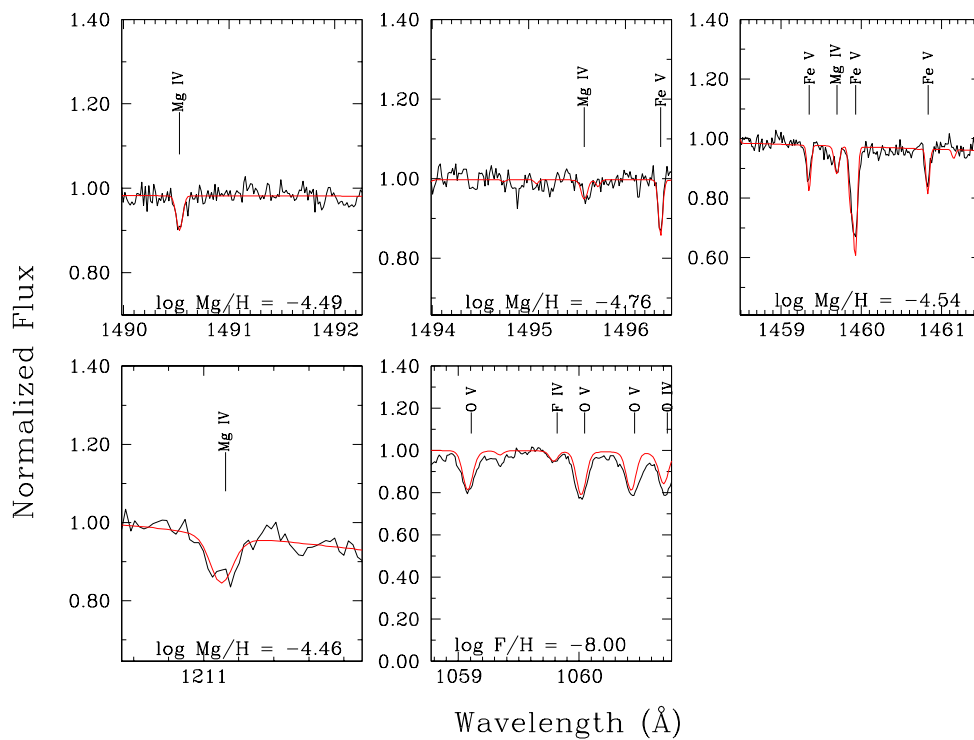
Supplementary Figure panel g



Supplementary Figure panel h



Supplementary Figure panel i



Supplementary Figure panel j

Chapitre 3

A NON-LTE ANALYSIS OF THE HOT SUBDWARF O STAR BD+28°4211. II. THE OPTICAL SPECTRUM

M. Latour¹, G. Fontaine¹, E.M. Green², and P. Brassard¹

¹ *Département de Physique, Université de Montréal, Succ. Centre-Ville, C.P. 6128,
Montréal, QC H3C 3J7, Canada*

² *Steward Observatory, University of Arizona, 933 North Cherry Avenue, Tucson, AZ 85721*

To be submitted to *The Astrophysical Journal*

3.1 Abstract

We present the second part of our detailed analysis of the hot sdO and spectroscopic standard star BD+28°4211 where we focus this time on the optical spectrum. In the first part, using UV spectra of the star, we determined the atmospheric chemical composition of BD+28°4211 and corroborated the fundamental parameters estimated in past studies ($T_{\text{eff}} \sim 82,000$ K, $\log g \sim 6.2$ dex). In this work, we aim at deriving those secured parameters on the basis of optical spectra in order to verify if optical spectroscopy alone can lead to reliable determinations of the atmospheric parameters of very hot stars of the kind. For this, we have gathered three optical spectra of BD+28°4211, all of them having exceptionally high S/N (> 900) and various resolutions and wavelength coverages. The initial grid of NLTE line-blanketed model atmospheres, including C, N, O, Mg, Si, S, Fe, and Ni with the abundances derived from the UV spectrum of BD+28°4211, did not give satisfactory results when we applied a standard simultaneous fitting procedure to the observed lines of our spectra. The lines in question were not well reproduced and the resulting effective temperatures were too low by some 10,000 K. In the second grid of models, the abundances of the metallic species were arbitrarily increased to ten times their solar values. This was done in order to mimic some (presumably) missing opacity and its influence on the atmospheric structure. Contrary to the first experiment, this metal-enriched grid allowed us to achieve significantly improved spectral fits. In particular, our three observed spectra are very well reproduced with models having parameters close to the expected ones. Our spectral fits suggest, however, a surface gravity of $\log g \sim 6.5$ dex, which is somewhat higher than the previously estimated value, but still within the quoted uncertainties. As an a posteriori test, we compared the detailed profiles of several model spectral lines with high resolution spectra culled from archived HIRES observations. The agreement between our synthetic lines and the observed ones is very convincing. It would thus appear that using models with artificially enhanced metal abundances could serve as an interim solution for estimating the atmospheric parameters of objects such as hot sdO's and white dwarfs on the basis of optical spectroscopy in the absence of UV data.

3.2 Introduction

Hot subluminous O stars form the hottest part of the extreme horizontal branch (EHB), which is itself a hot extension of the horizontal branch. The EHB region of the Hertzsprung-Russell (HR) diagram encompasses stars that span a wide range of effective temperature, from 22,000 K up to 100,000 K, and that are more compact ($4.8 \lesssim \log g \lesssim 6.4$) than the main sequence ones. This includes stars from two distinct spectral types, the cooler sdB's with their strong Balmer lines ($22,000 \text{ K} \leq T_{\text{eff}} \leq 38,000 \text{ K}$), and the hotter sdO's showing strong He II lines as well ($T_{\text{eff}} \geq 38,000 \text{ K}$). Most hot subdwarfs are believed to be helium core burning objects – or in a phase following immediately core helium exhaustion – with a layer of H-rich material too thin to sustain shell burning¹. From a spectroscopic point of view, sdB stars form a rather homogeneous group: they mostly cluster within the theoretical core helium burning region and its immediate surroundings in the HR diagram (the region between the Zero Age Extreme Horizontal Branch and the Terminal Age Extreme Horizontal Branch), and their atmospheres are depleted in helium (save for $\sim 5\%$ of the sdB's that are helium enriched). Numerous analyses were made on various samples of sdB stars and their global properties (helium content, metal content, rotational velocity, binary population, etc.) are now well documented. However the situation is different when speaking of the hotter sdO's; they are distributed among a much larger region in the HR diagram and this distribution is not as homogeneous as in the case of the sdB's. While most of the latter are helium poor, the majority of sdO stars have an atmosphere enriched in helium and they are thought to be the results of various peculiar evolutionary paths².

One striking fact about sdO stars is that they have been much less studied than their coolest counterparts. The most significant study in our view has been the one carried out by Stroeger et al. (2007) using an homogeneous sample of sdO's observed within the SPY survey. The sample of ω Centauri EHB stars in Moehler et al. (2007, 2011) also included a fair amount of sdO stars, but mostly cooler ones found at the transition between the spectral

¹Note that a few hot subdwarfs have been found to have a mass too low to sustain helium core burning (e.g. HD 188112 Heber et al. 2003). However, these low mass stars represent only a tiny fraction of the hot subdwarf population.

²A comprehensive review of the global properties and characteristics of hot subdwarf stars can be found in Heber (2009).

types B and O (i.e., below 40,000 K). While known sdO stars in the field are outnumbered by sdB's (these stars show a number ratio $\approx 1 : 3$), the true reason for this relative lack of investigations must be found in the inherent challenge associated with the atmospheric modeling and spectroscopic analyses of very hot stars. For a star having $T_{\text{eff}} \gtrsim 50,000$ K, the fundamental parameters determined by comparing the observed Balmer and helium lines in the optical with model ones bear important uncertainties. At temperatures higher than 70,000 K, the observed optical spectrum of a star has hardly ever been reproduced by models in a satisfactory way. This is mostly due to the so-called Balmer line problem, first noticed by Napiwotzki (1992, 1993) in hot central stars of old planetary nebulae. Basically, this problem comes down to the inability to simultaneously reproduce the observed Balmer lines with a unique set of fundamental parameters ($\log g - T_{\text{eff}}$). More specifically, the individual lines need different temperatures in order to be matched properly, with the higher lines in the series needing models at higher temperatures. For example, for BD+28°4211, $H\alpha$ was best reproduced at $T_{\text{eff}} \simeq 50,000$ K and $He\epsilon$ at around 85,000 K (Napiwotzki 1993). In a situation like that it is rather tricky to determine the temperature of the star without any additional information. In this particular case, the author could rely on UV data (from *IUE*) whose first analysis led to a value of $T_{\text{eff}} \simeq 82,000$ K (Dreizler & Werner 1993). This relatively high value of T_{eff} was also supported by the weakness of the He I 5876 Å line in the optical domain, which requires a high effective temperature. On the basis of these results, it was then concluded that the $He\epsilon$ line was the one that could provide the most realistic temperature estimate.

This “calibration” may have been useful at times, but it was not at all satisfactory on general grounds and different hypotheses were soon investigated to solve this embarrassing Balmer line problem (Napiwotzki & Rauch 1994). Most of them were rapidly rejected, save for the idea that the inclusion of metallic elements in the models might influence in a significant way the atmospheric structure, which in turn could change the shapes of the Balmer lines. Note that at the time this issue was first identified, model atmospheres used for these hot stars were using a non-LTE (NLTE) treatment but included only H and He; the treatment of line blanketing by metals was still in its early stages. Indeed, accounting for the effects of metallic elements via their colossal numbers of transition lines was, at the time, a real

computational challenge. Thanks to the work of Dreizler & Werner (1993) and Hubeny & Lanz (1995) on the development of numerical techniques allowing the inclusion of metals (such as C, N, O, and iron-group elements) and the treatment of their transition lines in NLTE calculations, it was subsequently shown that these elements can indeed strongly influence the thermodynamical structure of the atmosphere. However, the resulting effects on the Balmer lines were initially found to be surprisingly weak (Haas et al. 1996). It is Werner (1996) who brought up an important refinement in the treatment of light metals opacity: the inclusion of Stark broadening profiles for the CNO elements instead of the Doppler ones previously used. This addition led to an improved reproduction of the Balmer lines in his two test stars, BD+28°4211 itself and LS V+46°21, the DAO-type central star of a planetary nebulae. Despite this breakthrough, hot stars such as those presented in Werner (1996) were then never analyzed by attempting a simultaneous fit of all of the available Balmer and helium lines in optical spectra. This now widely used technique has proven itself to be a robust tool for the determination of fundamental parameters (T_{eff} , $\log g$, and sometimes also $N(\text{He})/N(\text{H})$) in cooler white dwarfs and sdB stars (Bergeron et al. 1994; Saffer et al. 1994). Rauch et al. (2007) later carried out a comprehensive spectral analysis of LS V+46°21, but they determined the effective temperature of the star using mainly the ionization equilibria of different metallic species whose lines were visible in the UV spectra of the star. The strongest He II lines ($\lambda\lambda 1640, 4686$) and $\text{H}\beta$ were mainly used to constrain the surface gravity. As for BD+28°4211, no further detailed studies were made on that star since Haas et al. (1996) estimated the abundance of a few metallic elements using the *IUE* data.

Given the particular status of BD+28°4211 as a spectroscopic standard star, both in the optical domain as well as in the UV range, modern data of extremely good quality are publicly available (through the Mikulski Archive for Space Telescopes, MAST³). Surprisingly, and until recently, these data have barely been exploited. In view of this state of affair, and given the availability of optical spectra of exceptionally high quality that one of us (E.M.G.) gathered over the years in the context of her spectroscopic programs, we undertook an in-depth spectral analysis of this star with the main aim of testing the simultaneous optical fitting method in

³<http://archive.stsci.edu/>

a very hot star. This is of importance for hot stars, the majority of them in fact, for which only optical spectroscopy is readily accessible while no UV data are available.

The first part of this analysis (Latour et al. 2013, hereafter Paper I) focussed on the UV spectral distribution of BD+28°4211 using the Space Telescope Imaging Spectrograph (STIS) and Far-Ultraviolet Spectroscopic Explorer (FUSE) spectra. We obtained in a self-consistent way the abundances of 11 elements with well defined lines in the UV, namely C, N, O, F, Mg, Si, P, S, Ar, Fe, and Ni. None of these elements was found to be enriched, the abundances rather lie between the solar value and 1/10 solar. With the help of the ionization equilibria of several metallic species, we were able to confirm the previously determined effective temperature and constrain it to a value of $82,000 \pm 5,000$ K. We also estimated conservatively the surface gravity of the star to be $\log g = 6.2_{-0.1}^{+0.3}$, which is also consistent with past results. By comparing the *Hipparcos* parallax measurement of BD+28°4211 (van Leeuwen 2007) with spectroscopic distances estimated from several model spectra we found that, in order to reconcile both values, the star needs either a $\log g$ higher than 6.2 (hence the larger upward uncertainty) or a mass significantly lower than the canonical value of $0.5 M_{\odot}$.

Having these informations at hand, we can now tackle the analysis of its optical spectrum. Past spectroscopic studies of hot stars like BD+28°4211 always relied on UV data, sometimes supported by optical ones, to get reliable fundamental parameters (e.g., Rauch et al. 2007; Fontaine et al. 2008; Ziegler et al. 2012). However, the need to rely on UV data can be very restrictive since they must be gathered with space missions, which are a lot less accessible than ground-based observations supplying optical spectra. Our goal here is to find a way, using our test case star, to obtain reliable fundamental parameters (T_{eff} , $\log g$ and $N(\text{He})/N(\text{H})$) using solely optical data. To achieve this, we exploit three very high sensitivity spectra having various resolutions and wavelength coverages. This material is described in more detail in the following section. The main part of this paper, Section 3.4, includes a description of the model grids we used as well as the subsequent spectroscopic analyses made. We also carried out some additional verifications to test our deduced fundamental parameters by comparing our best-fit models with additional high-resolution archive spectra. Finally, a discussion follows in Section 3.5.

3.3 Observational Material

BD+28°4211 is a well known, bright ($V = 10.5$) standard star and, as such, has been regularly observed for calibration purposes. In particular, as part of her spectroscopic programs at the University of Arizona, one of us (E.M.G.) has observed that standard star for many years using mainly three different instrumental setups, each corresponding to a different spectral resolution and coverage. Hence, by carefully combining the individual calibration data for each setup, we have obtained three exceptionally high quality spectra for BD+28°4211 on which is based a large part of the present analysis. This issue of S/N is quite important in the present context since we seek to detect differences between the observed and modeled line profiles that may be subtle at times.

It should also be pointed out that particular care has always been taken while observing BD+28°4211 in order to avoid contamination from the light of a nearby star. Indeed, rotating the slit to the parallactic angle at the midpoint of the exposure ensures that no light from the faint red companion of the star (Massey & Gronwall 1990) contaminates the spectrum of the sdO. Usually the companion was off the slit, however in the few cases when it fell within the slit, there was a clear spatial separation between the spectra of the companion and BD+28°4211, so it was always possible to extract only the sdO spectrum.

Our first instrumental setup is defined by the combination of the blue spectrograph and the 6.5 m Multiple Mirror Telescope (MMT). The 832 mm^{-1} grating is used in second order and, with the choice of a $1''$ slit width, this combination provides a resolution R of ~ 4250 (1.0 \AA) and covers the wavelength range $4000\text{--}4950 \text{ \AA}$. The careful combination of 20 individual spectra of BD+28°4211 observed at the MMT resulted in a spectrum having a formal S/N around $1,100^4$. This will be referred to as the MMT spectrum in what follows.

The other two instrumental setups make use of the Boller & Chivens (B&C) Cassegrain spectrograph mounted on the Steward Observatory's 2.3 m Bok Telescope at Kitt Peak. Hence, the 832 mm^{-1} grating in second order with a $1.5''$ slit is used to achieve a resolution of 1.3 \AA over a bluer wavelength range of $3675\text{--}4520 \text{ \AA}$. Twenty spectra were obtained with this

⁴The S/N calculation includes the summed star and sky photons plus the CCD readnoise. One thousand or more bias and flat images were taken during each run so that the processing of each spectral image introduces negligible additional noise.

particular setup, each flux calibrated and then combined with median filtering. The resulting S/N ratio is ~ 918 . This spectrum will later be referred to as the *blue* one.

The third set of observations covers a much wider wavelength interval, from 3620 to 6900 Å, but at the cost of a lower resolution of 8.7 Å. These observations are still very useful because they include two additional and important spectral lines in BD+28°4211 : He II at 5412 Å and H α . These low resolution spectra are obtained with a 400 mm⁻¹ grating in first order in conjunction with a 2.5'' slit. Our resulting 8.7 Å spectrum is the combination of 90 individual observations and has an overall whopping S/N of ~ 2500 . The resulting spectrum is referred to as the *lowres* one in what follows.

There are also many high resolution HIRES observations of BD+28°4211 available in the Keck Observatory Archive⁵ and extracted spectra, produced by an automated pipeline, are available for more than a hundred of them. Due to continuum placement difficulties, these echelle data are not particularly suited for a formal analysis aimed at simultaneously fitting the optical lines of hydrogen and helium. Nevertheless, the HIRES spectra are of very good quality and are highly interesting since they feature their fair share of details that cannot be seen in our own spectra. We thus retrieved some of the available spectra in order to make a posteriori comparisons between several observed lines and our optimal model spectra. After inspecting a lot of HIRES data, we ended up using four different spectrograms of BD+28°4211, among which two were mentioned in Herbig (1999). The observations we used were taken on the following nights: 1997-08-12, 1999-05-11, 2005-08-12 (ID 43185), and 2011-10-04 (ID 15969). However, there is major inconvenience with the HIRES spectra: the continuum of the various orders is uneven, in fact somewhat wavy. While this flaw can be overcome rather easily when studying narrow spectroscopic features, which is an important purpose of such high resolution observations, it is a hard thing to deal with when the lines of interest are tens of angstroms in width. The best way we found to flatten the continuum of the retained spectra was by using the continuum of adjacent orders which often had a similar shape. Continua from adjacent orders were shifted and superimposed to the spectra of interest and if both corresponded well enough, dividing the spectra by the continuum would flatten the former in a satisfactory way.

⁵<https://koa.ipac.caltech.edu>

3.4 Spectroscopic Analysis

3.4.1 Model Atmosphere Grids

Our grids of models were computed with the public codes TLUSTY and SYNSPEC⁶, which were run in parallel mode on CALYS, our cluster of computers currently containing 320 processors. Further technical details on the models can be found in Paper I, especially about the ionic species that were included. For this work, three distinct model grids were used. The first one is a metal-free grid of NLTE models, one of the grids that were built at the time of the analysis of the pulsating sdO star SDSS J160043.6+074802.9 (Latour et al. 2011). The purpose of using this grid is mainly for comparison purposes. The second grid is one especially suited for BD+28°4211, that includes eight of the main metallic constituents of the star’s atmosphere, namely C, N, O, Mg, Si, S, Fe, and Ni. The abundances of these elements were taken from the results of the UV analysis made in Paper I. This grid covers a parameter space centered around those of BD+28°4211, with T_{eff} varying from 76 kK up to 90 kK by steps of 2,000 K, $\log g$ from 5.4 to 6.8 dex by steps of 0.2 dex, and finally $\log N(\text{He})/N(\text{H})$ from -2.0 to 0.0 dex by steps of 0.5 dex. Finally, a third grid was built, out of necessity, after facing rather disappointing results with the second one. That third grid contains models with an enhanced metallicity of ten times the solar values for the eight elements mentioned above. As further indicated above, it was brought up in the past that adding a substantial amount of metals in LTE model atmospheres could improve the spectroscopic fits of stars in the sdOB transition region (T_{eff} around 35,000 K, O’Toole & Heber 2006; Geier et al. 2007). With that in mind, we hoped to see a similar improvement with our much hotter NLTE models. The third grid thus only differs from the second one by the fact that each element (except helium) has an abundance of ten times its solar values. Note that in the computation of the synthetic spectra of this grid (which is made with SYNSPEC), the metal abundances were reduced to the ones in BD+28°4211 to avoid unrealistic and strong metallic features in the optical spectra. In other words, the artificially enhanced metallicity was used only in the computation of the atmospheric structures (with TLUSTY).

⁶<http://nova.astro.umd.edu/index.html>

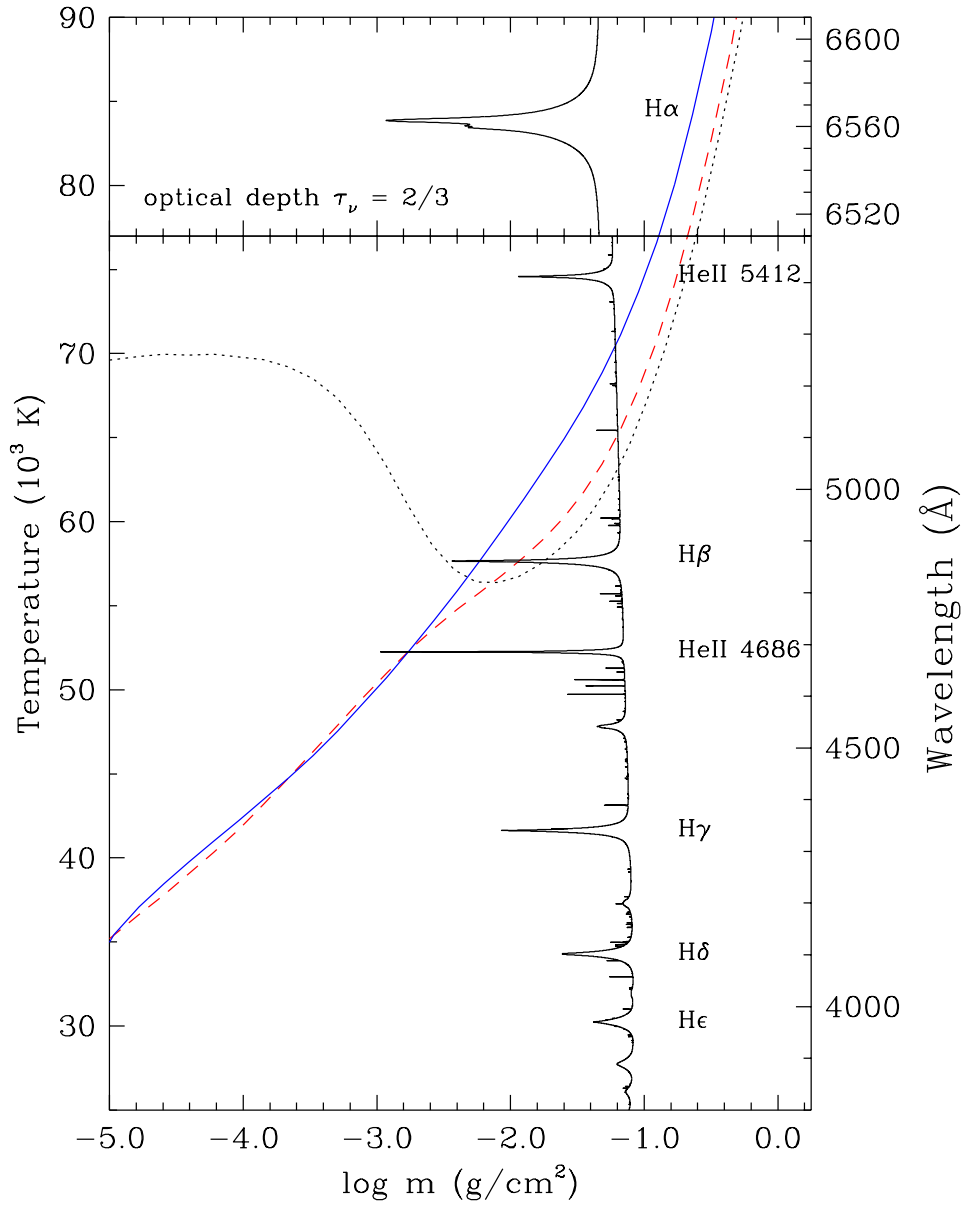


FIGURE 3.1 – Temperature stratification and monochromatic optical depth $\tau_\nu = 2/3$ as functions of depth, where m is the column density, for NLTE models defined by $T_{\text{eff}} = 82,000$ K, $\log g = 6.4$, and $\log N(\text{He})/N(\text{H}) = -1.0$. The temperature structure is shown for three model atmospheres having different compositions: with H and He only (black, dotted), with the metallic abundances of BD+28°4211 (red, dashed) and with ten times solar abundances (blue, solid). The $\tau_\nu = 2/3$ curve is from the latter model and shows wavelength intervals corresponding to the Balmer line series.

Figure 3.1 illustrates the effects of metals on the temperature structure of model atmospheres having fundamental parameters representing BD+28°4211: $T_{\text{eff}} = 82,000$ K, $\log g = 6.4$ and $\log N(\text{He})/N(\text{H}) = -1.0$. The first model is a metal-free one, showing the typical NLTE temperature inversion in the outer layer of the atmosphere (dotted line). Adding the metallic content of BD+28°4211 causes a drastic cooling of the outer layers while the deeper ones are heated (dashed curve). We showed in Paper I that the cooling is essentially due to the C, N, O, elements while both these elements and Fe heat the inner layers. When looking at the temperature stratification for a metal-enhanced model (solid curve), the most striking effect

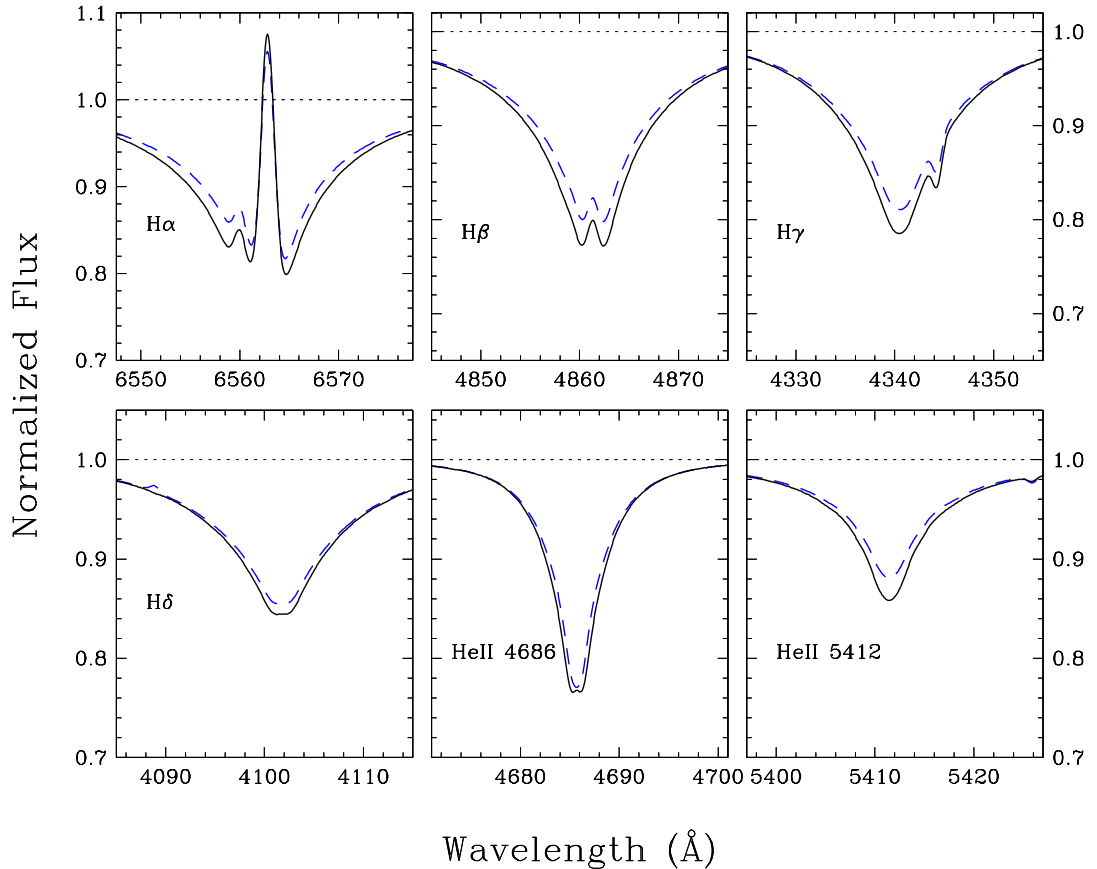


FIGURE 3.2 – Comparison of the strongest Balmer and helium lines in the optical spectra of model atmospheres having $T_{\text{eff}} = 82,000$ K, $\log g = 6.4$ and $\log N(\text{He})/N(\text{H}) = -1.0$. The blue dashed lines represent a NLTE model with the metallic content of BD+28°4211 and the solid lines a model with ten times solar abundances. The synthetic spectra are convolved at a resolution of 1.0 \AA .

is the significant warming, again of the inner layers, that is prominent in the line-forming region (between a depth of -1.0 and -2.0). This line-forming region can be localized with the help of the $\tau_\nu = 2/3$ curve, which indicates the depth (in column density) at which half the photons leave the atmosphere at a given wavelength.

The change expected in the spectral features of our ten times solar metallicity models is a deepening of the Balmer lines. This is in line with what was observed when adding a reasonable amount of metals in NLTE H, He models (Werner 1996; Gianninas et al. 2010; Latour et al. 2011). Indeed, Figure 3.2 illustrates a substantial deepening of the spectral lines in our metal-rich models, the less affected ones being H δ and He II at 4686 Å.

3.4.2 Derived Atmospheric parameters

The three optical spectra of BD+28°4211 were analyzed with the three model grids mentioned in the previous section. We stress that the spectra were analyzed in the same way as are usually handled the much cooler sdB stars: all of their lines being simultaneously fitted in a three-dimensional space (T_{eff} , $\log g$, and $\log N(\text{He})/N(\text{H})$). The χ^2 minimization procedure relies on the method of Levenberg-Marquardt, based on a steepest descend method (Bergeron et al. 1992). Normalized lines of both the observed and model spectra (convolved at the instrumental resolution) are thus compared.

Resulting fits obtained with the metal-free grid are displayed in Figure 3.3. Not surprisingly, the resulting temperature is way cooler than what is expected from the UV analysis, but the other parameters are in an acceptable range from the expected ones (see Table 3.1). The resulting fits are rather bad and assessing parameters on such results is not a good option. Note, however, that the very high S/N of our spectra helps a lot in terms of defining “badness” here! The fits of the *lowres* and *blue* spectra show a good example of the Balmer line problem, with the lowest lines in the series being too shallow in the model, while the trend shifts in H8 with a model line that is too deep. There is also a hint in the *lowres* spectral fit that the resulting temperature is too low when one looks at the helium lines: weak neutral helium lines are predicted by the model while the observed spectrum is clearly flat at these wavelengths and, in addition, the two main ionized helium lines are not strong enough in the

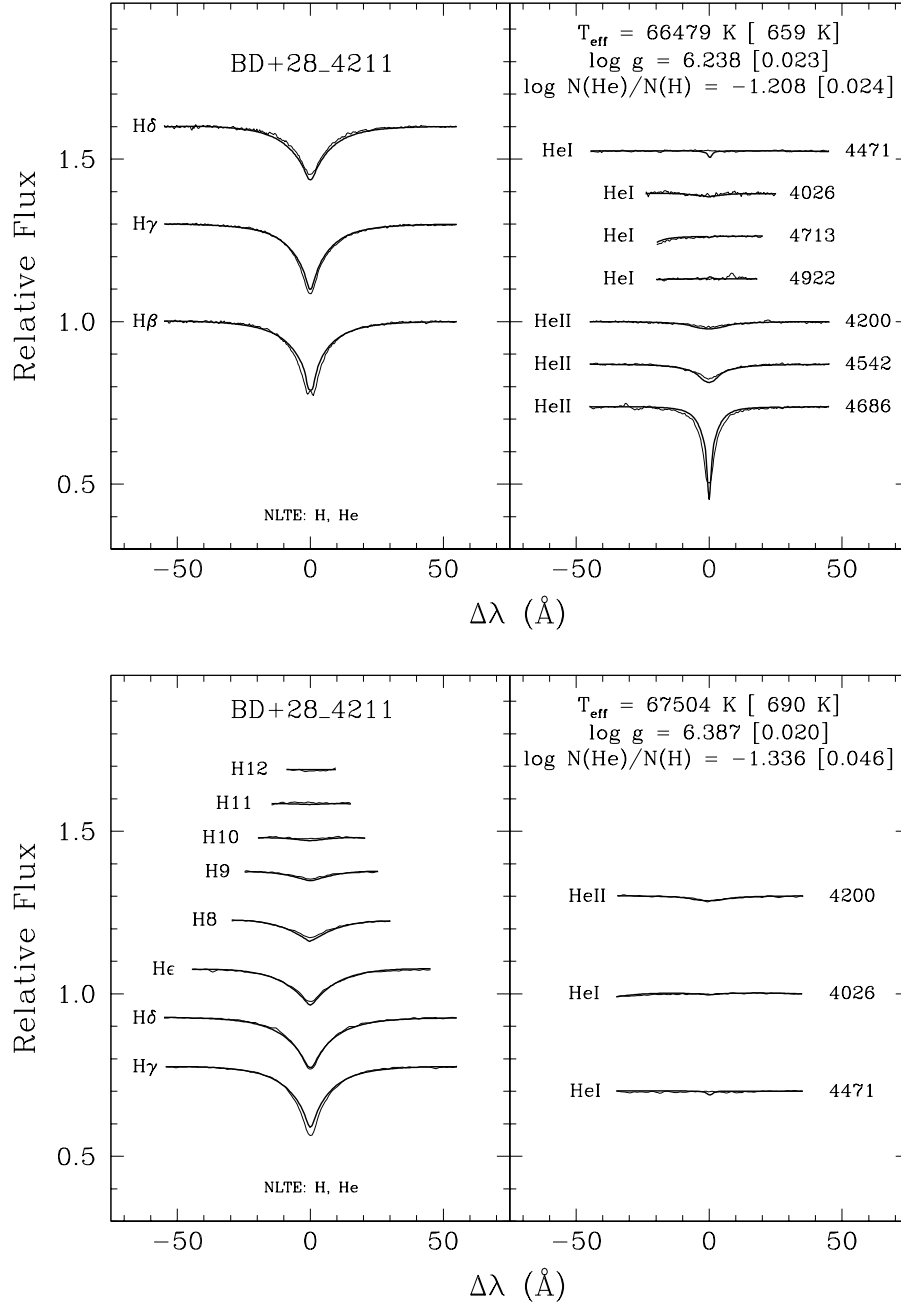


FIGURE 3.3 – Top – Best fit obtained with the 1 \AA resolution MMT spectrum of BD+28°4211 using our grid of NLTE metal-free models. Bottom – Best fit obtained with the *blue* 1.3 \AA resolution spectrum.

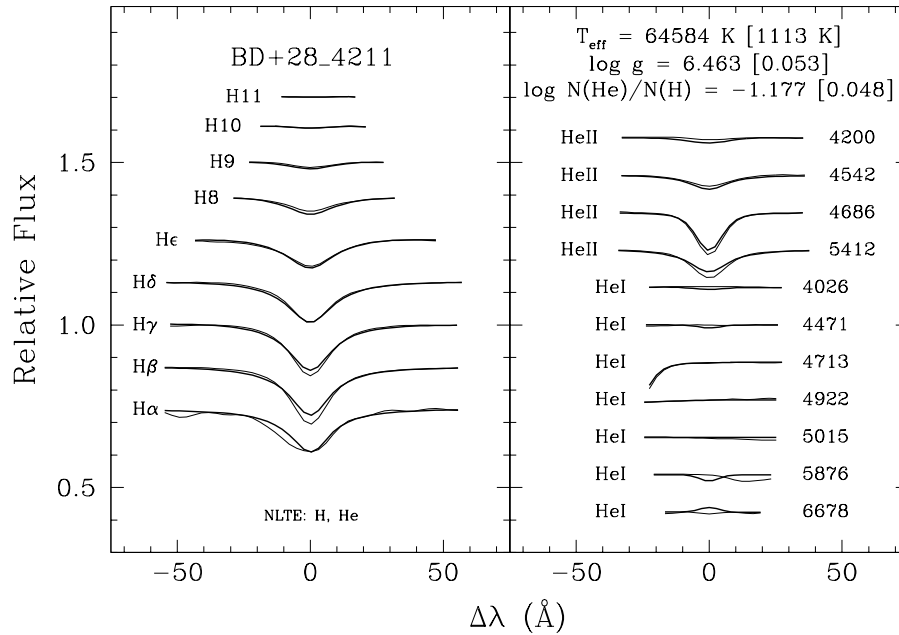


FIGURE 3.3 – Continued. Best fit with the lowest resolution spectrum (8.7 Å)

model spectrum.

The fits performed with the second grid having abundances fixed to the ones determined for BD+28°4211 in Paper I were expected to give more satisfying results. Compared to the metal-free case, the obtained temperatures are indeed higher, the same is true for the surface gravities, and the helium abundances are still around the solar value. Nevertheless, in spite of having included abundances that were self-consistently determined, and for which the main UV spectral lines were very well reproduced, the fitting procedure does not give appropriate temperatures. The results are too cool by roughly 10,000 K. A close look at the resulting fits (Figure 3.4) shows that they are significantly improved compared to the metal-free case, but they are not perfect either. A remnant of the Balmer line problem is still visible in our best fits and the He II line at 5412 Å cannot be reproduced properly.

At this point two things must be kept in mind. The first one is that in this range of T_{eff} and $\log g$, the Balmer and helium lines are only weakly sensitive to a change of parameters. A variation of effective temperature slightly changes the depth in the very core of the lines while the wings remain essentially the same. The surface gravity has a higher impact on the wings

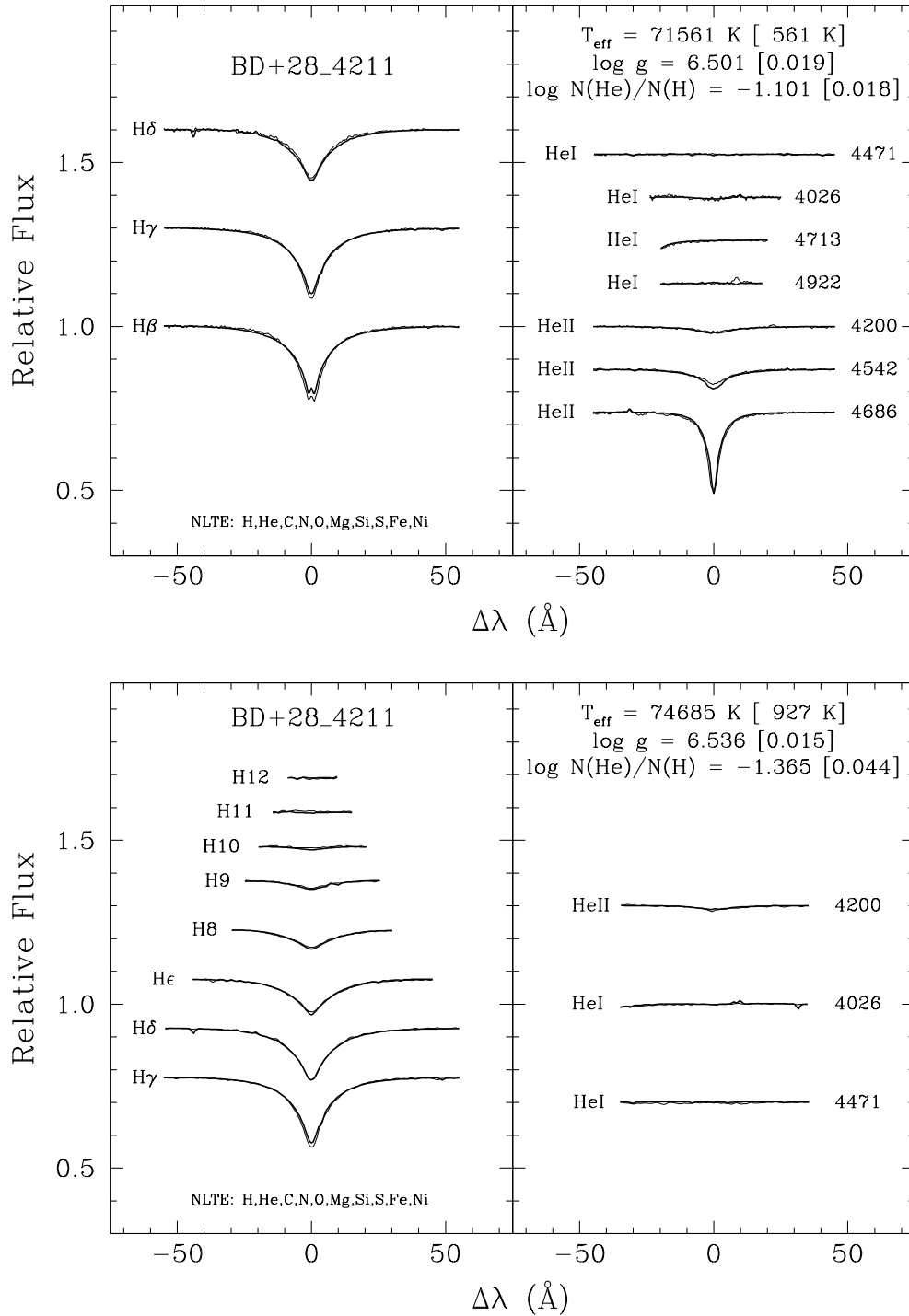


FIGURE 3.4 – Top – Best fit obtained with the 1 \AA resolution MMT spectrum of BD+28°4211 using the model grid that includes the following elements : C, N, O, Mg, Si, S, Fe, and Ni, and the abundances determined in Paper I. Bottom – Best fit obtained with the *blue* 1.3 \AA resolution spectrum.

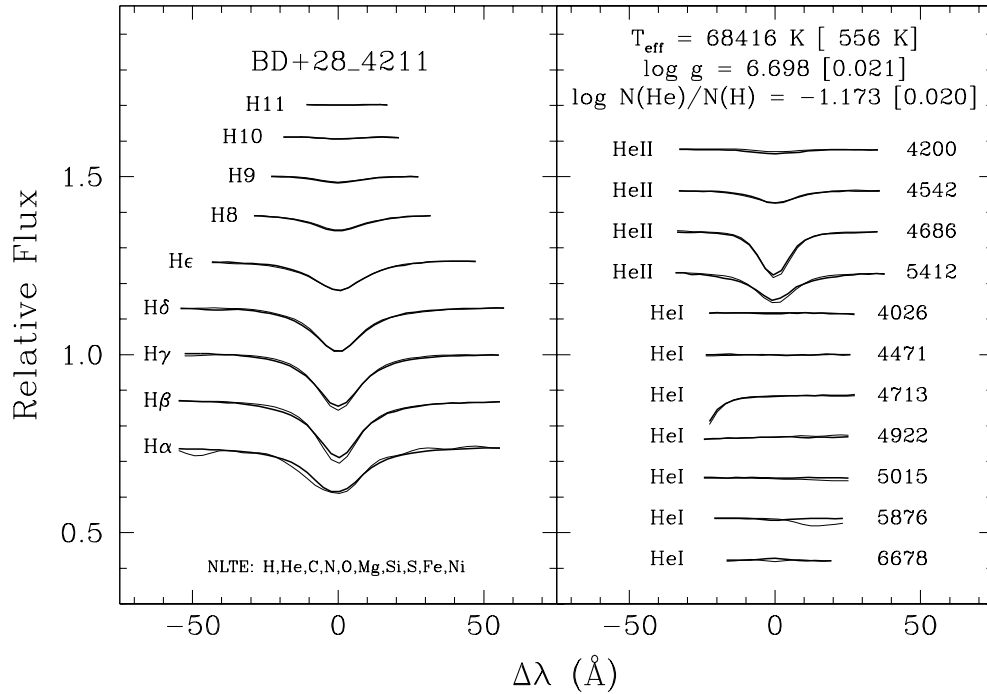


FIGURE 3.4 – Continued. Best fit with the lowest resolution spectrum (8.7 Å).

and also influences the depth, but again not by a very large amount (this will be discussed in more details in the next section). This causes an intrinsic uncertainty associated with any parameter determination based on optical data. Secondly, a consequence of the first point is that using very high quality spectra (in terms of S/N) allows to see the small discrepancies between our best-fit models and the observations. With spectra having a more representative sensitivity, the fits from Figure 3.4 might have looked acceptable and the parameters thus deduced would have been wrong. It should also be mentioned that forcing the temperature to a value of 82,000 K, while fitting the two other parameters, does not result in much better fits with this grid of models. Such a fit can be seen in Figure 4 of Latour et al. (2014).

Finally, we fitted our three spectra using the third grid of models, the one with enhanced abundances of ten times the solar ones for the eight elements previously mentioned. The resulting fits can be seen in Figure 3.5. Effective temperature around 80,000 K are obtained with this grid and the fits now reproduce very well the observed spectra. This is a rather encouraging result and, for the first time, we are able to obtain realistic atmospheric parameters

and to reproduce the observed optical spectrum of a hot sdO star through a formal fitting procedure.

The resulting parameters of our various fits are summarized in Table 3.1. An increase of the effective temperatures with the increasing metallic content of the models is easy to notice, culminating in realistic values when using the third grid of models. As mentioned previously, the helium abundances deduced with the various grids stay roughly the same, at values slightly lower than the solar one ($\log N(\text{He})/N(\text{H}) = -1.0$). Note that the lower helium abundances given by the *blue* spectrum are most likely due to the fact that only the very weak He II 4200 Å line is fitted in this spectrum. As for the surface gravity, the values obtained with the two line-blanketed grids are higher than the previously determined one of $\log g = 6.2$. Still a value of 6.5 dex is not incompatible with the conclusions we drew in Paper I of a surface gravity of $6.2^{+0.3}_{-0.1}$ dex, though it is the upper limit. Let us remind the reader that the UV metallic lines (mainly of iron) did not help in constraining very tightly the surface gravity, but

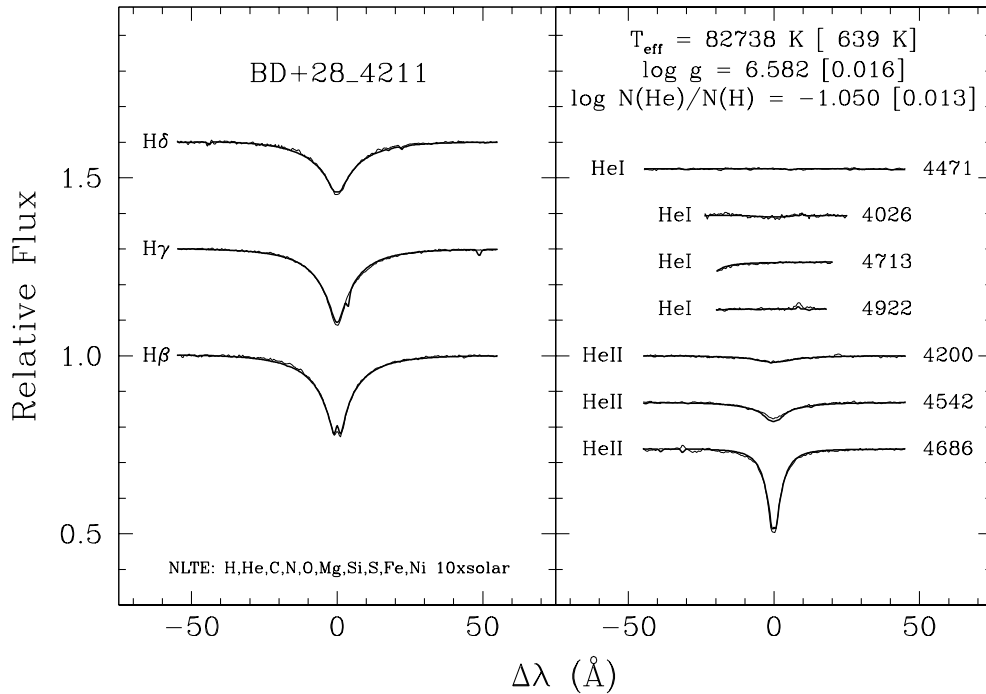


FIGURE 3.5 – Best fit obtained with the 1 Å resolution MMT spectrum of BD+28°4211 using our model grid with a enhanced metallicity of ten times the solar one (for the eight atomic species previously mentioned).

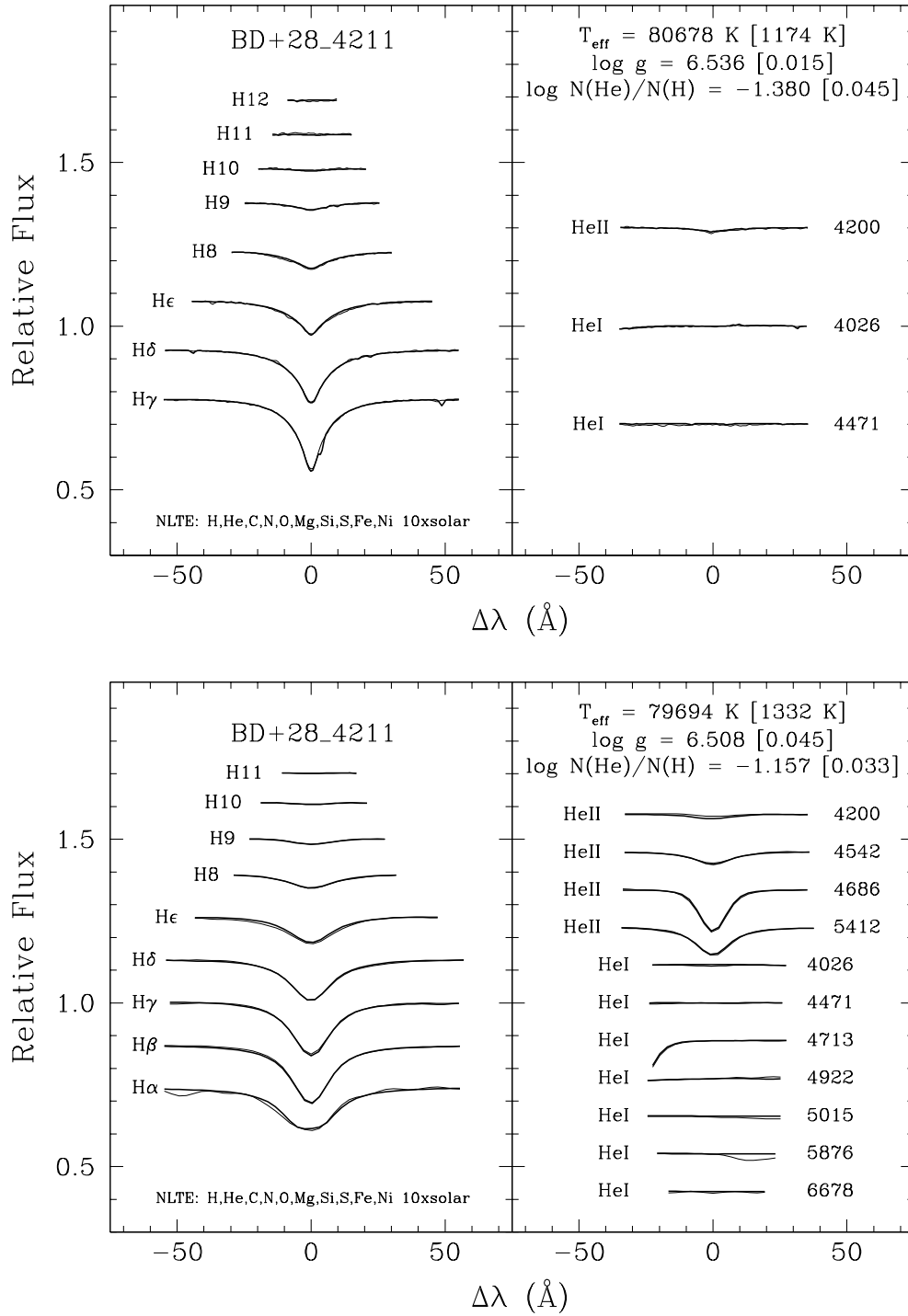


FIGURE 3.5 – Continued. Top – Best fit obtained with the *blue* 1.3 \AA resolution spectrum. Bottom – Best fit with the lowest resolution spectrum (8.7 \AA).

a slightly better match was nevertheless obtained with $\log g = 6.2$, hence the adopted value. On the other hand, when we compared the spectroscopic distance of BD+28°4211 for various combinations of masses and surface gravities with the one given by the *Hipparcos* parallax of the star, a $\log g \geq 6.4$ was needed, unless the mass of the star is significantly lower than the canonical value of $\sim 0.5 M_{\odot}$ for a hot subdwarf. This is why the upward uncertainty we adopted on $\log g$ allows for a surface gravity of at most 6.5 dex. This upper value gave good spectroscopic distances for masses between 0.4 and $0.5 M_{\odot}$ and still was not conflicting with the UV metal lines. We also checked the old *Hipparcos* parallax value for the star (Perryman et al. 1997) and the distance derived with this older value is between 88 and 126 pc. This is a little closer to the spectroscopic one but still does not allow for a good match of the distances with models having $\log g$ of 6.2 dex, unless the mass is around $0.3 M_{\odot}$. In the light of the present analysis, it is most likely that the true value of the surface gravity of BD+28°4211 is closer to 6.5 dex than to the value of 6.2 dex suggested in Paper I.

TABLE 3.1 – Results of our fitting procedures for BD+28°4211

Spectrum	T_{eff} (K)	$\log g$ (dex)	$\log N(\text{He})/N(\text{H})$ (dex)
NLTE H,He model grid			
MMT	$66,479 \pm 659$	6.238 ± 0.023	-1.208 ± 0.024
Blue 1.3 Å	$67,504 \pm 690$	6.387 ± 0.020	-1.336 ± 0.046
Lowres	$64,584 \pm 1,113$	6.463 ± 0.053	-1.177 ± 0.048
NLTE line-blanketed grid with the metallic abundances of BD+28°4211			
MMT	$71,561 \pm 561$	6.501 ± 0.019	-1.101 ± 0.018
Blue 1.3 Å	$74,685 \pm 927$	6.536 ± 0.015	-1.365 ± 0.044
Lowres	$68,416 \pm 556$	6.698 ± 0.021	-1.173 ± 0.020
NLTE line-blanketed grid with ten times solar abundances			
MMT	$82,738 \pm 639$	6.582 ± 0.016	-1.050 ± 0.013
Blue 1.3 Å	$80,678 \pm 1,174$	6.536 ± 0.015	-1.380 ± 0.045
Lowres	$79,694 \pm 1,332$	6.508 ± 0.045	-1.157 ± 0.033

3.4.3 Additional Verifications

3.4.3.1 High Resolution Optical Spectra

Herbig (1999) reported observations of BD+28°4211 made with the HIRES spectrograph at the Keck I telescope where he noted that the spectrum of the star, rather featureless at medium resolution save for the Balmer and helium lines, shows a lot of narrow metallic absorption lines and a handful of emission ones. They essentially originate from ions of oxygen, nitrogen, carbon, and silicon. Another interesting benefit of these high resolution observations (up to 0.1 \AA , depending on the slit used) is that they resolve the emission cores present in the lowest member of the Balmer series ($H\alpha$, $H\beta$) and the strongest He II lines. In our own spectra of BD+28°4211, only the emission of $H\beta$ is discernible. As discussed above, the HIRES spectra are not suitable for a formal multiline analysis, but we still can use them to test our model atmospheres and see if our metal-enhanced ones can reproduce, in their very details, some Balmer and helium lines featured in the high resolution data. The wavy continuum of the orders were flattened with the method described in Section 3.3. We usually checked a line in more than one dataset, to make sure the flattened results were similar.

The first line we looked at was the He II $\lambda 4686$. In our MMT spectrum, this line shows no central emission but the HIRES data show a well defined one. Referring to Figure 3.2 this line is among the less affected by the addition of metals in the model atmospheres. Nevertheless, with a resolution ten times better than that characterizing the MMT spectrum ($\Delta\lambda \sim 0.1 \text{ \AA}$ in the HIRES spectrum) there is a definite improvement in the way $\lambda 4686$ is reproduced when the metallicity is increased (Figure 3.6, left panel). In fact, the match between an optimal model spectra ($T_{\text{eff}} = 82,000 \text{ K}$, $\log g = 6.4$ and $\log N(\text{He})/N(\text{H}) = -1.0$, metal abundances ten times solar) and the HIRES observation of this helium line is very impressive. Comparing models having different values of $\log g$ between 6.2 and 6.6 dex shows that this particular line is rather insensitive to such a change although the larger values seem favored (Figure 3.6, right panel).

The next line we examined was $H\beta$, which was taken from a dataset where its position is farther from the edge of the order (2011-10-04), but still quite close, so the continuum level is

somewhat uncertain. Nevertheless, the agreement between this line and our models is also very good (Figure 3.7). The left panel shows that $H\beta$ is rather insensitive to changes of effective temperature while a change in the surface gravity has a small effect on the depth of the line (right panel). Note that in this comparison, as well as in the following ones in this subsection, the synthetic spectra are taken from the ten times solar metallicity grid, and the values of the fixed parameters are among $T_{\text{eff}} = 82,000$ K, $\log g = 6.4$, and $\log N(\text{He})/N(\text{H}) = -1.0$.

Another very interesting line to look at in the HIRES data is $H\alpha$, which has a very prominent emission core in its center and, also, a secondary one associated with the He II component of the line. In our own spectra, we only have this line at a resolution of 8.7 \AA where all of the emission is wiped off to leave only an unusual round shape. The challenge with this line in the HIRES data was that it is always positioned near the edge of an order, at least in the datasets we inspected in the KOA. Our best attempt at straightening up this line

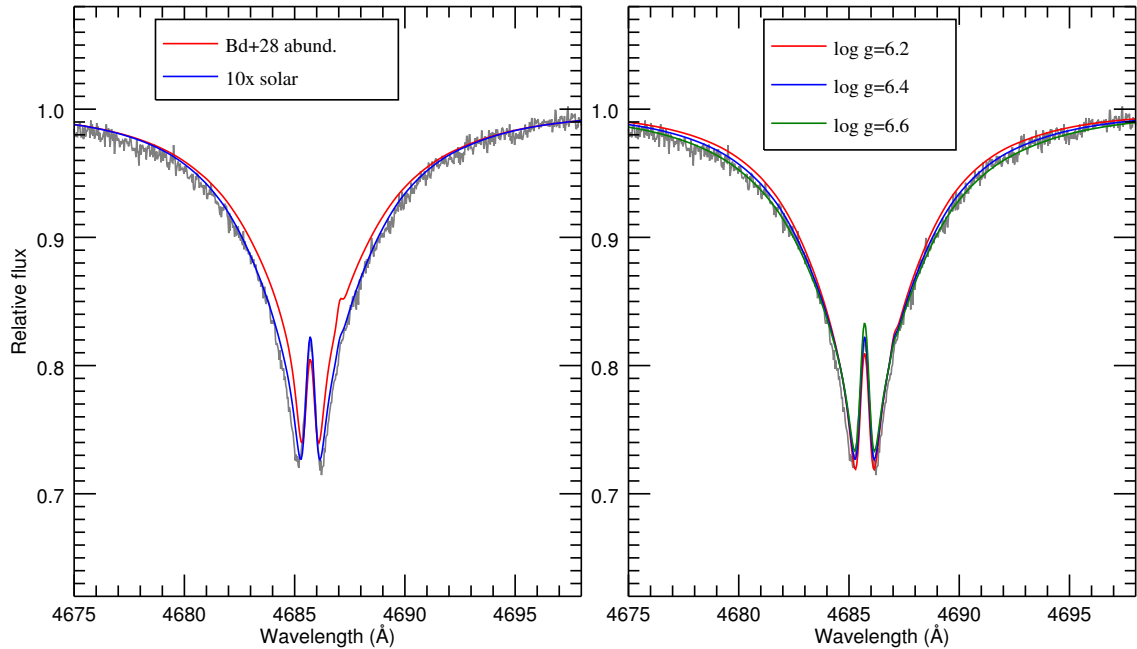


FIGURE 3.6 – Comparisons between synthetic spectra and the He II 4686 \AA line from HIRES (1997-08-12). Left – Synthetic spectra from models at $82,000$ K, $\log g = 6.4$, and $\log N(\text{He})/N(\text{H}) = -1.0$; in red the spectrum comes from a model with the abundances of BD+28°4211 determined in Paper I. In blue the spectrum is from a model with ten times the solar metallicity. Right – Spectra from the ten times solar metallicity grid, having various surface gravities.

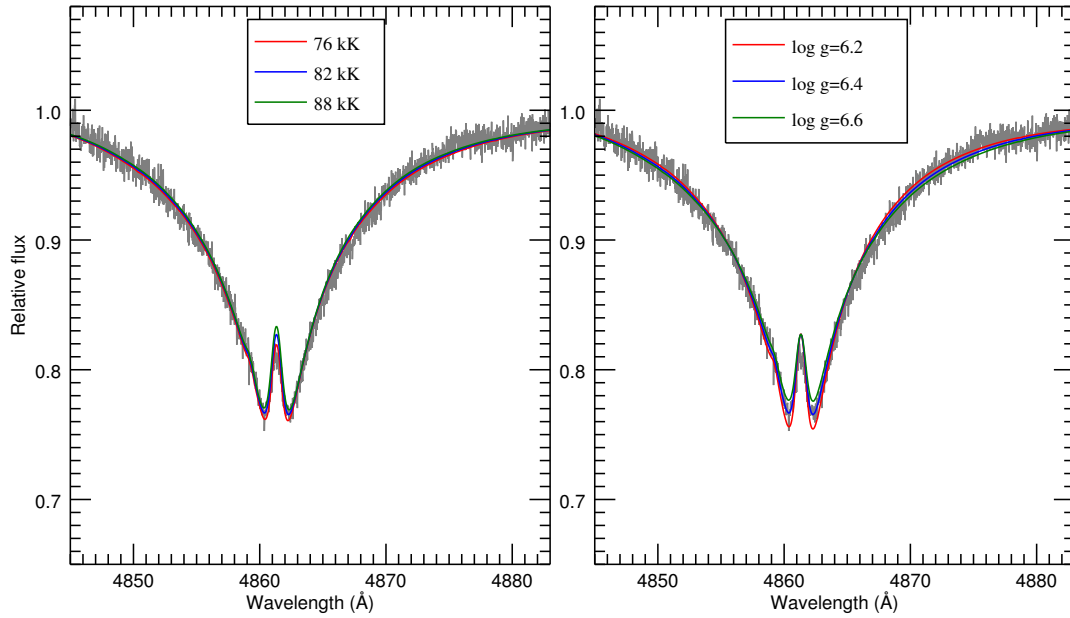


FIGURE 3.7 – Comparisons between synthetic spectra and the $H\beta$ line from HIRES (2011-10-04). Left – For models having different effective temperatures. Right – For models having different surface gravities.

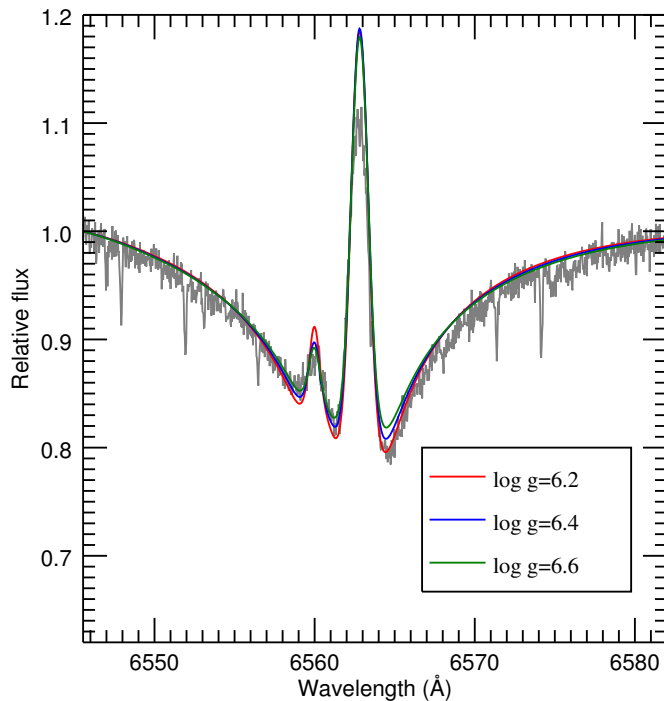


FIGURE 3.8 – Comparison between synthetic spectra having different $\log g$ and the $H\alpha$ line from HIRES (2011-10-04).

was with the same observation as $H\beta$, for which $H\alpha$ was also farther from the order's edge than in the other datasets. Figure 3.8 shows the resulting observed line, again with spectra having different surface gravities. Note that the small absorption lines in the $H\alpha$ region are telluric lines so they do not originate from the star. The effects resulting from an increased metallicity on $H\alpha$ are visible in Figure 3.2: the line is deepened in its core and the emission peak is slightly higher. Our comparison shows that the emission peak of our models is too high, but the depth and width of the line are well reproduced. We also compared the line with models from our second grid, having the abundances of BD+28°4211, and the emission peak is also higher than the observed one, but the model lines are neither deep nor wide enough.

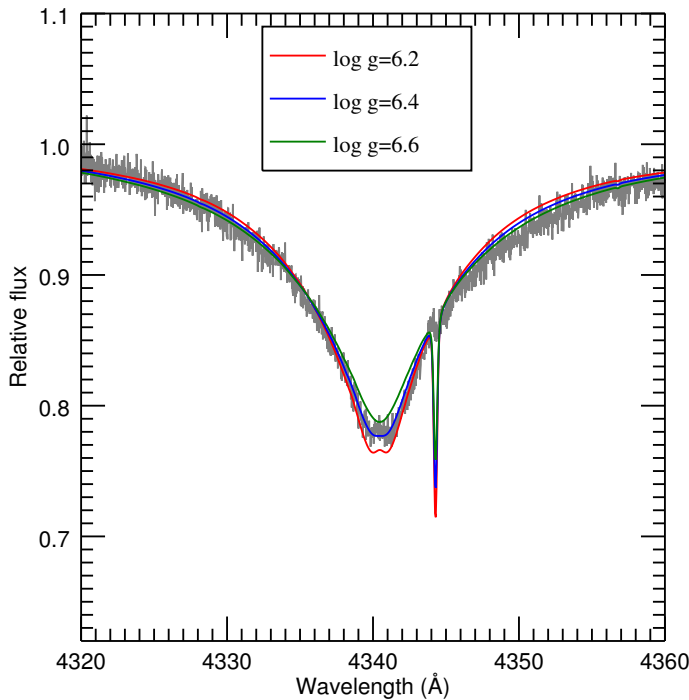


FIGURE 3.9 – Comparison between synthetic spectra having different $\log g$ and the $H\gamma$ line from HIRES (2011-10-04).

The comparison between $H\gamma$ and some of our models is shown in Figure 3.9. This line is also rather well reproduced with our models, but this time a surface gravity of 6.4 dex seems to offer a better match. The thing to note here is the presence of a small emission core in the observed line. Such an emission is not often seen in Balmer lines other than $H\alpha$ and $H\beta$. The high resolution is essential to see this type of feature. Emission is barely seen in our lowest gravity model and it is not strong enough to reproduce the observed one.

The last line to show an emission core is the He II line at 5412 Å. It is the second strong line for which we had observations only at low resolution. The match between our synthetic spectra and the HIRES one is not as good in this case; the model lines are too deep (Figure 3.10). The same conclusion holds with observations from two different datasets, so the flattening of the spectrum should not be the cause of this discrepancy. In fact, the depth of the observations coincides better with the depth of the line from models having the abundances of BD+28°4211, but in this case the line wings are too narrow. In both type of models, small emission cores are seen but they are too small when compared to the observations.

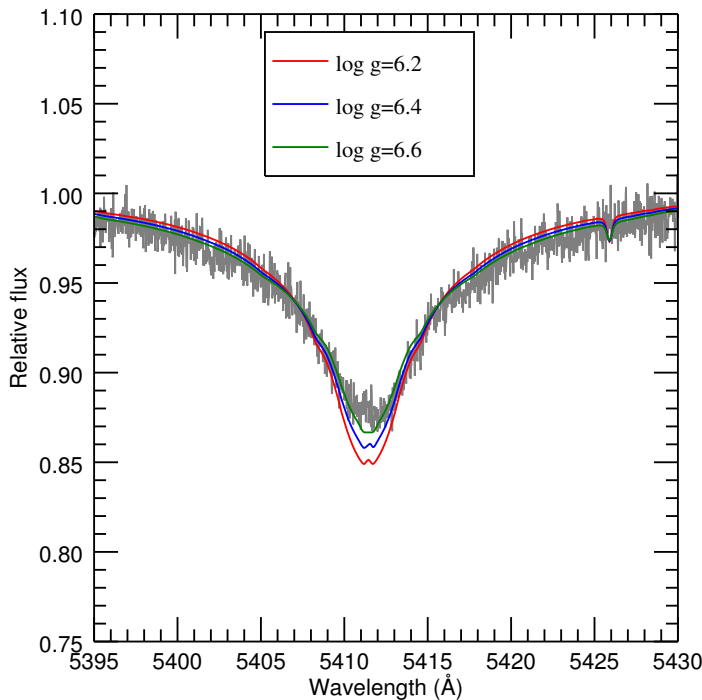


FIGURE 3.10 – Comparison between synthetic spectra having different $\log g$ and the He II line at 5412 Å from HIRES (2005-08-12). Note that this particular observation has a resolution of ~ 0.15 Å.

There is one last feature that was worth investigating with the HIRES spectra and that is the He I 5876 Å line. Napiwotzki (1993) used this line to secure the effective temperature he deduced for BD+28°4211 using the He I line. He compared model spectra having different temperatures with his observations and found a best match for an effective temperature between 80 and 85 kK (let us remember that metal-free NLTE models were used at the time). He had at his disposal a 0.4 Å resolution spectrum that appears to be more noisy than the HIRES ones. The feature he associated with He I $\lambda 5875$ is barely visible in his spectrum but

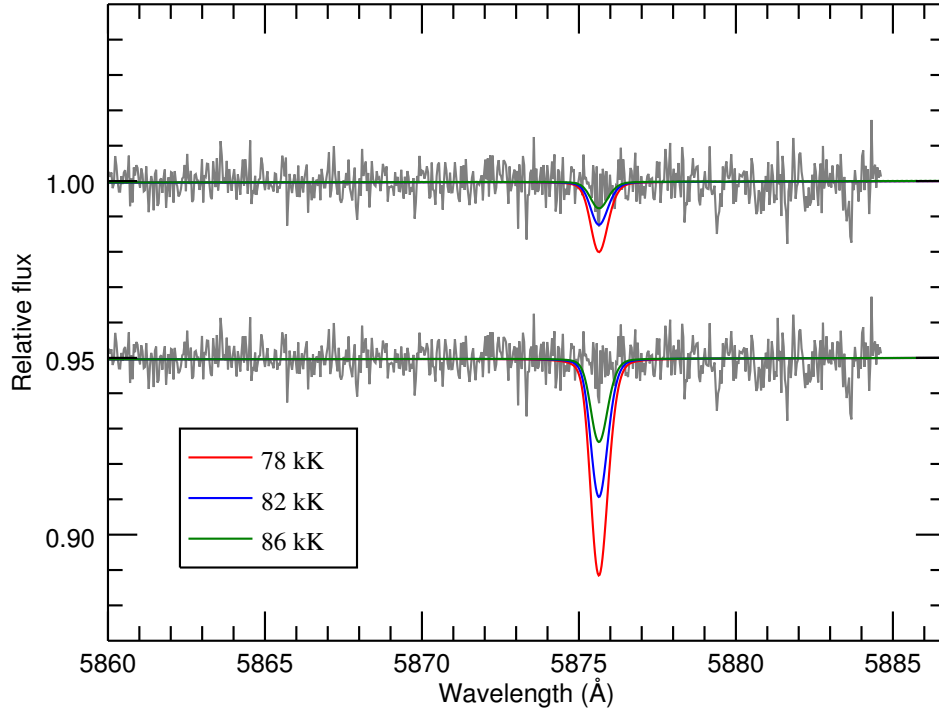


FIGURE 3.11 – Comparisons between synthetic spectra and the He I 5876 Å region from HIRES (1997-08-12) for models having different effective temperatures. Top – The model spectra are taken from our metal enriched grid. Bottom – The model spectra come from a metal-free model grid and have $\log g = 6.2$ dex, as those used by Napiwotzki (1993).

should be distinguishable in the HIRES ones. However, after a careful inspection we did not find any trace of this line in the three observations that included this region. If there is indeed a line, then it is weaker than the noise level. Figure 3.11 shows the region of interest for the observations of the night of the 1997-08-12. The top comparison is with three models having a different effective temperature, as usual taken from our metal-enhanced grid. With $T_{\text{eff}} \geq 82,000$ K, the line is predicted to be within the noise level. Since the helium line is not visible in the observations, we used the C IV emission line at 5811 Å (identified in Herbig 1999) present in the same order and shifted the observed spectrum so that its C IV line coincides with the one in our model spectra. In this way, we can be sure that the observed spectrum is properly shifted in wavelength. The bottom comparison is made with synthetic spectra analog to those used by Napiwotzki, i.e., metal-free and with a surface gravity of 6.2 dex. The lines

predicted are way too strong. In the light of these results, it may have been a happy accident that Napiwotzki (1993) secured properly the effective temperature of BD+28°4211.

3.4.3.2 UV Helium lines

The previous comparisons between high resolution optical lines and our model spectra with ten times solar abundances clearly demonstrated that our metal-enhanced models, overall, match very well the Balmer and helium lines seen in the HIRES spectrum of BD+28°4211. But what about the helium lines in the UV range, are they affected by an enhanced metallicity? This point is worth investigating because, referring to Figure 5 of Paper I in which an oxygen line is located just next the to He II 1640 Å line, one can notice that the helium line in question seems quite well reproduced by the model used then, while we just saw that the optical He II lines cannot be reproduced with such models.

Figure 3.12 shows comparisons of this line, first with models having various $\log g$ and

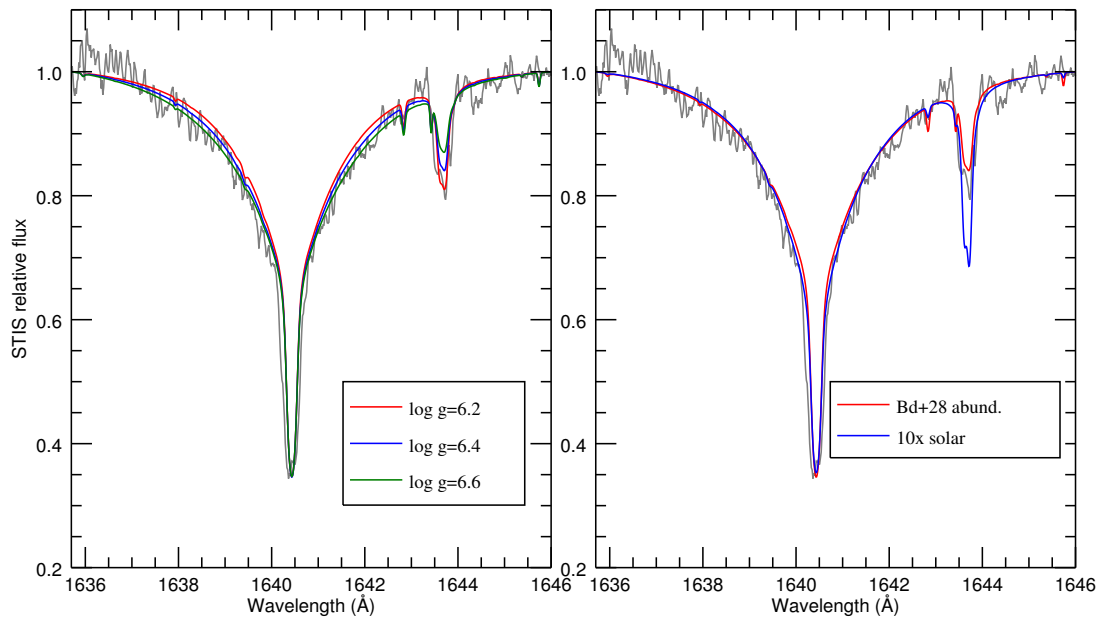


FIGURE 3.12 – Comparisons between synthetic spectra and the He II 1640 Å line from the STIS spectrum. Left – With models having metallic abundances corresponding to those of BD+28°4211: $T_{\text{eff}} = 82,000$ K, $\log N(\text{He})/N(\text{H}) = -1.0$ and various $\log g$. Right – With models having $\log g = 6.4$ but different metallic contents.

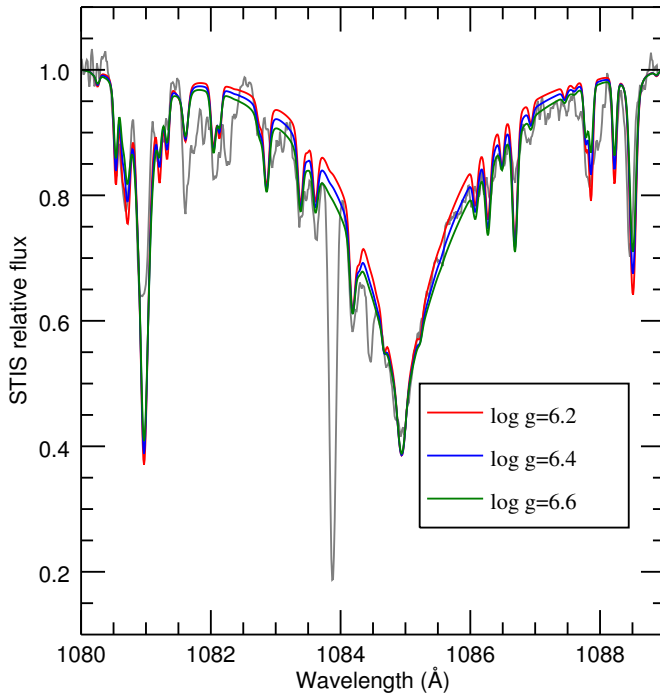


FIGURE 3.13 – Comparisons between synthetic spectra and the He II 1085 Å line from the FUSE spectrum. The models have the metallic content of BD+28°4211 and different values of $\log g$.

the abundances of BD+28°4211, where one can see that the changes thus induced are rather small. The wings are well reproduced by the models but the central absorption is wider in the observations. This is a bit intriguing and we verified that no change of parameters (T_{eff} , $N(\text{He})/N(\text{H})$) affects much the width of the core. The rotational velocity of the star is known to be quite small (Herbig 1999), so this option can be disregarded. As for a metallicity effect, the right panel of Figure 3.12 shows that there is only a slight difference in the line profile between a model having the abundances of BD+28°4211 and one having ten times the solar metallicity and this difference is not in the central core. We do not know why the central core is not reproduced correctly; it might have something to do with the theoretical line profile, since the core width remains unaffected by changes in the parameters of model atmospheres. We did not find in the literature any mention of this problem, but its solution would at least require the availability of a star having fundamental parameters relatively close to those of BD+28°4211 in order to display a similar line profile with a sharp central core absorption. Alternatively, microturbulence (not included in our synthetic spectra) might be at work here.

We finally also examined how the He II 1085 Å line featured in the FUSE spectrum

of BD+28°4211 is reproduced by our model spectra. We compared it with models having the metallic abundances determined in Paper I and various surface gravities in Figure 3.13. Again the variation of $\log g$ does not produce important differences in the line profile and the models having realistic abundances reproduce well this helium line. This is true also for metal-enhanced models.

3.5 Discussion

We began our comprehensive analysis of BD+28°4211 with the ultimate goal of retrieving the atmospheric parameters of the star by carrying out a standard fitting procedure of its optical spectrum alone, as it is done for the cooler hot subdwarfs. The challenge was to somehow “overcome” the Balmer line problem that prevents from modeling the observed Balmer series with a unique set of fundamental parameters. As discussed in Section 3.2, this problem is a major one in hot sdO stars and makes it very tricky to determine fundamental parameters of such stars, especially their effective temperatures. A careful inclusion of metal line-blanketing in model atmospheres seemed a promising way to solve this issue, or at least to diminish the discrepancies between observed and theoretical lines as was shown by Werner (1996).

The first part of this analysis, presented in Paper I, focussed on the UV spectrum, which is a standard way to study very hot stars and usually leads to sound results (Rauch et al. 2007; Ziegler et al. 2012; Rauch et al. 2013). By self-consistently fitting the numerous metallic lines in the UV spectra from *FUSE* and the *HST* spectrograph *STIS*, we were able to draw up a realistic chemical composition for the atmosphere of BD+28°4211. We also confirmed that the previously estimated fundamental parameters ($T_{\text{eff}} \sim 82,000$ K and $\log g \sim 6.2$) are in good agreement with the observed UV spectrum. The following step in our study, the subject of this article, was to use the abundances thus determined to build a grid of NLTE line-blanketed model atmospheres specifically suited to BD+28°4211 and use it to perform a spectroscopic fit of the star’s optical spectrum. However, even though significant improvements were obtained in the modeling of the observed optical lines as compared to the case where metal line-blanketing was neglected, we disappointedly realized that these custom-made models were still falling short of the desired results. And indeed, as seen in Figure 3.4 for example, the

best fits obtained with our three spectra gave effective temperatures too low by about 10,000 K and, in addition, the observed spectral lines are not well reproduced. However, note in this latter case that with much lower S/N data than our superlative spectra, it would have been very difficult, if not downright impossible, to detect the small but quite significant differences between the observed and computed line profiles in the panels of that figure.

In the past, some similar “fitting” problems were solved by artificially increasing the metallicity of LTE model atmospheres. This method proved useful in the sdOB transition range ($T_{\text{eff}} \sim 35,000$ K) where the LTE metal-rich models (with ten times the solar metallicity) yield improved matches between the observed lines and the best-fitting models, but this without changing much the fundamental parameters derived (O’Toole & Heber 2006; Geier et al. 2007). In that temperature range, the mismatch between observed and model spectra is not so much in the Balmer lines themselves but rather in the helium ones, for which the lines originating from both ionization stages cannot be correctly reproduced without this artefact. The Balmer line problem is also seen in hot white dwarfs and a few of those analyzed in Gianninas et al. (2010) were much better reproduced with NLTE model atmospheres including C,N,O with ten times their solar abundances. It is thought that this approach compensates, at least partially, for some unknown opacity sources to the point where the atmospheric structure is affected in the “correct” way.

With these informations in mind, and as a fallback position, we built a grid of NLTE line-blanketed model atmospheres including metals having ten times their solar abundances. This metal-enhanced grid ultimately allowed us to derive satisfactory fundamental parameters for BD+28°4211 on the basis of our optical spectra. Moreover, the fits obtained reproduce simultaneously very well all of the observed spectral lines. As can be noticed in Table 3.1, an increase of the metal content of the models, from zero to ten times solar, raises the effective temperatures derived. The correct, well established value of T_{eff} ($82,000 \pm 5000$ K) from Paper I is reached when using the metal-enriched grid. The associated surface gravities thus derived ($\log g \sim 6.5$) are higher than the favored value of 6.2 dex obtained in Paper I, but are still within the uncertainty range quoted there. With this new preferred value of $\log g$ for BD+28°4211, the measured *Hipparcos* distance now becomes compatible with a mass of ~ 0.45

M_{\odot} for that star (see Table 3 in Paper I), well within the canonical range of accepted values for hot subdwarf stars. Table 3.1 also indicates that the optimal value of the helium abundance, $\log N(\text{He})/N(\text{H}) \simeq -1.1$, is perfectly compatible with the value assumed in Paper I.

As an a posteriori test, we exploited some of the HIRES data of BD+28°4211 available in the KOA. With their very high resolution and good S/N, they provide an incomparable insight into the detailed profiles of several Balmer and helium lines of the star. We were able to overcome the drawback that comes with these data, the wavy continuum, and ended up with observed lines that could be compared with our models. That way we tested if our optimal model atmospheres, with their artificially enhanced metal abundances, could reproduce the detailed observations of HIRES. We also took this opportunity to check if a $\log g$ higher than 6.2 indeed allows for a better match of the high resolution observations. Our comparisons showed that our metal-enriched models indeed reproduce very well the following lines : He II $\lambda 4686$, H α , H β , and H γ . In the details, there is a small discrepancy between our models and the emission peak observed in H α , which is predicted to be higher. A tiny emission bump is also discernible in the core of H γ but was not fully reproduced by our models. The worst match was with He II 5412 Å line, for which the line core is predicted somewhat too deep. As for the surface gravity, He II $\lambda 4686$, H β and H α are barely affected by a change of surface gravity between 6.2 and 6.6 dex, even at a resolution of 0.1 Å. In contrast, H γ offers a better match with the model at $\log g = 6.4$. Still, given a certain uncertainty in the continuum level, our comparisons with these lines do not allow us to rule out any of the surface gravities tested. We also looked at the results of a fitting procedure (using the MMT and the *blue* spectra) where the effective temperature and the surface gravity were fixed at 82,000 K and 6.2 dex, respectively. The lines that are the most affected by the imposition of this surface gravity value are H δ , H ϵ , and He II at 4542 Å. Their match is not as good at $\log g = 6.2$ as it is in Figure 3.5. The “pull” towards a higher surface gravity thus comes from these lines in our fits.

What we learned from our analysis is that despite the fact that the UV spectrum can be very well reproduced by model atmospheres including the metal abundances derived for BD+28°4211, such models fail to reproduce the optical Balmer and helium lines. In order to achieve adequate results in the optical domain, we had to include in our models metal

abundances ten times larger than their solar values. The good side to this is that we were then able to derive appropriate fundamental parameters for BD+28°4211, based only on its optical spectrum. The downside is that to get these results we had to set our metal abundances to unrealistic values. These large abundances somehow affect the atmospheric structure of our models in a way that makes the optical lines correctly modeled. Maybe the additional blanketing brought about by the enhanced abundances of the species included in our models account for some missing opacities present in the star but not in our models. It is possible that these missing opacities come from atomic species not included in our models (these species should not be dominant in the star numberwise, but their opacities might be important), transition lines not accounted for, or improper broadening of some metal lines. However, it seems a little odd that such missing opacities would significantly affect the Balmer and helium optical lines, while the UV ones can be accounted for very well without the induced change in the atmospheric structure. In any case, this knowledge should be very useful for obtaining more accurate fundamental parameters for hot sdO stars (and possibly also for very hot white dwarfs) when observations in the optical range are the only ones available. One must not forget though that at such high temperatures, as we saw in the previous section, some optical lines can be rather insensitive to changes in parameters. This constitutes an intrinsic limitation to the precision that can be achieved with optical data and also requires a certain minimal quality for the observational data themselves.

In the light of our results and of previous investigations, we thus propose, along with earlier researchers, that the atmospheric structures of hot stars be computed with artificially enriched metal abundances as an interim solution for estimating their atmospheric parameters if only optical spectroscopy is available. In the specific case of BD+28°4211, we found that increasing the metallicity tenfold with respect to the Sun was adequate to account very well for its optical spectrum. But what about a star cooler than 80,000 K? The Balmer line problem is also seen in stars in the range from 40 to 60 kK, for which estimated temperatures, based on optical spectra only, are very uncertain. This is especially relevant in the case of the newly discovered pulsating stars in ω Cen (Randall et al. 2011) which are among the rare sdO stars known to pulsate. Their temperature determination via the fitting of their Balmer and helium

lines with a grid of NLTE line-blanketed model spectra with normal metallic abundances yield values around 50,000 K. However, preliminary non-adiabatic exploration of the sdO star region did not show pulsational instabilities around this particular effective temperature (Randall et al. 2012), but only at higher values. A legitimate question that might be raised in this case is about the validity of the spectroscopically derived temperature, which must certainly be underestimated according to the present findings.

In order to explore in a very preliminary way the effects of an enhanced metallicity over a wider range of effective temperature, we built a small grid of dedicated model atmospheres. It includes eight effective temperatures between 22,000 and 90,000 K. The temperature of the models between 40,000 and 90,000 K varies by step of 10,000 K, and they have $\log g = 6.0$ and $\log N(\text{He})/N(\text{H}) = -1.0$, representative of hot sdO's. The two coolest models, in order to be more representative of EHB stars, have the following parameters: $T_{\text{eff}} = 22,000$ K, $\log g = 5.4$ and $T_{\text{eff}} = 30,000$ K with $\log g = 5.6$ and they both have $\log N(\text{He})/N(\text{H}) = -2.0$. For each of these nine sets of parameters, we built metal-free model atmospheres and models including the line blanketing of C, N, O and Fe at solar and ten times solar abundances. All of these models were computed in NLTE. Figures 3.14 and 3.15 feature the four lowest Balmer lines ($\text{H}\alpha$ to $\text{H}\delta$) and the He II $\lambda\lambda 4686, 5412$ lines convolved at a resolution of 1.0 \AA for our entire set of model atmospheres. The models are shown in order of increasing temperature from bottom to top; indeed the depth of the Balmer lines decreases with increasing effective temperature. For the two coolest models, the effects of metals are rather subtle. These effects become more pronounced in the 40,000 K model. An increase in metallicity causes a deepening and a widening of the lines in most cases, the exceptions being when an emission core starts to form. In these cases, the core of the line will appear more shallow. These emission cores are enhanced by the presence of metallic elements. The two figures show that the effects of line blanketing, with solar and ten times solar abundances, are important in all models hotter than 40,000 K. It is possible that stars having different effective temperatures need different amount of metals in order for their observed lines to be best reproduced. Such tests using high quality spectra of a few sdO stars having different effective temperatures would be an interesting endeavor to pursue in future work. The sdO star Feige 34, for example, is

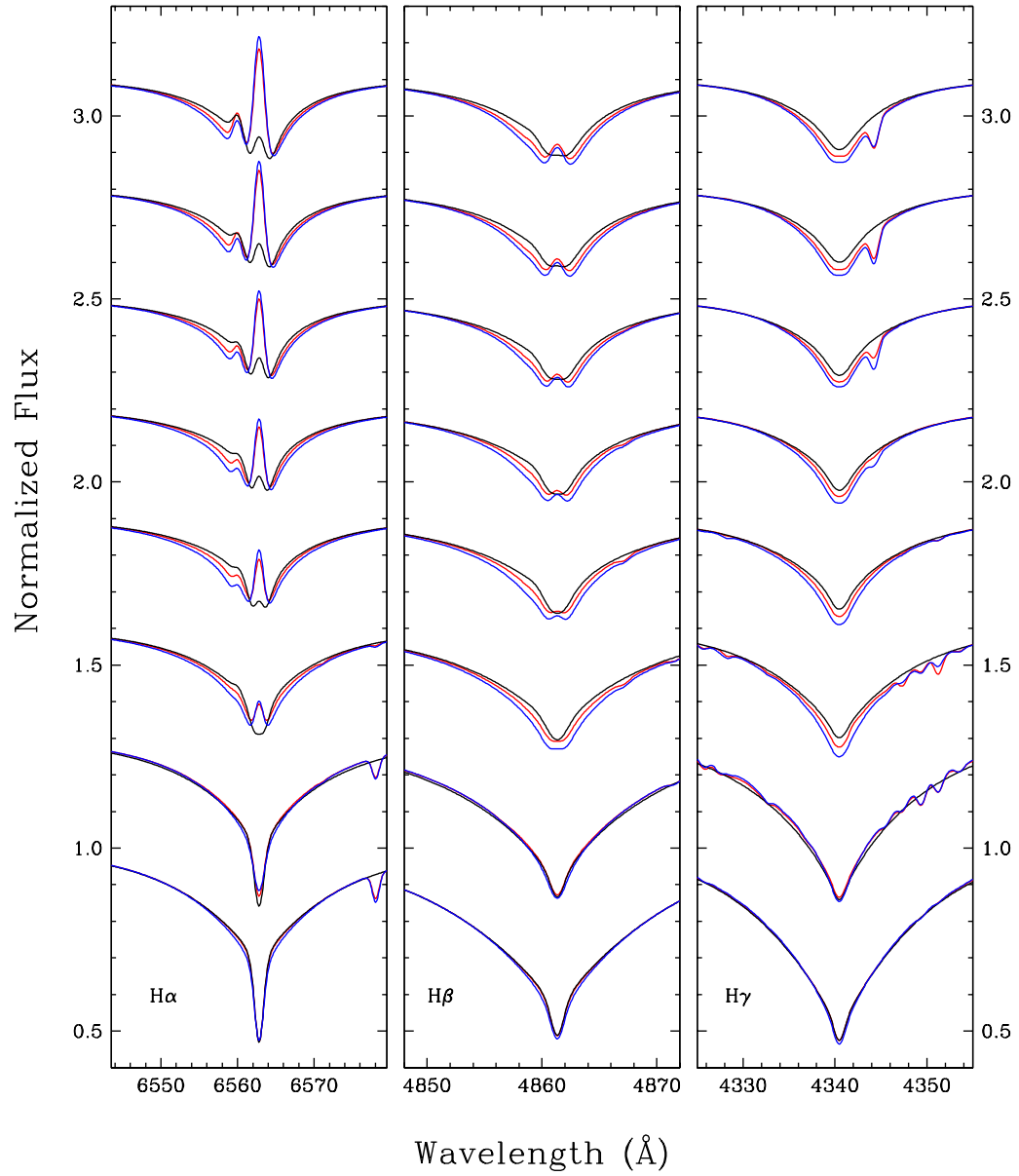


FIGURE 3.14 – Model optical lines (H α , H β and H γ) for various T_{eff} : 22,000 K to 90,000 K from bottom to top. Three metallicities are represented: H, He only (black), plus C, N, O and Fe in solar abundances (red) and ten times solar (blue). See the text for more detail on the models parameters.

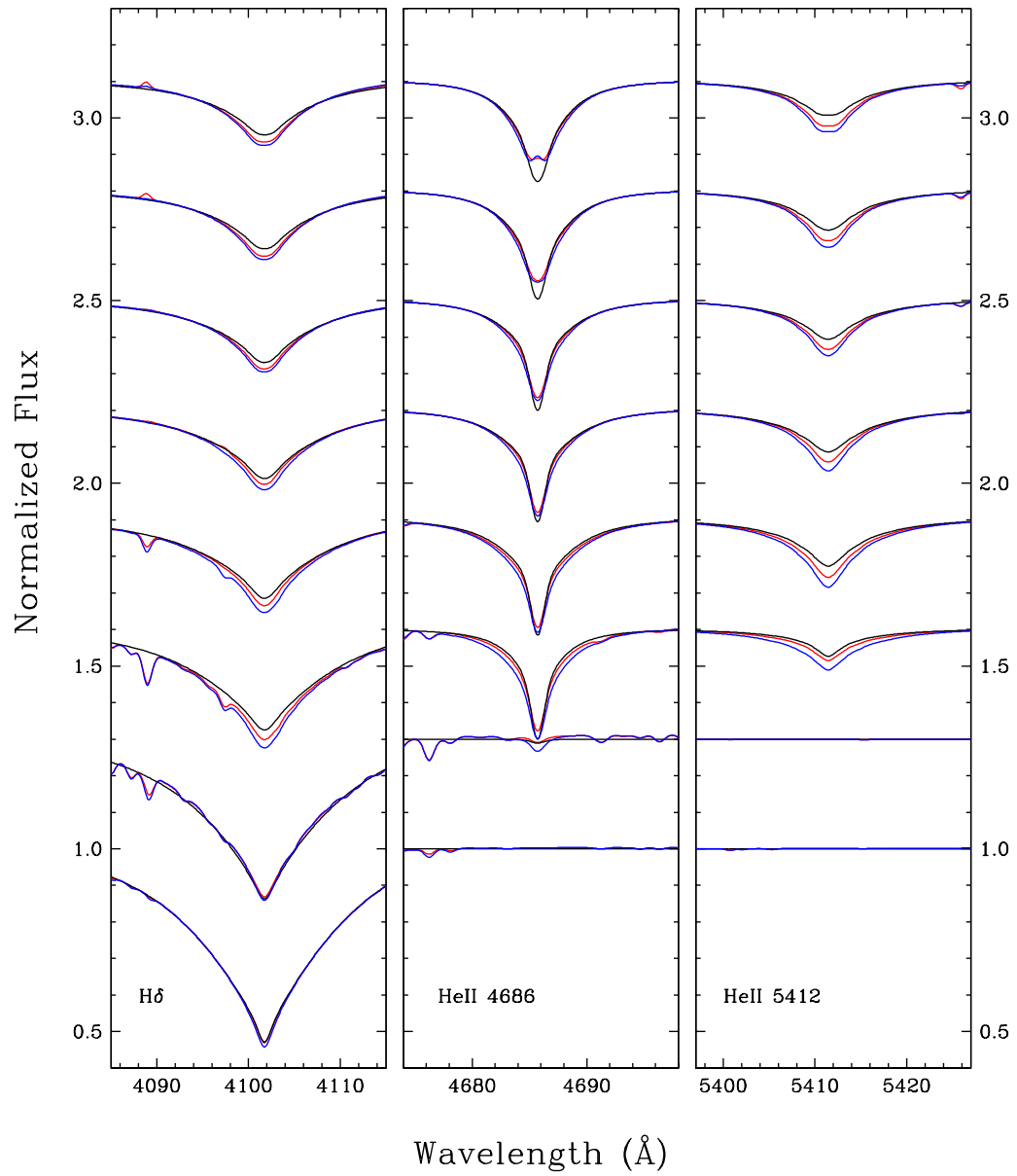


FIGURE 3.15 – Same as Figure 3.14 but for three additional lines: $H\gamma$ and He II $\lambda\lambda$ 4686, 5412.

likely a good candidate. Like BD+28°4211 it is a spectroscopic standard star for which good observational data (UV and optical) are available. Its spectrum suggests that it is cooler than BD+28°4211, but still quite hot ($T_{\text{eff}} \sim 60,000\text{--}65,000$ K).

This work was supported in part by the NSERC Canada through a fellowship awarded to Marilyn Latour and through a research grant awarded to Gilles Fontaine. The latter also acknowledges the contribution of the Canada Research Chair Program. This work has made use of the Keck Observatory Archive (KOA), which is operated by the W. M. Keck Observatory and the NASA Exoplanet Science Institute (NExScI), under contract with the National Aeronautics and Space Administration. We are also grateful to the PI's of the HIRES observations we used : A. Boesgaard, G. Herbig, D. Tytler, and W. Sargent.

3.6 References

- Bergeron, P., Saffer, R. A., & Liebert, J. 1992, *ApJ*, 394, 228
- Bergeron, P., Wesemael, F., Beauchamp, A., Wood, M. A., Lamontagne, R., Fontaine, G., & Liebert, J. 1994, *ApJ*, 432, 305
- Dreizler, S. & Werner, K. 1993, *A&A*, 278, 199
- Fontaine, M., Chayer, P., Oliveira, C. M., Wesemael, F., & Fontaine, G. 2008, *ApJ*, 678, 394
- Geier, S., Nesslinger, S., Heber, U., Przybilla, N., Napiwotzki, R., & Kudritzki, R.-P. 2007, *A&A*, 464, 299
- Gianninas, A., Bergeron, P., Dupuis, J., & Ruiz, M. T. 2010, *ApJ*, 720, 581
- Haas, S., Dreizler, S., Heber, U., Jeffery, S., & Werner, K. 1996, *A&A*, 311, 669
- Heber, U. 2009, *ARA&A*, 47, 211
- Heber, U., Edelmann, H., Lisker, T., & Napiwotzki, R. 2003, *A&A*, 411, L477
- Herbig, G. H. 1999, *PASP*, 111, 1144
- Hubeny, I. & Lanz, T. 1995, *ApJ*, 439, 875
- Latour, M., Fontaine, G., Brassard, P., Green, E. M., Chayer, P., & Randall, S. K. 2011, *ApJ*, 733, 100
- Latour, M., Fontaine, G., Chayer, P., & Brassard, P. 2013, *ApJ*, 773, 84
- Latour, M., Fontaine, G., Chayer, P., Green, E. M., & Brassard, P. 2014, in *Astronomical Society of the Pacific Conference Series*, Vol. 481, 6th Meeting on Hot Subdwarf Stars and Related Objects, ed. V. Van Grootel, E. M. Green, G. Fontaine, & S. Charpinet, 67
- Massey, P. & Gronwall, C. 1990, *ApJ*, 358, 344
- Moehler, S., Dreizler, S., Lanz, T., Bono, G., Sweigart, A. V., Calamida, A., Monelli, M., & Nonino, M. 2007, *A&A*, 475, L5
- Moehler, S., Dreizler, S., Lanz, T., Bono, G., Sweigart, A. V., Calamida, A., & Nonino, M. 2011, *A&A*, 526, A136
- Napiwotzki, R. 1992, in *Lecture Notes in Physics*, Berlin Springer Verlag, Vol. 401, *The Atmospheres of Early-Type Stars*, ed. U. Heber & C. S. Jeffery, 310–+

- Napiwotzki, R. 1993, *Acta Astronomica*, 43, 343
- Napiwotzki, R. & Rauch, T. 1994, *A&A*, 285, 603
- O’Toole, S. J. & Heber, U. 2006, *A&A*, 452, 579
- Perryman, M. A. C., Lindegren, L., Kovalevsky, J., et al. 1997, *A&A*, 323, L49
- Randall, S. K., Calamida, A., Fontaine, G., Bono, G., & Brassard, P. 2011, *ApJ*, 737, L27+
- Randall, S. K., Fontaine, G., Calamida, A., et al. 2012, in *Astronomical Society of the Pacific Conference Series*, Vol. 452, Fifth Meeting on Hot Subdwarf Stars and Related Objects, ed. D. Kilkenny, C. S. Jeffery, & C. Koen, 241
- Rauch, T., Werner, K., Bohlin, R., & Kruk, J. W. 2013, *A&A*, 560, A106
- Rauch, T., Ziegler, M., Werner, K., Kruk, J. W., Oliveira, C. M., Vande Putte, D., Mignani, R. P., & Kerber, F. 2007, *A&A*, 470, 317
- Saffer, R. A., Bergeron, P., Koester, D., & Liebert, J. 1994, *ApJ*, 432, 351
- Stroeer, A., Heber, U., Lisker, T., Napiwotzki, R., Dreizler, S., Christlieb, N., & Reimers, D. 2007, *A&A*, 462, 269
- van Leeuwen, F. 2007, *A&A*, 474, 653
- Werner, K. 1996, *ApJ*, 457, L39
- Ziegler, M., Rauch, T., Werner, K., Köppen, J., & Kruk, J. W. 2012, *A&A*, 548, A109

Chapitre 4

Improved determination of the atmospheric parameters of the pulsating sdB star Feige 48

M. Latour¹, G. Fontaine¹, E.M. Green², P. Brassard¹ and P. Chayer³

¹ *Département de Physique, Université de Montréal, Succ. Centre-Ville, C.P. 6128,
Montréal, QC H3C 3J7, Canada*

² *Steward Observatory, University of Arizona, 933 North Cherry Avenue, Tucson, AZ 85721*

³ *Space Telescope Science Institute, 3700 San Martin Drive, Baltimore, MD 21218*

Submitted to *The Astrophysical Journal*

Janvier 2014

4.1 Abstract

As part of a multifaceted effort to better exploit the asteroseismological potential of the pulsating sdB star Feige 48, we present an improved spectroscopic analysis of that star based on new grids of NLTE, fully line-blanketed model atmospheres. To that end, we gathered four high S/N time-averaged optical spectra of varying spectral resolution from 1.0 Å to 8.7 Å, and we made use of the results of four independent studies to fix the abundances of the most important metals in the atmosphere of Feige 48. The mean atmospheric parameters we obtained from our four spectra of Feige 48 are : $T_{\text{eff}} = 29,850 \pm 60$ K, $\log g = 5.46 \pm 0.01$, and $\log N(\text{He})/N(\text{H}) = -2.88 \pm 0.02$. We also modeled for the first time the He II line at 1640 Å from the STIS archive spectrum of the star and we found with this line an effective temperature and a surface gravity that match well the values obtained with the optical data. With some fine tuning of the abundances of the metals visible in the optical domain we were able to achieve a very good agreement between our best available spectrum and our best-fitting synthetic one. Our derived atmospheric parameters for Feige 48 are in rather good agreement with previous estimates based on less sophisticated models. This underlines the relatively small effects of the NLTE approach combined with line blanketing in the atmosphere of this particular star, implying that the current estimates of the atmospheric parameters of Feige 48 are reliable and secure.

4.2 Introduction

Koen et al. (1998) first reported the discovery of short-period (340-380 s) pulsations in the hot B subdwarf (sdB) star Feige 48. Since then, that star has attracted attention because it is relatively bright ($V = 13.48$) for this kind of pulsator, and because its optical light curve shows relatively large pulsation amplitudes that may reach a few percent of the mean intensity of the star. This made it an ideal candidate for follow-up studies aimed at ultimately exploiting its full asteroseismic potential.

As a pulsator, Feige 48 was identified by Koen et al. (1998) to the then newly-found short-period p -mode oscillators of the EC 14026 type discovered shortly before (Kilkenny et al. 1997;

Koen et al. 1997; Stobie et al. 1997; O’Donoghue et al. 1997). Interestingly, the existence of this class of pulsators had been predicted independently by theory (Charpinet et al. 1996, 1997). These pulsators are now officially known as V361 Hya stars, and informally referred to as sdB_r stars (Kilkenny et al. 2010). There exists another category of pulsating sdB ’s, the long-period g -mode pulsators of the V1093 type (or sdB_s) discovered by Green et al. (2003). Fontaine et al. (2003) showed that the same basic process, a κ -mechanism fed by radiative levitation of iron-peak elements, is responsible for the excitation of pulsation modes in both types of pulsating hot B subdwarfs. Feige 48 finds itself at the common boundary between the hotter, higher gravity sdB_r stars and the cooler, less compact sdB_s pulsators in the g - T_{eff} diagram (see, e.g., Fig. 1 of Charpinet et al. 2013).

These two families of pulsating hot subdwarf stars show strong similarities with the pair β -Cephei / Slowly Pulsating Blue stars on the main sequence. However, sdB ’s are evolved stars that lie well below the main sequence in the Hertzsprung-Russell diagram on the so-called Extreme Horizontal Branch. They are hot ($22,000 \text{ K} \leq T_{\text{eff}} \leq 38,000 \text{ K}$), compact ($5.2 \leq \log g \leq 6.2$) core helium burning objects. The hot B subdwarf stars are also chemically peculiar, showing strong He deficiencies and unusual metal abundance patterns (see, e.g., Geier 2013). Heber (2009) provides a comprehensive review of the properties of these intrinsically interesting, but still often neglected stars.

On the asteroseismological front, follow-up photometric observations gathered by Reed et al. (2004) with small telescopes over a period of five years confirmed the initial detection of five pulsation modes in Feige 48 as reported by Koen et al. (1998). Independent observations gathered with the CFHT/LAPOUNE combination produced a significant improvement of sensitivity leading to the uncovering of nine distinct pulsation modes, including the five previously known (Charpinet et al. 2005a). These modes were found to belong to four multiplet structures (two triplets, one doublet, and one singlet) associated with rotational splitting. For comparison with nonrotating models, only the four central periods of these complexes could be used, however. On this basis, Charpinet et al. (2005a) presented a preliminary seismic model of Feige 48 following the forward method developed by Brassard et al. (2001). By incorporating rotation at the outset in their models, Van Grootel et al. (2008) were able to make

full use of the nine distinct pulsation modes previously detected in the CFHT/LAPOUNE campaign and infer part of the internal rotation profile of Feige 48. This was used to test in a preliminary way spin-orbit synchronism in the close binary system that Feige 48 belongs to. Indeed, using HST/STIS observations and archive FUSE data, O’Toole et al. (2004) had previously found that Feige 48 is a member of such a system, with an orbital period of about 9 h. According to these authors, the unseen companion is likely a white dwarf, although the hypothesis of a cool main sequence star could not be completely ruled out.

Given the intrinsic importance of testing spin-orbit synchronism in close binary systems in general, we decided to exploit further the opportunity offered by the Feige 48 system. To this end, we first invested in a major white light photometric campaign from the ground, with the main objective of detecting many more pulsation modes than the nine uncovered previously. We were able to gather nearly 400 h of very high S/N data using the Mont4K camera attached to the Kuiper Telescope of the Steward Observatory Mount Bigelow Station. This was highly successful as some 46 pulsation modes were detected in Feige 48. Details will be reported elsewhere by Green et al. (in preparation).

As an integral part of these efforts, which will culminate with a new detailed seismic analysis of Feige 48 (Van Grootel et al., in preparation), we have pursued a spectroscopic campaign to obtain accurate radial velocity measurements and high S/N time-averaged spectra. The latter were used to obtain a more accurate determination of the atmospheric parameters of Feige 48, and this is what we report in this paper. As shown specifically in both Charpinet et al. (2005a) and Van Grootel et al. (2008), independent estimates of the atmospheric parameters of the pulsator – as provided by spectroscopy coupled to model atmosphere calculations – have been necessary to lift degeneracies in seismic solutions. This operation was then deemed crucial to our present multipronged efforts to understand better Feige 48 as a pulsator. We briefly review below what has been done in the past in terms of atmospheric analyses of the sdB star Feige 48, and we present the results of our own efforts based on the combination of the NLTE approach with the inclusion of detailed metal line blanketing in the atmosphere models.

4.3 Some Background

Hot subdwarf stars span a wide range of effective temperatures, from around 22,000 K for the coolest sdB's to almost 100,000 K in the hottest sdO's. Depending on the effective temperature, model atmospheres of varying sophistication need to be used in order to determine in a reliable way the atmospheric parameters and chemical composition of a hot subdwarf. For sdO stars, it has been shown that model atmospheres using the local thermodynamic equilibrium (LTE) approximation fail to reproduce observed spectra and lead to incorrect atmospheric parameters when one tries to fit the observed Balmer and helium lines with this type of model. In these stars, the non-LTE (NLTE) effects are undeniably important and must be taken into account when modeling their atmospheric layers. On the other hand, for the coolest sdB stars, the LTE approximation usually gives correct results in terms of atmospheric parameters. The NLTE effects begin to be nonnegligible in the hottest sdB's with effective temperatures around and beyond 30,000 K, which is also the temperature where He II lines become visible in the optical spectra (Napiwotzki 1997). For these hot sdB's (sometimes referred to as sdOB stars), it becomes difficult to reproduce simultaneously both the He I and II lines, as is the case, for example, of the star PG 1219+534 where both LTE and NLTE approaches with metal-free models fail to reproduce helium lines from both ionization stages (Heber et al. 2000 and Charpinet et al. 2005b).

The situation concerning the importance of NLTE effects in sdB stars is, in fact, more complicated than the simple rule of thumb proposed by Napiwotzki (1997), namely, that these effects are negligible below $T_{\text{eff}} \sim 30,000$ K. There is also a dependency on the surface gravity and on the helium content. Figure 4.1 illustrates the results of analyzing a grid of synthetic spectra computed from metal-free NLTE models and treated as “observational” data, with a grid of theoretical spectra based on a similar grid of metal-free models, but computed, this time, in the LTE approximation. The helium abundance in this diagram refers to a value close to that found in Feige 48 (see below). The dots indicate the original values of the parameters of the NLTE models, while the end of each line segment indicates the fake values of these parameters as inferred with the LTE models. As expected, the largest deviations occur for the hotter and less compact atmospheres. And while it is true that the magnitude of the

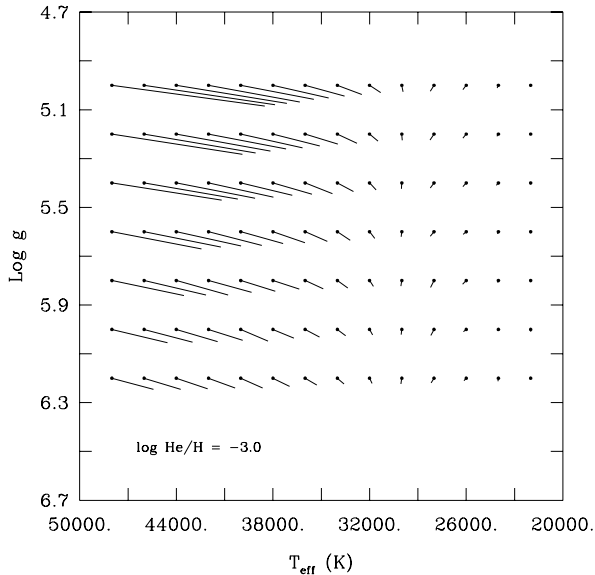


FIGURE 4.1 – NLTE effects in the $\log g$ - T_{eff} plane. The dots give the original values of the atmospheric parameters for NLTE models with $\log N(\text{He})/N(\text{H}) = -3.0$ and no metals. The opposite end of each vector indicates the fictitious values of these parameters when the original spectra (treated as observational data) are analyzed with a grid of LTE models (again with no metals)

NLTE vectors becomes relatively small below $T_{\text{eff}} \sim 30,000$ K, the behavior is complex and not simply monotonic as revealed by the “rotating” vectors.

Another important ingredient in atmosphere modeling are the metallic elements that cause line blanketing and thus change the shape of the spectral energy distribution of the star. Changes in the emergent spectrum are more important in the UV domain and at shorter wavelengths where a large number of absorption lines, mainly from iron-peak elements, block an important fraction of the flux. The flux must nevertheless come out of the star, and it does so at larger wavelengths, increasing the continuum level of these regions. The line blanketing caused by metals also has an effect on the thermodynamical structure of the atmosphere by heating the inner layers and cooling the outer ones. All of this has repercussions in the optical domain where the Balmer and helium lines used to determine the atmospheric parameters of a star are found. If these lines are affected by the presence of metallic elements, so will the atmospheric parameters derived by fitting them.

Adding elements heavier than helium into model atmospheres computed in the LTE approximation is now a common practice and LTE line-blanketed model atmospheres are often used to study sdB stars. As for NLTE models, including metals in them is a much more complicated task than doing it in their LTE counterparts. As a consequence, and to our knowledge, the only extensive and detailed grids of atmosphere models for sdB stars combining the NLTE

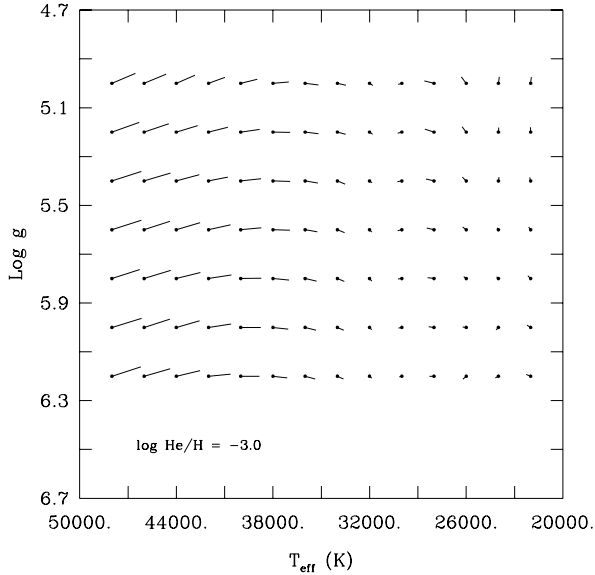


FIGURE 4.2 – Metal blanketing effects in the $\log g$ - T_{eff} plane. The dots give the original values of the atmospheric parameters for NLTE models with $\log N(\text{He})/N(\text{H}) = -3.0$ and a metallicity specified by C(0.1 solar), N(solar), O(0.1 solar), Si (0.1 solar), S(solar), and Fe(solar). The opposite end of each vector indicates the fictitious values of these parameters when the original spectra (treated as observational data) are analyzed with a grid of NLTE models with no metals.

approach with metals have been those of Brassard et al. (2010) and Németh et al. (2012). Figure 4.2 based on some of the models of Brassard et al. (2010) illustrates particularly well the effects of including C, N, O, Si, S, and Fe in NLTE calculations for sdB stars on the derived atmospheric parameters. Those elements are the most abundant metals that have been measured in a sample of five sdB_s stars by Blanchette et al. (2008) on the basis of FUSE data, and their average abundances have been adopted as a representative metallicity in the NLTE calculations of Brassard et al. (2010). Given that previous estimates of the atmospheric parameters of Feige 48 have led to $T_{\text{eff}} \simeq 30,000$ K and $\log g \simeq 5.5$ (see below), one can anticipate from Figure 2 that the effects of metal line blanketing cannot be very large in the atmosphere of that star. Still, given the importance of Feige 48 as a pulsator in a close binary system, we have felt it worthwhile to carry out the present analysis using the state of the art models in the field.

4.4 Spectral Analysis of Feige 48

4.4.1 Previous Studies

The first estimates of the atmospheric parameters of Feige 48 based on a spectroscopic analysis were obtained by Koen et al. (1998) when they found the star to be an EC 14026

pulsator. They used a grid of LTE model atmospheres with pure hydrogen, and this led to an effective temperature of $28,900 \pm 300$ K and a $\log g$ of 5.45 ± 0.05 . Later, Heber et al. (2000) revised these values a bit upward with their detailed analysis of a Keck/HIRES spectrum of Feige 48. They derived atmospheric parameters by fitting the Balmer and He I lines with three kinds of models: LTE with a solar metallicity, metal-poor LTE with $[M/H] = -2.0$, and NLTE without metals (H and He only). Their temperature estimates agreed well with each other, and they were slightly higher than the one found by Koen et al. (1998). Taking the mean value of their three estimates and the one from Koen et al. (1998), they finally adopted $29,500 \pm 350$ K as the effective temperature of Feige 48. Their values of $\log g$ obtained with the three types of models are similar, and using the same approach as they did for the temperature, Heber et al. (2000) got a mean $\log g$ of 5.50 ± 0.05 . Finally, the helium abundance was basically also the same for each type of models, and they got a final value of $\log N(\text{He})/N(\text{H}) = -2.93 \pm 0.05$.

When Feige 48 was studied from an asteroseismological point of view by Charpinet et al. (2005a), these authors also obtained a new, independent derivation of its atmospheric parameters. Charpinet et al. (2005a) combined a high S/N, medium resolution (~ 1 Å) spectrum that they gathered at the MMT with a grid of metal-free H, He NLTE model atmospheres, obtaining $T_{\text{eff}} = 29,580 \pm 370$ K, $\log g = 5.48 \pm 0.05$, and $\log N(\text{He})/N(\text{H}) = -2.95 \pm 0.08$. Their asteroseismic analysis confirmed the spectroscopic value of the gravity with a best match at $\log g = 5.44$. Hence, according to the previous available spectroscopic analyses, the atmospheric parameters of Feige 48 seem to be well constrained and do not show an important dependence on either the type of model atmospheres (LTE or NLTE) or the presence of metallic elements in LTE models.

In the past few years, we developed an efficient way of computing NLTE line-blanketed model atmospheres using parallelized versions of the public codes TLUSTY and SYNSPEC (Lanz & Hubeny 2003, 2007) running on a cluster of dedicated PC's that now include 320 processors (see Latour et al. 2011 for more details on the setup). This made it straightforward for us to use this more sophisticated approach for modeling the atmosphere of Feige 48. This allows for exploiting at their full potential the spectroscopic data that we gathered on Feige

48, and for supporting its forthcoming seismic analysis with the most accurate atmospheric parameters that can be currently obtained.

4.4.2 Observational Material

We have at our disposal four optical spectra of Feige 48, spanning different wavelength ranges and having different resolutions. Our best data set is a combination of medium resolution (1 \AA) spectra acquired between 2002 and 2013 with the blue spectrograph attached to the 6.5 m Multiple Mirror Telescope (MMT). This was part of the ongoing radial velocity program on sdB stars carried out by one of us (E.M.G.). Throughout the observing seasons, the same experimental setup was consistently used. The 832 mm^{-1} grating in second order and $1''$ slit provide a resolution R of ~ 4250 (1.05 \AA) over the wavelength range $4000\text{--}4950 \text{ \AA}$. The slit was always aligned at the parallactic angle during the observations. Exposures of 240 to 475 s, depending on conditions, resulted in signal-to-noise ratios (S/N) of about 80 to 150 for individual spectra, which is sufficient to achieve velocity errors of 1 to 2 km s^{-1} for sdB stars. One to four spectra per night were obtained. The spectrum used for the present spectroscopic analysis is the combination of 17 mean nightly spectra gathered during different runs, median-filtered and shifted to the same velocity prior to combining. Thus the resulting spectrum has a remarkably high formal S/N of ~ 460 . This spectrum will be referred to as MMT. We point out that an earlier, reduced sensitivity version of this spectrum was used by Charpinet et al. (2005a) in their seismic analysis.

Our second spectrum is also a medium-resolution one obtained from the combination of several individual spectra gathered over the last several years within the context of the radial velocity program of E.M.G. carried out on sdB stars. These data were obtained with the Boller & Chivens (B&C) Cassegrain spectrograph at Steward Observatory's 2.3 m Bok Telescope on Kitt Peak. The 832 mm^{-1} grating in second order with a $1.5''$ slit were used to achieve 1.9 \AA resolution over a wavelength range of $3675\text{--}4520 \text{ \AA}$. The slit was aligned with the parallactic angle at the midpoint of each exposure, and comparison HeAr spectra were taken before and after each stellar spectrum. Exposure times between 500 and 875 s for the individual spectra led to S/N of about 50 to 80. The final spectrum is the combination of 50 exposures and

has a resulting S/N of ~ 375 . This spectrum will be referred to as BG2 (as in “Betsy Green’s $\sim 2 \text{ \AA}$ spectrum”).

Another spectrum of Feige 48 was kindly gathered for us by Pierre Bergeron using again the B&C spectrograph on the 2.3 m Bok telescope. This was part of a request to observe for us several pulsating sdB stars during two of his white dwarf observing runs going back to 2006. In that case, the 4.5” slit together with the 600 mm^{-1} grating blazed at 3568 \AA in first order provided a spectral coverage from about 3030 to 5250 \AA at a resolution of $\sim 6.0 \text{ \AA}$. The S/N of this single spectrum is ~ 80 . Even though this spectrum is of lower quality than the previous ones in terms of sensitivity and resolution, we felt that it would be worthwhile to analyze all spectral data available to us on our target star. This third spectrum is referred to as PB6 in what follows.

Finally, we have at our disposal an older (2004) high-sensitivity, low-resolution spectrum of Feige 48 gathered again with the B&C spectrograph on the 2.3 m Bok telescope. It is the combination of 5 exposures using the 400 mm^{-1} grating in first order in conjunction with a 2.5” slit to obtain a typical resolution of 8.7 \AA over the wavelength interval 3620–6900 \AA , thus including $\text{H}\alpha$. The instrument rotator was set prior to each exposure, to align the slit within $\sim 2^\circ$ of the parallactic angle at the midpoint of the exposure. HeAr comparison spectra were obtained immediately following each stellar exposure. The blue part of the combined spectrum reaches $\text{S/N} \simeq 248$. This spectrum is to be referred to as BG9. It was used previously by Charpinet et al. (2005a) in their analysis of Feige 48.

Inspection of our optical data revealed no sign of He II lines in the spectra. There is also no hint for the presence of He II $\lambda 4686$ or other weaker features associated with that ionization stage in the high-resolution HIRES spectrum of Feige 48 obtained by Heber et al. (2000). However, since Feige 48 has been observed with the STIS spectrograph and these data are available in the Mikulski Archive for Space Telescopes (MAST)¹, we checked the UV spectrum in order to verify if the strongest expected He II feature in that wavelength range, the $\lambda 1640$ line, could be detected (see O’Toole & Heber 2006 for more details on the data). Indeed, the line is present, although somewhat weak and noisy, but it is still sufficiently useful as the sole

¹<http://archive.stsci.edu/>

indicator of that ionization stage of helium to provide us below with a nice test of the validity of our derived atmospheric parameters based on the optical data.

4.4.3 Model Atmospheres

4.4.3.1 The Metallicity of Feige 48

In order to fix a suitable chemical composition for the grid of models, we searched the literature for abundance studies done on Feige 48. Because of its status of pulsating star and its brightness, Feige 48 has been thoroughly studied and its atmospheric chemical composition has been analyzed in at least four different studies that we know of. First, after their determination of the atmospheric parameters of the star on the basis of a HIRES spectrum, Heber et al. (2000) carried out an abundance analysis of visible metals and found the star to have subsolar abundances for all of the eight elements they studied, except for iron which was found to be solar. For their part, Chayer et al. (2004) made a comparison of the chemical composition of Feige 48 and Feige 87 (a non-variable sdB with atmospheric parameters very similar to those of Feige 48) using UV metallic lines present in the star's FUSE spectrum. O'Toole & Heber (2006) also undertook an abundance analysis of a sample of pulsating and constant sdB stars (among them Feige 48) in order to test the hypothesis that pulsating sdB's might show a different abundance pattern than the nonpulsating ones. This was not the case, but they nevertheless got a rather good picture of the abundance patterns in the five stars they studied. Finally, in an attempt to go further into deriving general trends for the metallic abundances in sdB stars, Geier (2013) analyzed a much larger sample of sdB's (among them Feige 48) using high-resolution optical spectra. Among other results, he obtained a fourth set of metal abundances for the star of interest.

Table 4.1 reports our compilation of the abundances obtained in the four previously mentioned studies. A weighted mean abundance was computed for each element, and since the uncertainty is used as weight, we attributed a value of ± 0.5 dex whenever there was no uncertainty quoted in the reference paper. We included in our model grid the eight metals that are indicated in bold in the table. We limited ourselves to the inclusion of ten atomic species (including H and He) in our models, for stability and convergence reasons. Therefore, we chose

TABLE 4.1 – Abundances of Metals Detected in the Atmosphere of Feige 48 : $\log N(Z)/N(H)$

Element Z	Heber et al. (2000) Keck/HIRES	Chayer et al. (2004) <i>FUSE</i>	O’Toole & Heber (2006) <i>HST/STIS</i>	Geier (2013) Keck/HIRES	Mean	Solar ^a
C	-4.64±0.03	-5.2±0.5	-4.79±0.10	-4.65±0.35	-4.65±0.03	-3.57
N	-4.29±0.10	-4.6±0.5	-4.38±0.38	-4.72±0.12	-4.47±0.07	-4.17
O	-4.21±0.12	< -4.2	...	-4.35±0.20	-4.25±0.10	-3.31
Ne	-4.90±0.31	< -4.06	-4.90±0.31	-4.07
Mg	-5.09±0.50	-5.2±0.50	-5.15±0.35	-4.40
Al	-5.50±0.18	< -5.8	-6.49±0.10	-6.4±0.5	-6.49±0.09	-5.55
Si	-5.67±0.27	-5.7±0.5	-5.73±0.19	-5.45±0.06	-5.49±0.06	-4.49
P	...	-7.1±0.5	-7.59±0.50	< -7.02	-7.35±0.35	-6.59
S	-5.85±0.50	-5.7±0.5	...	-6.05±0.07	-6.04±0.07	-4.88
Cl	...	< -8.5	< -8.5	-6.50
Ar	...	< -6.8	< -5.0	< -5.18	< -6.8	-5.60
K	< -6.07	< -6.07	-6.97
Ca	-4.69±0.50	...	-4.69±0.50	-5.66
Sc	< -9.0	...	< -9.0	-8.85
Ti	...	< -7.6	-6.81±0.13	< -6.26	-6.81±0.13	-7.05
V	...	< -8.3	...	< -5.03	< -8.3	-8.07
Cr	...	-7.0±0.5	-5.95±0.15	...	-6.04±0.14	-6.36
Mn	...	-7.0±0.5	-6.38±0.21	...	-6.47±0.19	-6.57
Fe	-4.45±0.19	-4.8±0.5	-4.30±0.14	-4.54±0.21	-4.41±0.10	-4.50
Co	...	-7.6±0.5	-6.11±0.18	...	-6.28±0.17	-7.01
Ni	...	< -5.7	-5.31±0.15	...	-5.31±0.15	-5.78
Cu	-6.75±0.40	...	-6.75±0.40	-7.81
Zn	-6.70±0.22	...	-6.70±0.22	-7.44
Ga	-7.30±0.50	...	-7.30±0.50	-8.96
Ge	-7.98±0.08	...	-7.98±0.08	-8.35
Sn	-9.06±0.50	...	-9.06±0.50	-9.96
Pb	-8.20±0.50	...	-8.20±0.50	-10.25

^a Asplund et al. (2009)

to include the eight most abundant metallic species, except for calcium which we left aside because its abundance is based on a single optical line.

It is worth mentioning that Heber et al. (2000), O’Toole & Heber (2006), and Geier (2013) used the following parameters for their abundance analyses: $T_{\text{eff}} = 29,500$ K, $\log g = 5.54$, and $\log N(\text{He})/N(\text{H}) = -2.9$. The remaining study of Chayer et al. (2004) used parameters quite similar. O’Toole & Heber (2006) used line-blanketed LTE model atmospheres with solar metallicity. Otherwise, the three other studies also used LTE models (although it is not clearly mentioned in Heber et al. 2000) with a certain amount of metallic elements that was not explicitly mentioned.

4.4.3.2 Model Grids

Having determined the metallicity to be included in our models, we first built a small grid of 150 NLTE line-blanketed model atmospheres especially suited for Feige 48. The grid includes 5 values of T_{eff} between 26,000 K and 34,000 K in steps of 2000 K, 6 values of $\log g$

between 5.0 and 6.0 in steps of 0.2 dex, and 5 helium abundances between $\log N(\text{He})/N(\text{H}) = -4.0$ and -2.0 in steps of 0.5 dex. Our models contains the following ions : H I, He I to III, C II to C V, N II to N VI, O II to O VI, Ne I to Ne V, Mg I to Mg III, Si II to Si V, Fe II to Fe VI, and finally Ni III to Ni VI. Note that the highest ionization stage of each element is taken as a one-level atom. Each model includes overall almost 1000 explicit energy levels and more than 18,000 atomic transitions. Before performing the fitting procedure on the spectra of Feige 48, we examined a few properties of our models.

We first looked at the differences produced on the temperature structure by the metallic elements included in the atmosphere as compared to the metal-free case. Figure 4.3 shows the temperature structures for four model atmospheres having the same parameters ($T_{\text{eff}} = 30,000$ K, $\log g = 5.4$, and $\log N(\text{He})/N(\text{H}) = -3.0$), except for their metallicity. The black curve is from a model including only hydrogen and helium, showing the typical NLTE temperature inversion in the upper layers of a metal-free atmosphere. The red curve illustrates the case where only our six “lighter” metals were included in the calculations. Their main effect is to cool down the upper layers. The most noteworthy effect of adding iron (green curve) is the concomitant back-warming of the deeper layers, which results in a higher temperature at a given depth. We also included the temperature profile (blue curve) of a fully line-blanketed model which includes all of the eight metallic elements. The only difference between the blue and the green curves is the addition of nickel and it can be seen that, at least for a model representing Feige 48, the influence of this element on the thermodynamical structure of the model remains rather small. Overall, the line-blanketing effects are qualitatively the same as what is seen in model atmospheres at higher temperature (for sdO stars), but to a lesser extent. The drop in the surface temperature is around 7,000 K for our Feige 48 models, while it can be around 40,000 K in 80,000 K sdO models (see, e.g., Fig. 1 of Latour et al. 2013). In the deeper layers ($\log m \gtrsim -3.0$), the rise of the temperature due to the metals is around four percent. Also featured in Figure 4.3 is the optical depth $\tau_\nu = 2/3$ as a function of the column density (m), allowing one to infer where, in the atmosphere, the Balmer and metallic lines as well as the continuum are formed.

We also wanted to verify how these changes in the structure of our models might affect

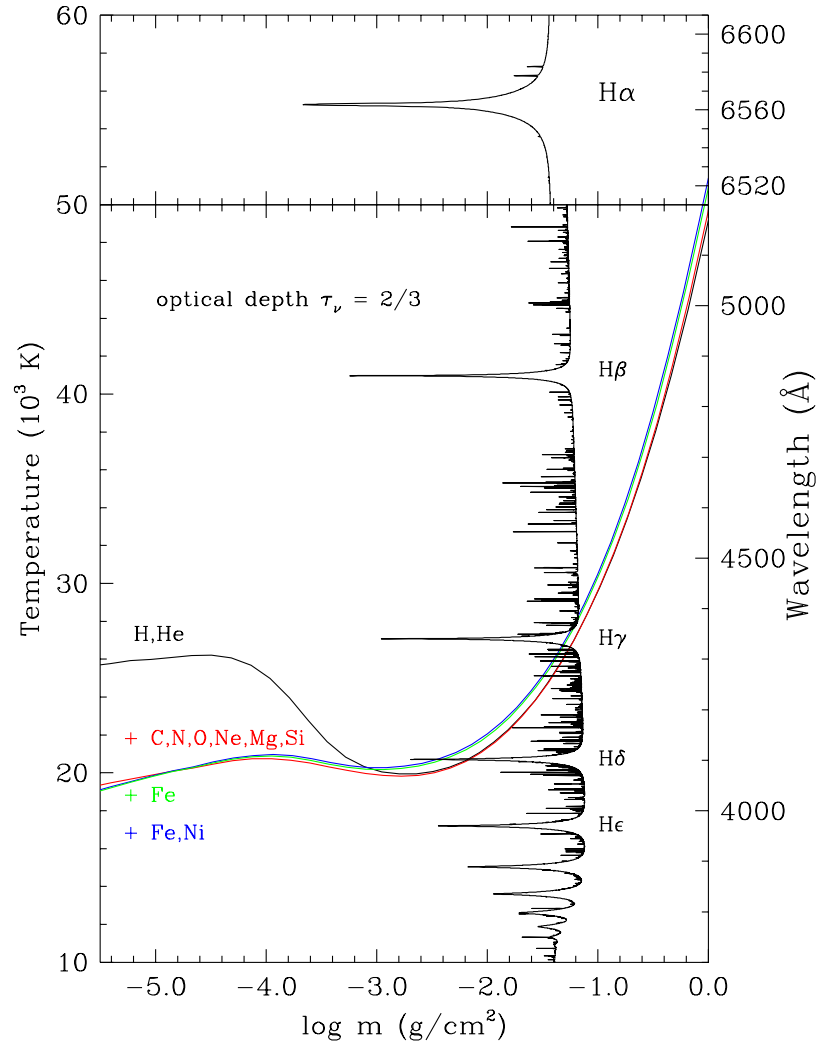


FIGURE 4.3 – Temperature stratification and monochromatic optical depth $\tau_\nu = 2/3$ as functions of depth, where m is the column density, for NLTE models defined by $T_{\text{eff}} = 30,000$ K, $\log g = 5.4$, and $\log N(\text{He})/N(\text{H}) = -3.0$. The temperature structure is shown for four model atmospheres having different compositions : with H and He only (black), with C, N, O, Ne, Mg, Si in addition (red), with Fe added to the previously mentioned elements (green), and finally with Ni on top of that (blue). The $\tau_\nu = 2/3$ curve is from the latter model and shows wavelength intervals corresponding to the Balmer line series.

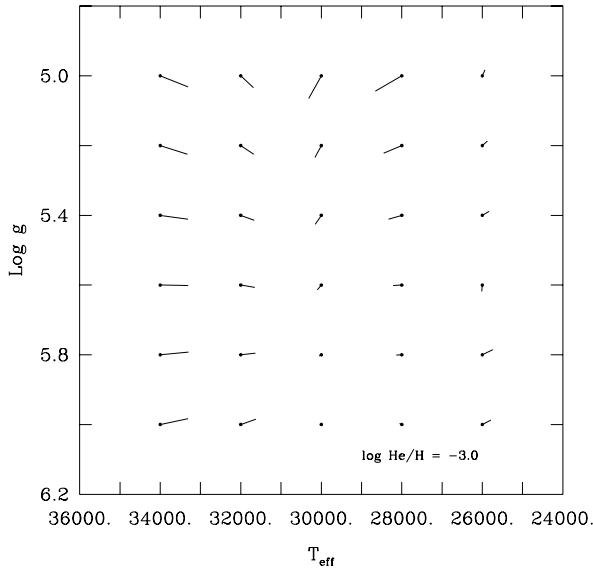


FIGURE 4.4 – Map illustrating the effects of metal line blanketing on the inferred atmospheric parameters. T_{eff} and $\log g$ are obtained for some models of our NLTE line-blanketed grid fitted with a grid of NLTE H, He models. The atmospheric parameters of the models are indicated by dots while the end of line segments correspond to the parameters obtained by the fitting procedure. The helium abundance is kept fixed at the model value of $\log N(\text{He})/N(\text{H}) = -3.0$.

the computed optical spectrum and, by extension, any derived atmospheric parameters. To illustrate this, we created the map featured in Figure 4.4. This is similar to our Figure 4.2 above, but specialized to the specific metallicity used to model Feige 48. To construct this map, spectra from one grid of models are considered as “observed” spectra and are fitted with a different grid of synthetic spectra. We performed our fitting procedure in the 4020–4910 Å interval, which includes three Balmer lines and four He I lines, with models convolved at 1 Å resolution in order to mimic the MMT spectrum. Because we wanted to check the effects of line blanketing, spectra from our fully-blanketed grid were taken as the observed ones and we fitted them with a grid of theoretical spectra obtained with model atmospheres including only hydrogen and helium. Our χ^2 fits were done in order to derive an optimal solution in terms of effective temperature and surface gravity, while the helium abundance was kept fixed at its real value. Figure 4.4 shows our results for a helium abundance similar to the one found in Feige 48 ($\log N(\text{He})/N(\text{H}) = -3.0$). We can see, once again and in complement to Figure 4.2, that the effects of metals on the derived atmospheric parameters remain small throughout the domain investigated. Somewhat accidentally in the specific case of Feige 48 with $T_{\text{eff}} \simeq 30,000$ K and $\log g \simeq 5.5$, the effects are particularly small.

4.4.4 Derived Atmospheric Parameters

We analyzed the four spectra with both our fully-blanketed model grid and a more classic metal-free NLTE, H,He grid that was also computed as indicated just above. We used a χ^2 minimization procedure similar to that of Saffer et al. (1994). A simultaneous fit of the Balmer and helium lines available in our spectra was carried out in order to find the optimal solution in the three-dimensional space defined by the parameters T_{eff} , $\log g$, and $\log N(\text{He})/N(\text{H})$. Prior to that exercise, all the synthetic spectra (defined by 32001 wavelength points in the range 3500–6700 Å) were degraded by convolution to the experimental resolution of each of the available spectrum of Feige 48. The four panels of Figure 4.5 show our resulting fits when using the fully-blanketed grid described in the previous subsection. Panel a) shows the results achieved for the MMT spectrum, Panel b) for the BG2 spectrum, Panel c) for the PB6 spectrum, and Panel d) for the BG9 spectrum. The results of these fits, as well as the ones obtained with the H,He grid, are also reported in Table 4.2. Note that the quoted uncertainties only reflect the quality of the fits; they are formal fitting errors.

When examining the resulting T_{eff} and $\log g$ entries for both grids in Table 4.2, one can notice a small systematic trend in the determined values: from top (MMT) to bottom (BG9), with decreasing resolution, both the derived effective temperature and the surface gravity increase slightly. The differences are not large (at most 600 K and ~ 0.09 dex), but the trend is nevertheless noticeable. However, the resolution is not the only difference between the four spectra; the spectral range also varies and, thus, the lines featured and fitted in each spectrum are not the same. Hence, the differences in the fitted spectral range could very well affect the resulting parameters in a systematic way. In order to check the effects of varying the spectral range, we carried out some additional fits with the two lowest resolution spectra. We thus fitted the BG9 spectrum over the reduced spectral ranges of the MMT, BG2, and PB6 spectra, and the PB6 spectrum over the MMT and BG2 ranges. The results are shown in Table 4.2 below the weighted mean values of the four “conventional” fits for the two different grids. It should be mentioned here that our fits usually start at 3740 Å (just to the red of the H12 line), except for the MMT spectrum whose blue limit is at 4000 Å.

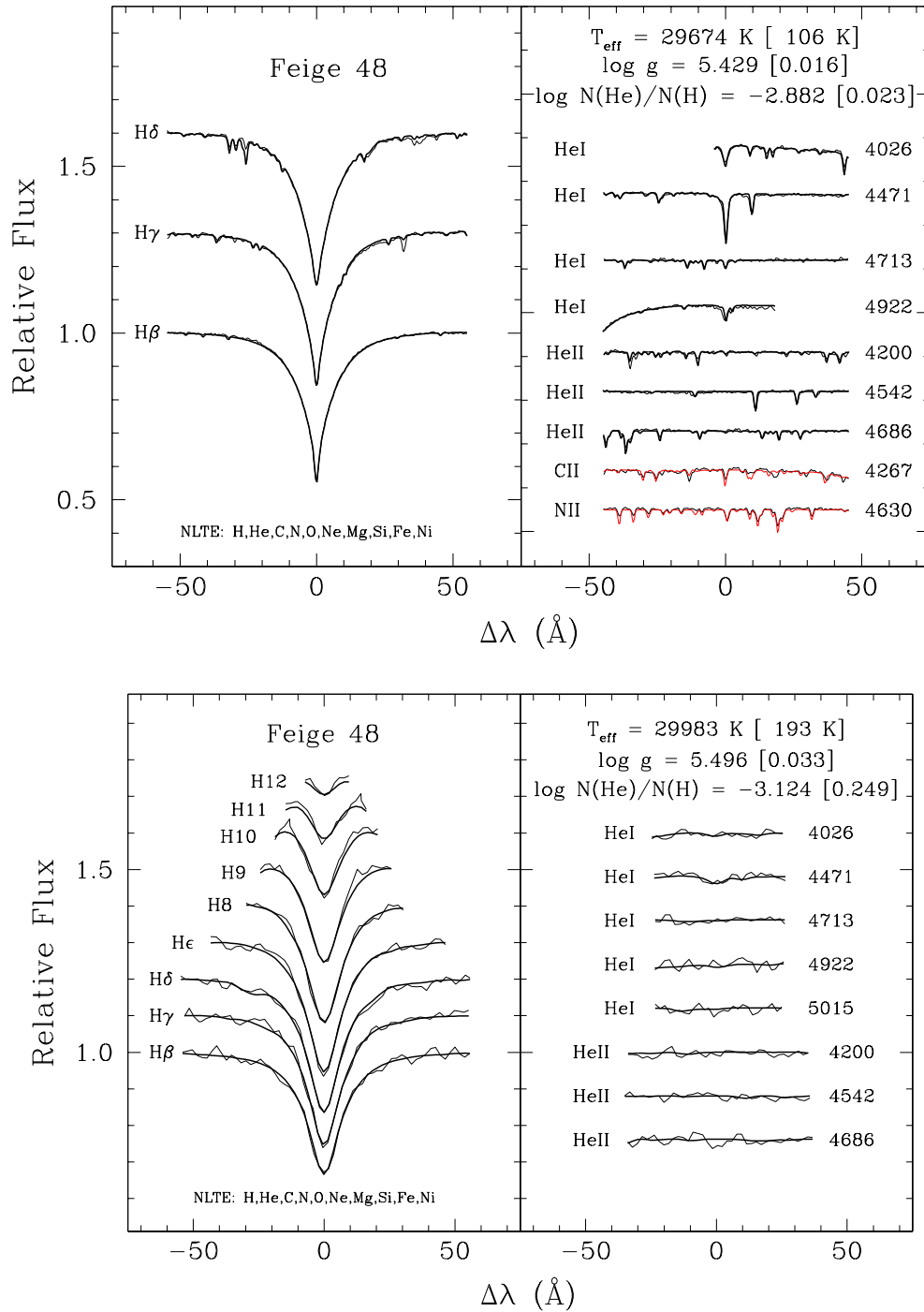


FIGURE 4.5 – Top - a) Best fit obtained with the 1 Å resolution MMT spectrum of Feige 48 using our grid of NLTE line-blanketed model atmospheres described in the last section. The Balmer and He I lines are all very well reproduced by the optimal model. Bottom - b) Best fit obtained with the bluer 1.9 Å resolution spectrum (BG2)

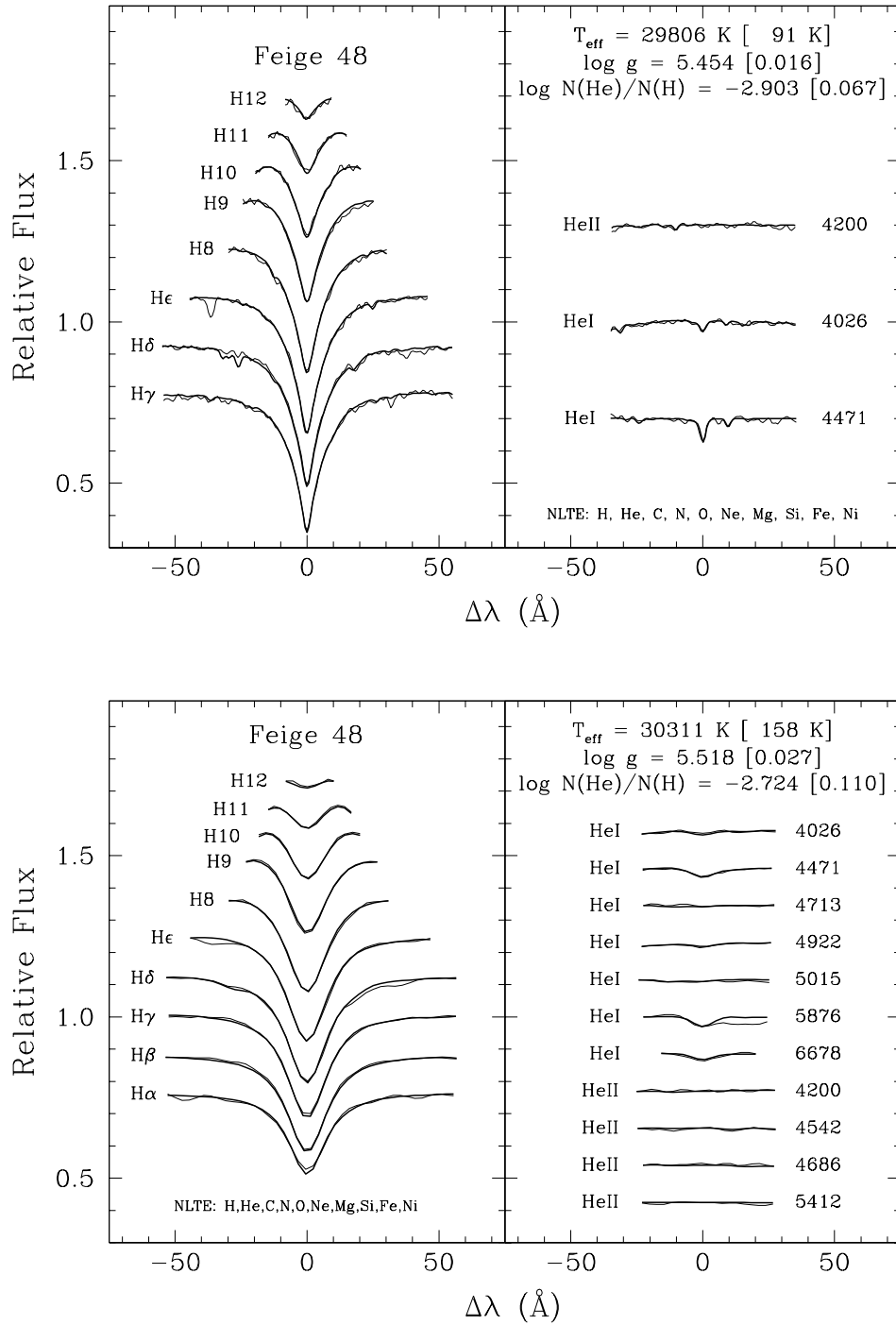


FIGURE 4.5 – Continued. Top - c) Best fit with the 6 Å resolution spectrum (PB6). Note that a sole line of He I at 4471 Å is discernible in this spectrum, which explains the lower helium abundance found ($\log N(\text{He})/N(\text{H}) = -3.124$) and the larger error associated with this value. Bottom - d) Best fit with the lowest resolution spectrum (8.7 Å) BG9. In spite of its low resolution, the high S/N allows to distinguish three He I lines and guess the 4026 Å one.

TABLE 4.2 – Results of our fitting procedure for Feige 48

Spectrum	T_{eff} (K)	$\log g$ (dex)	$\log N(\text{He})/N(\text{H})$ (dex)	Note
With our NLTE fully line-blanketed model grid				
MMT	$29,674 \pm 106$	5.429 ± 0.016	-2.882 ± 0.023	
BG2	$29,806 \pm 91$	5.454 ± 0.016	-2.903 ± 0.067	
PB6	$29,983 \pm 193$	5.496 ± 0.033	-3.124 ± 0.249	
BG9	$30,311 \pm 158$	5.518 ± 0.027	-2.724 ± 0.110	
Mean	$29,854 \pm 60$	5.459 ± 0.013	-2.880 ± 0.021	
PB6	$30,010 \pm 169$	5.487 ± 0.035	-3.094 ± 0.256	with BG2
PB6	$29,765 \pm 639$	5.488 ± 0.093	-3.247 ± 0.290	with MMT
BG9	$30,264 \pm 113$	5.517 ± 0.020	-2.803 ± 0.101	with PB6
BG9	$30,220 \pm 130$	5.543 ± 0.024	-2.836 ± 0.128	with BG2
BG9	$30,483 \pm 384$	5.521 ± 0.057	-2.779 ± 0.099	with MMT
With our NLTE H,He model grid				
MMT	$29,840 \pm 141$	5.441 ± 0.024	-2.898 ± 0.032	
BG2	$30,013 \pm 83$	5.466 ± 0.016	-2.897 ± 0.068	
PB6	$30,161 \pm 167$	5.502 ± 0.033	-3.135 ± 0.259	
BG9	$30,520 \pm 130$	5.522 ± 0.027	-2.736 ± 0.107	
Mean	$30,105 \pm 59$	5.474 ± 0.011	-2.889 ± 0.028	
PB6	$30,182 \pm 173$	5.502 ± 0.035	-3.078 ± 0.258	with BG2
PB6	$29,879 \pm 561$	5.478 ± 0.094	-3.265 ± 0.321	with MMT
BG9	$30,493 \pm 101$	5.521 ± 0.021	-2.805 ± 0.105	with PB6
BG9	$30,455 \pm 112$	5.549 ± 0.025	-2.847 ± 0.131	with BG2
BG9	$30,694 \pm 340$	5.537 ± 0.063	-2.779 ± 0.111	with MMT

From Table 4.2, one can realize that the inferred parameters (effective temperature, surface gravity, helium abundance) are essentially the same for the four different spectral ranges considered when using the BG9 spectrum. And indeed, the derived values are the same within the formal fitting errors, and this is the case for both types of model grids as well. This is true also for the three different spectral ranges used in conjunction with the PB6 spectrum. We thus conclude that, at low enough resolution, no significant systematic trend is associated with the choice of the spectral range. On the other hand, resolution does matter here as can be seen by comparing the derived parameters obtained with the MMT spectrum, the PB6 spectrum fitted over the MMT range only, and the BG9 spectrum again fitted over the MMT range only. Although the formal uncertainties overlap between the MMT and PB6+MMT cases, there is indeed a small but significant trend such that the effective temperature and the surface gravity increase slightly with decreasing resolution as can be inferred by comparing

the MMT and BG9+MMT cases. For its part, the helium abundance is essentially unchanged as a function of resolution taking into account the formal errors of the fits. A final look at the effects of changing the resolution is provided by an experiment in which we degraded the resolution of the original MMT spectrum through convolution with a Gaussian with a FWHM of 8.7 \AA . The new inferred parameters using this degraded spectrum are $T_{\text{eff}} = 29,922 \pm 100 \text{ K}$, $\log g = 5.477 \pm 0.015$, and $\log N(\text{He})/N(\text{H}) = -2.805 \pm 0.025$, to be compared with the first line in Table 2 giving $T_{\text{eff}} = 29,674 \pm 106 \text{ K}$, $\log g = 5.429 \pm 0.016$, and $\log N(\text{He})/N(\text{H}) = -2.882 \pm 0.023$.

Finally, comparing the atmospheric parameters obtained with the line-blanketed grid versus the H,He one, we note that adding metals to NLTE models leads to only slightly lower effective temperatures and surface gravities. This is exactly what Figure 4.4 above shows for the parameters appropriate for Feige 48. As for the effects on the helium abundance, they are completely negligible. Having done all those fits, we at last end up with the following atmospheric parameters for Feige 48: $T_{\text{eff}} = 29,854 \pm 60 \text{ K}$, $\log g = 5.459 \pm 0.013$, and $\log N(\text{He})/N(\text{H}) = -2.880 \pm 0.021$. These are our best estimates, based on the weighted averages of the values obtained when fitting the four available spectra with the fully-blanketed grid of model atmospheres (the first four lines in Table 4.2). Of course, the quoted uncertainties only reflect the quality of the fits.

A potentially interesting test of our derived atmospheric parameters for Feige 48 is to attempt fitting the He II $\lambda 1640$ line detected in the UV and available in the MAST archives (see Section 4.4.2). This spectral feature is the only one corresponding to the He II ionization stage that is available for that star. Otherwise, there are no He II lines visible in the optical spectrum of Feige 48 because of its relatively low effective temperature and its low helium abundance as determined just above. Our first attempt to fit the He II $\lambda 1640$ line in our standard three-dimensional search domain (T_{eff} , $\log g$ and $\log N(\text{He})/N(\text{H})$) would not converge to a unique solution, most likely because of the numerous metallic lines in the vicinity of the helium line. So we redid the exercise, this time keeping the helium abundance fixed to the value found previously (-2.88), and leaving the fitting procedure find the best match in terms of effective temperature and gravity only. The program did converge this time to a solution giving $T_{\text{eff}} =$

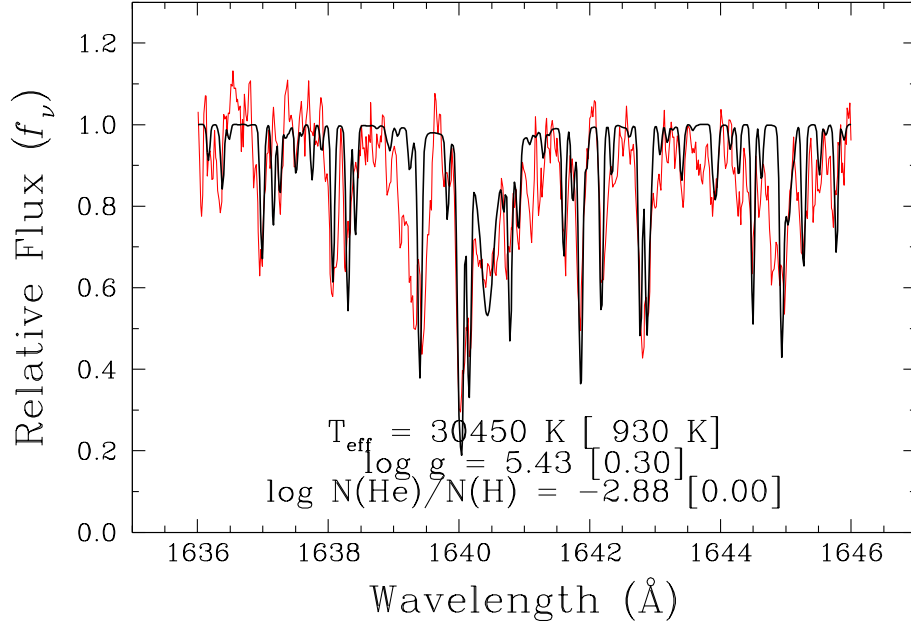


FIGURE 4.6 – Our best fit of the He II $\lambda 1640$ line in the STIS spectrum of Feige 48 in terms of effective temperature and surface gravity.

$30,450 \pm 930$ K and $\log g = 5.43 \pm 0.30$, which is perfectly consistent with our previous results. Even though the fitting errors for the sole He II $\lambda 1640$ line are larger than what was obtained with the whole visible spectra, we take this as a nice consistency check for the validity of our derived atmospheric parameters. The resulting fit is presented in Figure 4.6, where it is possible to see the He II line blended with Fe IV and Ni III lines around 1640 \AA and other Fe IV lines in its red wing.

4.4.5 Fine Tuning of the Metal Abundances

Our MMT spectrum, because of its good resolution and excellent signal-to-noise ratio, features a lot of discernible metallic lines. When looking closely at our best-fit model shown in Figure 4.5a, it can be noticed that the lines of some elements are systematically stronger or fainter than the observed ones, thus calling for a bit of fine tuning in order to obtain a better match with the observations. So we fitted the elements whose lines are visible in the wavelength

range of the MMT spectrum (4020–4950 Å), namely C, N, O, Mg, Si, S and Fe. These fits were done by using a model atmosphere having the atmospheric parameters determined by our fit of the MMT spectrum (first line in Table 4.2) and the chemical composition mentioned in Section 4.4.3.1 (with the exception of iron which was not included in the model atmosphere; see discussion below). Using this model, we computed several families of synthetic spectra with six or seven different abundances for each element analyzed. The abundance of the element was changed only in the computations of the emergent spectrum by SYNSPEC (see the SYNSPEC user’s guide for more details²).

The detailed comparison of the observed MMT spectrum with our final best synthetic one (having adjusted metal abundances) is shown in Figure 4.7. With respect to our best fit featured in the previous subsection, there is a clear improvement in the way the various metallic lines are reproduced. Specifically, we decreased by a few tenths of a dex the abundances of carbon, nitrogen and oxygen. Using logarithmic abundances of -4.94 , -4.61 and -4.47 dex for C, N, O respectively resulted in a better agreement between the observed and synthetic spectrum for most of the lines originating from O II, N II, and the C II doublet at 4267 Å. The only noteworthy remaining discrepancies (after our adjustments) for these elements are the O II lines at 4075.8 Å that are still too strong. Magnesium and silicon kept roughly the same abundances we considered initially; in those cases, their lines were already well reproduced with our best-fit model shown in Figure 4.5a. Their adjusted abundances are $\log N(\text{Mg})/N(\text{H}) = -5.18$ and $\log N(\text{Si})/N(\text{H}) = -5.38$. Sulfur was not included in the model atmospheres at the outset, but when added into the synthetic spectrum, its lines, including one blended with an O II line at our resolution, were better reproduced (see Figure 4.7b) with an abundance of -5.71 dex, which is a bit higher than the mean one indicated in Table 4.1.

Finally, iron was a particular case. We noticed that most of the iron lines were too shallow in our optimal synthetic spectrum, and we were unable to obtain a good match when changing the abundance in the synthetic spectra or in the model atmosphere directly. After a thorough inspection of the synthetic spectra, it appears that some emission was occurring in a few iron lines, an unexpected and certainly unrealistic result. The two most problematic sets of

²<http://nova.astro.umd.edu/Tlusty2002/tlusty-frames-guides.html>

lines (the complex around 4372 Å and Fe III λ 4310.355) originate from within two specific superlevels, and we suspect that there might be a problem with the populations of the different components of the superlevels. These components (within a given superlevel) are assumed to be in Boltzmann equilibrium with respect to each other. The solution we found to avoid this problem was to add iron in a synthetic spectrum computed from a model atmosphere that does not include iron. In this way, SYNSPEC computes the iron population in LTE and no strange emission occurs. When using these kind of spectra, we found a good match to the observed lines corresponding to an optimal iron abundance of $\log N(\text{Fe})/N(\text{H}) = -4.48$, which is very near the mean value obtained in Table 4.1.

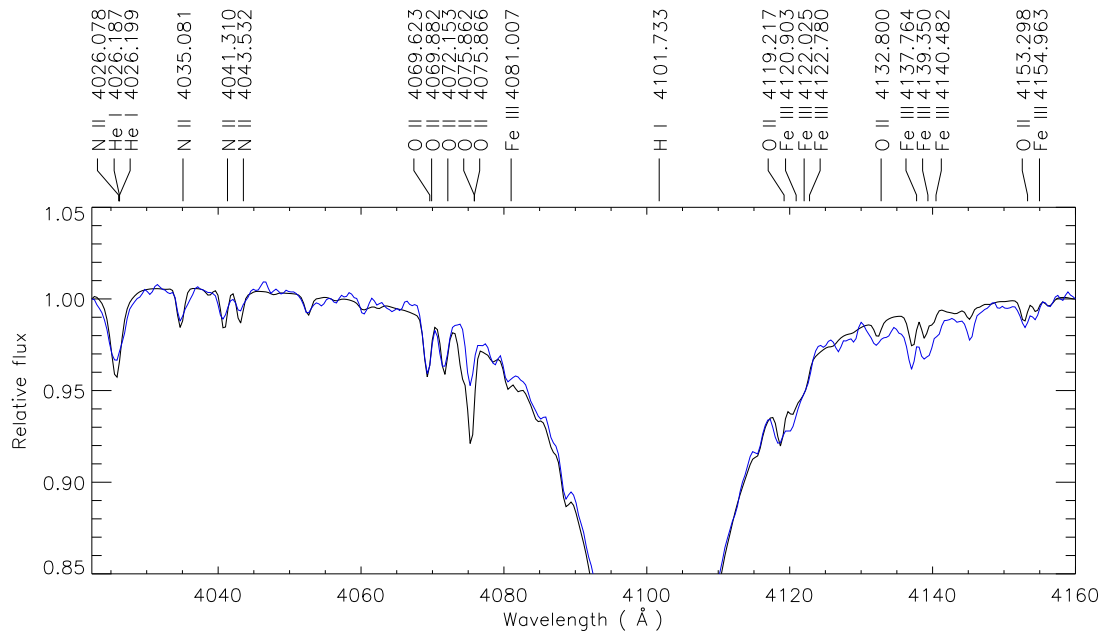


FIGURE 4.7 – a - Detailed comparison of the observed MMT spectrum (blue line) with a synthetic spectrum (black line) having the abundances fine tuned in order to obtain a better match. The model atmosphere used for generating the synthetic spectrum has the parameters found by the fitting procedure of the MMT spectrum : $T_{\text{eff}} = 29,674$ K, $\log g = 5.43$ and $\log N(\text{He})/N(\text{H}) = -2.88$. The main absorption features are indicated with the name of the ion and the wavelength of the transition.

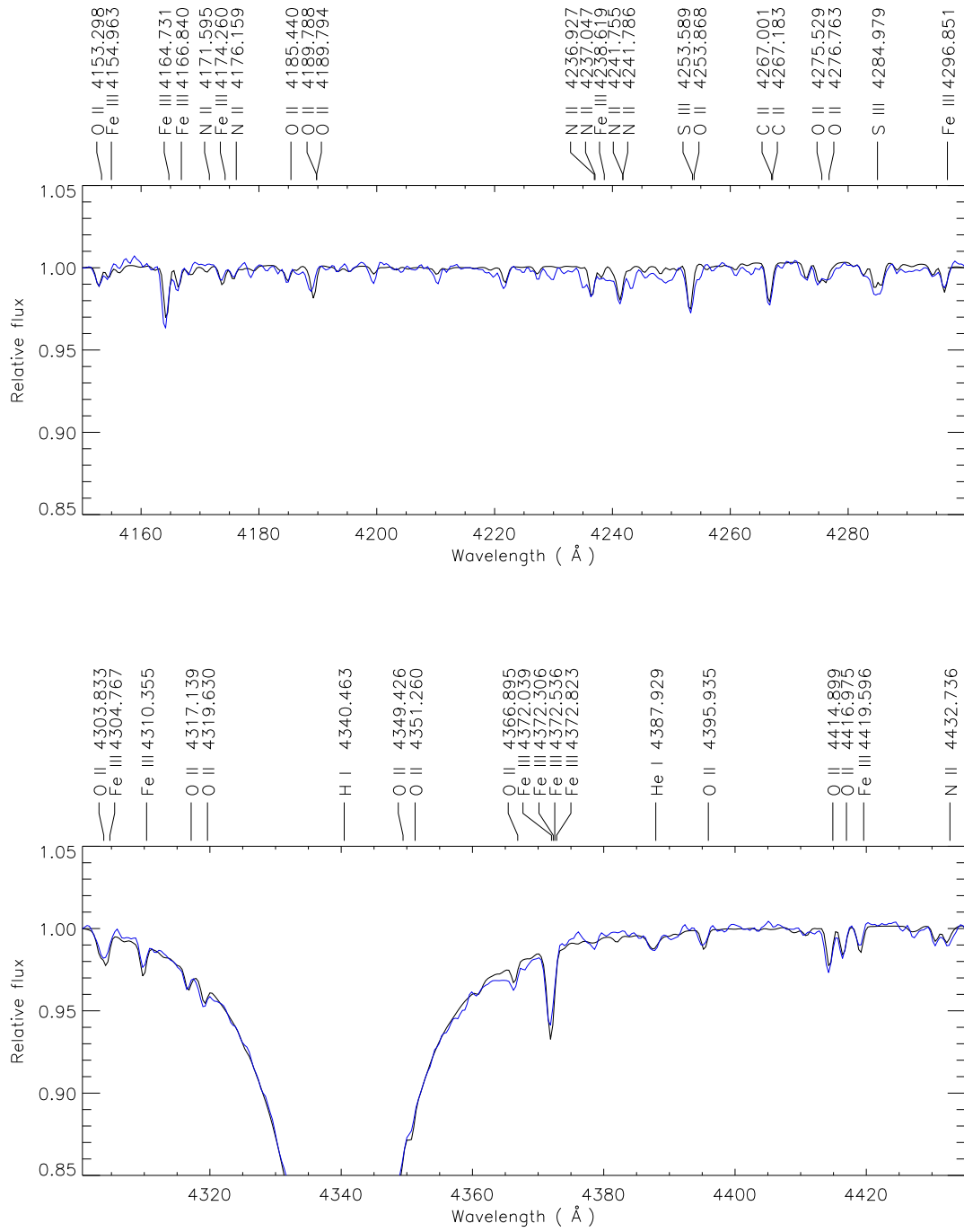


FIGURE 4.7 – Continued. Top b). Bottom c).

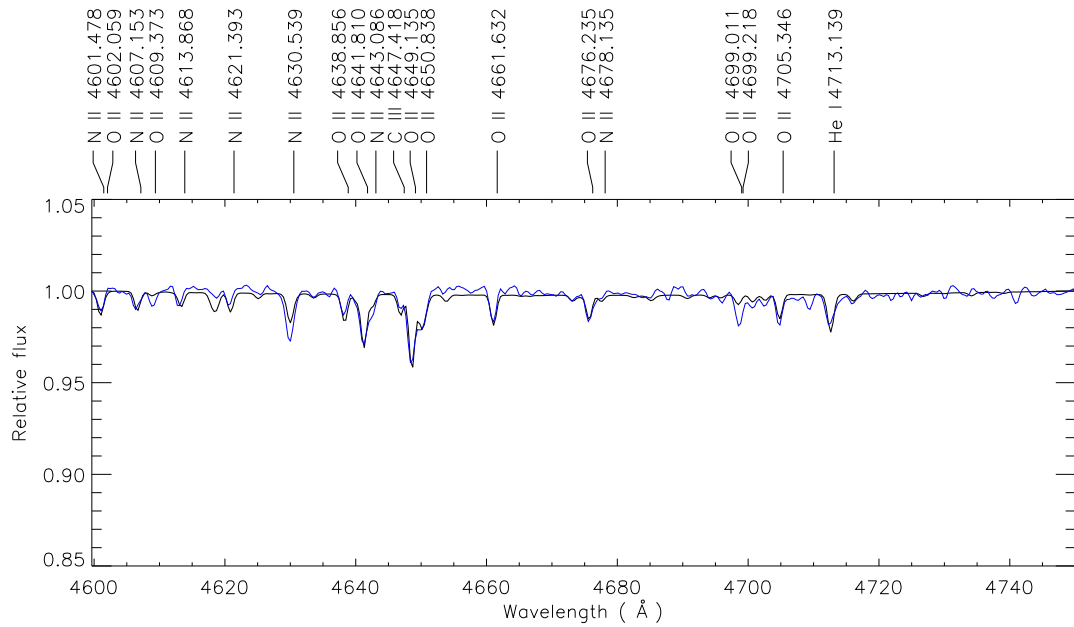
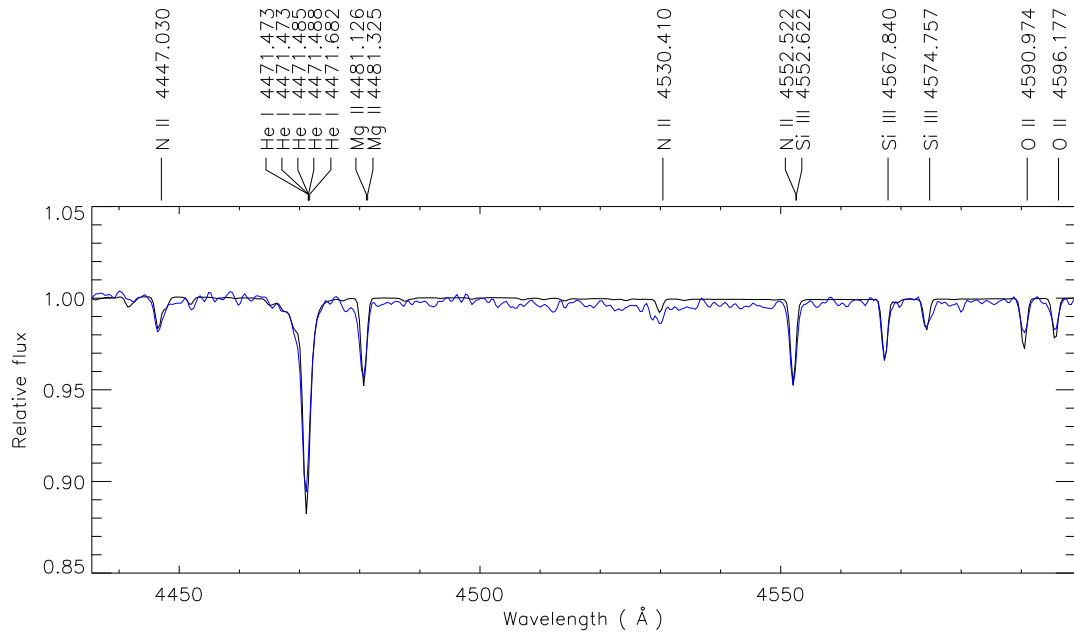


FIGURE 4.7 – Continued. Top d). Bottom e).

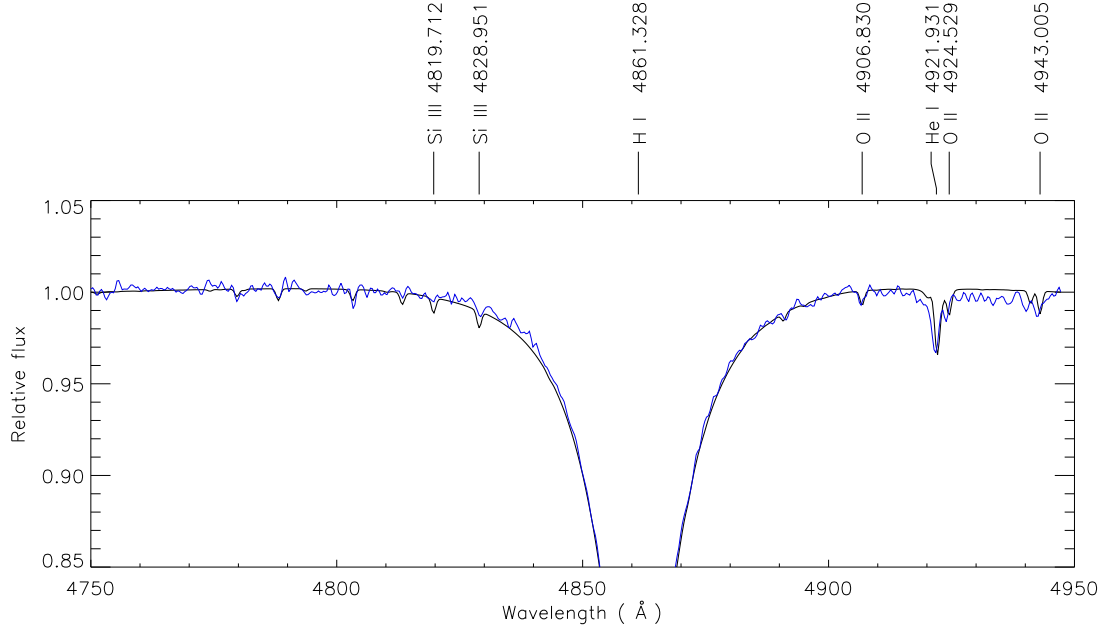


FIGURE 4.7 – Continued. f) There is an offset of the wavelengths from the He I $\lambda 4922$ until the end of the spectrum, probably due to the wavelength calibration that is not exactly right at the very end of the spectrum.

4.5 Conclusion

As part of an ongoing major effort to exploit fully the asteroseismic potential of Feige 48 (a rare bright rapid pulsator part of a close binary system), our work aimed at obtaining the most accurate atmospheric parameters possible for this sdB star. To achieve that goal, we analyzed four time-averaged optical spectra of this star, three of them having exceptionally high S/N, with state-of-the-art NLTE line-blanketed model atmospheres including the eight most abundant metallic species observed in the star’s atmosphere, namely, C, N, O, Ne, Mg, Si, Fe, and Ni. In comparison, previous atmospheric studies of Feige 48 were based on either line-blanketed LTE models with arbitrary metallicities or metal-free LTE and NLTE models.

Our final adopted parameters are the weighted mean of the solutions found with the different spectra: $T_{\text{eff}} = 29,850 \pm 60$ K, $\log g = 5.46 \pm 0.01$, and $\log N(\text{He})/N(\text{H}) = -2.88 \pm$

0.02, with the quoted uncertainties measuring only the quality of the spectral fits. A similar analysis made, this time, with more classical metal-free, H, He NLTE models led to very similar atmospheric parameters as indicated in Table 4.2. This demonstrates that the effects of combining the NLTE approach with metal line blanketing are not very large in the atmosphere of Feige 48. As depicted in Figure 4.4, part of this is accidental and specific to this particular star. Presumably, this coincidence explains why our derived parameters agree rather well with previous estimates based on less sophisticated models, implying that the current estimations of the atmospheric parameters of Feige 48 are reliable and sound. This is a good thing, particularly from an asteroseismological point of view, because it means that the spectroscopic constraints to be used in seismic studies, including past efforts, can be trusted.

During our investigations, we noticed a slight, but possibly significant systematic trend suggesting an increase of both the derived effective temperature and the surface gravity with decreasing resolution (from 1.0 to 8.7 Å in our data), while the helium abundance appeared to be insensitive. The overall differences are relatively small, ~ 600 K and ~ 0.09 dex, but the trend is seen in the fits carried out with both the metal-free and the line-blanketed grids. This is the first time we observe this effect in a sdB star, possibly because we had at our disposal exceptionally high S/N spectra. A contrario, we found that for the lower resolution spectra (PB6 and BG9), changing the spectral range of the fit leads to, within the fitting errors, the same estimates of the derived parameters and, thus, no observable systematic effects.

We also inspected the effects that the various metallic elements considered in the NLTE models have on the atmospheric structure. In the specific case of the models computed for Feige 48, the temperature in the outermost atmospheric layers is highly sensitive to the presence of the light metals, while the influence of iron and nickel is mostly confined to layers deeper than $\log m \simeq -3.0$. The actual amount of nickel present in the atmosphere of the star, $\log N(\text{Ni})/N(\text{H}) = -5.31$, does not produce a significant added effect on the temperature structure modified already by the presence of the light metals and iron.

As a consistency check, we fitted the only He II spectral feature that we could find in the spectrum of Feige 48 which, otherwise, contains only H I and He I lines. And indeed, through the MAST archives, we retrieved and fitted the weak He II line at 1640 Å present in the STIS

spectrum of Feige 48. This was done in terms of effective temperature and surface gravity only (the helium abundance being fixed), leading to the independent estimates of $T_{\text{eff}} = 30,450 \pm 930$ K and $\log g = 5.43 \pm 0.30$, fully consistent with our values derived from the optical data.

Our best data set was the MMT spectrum, characterized by the relatively high resolution of 1.0 \AA over a spectral range $4000\text{--}4950 \text{ \AA}$, and the very high value of $S/N \simeq 460$. This particular spectrum shows a host of distinct metallic lines that could be examined in details. With the initial metallicity specified as in Table 1, a good agreement was obtained between the observed and predicted metal lines as can be seen in Figure 4.5a. However, a distinct improvement was reached when slightly adjusting the individual metal abundances as was done in Subsection 3.5. The detailed results are presented in the series of Figure 4.7.

The atmospheric parameters derived here for Feige 48 will provide an essential ingredient in the upcoming new seismic analysis of that star, which will be based on the recent extensive photometric campaign that has revealed some 46 pulsation modes compared to the 9 modes previously known (Green et al., in preparation). Likewise, these estimates form the basis of the method that is used to exploit the signature that the degree index ℓ of a pulsation mode leaves on the wavelength-amplitude relationship (see, e.g., Randall et al. 2005). In the specific case of Feige 48, Fontaine & Chayer (2006) and Quirion et al. (2010) have presented preliminary efforts to exploit this signature by comparing optical with FUV amplitudes, and these certainly deserves to be pushed further on the basis of our improved determinations of the atmospheric parameters of that pulsator. A priori mode identification can be extremely useful in the search for an optimal seismic model in parameter space.

This work was supported in part by the Natural Sciences and Engineering Research Council of Canada through a doctoral fellowship awarded to M.L. and through a research grant awarded to G.F. The latter also acknowledges the contribution of the Canada Research Chair Program. We are also most grateful to Pierre Bergeron for providing us with a spectrum of Feige 48.

4.6 References

- Asplund, M., Grevesse, N., Sauval, A. J., & Scott, P. 2009, *ARA&A*, 47, 481
- Blanchette, J.-P., Chayer, P., Wesemael, F., Fontaine, G., Fontaine, M., Dupuis, J., Kruk, J. W., & Green, E. M. 2008, *ApJ*, 678, 1329
- Brassard, P., Fontaine, G., Billères, M., Charpinet, S., Liebert, J., & Saffer, R. A. 2001, *ApJ*, 563, 1013
- Brassard, P., Fontaine, G., Chayer, P., & Green, E. M. 2010, in *American Institute of Physics Conference Series*, Vol. 1273, *American Institute of Physics Conference Series*, ed. K. Werner & T. Rauch, 259–262
- Charpinet, S., Fontaine, G., Brassard, P., Billères, M., Green, E. M., & Chayer, P. 2005a, *A&A*, 443, 251
- Charpinet, S., Fontaine, G., Brassard, P., Chayer, P., Rogers, F. J., Iglesias, C. A., & Dorman, B. 1997, *ApJ*, 483, L123
- Charpinet, S., Fontaine, G., Brassard, P., & Dorman, B. 1996, *ApJ*, 471, L103
- Charpinet, S., Fontaine, G., Brassard, P., Green, E. M., & Chayer, P. 2005b, *A&A*, 437, 575
- Charpinet, S., Van Grootel, V., Brassard, P., Fontaine, G., Green, E. M., & Randall, S. K. 2013, in *European Physical Journal Web of Conferences*, Vol. 43, *European Physical Journal Web of Conferences*, 4005
- Chayer, P., Fontaine, G., Fontaine, M., Lamontagne, R., Wesemael, F., Dupuis, J., Heber, U., Napiwotzki, R., & Moehler, S. 2004, *Ap&SS*, 291, 359
- Fontaine, G., Brassard, P., Charpinet, S., Green, E. M., Chayer, P., Billères, M., & Randall, S. K. 2003, *ApJ*, 597, 518
- Fontaine, G. & Chayer, P. 2006, in *Astronomical Society of the Pacific Conference Series*, Vol. 348, *Astrophysics in the Far Ultraviolet: Five Years of Discovery with FUSE*, ed. G. Sonneborn, H. W. Moos, & B.-G. Andersson, 181
- Geier, S. 2013, *A&A*, 549, A110
- Green, E. M., Fontaine, G., Reed, M. D., et al. 2003, *ApJ*, 583, L31

- Heber, U. 2009, *ARA&A*, 47, 211
- Heber, U., Reid, I. N., & Werner, K. 2000, *A&A*, 363, 198
- Kilkenny, D., Fontaine, G., Green, E. M., & Schuh, S. 2010, *Information Bulletin on Variable Stars*, 5927, 1
- Kilkenny, D., Koen, C., O'Donoghue, D., & Stobie, R. S. 1997, *MNRAS*, 285, 640
- Koen, C., Kilkenny, D., O'Donoghue, D., van Wyk, F., & Stobie, R. S. 1997, *MNRAS*, 285, 645
- Koen, C., O'Donoghue, D., Pollacco, D. L., & Nitta, A. 1998, *MNRAS*, 300, 1105
- Lanz, T. & Hubeny, I. 2003, *ApJS*, 146, 417
- . 2007, *ApJS*, 169, 83
- Latour, M., Fontaine, G., Brassard, P., Green, E. M., Chayer, P., & Randall, S. K. 2011, *ApJ*, 733, 100
- Latour, M., Fontaine, G., Chayer, P., & Brassard, P. 2013, *ApJ*, 773, 84
- Napiwotzki, R. 1997, *A&A*, 322, 256
- Németh, P., Kawka, A., & Vennes, S. 2012, *MNRAS*, 427, 2180
- O'Donoghue, D., Lynas-Gray, A. E., Kilkenny, D., Stobie, R. S., & Koen, C. 1997, *MNRAS*, 285, 657
- O'Toole, S. J. & Heber, U. 2006, *A&A*, 452, 579
- O'Toole, S. J., Heber, U., & Benjamin, R. A. 2004, *A&A*, 422, 1053
- Quirion, P.-O., Podmore, H., & Dupuis, J. 2010, in *American Institute of Physics Conference Series*, Vol. 1273, *American Institute of Physics Conference Series*, ed. K. Werner & T. Rauch, 554–557
- Randall, S. K., Fontaine, G., Brassard, P., & Bergeron, P. 2005, *ApJS*, 161, 456
- Reed, M. D., Kawaler, S. D., Zola, S., Jiang, X. J., & et al. 2004, *MNRAS*, 348, 1164
- Saffer, R. A., Bergeron, P., Koester, D., & Liebert, J. 1994, *ApJ*, 432, 351
- Stobie, R. S., Kawaler, S. D., Kilkenny, D., O'Donoghue, D., & Koen, C. 1997, *MNRAS*, 285, 651

Van Grootel, V., Charpinet, S., Fontaine, G., & Brassard, P. 2008, *A&A*, 483, 875

Chapitre 5

Analysis of Extreme Horizontal Branch stars in ω Centauri: The He-rich star puzzle and carbon pollution¹

M. Latour¹, S. K. Randall², G. Fontaine¹, P. Brassard¹

¹ *Département de Physique, Université de Montréal, Succ. Centre-Ville, C.P. 6128,
Montréal, QC H3C 3J7, Canada*

² *ESO, Karl-Schwarzschild-Str. 2, 85748 Garching bei München, Germany*

To be submitted to *The Astrophysical Journal*

¹Based on observations collected at the European Organisation for Astronomical Research in the Southern Hemisphere, Chile (proposal ID 386.D-0669 and 091.D-0791)

5.1 Abstract

We take advantage of the recent availability of FORS2/VLT spectroscopy for a sample of extreme horizontal branch stars initially observed for mapping the new ω Cen sdO instability strip in the $\log g$ - T_{eff} diagram. We isolate 38 spectra well suited for detailed atmospheric studies, and we determine the fundamental parameters (T_{eff} , $\log g$, and $\log N(\text{He})/N(\text{H})$) of these hot stars using NLTE, metal line-blanketed models. We find that our targets can be divided in three groups: 6 stars, including 4 pulsators, are hot ($T_{\text{eff}} \gtrsim 45,000$ K) H-rich sdO subdwarfs, 7 stars are typical H-rich sdB stars ($T_{\text{eff}} \lesssim 35,000$ K), and the remaining 25 targets, with intermediate effective temperatures, are He-rich ($\log N(\text{He})/N(\text{H}) \gtrsim -1.0$) subdwarfs. Surprisingly and quite interestingly, these He-rich hot subdwarfs in ω Cen bunch together in a narrow range of temperature ($\sim 35,000$ K to $\sim 40,000$ K), which is a good 10,000 K cooler than the strip in which most He-rich subdwarfs are found in the field. This must be of importance for ultimately understanding the formation process of He-rich hot subdwarfs in different environments. In addition, we measure the abundance of carbon in the atmospheres of our sample stars (30 determinations and 8 upper limits) with the help of further dedicated models. We find a most interesting positive correlation between the carbon and helium atmospheric abundances. This correlation bears the signature of diffusion processes, most likely gravitational settling slowed down by stellar winds or internal turbulence. Again, this finding must have an impact on our understanding of the formation process of hot subdwarfs in ω Cen, particularly of He-rich objects. Using standard, accepted values for the photospheric parameters of the cluster (distance modulus, reddening, and absorption), we determine the absolute B magnitude of each target star and compute from these a spectroscopic mass distribution. In agreement with the previous findings of other researchers, we find that the masses thus inferred are too small (on the average, below the minimum mass for sustaining core helium burning). We further discuss this point in the text.

5.2 Astrophysical Context

Globular clusters are privileged environments for the understanding and study of stellar formation and evolution. However, this task has turned out to be rather complex and challenging in cases where multiple stellar populations within individual clusters themselves are found. This phenomenon has been discovered and documented in a few massive globular clusters, including ω Cen and NGC 2808 (Bedin et al. 2004; D’Antona et al. 2005). The presence of more than one main sequence (MS) in these clusters is likely due to the formation of secondary stellar generations.

Stars from subsequent generations form bluer MS’s as a consequence of their higher metallicity and enhanced helium content. In ω Cen, a second MS has been discovered by Anderson (1997), and this subpopulation was indeed found to be He-rich ($Y \sim 0.4$; Piotto et al. 2005). The presence of two stellar generations, with distinct chemical compositions and ages, also has repercussions on the characteristics of the more evolved stellar populations, such as the helium burning horizontal branch (HB) stars. Indeed, the peculiar morphology of the HB stars and its bluer extension, the extreme horizontal branch (EHB), in massive globular clusters with complex populations might be explained with the help of the helium-enriched population. These stars leave the main sequence with a lower mass at a given globular cluster age. This results in a higher temperature when they reach their helium burning phase on the HB, thus explaining qualitatively its bluer morphology (D’Antona et al. 2002; Busso et al. 2007) .

A more puzzling feature of the HB is a fainter extension, at its hot end, usually referred to as a “blue hook”, observed in ω Cen and NGC 2808 at first (D’Cruz et al. 2000; Brown et al. 2001), and then reported lately in a few more globular clusters (Brown et al. 2010). These subluminescent EHB stars cannot be explained in terms of canonical evolution. The usual scenario invoked to account for their existence is that these stars experienced a helium core flash after having evolved away from the red giant branch. Such a scenario has been modeled in a certain number of studies (e.g., Castellani & Castellani 1993; D’Cruz et al. 1996; Brown et al. 2001) and indeed, this evolutionary path takes stellar models to a similar region than the blue hook stars in a color-magnitude diagram. Depending on the evolutionary stage of the star when the helium flash happens, different “flavors” of hot flashers may occur. Basically, if

the ignition of helium happens when the star has not yet settled onto the white dwarf cooling curve, the hydrogen-burning shell forms a barrier that prevent the inner convection zone to reach the envelope of the star. This situation is often referred to as an “early hot flash” and results in a typical EHB star with a H-rich atmosphere. On the other hand, if the flash occurs while the star has reached the white dwarf cooling sequence, the weaker hydrogen-burning shell has not enough entropy to restrain the convective zone to the core of the star. The convection zone will thus reach the surface and mix the helium and carbon from the core with the hydrogen present in the atmosphere. This is usually referred to as a “late flash”. The flash mixing occurring in late flashers is likely to burn most of the hydrogen carried into the interior and the resulting star will thus arrive on the EHB with an atmosphere dominated by helium. The surface composition found by late flash modeling is around 95 to 96 % helium by mass and 3 to 4 % carbon (Brown et al. 2001; Cassisi et al. 2003). Evolutionary paths for different types of hot flashers can be found in Figure 4 of Brown et al. (2001).

It should be mentioned that the hot flasher scenario is of interest not only in globular clusters, but is also invoked to explain the presence of He-rich sdO stars in the field (Lanz et al. 2004; Miller Bertolami et al. 2008). The formation of the field EHB stars, the hot subdwarfs of spectral type sdB and sdO, is not less ambiguous than the formation of their analogs in globular clusters. Canonical scenarios implying a large amount of mass loss on the red giant branch (RGB) predict the existence of He-poor sdB stars to be found on the EHB (Dorman et al. 1993). Scenarios involving binary interactions such as Roche lobe overflow and common envelope evolution are also important since approximately half of the field sdB stars are part of binary systems (see Heber 2009 for a review of formation mechanisms). However, the mechanism that allows a certain amount of helium to stay visible in the atmosphere of these stars is still elusive, but is thought to be an interplay between radiative forces, weak stellar winds and/or turbulence (Fontaine & Chayer 1997; Unglaub 2008; Hu et al. 2011 and references therein). Complications appear with the helium-enriched subdwarfs whose existence cannot be explained in such terms. In these cases, alternate scenarios have to be invoked, such as the late helium flash discussed above and the merger of two white dwarfs (Saio & Jeffery 2000). However, those have their own problems, namely the fact that, upon forming according

to these scenarios, He-rich hot subdwarfs should quickly settle on the zero age helium main sequence (ZAHEMS), contrary to what is observed. Indeed, He-rich subdwarfs in the field rather distribute themselves quite differently in the $\log g-T_{\text{eff}}$ diagram. So, whether being in the field or in globular clusters, the formation of He-rich subdwarfs and blue hook stars is still not well understood.

In this context, it remains essential to characterize as many hot subdwarfs as possible, particularly those found in globular clusters as they have been a lot less studied than their field counterparts due to obvious added severe observational difficulties. Important work in that direction has nevertheless been undertaken to study the HB, EHB, and blue hook stars in ω Cen with the aim of gaining insight on the formation mechanism and evolutionary status of these objects (see, e.g., Moehler et al. 2002, 2007, 2011, and Moni Bidin et al. 2012). These authors combined spectroscopic observations and model atmosphere techniques to derive the fundamental parameters of several hot subdwarf stars in that cluster to form the basis for their interesting discussion.

Another development connecting ω Cen and its population of hot subdwarfs has been the recent discovery of short-period EHB pulsators as reported by Randall et al. (2009, 2011, 2012, 2013). Contrary to initial expectations, these variables turned out not to be the analogs of field sdB pulsators discovered almost two decades ago (Kilkenny et al. 1997), but members of a brand new family of pulsating stars made of hot H-rich sdO stars with effective temperatures clustering around 50,000 K. Interestingly, and despite sensitive searches (Johnson et al. 2013), no field counterparts to those sdO pulsators have been found². In an effort to map this new ω Cen instability strip in the $\log g-T_{\text{eff}}$ diagram, follow-up FORS spectroscopy was carried out at the VLT for an initial sample of 60 EHB and candidate stars. Preliminary results for 19 stars were reported in Randall et al. (2013) and the complete study will be presented elsewhere (Randall et al., in preparation). In the meantime, we examined closely the available spectra and were able to isolate 38 stars for more detailed spectroscopic modeling. In particular, we realized that the majority of them have He-rich atmospheres and, moreover, that carbon features can be seen in 30 of them, thus opening up the possibility of investigating further the

²Pulsating hot subdwarfs have also been discovered quite recently in the globular cluster NGC 2808 as reported by Brown et al. 2013. These remain to be characterized in detail.

relationship between helium richness and carbon abundance in hot subdwarfs in the particular environment of a globular cluster. As a spinoff of the ω Cen instability strip, we felt that this would be a most worthwhile endeavour to pursue, with the hope that some useful insight and/or constraints on the question of the formation of He-rich subdwarfs might ultimately be gained.

5.3 Observational Material

The spectra used here were culled from an initial sample of 60 ω Cen EHB stars/candidates as described in detail by Randall et al. (in preparation). They were obtained in March 2011 and April 2013 using the MXU mode of FORS mounted at the VLT on Cerro Paranal, Chile. Each spectrum is based on the combination of two 2750 s exposures obtained with the 600B grating and a slit width of $0.7''$, and has a wavelength resolution of $\sim 2.6 \text{ \AA}$. The nominal wavelength coverage of the sample is 3400-6100 \AA , however some of the spectra are cut at one end due to their position on the CCD. The spectra were reduced using a combination of the FORS pipeline (bias subtraction, flatfielding, wavelength calibration) and a customised IRAF procedure (extraction, cosmic ray removal, flux calibration).

The spectroscopic targets had been selected as EHB star candidates based on their brightness and colour in the ω Cen WFI/ACS catalogue (Castellani et al. 2007). The color cut favors the hotter part of the EHB domain ($T_{\text{eff}} \gtrsim 30,000 \text{ K}$) as appropriate for mapping the sdO instability strip. Although we attempted to focus on targets suffering minimal contamination from nearby stars, around one third of the extracted spectra turned out to be too polluted to derive reliable atmospheric parameters. These were excluded in our analysis, leaving us with 38 uncontaminated EHB star spectra that our study is based upon.

A close examination of the spectra revealed that the majority of them show spectral features of carbon and, at the same time, that they are He-rich objects. The series of plots, presented in Figure 5.1, illustrates each available spectrum in the wavelength range where the carbon features are the most prominent (when present). Note that the quality of the data is rather remarkable given the relative faintness of the target stars (they are characterized by a mean B magnitude of ~ 18.6). The spectra depicted appear in the same order as the data

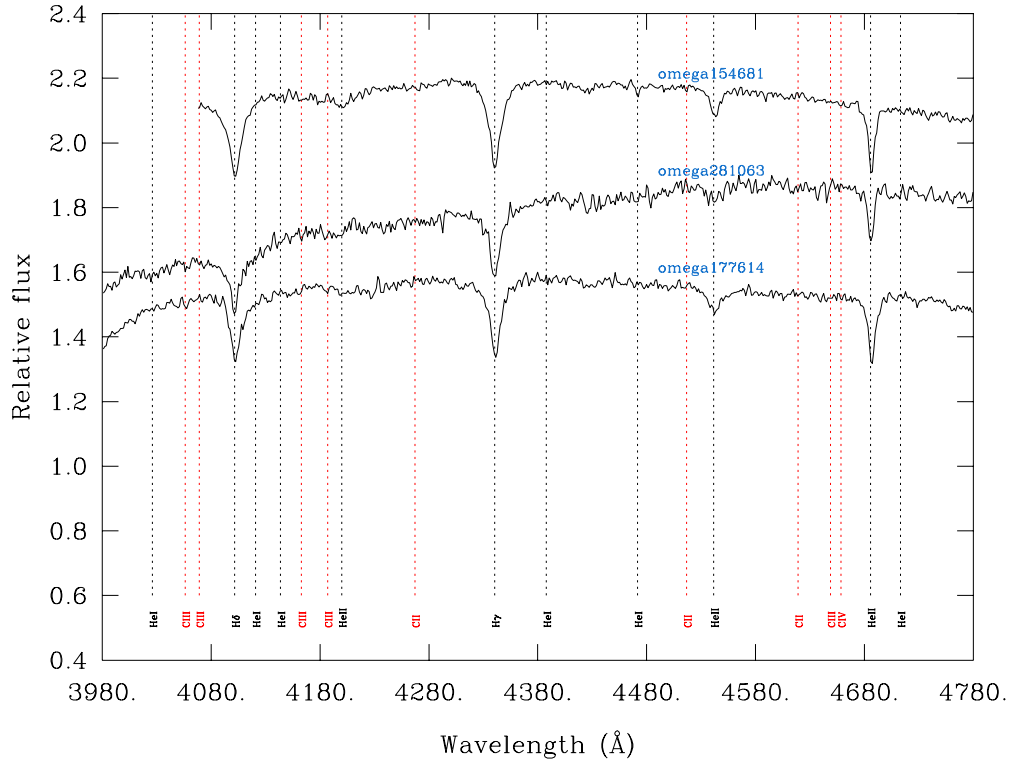


FIGURE 5.1 – Continued. Panel h.

In order to quantify this pollution somewhat better, we measured the equivalent width of the C III complex near 4650 \AA for each spectrum and compared it to the derived He abundance as obtained in a preliminary spectral analysis. The results of this operation are summarized in Figure 5.2 which shows that the C III feature is detectable in 25 of our sample of 38 stars. Most interestingly, however, Figure 5.2 suggests a clear correlation between the He abundance and the strength of that feature. To us, this was the main incentive to push further and attempt to derive quantitatively the carbon abundance through detailed atmosphere modeling.

5.4 Spectroscopic Analysis

5.4.1 Fundamental Parameters

In order to estimate the fundamental parameters of the stars in our sample in a homogeneous way, given that the spectra appear to span a significant range in effective temperature

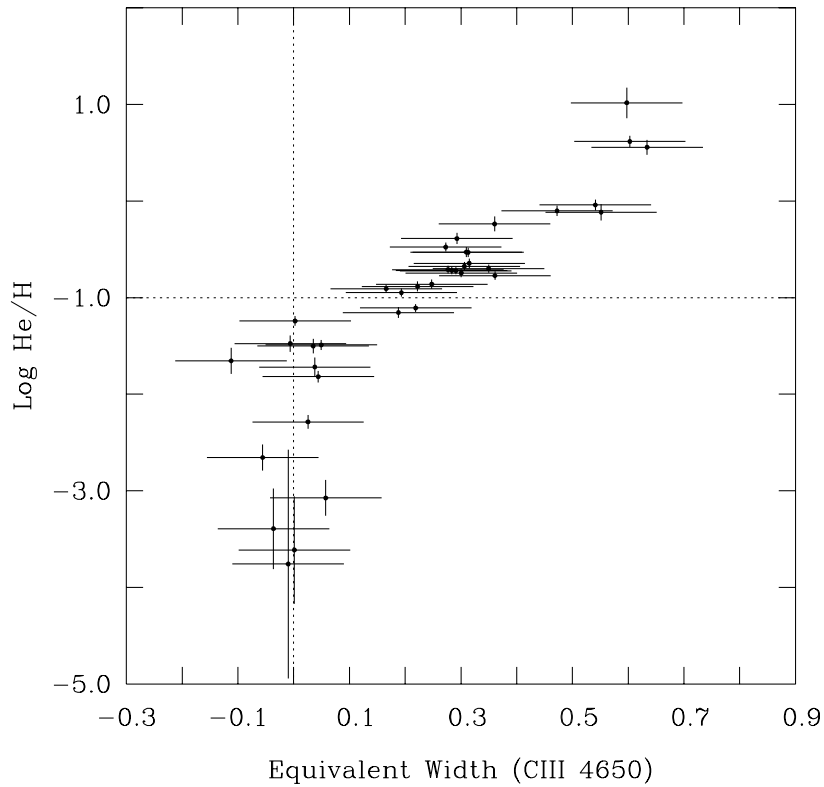


FIGURE 5.2 – Correlation between the He abundance and the equivalent width of the CIII 4650 complex detected formally in 23 of our 38 sample stars. The equivalent width is evaluated in arbitrary units.

and helium abundance, it was necessary to build new grids of NLTE model atmospheres. Because most of the stars were expected to be hotter than typical sdB's (He II lines are present in most spectra) and also richer in helium, we adopted initially solar abundances for carbon, nitrogen, and oxygen in our models. This is to be seen as a proxy metallicity with no other justification beyond the fact that these elements are the most important perturbators of the atmospheric structure of a hot star at their normal abundances. Note that we did not add iron in our computations because a solar amount of that element would not have further changed significantly the atmospheric structure in the presence of CNO in solar proportions (Haas et al. 1996; Latour et al. 2011), and because its inclusion would have been too time consuming in regard to its added limited benefits. Our model atmospheres and synthetic spectra were computed with the public codes TLUSTY and SYNSPEC and include the following

ions (besides those of H and He) : C II to C V, N II to N VI and O II to O VII. Note that, as usual with TLUSTY, the highest ionization stage of each element is taken as a one-level atom and additional information on model atoms can be found on TLUSTY's Web site³ and in Lanz & Hubeny (2003; 2007). The grid we computed included models with T_{eff} between 26,000 K and 58,000 K in steps of 2,000 K, $\log g$ between 5.2 and 6.4 in steps of 0.2 dex, and $\log N(\text{He})/N(\text{H})$ from -4.0 to $+1.5$ in steps of 0.5. That grid was generated by running TLUSTY and SYNSPEC in parallel mode on our cluster CALYS made up of 320 fast processors.

For most of the stars, the Balmer series from $H\beta$ up to and including H11 as well as all the strong helium lines of both ionization stages present between $\lambda 5412$ in the red and the Balmer jump in the blue were simultaneously fitted using a χ^2 minimization procedure similar to that of Saffer et al. (1994). However, a few observed spectra did not include the He II line at 5412 \AA , and a few others were cut in the blue due to their peculiar positions on the CCD chip so that the higher Balmer lines (between H8 and H11) could not always be included. In addition, the H ϵ line was explicitly disregarded due to interstellar pollution caused by the H line of Ca II. Our resulting parameters (T_{eff} , $\log g$, and $\log N(\text{He})/N(\text{H})$) are listed in Table 5.1, and Figure 5.3 display representative fits for four stars. Given the relative faintness of the targets, the results we achieved are quite satisfactory in terms of simultaneously fitting all of the available lines. This suggests that the derived atmospheric parameters rest on good grounds. Note, however, that the quoted uncertainties refer only to the formal errors of the fits; the true uncertainties must certainly be larger.

A cursory inspection of our results suggests that our target stars can naturally be divided into three groups, and this is indicated in Table 5.1. The seven coolest objects in the table⁴ form our Group 1 and are typical H-rich sdB stars. Our Group 2 is constituted of the 25 following stars, which are He-rich subdwarfs with $\log N(\text{He})/N(\text{H}) \gtrsim -1.0$. Note that for our present purposes, we will consider 5142999 and 75981 as ‘‘He-rich’’ stars even though their helium abundance is found a tad below that limit. Our Group 3 is made of the 6 hottest objects in our sample, a collection of hot H-rich sdO subdwarfs, including 4 pulsators (5034421,

³<http://nova.astro.umd.edu/>

⁴5180753 is formally hotter than 5142999.

177238, 154681, 281063).

TABLE 5.1 – Atmospheric and Other Parameters for the 38 Stars of our Sample

Number	T_{eff} (K)	$\log g$	$\log N(\text{He})/N(\text{H})$	M_B	M/M_{\odot}
5238307	25711 \pm 400	5.35 \pm 0.06	-2.27 \pm 0.08	4.428 \pm 0.147	0.231 \pm 0.102
5139614	27594 \pm 468	5.48 \pm 0.06	-3.74 \pm 1.06	4.661 \pm 0.147	0.211 \pm 0.102
204071	28828 \pm 602	5.53 \pm 0.09	-3.00 \pm 0.14	3.767 \pm 0.148	0.618 \pm 0.130
168035	29770 \pm 454	5.38 \pm 0.07	-3.27 \pm 0.20	3.767 \pm 0.147	0.401 \pm 0.111
5262593	31161 \pm 280	5.48 \pm 0.05	-3.07 \pm 0.29	3.648 \pm 0.146	0.531 \pm 0.092
5243164	32403 \pm 281	5.41 \pm 0.05	-2.65 \pm 0.17	4.044 \pm 0.146	0.242 \pm 0.093
5180753	34850 \pm 317	5.75 \pm 0.06	-1.46 \pm 0.06	4.238 \pm 0.147	0.466 \pm 0.101
5142999	34477 \pm 392	5.67 \pm 0.07	-1.09 \pm 0.05	4.387 \pm 0.146	0.308 \pm 0.110
5222459	35008 \pm 327	5.73 \pm 0.05	-0.73 \pm 0.04	4.663 \pm 0.146	0.253 \pm 0.093
5119720	35018 \pm 403	5.77 \pm 0.07	-0.81 \pm 0.05	4.457 \pm 0.147	0.381 \pm 0.110
53945	35216 \pm 316	5.91 \pm 0.05	-0.61 \pm 0.04	4.562 \pm 0.146	0.493 \pm 0.092
75981	35929 \pm 307	5.71 \pm 0.05	-1.05 \pm 0.05	4.151 \pm 0.146	0.432 \pm 0.093
5164025	36020 \pm 428	5.84 \pm 0.07	-0.55 \pm 0.05	4.716 \pm 0.146	0.315 \pm 0.110
5205350	36251 \pm 335	5.54 \pm 0.06	-0.61 \pm 0.04	4.300 \pm 0.146	0.193 \pm 0.101
5165122	36331 \pm 328	5.71 \pm 0.06	-0.64 \pm 0.04	4.439 \pm 0.146	0.288 \pm 0.101
165943	36479 \pm 401	5.76 \pm 0.07	-0.68 \pm 0.05	4.351 \pm 0.147	0.383 \pm 0.110
5141232	36583 \pm 402	5.72 \pm 0.07	-0.61 \pm 0.05	4.416 \pm 0.146	0.300 \pm 0.110
274052	36640 \pm 506	5.59 \pm 0.09	-0.35 \pm 0.06	4.558 \pm 0.147	0.140 \pm 0.130
5242504	36653 \pm 387	5.75 \pm 0.07	-0.45 \pm 0.05	4.495 \pm 0.146	0.298 \pm 0.110
264057	36696 \pm 408	5.70 \pm 0.07	-0.80 \pm 0.05	4.421 \pm 0.147	0.280 \pm 0.111
5142638	36740 \pm 428	5.71 \pm 0.07	-0.38 \pm 0.05	4.649 \pm 0.146	0.210 \pm 0.110
5102280	36948 \pm 327	5.70 \pm 0.06	-0.94 \pm 0.05	4.195 \pm 0.146	0.374 \pm 0.101
177711	37093 \pm 433	5.72 \pm 0.07	-0.45 \pm 0.05	4.429 \pm 0.147	0.287 \pm 0.111
5220684	37544 \pm 368	5.82 \pm 0.07	-0.86 \pm 0.05	4.338 \pm 0.147	0.435 \pm 0.110
5062474	37554 \pm 863	5.90 \pm 0.14	-0.09 \pm 0.09	4.757 \pm 0.148	0.330 \pm 0.183
5138707	37855 \pm 599	5.93 \pm 0.09	0.57 \pm 0.05	4.932 \pm 0.147	0.283 \pm 0.130
5124244	38432 \pm 530	5.97 \pm 0.09	-0.01 \pm 0.05	4.730 \pm 0.146	0.407 \pm 0.130
5170422	38533 \pm 340	5.60 \pm 0.06	-0.77 \pm 0.04	4.190 \pm 0.146	0.240 \pm 0.101
5047695	38578 \pm 549	5.69 \pm 0.12	-0.18 \pm 0.07	4.806 \pm 0.150	0.106 \pm 0.163
5085696	39072 \pm 371	5.66 \pm 0.08	-0.04 \pm 0.05	4.585 \pm 0.146	0.147 \pm 0.120
5039935	39804 \pm 523	6.06 \pm 0.11	0.49 \pm 0.07	4.998 \pm 0.148	0.353 \pm 0.151
165237	43843 \pm 362	6.01 \pm 0.11	0.75 \pm 0.10	4.173 \pm 0.147	0.579 \pm 0.149
5242616	44959 \pm 637	5.88 \pm 0.08	-1.41 \pm 0.08	4.265 \pm 0.146	0.392 \pm 0.120
5034421	49113 \pm 824	5.89 \pm 0.07	-1.76 \pm 0.09	4.137 \pm 0.147	0.408 \pm 0.112
177238	49328 \pm 877	6.07 \pm 0.08	-1.73 \pm 0.11	4.138 \pm 0.147	0.621 \pm 0.121
154681	50635 \pm 758	5.89 \pm 0.08	-1.25 \pm 0.05	4.043 \pm 0.146	0.434 \pm 0.120
281063	58789 \pm 1910	6.12 \pm 0.11	-1.67 \pm 0.13	4.344 \pm 0.147	0.487 \pm 0.152
177614	59724 \pm 1288	6.02 \pm 0.08	-1.32 \pm 0.09	4.281 \pm 0.147	0.392 \pm 0.120

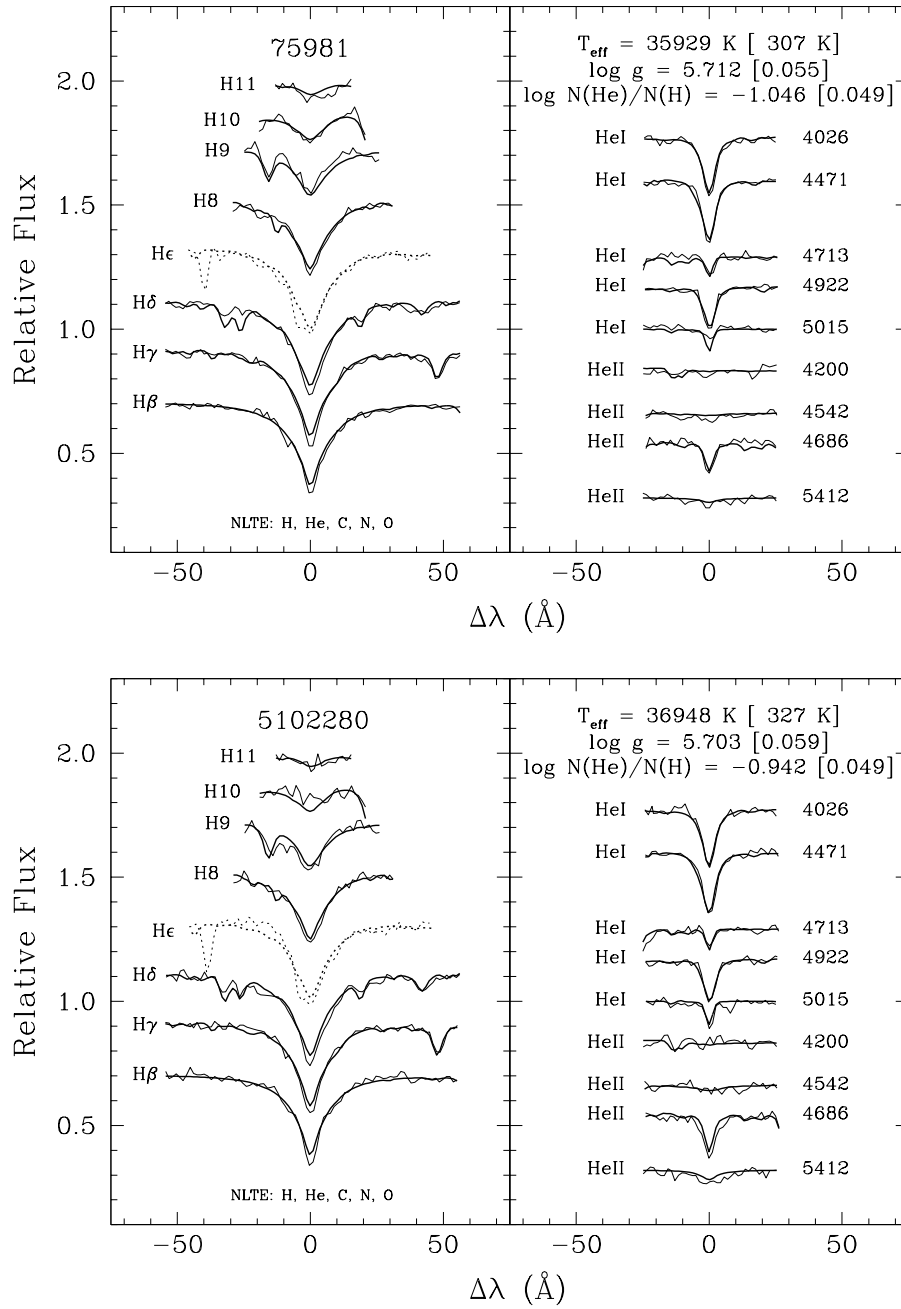


FIGURE 5.3 – Panels a (top) and b (bottom) feature stars of Group 2 having a helium abundance around the solar value. The He I and II lines are well reproduced but some residual Balmer line problem is seen in the lower hydrogen lines. Note that He ϵ , in dashed line, was not included in the fitting procedure because it is polluted by a fairly strong H component of the Ca II doublet (the K component is also seen in the observed spectrum).

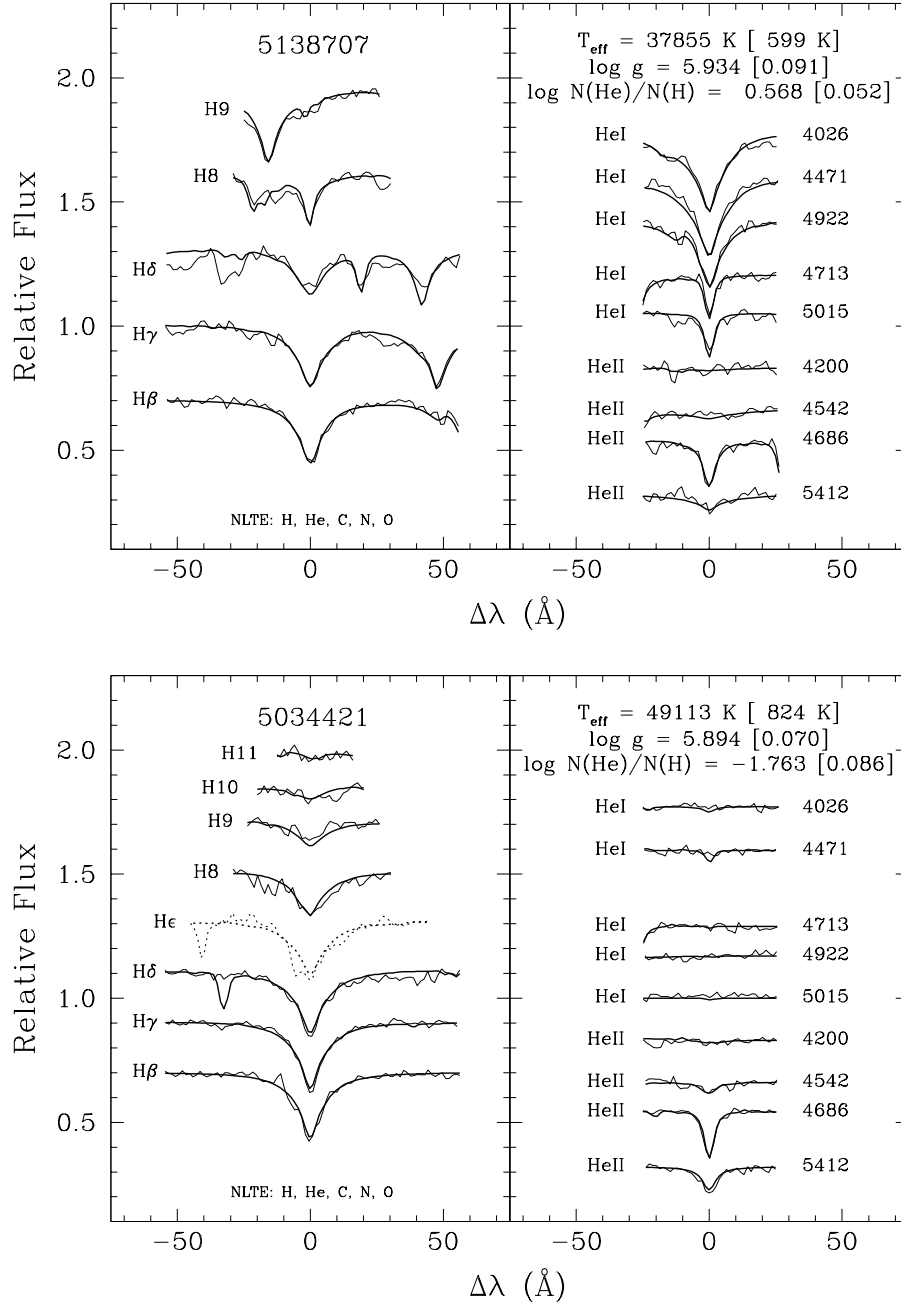


FIGURE 5.3 – Panel c (top) shows the fit for a helium enriched star, and panel d (bottom) illustrates the fit for a hotter, helium depleted star which is also the pulsating star identified as V1 in Randall et al. (2011).

The natural separation between the three groups of star is easy to see in Figure 5.4, which depicts helium number abundance (relative to hydrogen) as a function of effective temperature for the 38 stars of our sample. The coolest and hottest stars show significant underabundances of helium, while among the He-rich objects (Group 2, in red) a positive correlation is seen between the two parameters. Interestingly, a correlation between the effective temperature and helium abundance has also been noticed in the He-rich field subdwarfs (Stroeer et al. 2007; Németh et al. 2012), but it occurs at higher effective temperatures (above 40,000 K) and it is negative! This might be due either to the difference in effective temperature or to the difference in the populations involved: field versus globular cluster.

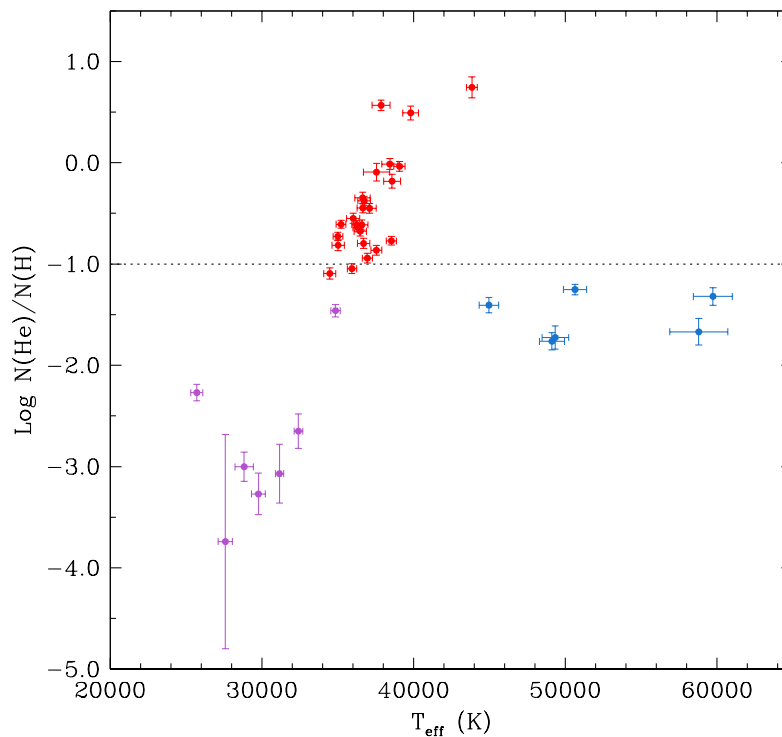


FIGURE 5.4 – Helium abundance versus effective temperature for the 38 stars of our sample. Group 1 stars are found at lower temperatures and are illustrated in purple. Group 2 stars are depicted in red and are generally He-rich objects. A clear trend of increasing helium abundance with effective temperature can be noticed among them. Finally, the hottest stars forming Group 3 are in blue. The error bars include only the formal uncertainties of the fitting procedure and should be regarded as lower limits. The dotted line indicates the solar helium abundance.

Figure 5.5 shows our sample in the $\log N(\text{He})/N(\text{H})$ - $\log g$ plane where our six coolest stars stand out in particular with their low helium abundances and surface gravities. Coupled to their lower effective temperatures, these characteristics of Group 1 stars make them look like indeed typical helium core burning field sdB stars nicely sitting on or close to the EHB. In contrast, the Group 3 stars must certainly be the analogs of post-EHB H-rich hot sdO subdwarfs contracting on their way to the white dwarf regime.

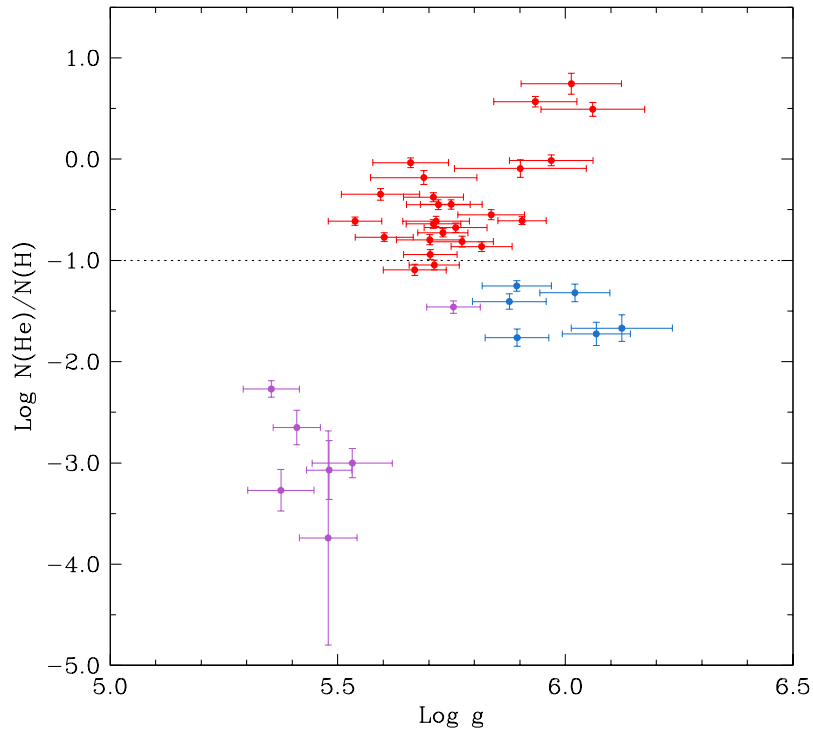


FIGURE 5.5 – Similar to Fig. 5.4, but showing helium abundance versus surface gravity. Though no clear systematic trends are seen, each group of stars stays fairly well defined in this diagram. The position of Group 1 stars (in purple) is consistent with typical EHB subdwarf B stars.

The distribution of our sample of stars in the $\log g$ - T_{eff} diagram is illustrated in Figure 5.6. To aid the eye, we plotted the location of the ZAHEMS for zero metallicity, as well as the locations of the zero age extreme horizontal branch (ZAEHB) and of the terminal age extreme horizontal branch (TAEHB) for a mass of $0.47 M_{\odot}$, both again for zero metallicity. These models were computed with our local hot subdwarf evolutionary code at Université de Montréal. The value of $0.47 M_{\odot}$ was chosen solely as a representative one and is based on

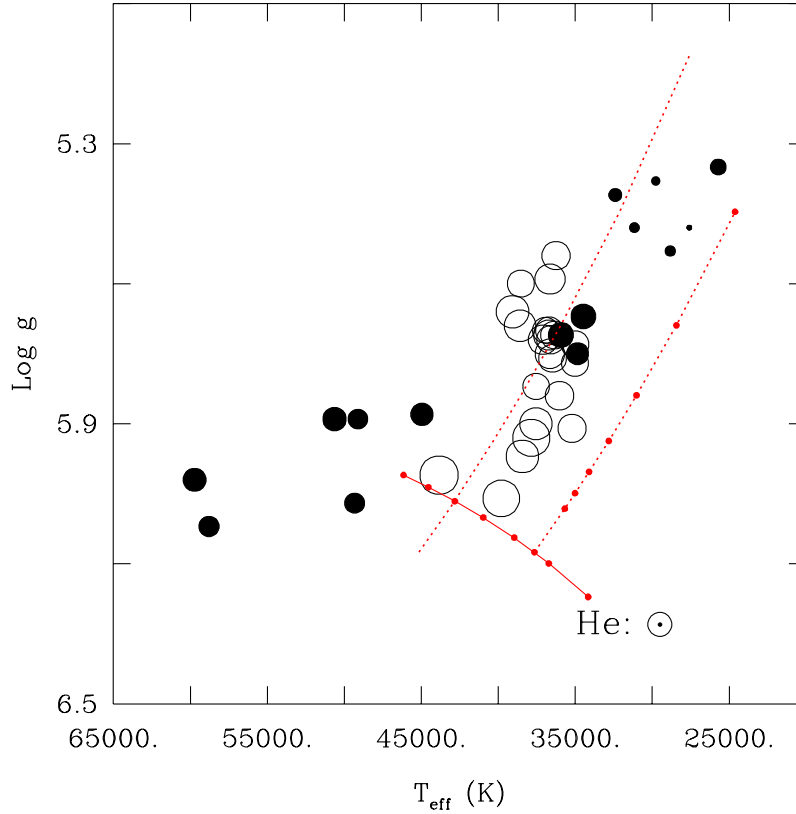


FIGURE 5.6 – Distribution of our sample of ω Cen EHB stars in the $\log g$ - T_{eff} plane. The dimension of a given circle is a logarithmic measure of the He abundance relative to that of H. He-poor and He-rich stars are represented by filled and open circles, respectively. The ZAEHB for zero metallicity models is indicated by the solid curve. From left to right, the model mass along that curve is 0.70, 0.65, 0.60, 0.55, 0.50, 0.47, 0.45, and 0.40 M_{\odot} . Likewise, the ZAEHB for zero metallicity 0.47 M_{\odot} models is depicted by the dotted curve on the right; each dot along that curve indicates the fractional mass of the outer H-rich layer, from $\log q(\text{H}) = -2.0$ at the top right and decreasing to $\log q(\text{H}) = -5.0$ in steps of 0.5 dex moving down along the curve. The dotted curve on the left defines the location of the TAEHB for the same 0.47 M_{\odot} models.

the mean mass of field hot subdwarfs obtained mostly through asteroseismology (Fontaine et al. 2012). While the locations, between the ZAEHB and TAEHB, and allowing for a small mass spread, of the coolest H-rich objects (Group 1) are consistent with the proposition that these are normal mass helium core burning sdB subdwarfs, and while the locations of the six hottest H-rich stars (Group 3) are consistent with the idea that these are evolved, post-

EHB sdO stars, the tight grouping of the He-rich objects in our sample (Group 2) is both unexpected and extremely interesting.

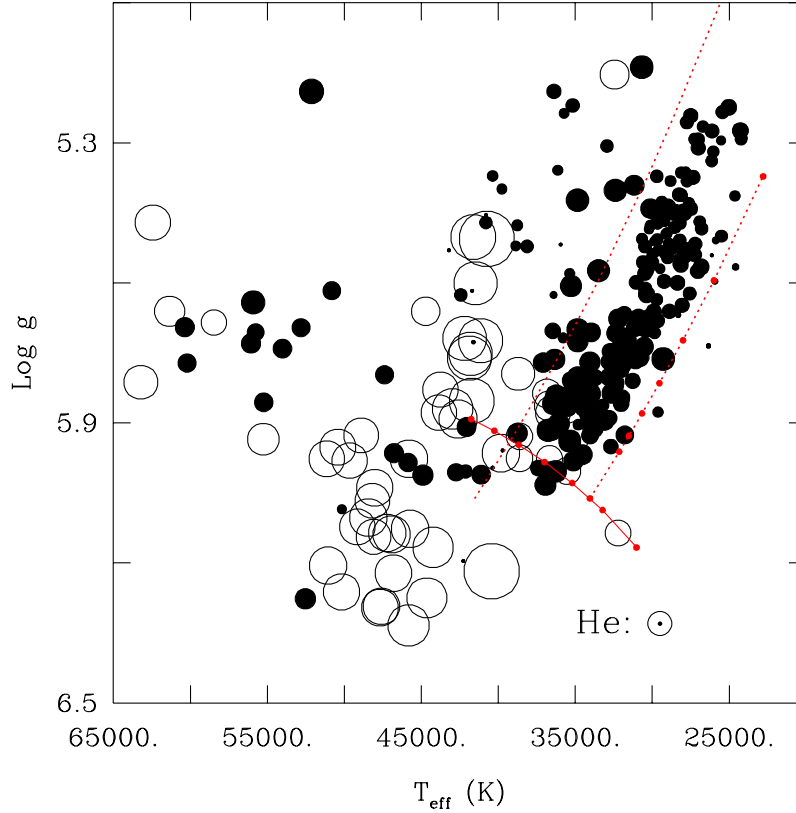


FIGURE 5.7 – Similar to Fig. 5.6, but depicting this time the distribution of hot subdwarfs in the field. The ZAHEMS, ZAEHB ($0.47 M_{\odot}$), and TAEHB ($0.47 M_{\odot}$) now refer to models with a metallicity of $Z=0.02$.

To put this result into perspective, we provide in Figure 5.7 an equivalent picture but referring, this time, to the situation in the field. These represent the results of many years of efforts first presented by Green et al. (2008) through the Arizona-Montréal Spectroscopic Program and updated recently by Fontaine et al. (2014) using atmosphere models comparable to those computed in the present study. In Figure 5.7, the ZAHEMS, ZAEHB, and TAEHB have now been computed with a metallicity of $Z = 0.02$, representative of the field stars, and a mass of $0.47 M_{\odot}$ was again considered for the ZAEHB and TAEHB. Note, in particular, how most of the H-rich objects fall tightly between the ZAEHB and TAEHB as expected,

while the other H-rich stars must be interpreted as evolved, post-EHB objects on their way to the white dwarf cooling domain. But it is the location of the bulk of the He-rich stars in the field in relation to their location in ω Cen that is particularly fascinating. We thus find that He-rich stars in the field tend to bunch together at an effective temperature that is some 7,000 K higher than their counterparts in the cluster. This must be of importance for ultimately understanding the formation process of He-rich subdwarfs in different environments.

In view of the significance of this finding, we have searched the literature to check if systematic effects, of unknown origin, could perhaps cloud our conclusion. In the case of the cluster ω Cen, we are aware of the independent spectroscopic study of Moehler et al.

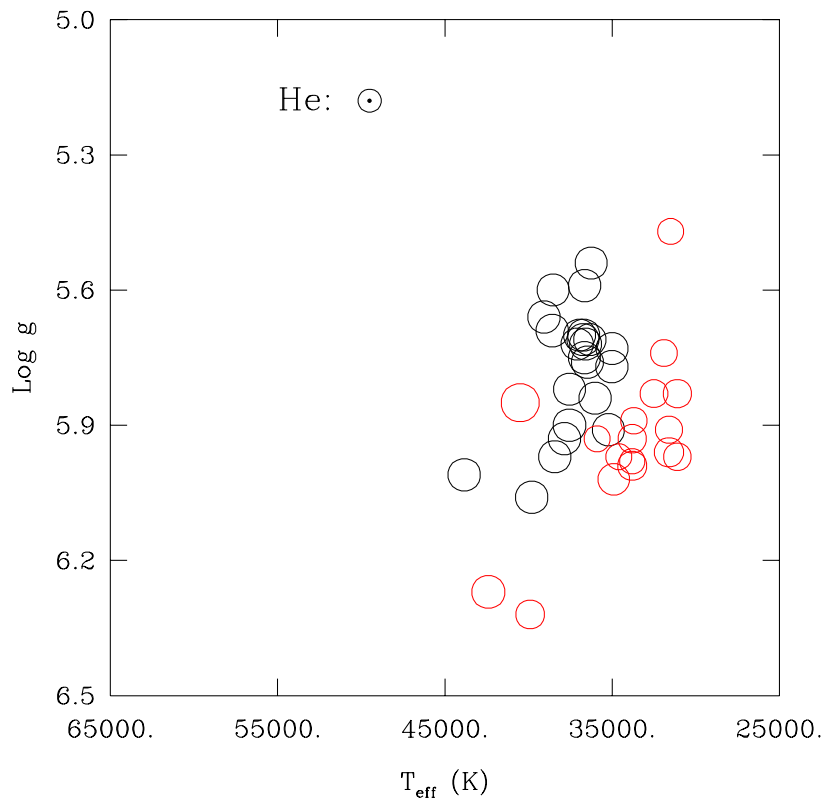


FIGURE 5.8 – Comparison of the $\log g-T_{\text{eff}}$ distribution of the 23 He-rich subdwarfs (black circles) in our sample with that of 17 similar He-rich stars (red circles) analyzed by Moehler et al. (2011), all members of the ω Cen cluster. As before, the dimension of a given circle is a logarithmic measure of the He abundance relative to that of H. Only one object is in common between the two samples.

(2011) which, among other things, has led to the characterization of 17 He-rich subdwarfs. We compare in Figure 5.8 the locations of these objects in the $\log g$ - T_{eff} diagram as obtained by Moehler et al. (2011) with the locations of the 23 truly He-rich subdwarfs in our sample as summarized in Table 5.1. It is not clear if the differences that we see in the plot is truly a systematic effect or the consequence of a different color cutoff that would favor bluer stars in our case and redder ones in Moehler et al.'s case. As it is, only one star is in common (53945) and the two sets of estimates agree rather well. From Table 5.1 we have for 53945 $T_{\text{eff}} = 35216 \pm 316$ K, $\log g = 5.91 \pm 0.05$, and $\log N(\text{He})/N(\text{H}) = -0.61 \pm 0.04$, to be compared with Moehler et al. (2011) giving instead $T_{\text{eff}} = 34600 \pm 1600$ K, $\log g = 5.97 \pm 0.26$, and $\log N(\text{He})/N(\text{H}) = -0.82 \pm 0.16$. Be it as it may, Moehler et al. (2011) locate the bulk of their He-rich subdwarfs in ω Cen at still lower effective temperatures than we do.

Figure 5.9 provides the counterpart for field stars. Here we compare the locations of the 52 He-rich subdwarfs in the Arizona-Montréal sample (black circles) with the locations of the 33 He-rich objects (blue circles) in the sample of Stroerer et al. (2007) and the locations of the 27 He-rich subdwarfs (red circles) in the sample of Németh et al. (2012). From the figure, the three independent studies seem to give very coherent results, with no obvious systematic differences. There is only one star in common between the Arizona-Montréal sample and the Stroerer et al. sample (the latter being a southern hemisphere study based on the SPY project), and that is the very helium rich star HZ 1 for which Stroerer et al. (2007) give $T_{\text{eff}} = 41344$ K, $\log g = 5.68$, and $\log N(\text{He})/N(\text{H}) = 3.00$, compared to $T_{\text{eff}} = 40744 \pm 393$ K, $\log g = 5.52 \pm 0.10$, and $\log N(\text{He})/N(\text{H}) = 3.04 \pm 0.52$ as derived by Fontaine et al. (2014) and in excellent agreement. Likewise, we find that there is excellent agreement in the estimated atmospheric parameters of the 4 stars in common (PG 0314+146, FBS 0730+617, PG 0838+133, and LSIV+10-9) between the Arizona-Montréal sample and that of Németh et al. (2012), leading to rms deviations of only 313 K in T_{eff} , 0.14 dex in $\log g$, and 0.09 dex in $\log N(\text{He})/N(\text{H})$. Dreizler & Werner (1993) also analyzed LSIV+10-9 mainly on the basis of optical data. He derived a similar effective temperature than in ? and Németh et al. (2012) but its surface gravity of $\log g = 5.55$ / ± 0.15 is lower than the values of $\log g$ around 6.1 dex obtained in the two other studies. In contrast, as indicated by the dotted lines in Figure 5.9, there appears to be huge

systematic effects, particularly marked in gravity, between the estimates obtained by Ahmad & Jeffery (2003) and the three other groups of modelers. We suspect that the LTE models used by these authors may have been flawed. In any case, we can safely conclude that the temperature offset in the location of the bulk of He-rich subdwarfs between the field and in ω Cen is well established.

5.4.2 Carbon Abundances

As mentioned in the introductory section, a careful inspection of the 38 spectra of our sample quickly led to the realization that there is a correlation between the presence (and strength) of carbon lines and those of helium. Basically, we noticed the same phenomenon originally mentioned in Stroeger et al. (2007), linking helium enrichment with the presence of carbon and/or nitrogen lines. Given that, by default, our spectra of ω Cen stars are limited in resolution and sensitivity, they are not optimally suited for studying weak metallic lines in the optical domain. Nevertheless, carbon lines could easily be distinguished in our spectra, even in the not-so-helium-rich stars, thanks to the strong C III complexes around 4070 Å and 4650 Å (see Fig. 5.1). Nitrogen lines being weaker, some features in the spectra could be associated with N II and III lines, but this was possible only in the most helium-rich stars or so. Therefore, we decided to focus our efforts on the carbon lines and specifically on quantifying the amount of carbon present in the atmosphere of these stars.

Deriving the carbon abundance for every star in our sample means that for each of them, we had to build a small grid of model atmospheres with different assumed carbon abundances, while the fundamental parameters of the models would be fixed at the values given in Table 5.1. When looking at the spectroscopic fits we obtained for our Group 1 stars, it was obvious that a solar abundance for C, N, and O was way too much, resulting in the presence of important metallic lines in the synthetic spectra. Moreover, no metallic lines (except a few weak ones in the hottest star of the group) were seen in the spectra of Group 1 stars. So, with this fact in mind, coupled to the annoying tendency of our strongest C lines to blend with O II ones (we come back on this issue just below), we decided to include only carbon as a metallic element in our small model grids for Group 1 stars. For the other helium-poor stars

in Group 3, their higher effective temperatures wipe out most of the metallic lines, even at solar abundances, so the carbon abundance for these stars was obtained with models including the original solar amount of oxygen and nitrogen. For these two groups, we varied the carbon abundance of our models from $\log N(\text{C})/N(\text{H}) = -6.0$, where no C lines are visible, to -3.5 ,

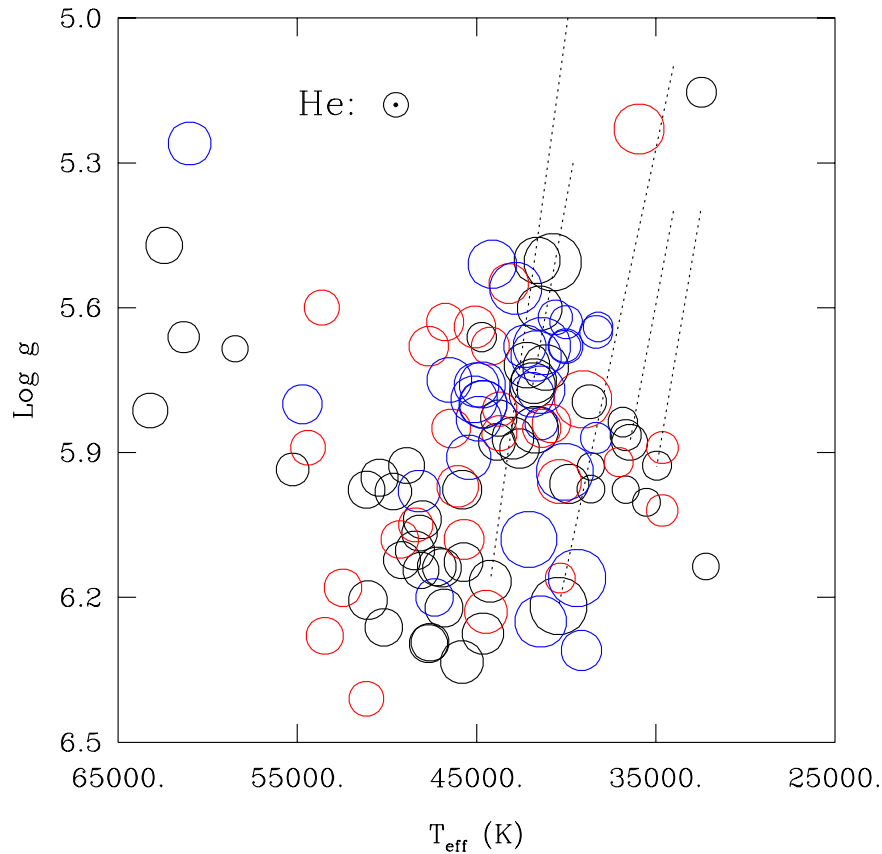


FIGURE 5.9 – Comparison of the $\log g$ - T_{eff} distribution of the 52 He-rich subdwarfs (black circles) in the field sample of Green et al. (2008) with the distribution of 33 He-rich field subdwarfs (blue circles) analyzed by Stroerer et al. (2007), and the distribution of 27 He-rich field subdwarfs (red circles) discussed by Németh et al. (2012). The dimension of a given circle is a logarithmic measure of the He abundance relative to that of H. There are four stars in common between the Green et al. and the Németh et al. samples, and only one star in common between the Green et al. and the Stroerer et al. samples. While the comparisons indicate that there are no obvious systematic differences between these three sources, such is not the case with the sample of Ahmad & Jeffery (2002) which has five stars in common with Green et al. (2008). The important systematic offsets between the respective atmospheric estimates are indicated by the dotted lines.

approximately the solar abundance, by steps of 0.5 dex.

Stars forming Group 2 were subdivided into two categories for their carbon abundance analysis. Seven of these stars show clear and strong C lines requiring, at first sight, an oversolar abundance. These seven stars also happen to be the most helium-rich of Group 2 and they form the hottest subfamily of Group 2. Their carbon abundance was obtained with model atmospheres containing a solar amount of nitrogen and oxygen while the carbon content was extended up to $\log N(\text{C})/N(\text{H}) = -1.0$ in the grids. For the remaining stars in Group 2, showing moderately strong C lines, the blending of $\lambda\lambda 4070, 4650$ C III complexes with O II lines became problematic because a solar amount of oxygen in a model without carbon produces small features mimicking weak C III lines at the observed resolution (2.6 \AA). So this is why we reduced the amount of oxygen to $\log N(\text{O})/N(\text{H}) = -4.5$ (roughly 1/10 solar) in the carbon grids of the 18 remaining Group 2 stars. It should be mentioned here that we checked our spectra for hints of oxygen lines, such as $\lambda\lambda 4415, 4276, 4609$ and the doublet around 4700, but no stars showed convincing evidence for oxygen lines.

Five regions featuring carbon lines were individually fitted, including the C III complexes around 4070 \AA and 4650 \AA , C III lines at 4162.9 and 4186.9 \AA , the C II lines at $4267.3, 4516.8$ and 4619.0 \AA , and C IV at 4658.3 \AA . The abundances obtained from these five spectral regions are listed in Table 5.2, as well as the weighted mean that was adopted as the final abundance for each star. In a few spectra, no C lines were visible (or barely), so we deduced an upper limit on the abundance using the strongest C line (usually $\lambda 4070$). Otherwise, for the rest of the stars, only the regions showing carbon lines were analyzed, hence the empty spaces in Table 5.2. Performing a formal fit on a line was not always possible, mostly because of an uneven continuum, and in these cases, we evaluated the appropriate abundance by eye and associated an uncertainty of 0.5 dex with these abundances. Otherwise, the uncertainties are the formal ones given by the fitting procedure (which is the same as the one used to determine the fundamental parameters but in one dimension only, the carbon abundance). Examples of our results are plotted in Figure 5.10 which shows, for the same four stars whose fits are displayed in Fig. 5.3, a comparison between the observed spectrum and the model one having the abundance of carbon determined for the displayed spectral region. If a region displayed

was not fitted, we used the mean carbon abundance in the model spectrum. We noticed some systematic disparities between the abundances indicated by the different carbon lines, such as the two main C II lines which need a higher abundance than the average in order to be well reproduced (thus they appear too weak in our models) and the C III line at 4070 Å that often gives a lower abundance than its counterpart at 4658 Å. The C II doublet around 4074.5 Å also often appears too strong at the abundance needed to reproduce its neighbouring C III complex. An example of this last behaviour is seen in 5138707 (see Fig. 5.10). The reasons underlying these inconsistencies still remain unclear.

At last, Figure 5.11 features another striking result of this spectroscopic study of EHB stars in ω Cen: a strong correlation between the helium and carbon abundances. The different groups of stars are also easily distinguishable in this plot: the most He-rich stars of Group 2 form the carbon-enriched population, the rest of Group 2 forms a clump around the solar abundance of carbon, while Group 3 hot stars form the lower abundance part of this relation. Finally, the six coolest Group 1 stars rest apart with their sole upper abundance determination of carbon. It might also be worth mentioning here that in spite of the disparities in the carbon abundance given by the different lines, this correlation is seen for each of the five regions fitted. A linear regression made between the mean abundance of carbon and the helium abundance, including the 30 stars for which an amount of carbon was determined, is plotted in Figure 5.11. The line can be described with the following equation,

$$\log N(\text{C})/N(\text{H}) = 1.36(\pm 0.039) \times \log N(\text{He})/N(\text{H}) - 2.56(\pm 0.027). \quad (5.1)$$

A similar positive correlation was found by Németh et al. (2012) in their study of field subdwarfs though their slope is steeper.

It is not clear at all if this correlation can be given a physical interpretation, particularly its extension in the low-abundance regime. On the other hand, in the He-rich domain, the He-C relation bears the strong signature of diffusion effects. For instance, assuming that He-rich subdwarfs are born with more or less the same atmospheric composition as predicted by late flasher scenarios (a mixture containing He as the dominant species, C as an important

secondary constituent, and H as a trace element), it is certain that such composition cannot resist the action of gravitational settling in the absence of competing mechanisms. Indeed, if left unimpeded, diffusion will transform the atmospheric composition of such an initially He-rich star into a H-dominated one over a timescale much shorter than typical lifetimes ($\sim 10^8$ yr) of helium core burning hot subdwarfs. An example of this is provided by Miller Bertolami et al. (2008) who estimated a separation timescale of only $\sim 10^6$ yr. Hence, diffusion must be slowed down in these He-rich subdwarfs if they are to be detected as such. The more likely

 TABLE 5.2 – Inferred Carbon Abundances ($\log N(\text{C})/N(\text{H})$)

Name	C III 4070 Å	C III 4163, 4187 Å	C III 4650 Å	C II 4267 Å	C II 4517 Å	C weighted mean
5238307	-5.00 ± 0.00	-5.00 ± 0.00
5139614	-4.30 ± 0.00	-4.30 ± 0.00
204071	-5.00 ± 0.00	-5.00 ± 0.00
168035	-5.00 ± 0.00	-5.00 ± 0.00
5262593	-5.00 ± 0.00	-5.00 ± 0.00
5243164	-4.50 ± 0.00	-4.50 ± 0.00
5180753	-4.50 ± 0.50	...	-4.55 ± 0.70	-4.52 ± 0.41
5142999	-3.50 ± 0.50	...	-3.45 ± 0.30	-3.46 ± 0.26
5222459	-4.00 ± 0.50	-3.70 ± 0.40	-3.50 ± 0.20	-4.10 ± 0.70	...	-3.62 ± 0.16
5119720	-4.00 ± 0.50	...	-4.70 ± 1.00	-3.00 ± 0.80	...	-3.87 ± 0.39
53945	-3.60 ± 0.50	...	-3.40 ± 0.20	-3.00 ± 0.40	-3.00 ± 0.50	-3.32 ± 0.16
75981	-4.00 ± 0.50	...	-3.60 ± 0.20	-2.45 ± 1.50	...	-3.64 ± 0.18
5164025	-3.30 ± 0.50	...	-3.30 ± 0.20	-2.90 ± 0.60	-2.90 ± 0.50	-3.22 ± 0.17
5205350	-3.30 ± 0.50	-3.50 ± 0.50	-3.50 ± 0.20	-2.80 ± 0.50	...	-3.40 ± 0.16
5165122	-4.00 ± 0.50	...	-4.00 ± 0.30	-3.00 ± 0.70	...	-3.88 ± 0.24
165943	-4.20 ± 0.50	...	-3.80 ± 0.50	-4.00 ± 0.35
5141232	-3.60 ± 0.50	-3.80 ± 0.60	-3.60 ± 0.30	-2.60 ± 0.30	...	-3.24 ± 0.19
274052	-3.70 ± 0.50	...	-3.46 ± 0.30	-3.52 ± 0.26
5242504	-3.30 ± 0.50	-3.50 ± 0.50	-3.40 ± 0.20	-2.90 ± 0.70	...	-3.37 ± 0.17
264057	-4.00 ± 0.50	-3.30 ± 0.50	-4.30 ± 0.40	-3.94 ± 0.26
5142638	-4.00 ± 0.50	...	-3.50 ± 0.20	-3.80 ± 0.90	...	-3.58 ± 0.18
5102280	-3.80 ± 0.30	-3.50 ± 0.50	-3.50 ± 0.20	-3.00 ± 0.70	-3.60 ± 0.70	-3.56 ± 0.15
177711	-3.70 ± 0.50	-3.50 ± 0.50	-3.00 ± 0.20	...	-3.40 ± 0.70	-3.16 ± 0.17
5220684	-4.10 ± 0.30	...	-4.10 ± 0.30	-3.10 ± 0.60	...	-3.99 ± 0.20
5062474	-2.80 ± 0.50	-2.80 ± 0.50	-2.50 ± 0.30	-1.50 ± 0.50	...	-2.43 ± 0.21
5138707	-2.30 ± 0.50	-2.30 ± 0.50	-1.80 ± 0.10	-1.10 ± 0.20	-1.70 ± 0.30	-1.70 ± 0.08
5124244	-2.80 ± 0.50	-2.80 ± 0.50	-2.70 ± 0.20	-1.90 ± 0.40	-2.30 ± 0.50	-2.57 ± 0.15
5170422	-4.00 ± 0.30	-3.50 ± 0.40	-3.65 ± 0.20	...	-3.20 ± 0.40	-3.65 ± 0.14
5047695	-3.20 ± 0.30	-3.20 ± 0.30	-3.30 ± 0.40	-2.30 ± 0.10	-2.50 ± 0.50	-2.50 ± 0.09
5085696	-3.10 ± 0.20	-3.10 ± 0.50	-2.60 ± 0.10	-2.00 ± 0.50	-2.60 ± 0.10	-2.65 ± 0.07
5039935	-2.40 ± 0.50	-2.40 ± 0.50	-1.80 ± 0.20	-1.04 ± 0.40	-1.90 ± 0.50	-1.81 ± 0.15
165237	-1.90 ± 0.10	-1.70 ± 0.20	-1.40 ± 0.10	-1.40 ± 0.50	-1.00 ± 0.50	-1.64 ± 0.07
5242616	-4.40 ± 0.30	-3.50 ± 0.50	-4.10 ± 0.50	-4.15 ± 0.23
5034421	-4.60 ± 0.50	...	-4.60 ± 0.50	-4.60 ± 0.35
177238	-4.90 ± 0.40	...	-4.37 ± 0.60	-4.74 ± 0.33
154681	-4.60 ± 0.10	-4.60 ± 0.10
281063	-4.50 ± 0.00	-4.50 ± 0.00
177614	-4.50 ± 0.00	-4.50 ± 0.00

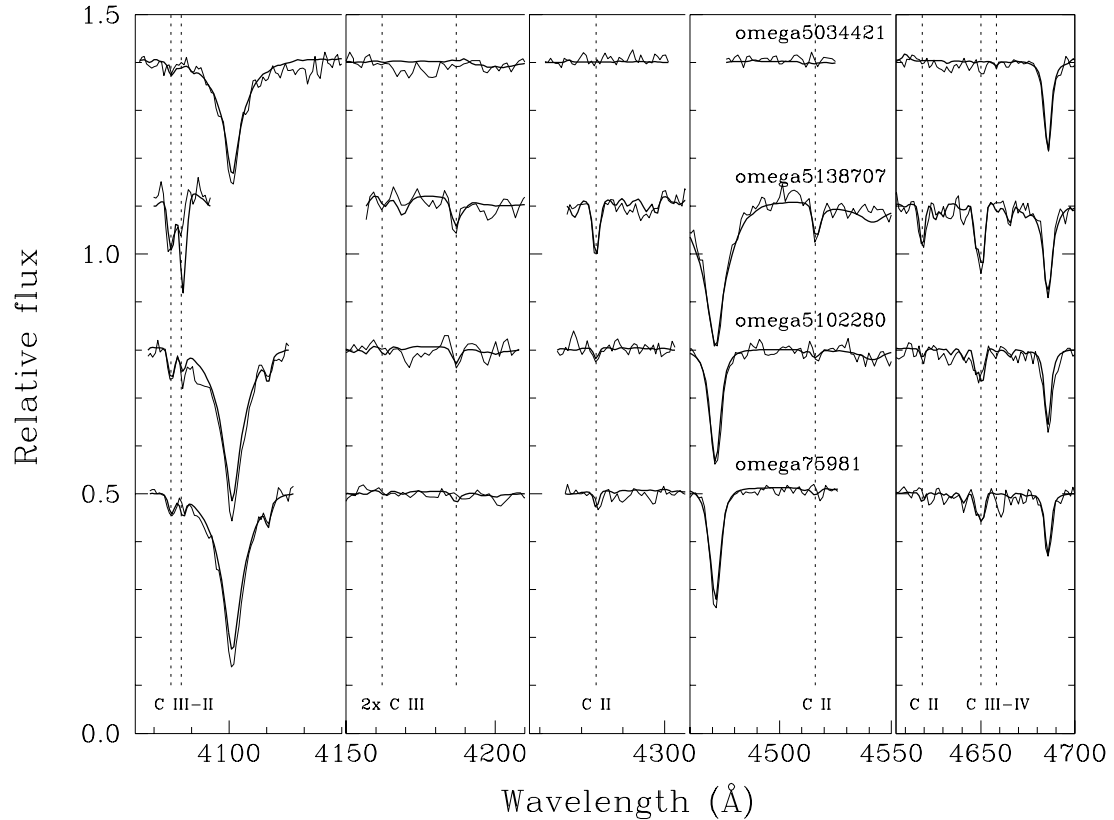


FIGURE 5.10 – Results of our fitting procedure for five regions containing carbon lines for the four stars presented in Fig. 5.3. The abundance of carbon in the model is the one listed in Table 5.2 for the respective region, and if the region was not fitted, the mean abundance was used in the model.

competing mechanisms that might be at work are stellar winds or internal turbulence. The very fact that the correlation between the C and He abundances is positive and, moreover, that the slope (1.36) is larger than 1 in a log-log C vs He abundance plot (see again Fig. 5.11) is a strong indication that chemical separation is going on in these stars, albeit slowed down by a competing agent, with carbon sinking faster than helium as can be expected⁵. Whatever

⁵Radiative levitation is not a dominant factor in these processes since it can only maintain a subsolar amount of carbon in the atmosphere of a typical $g = 5.8$, $T_{\text{eff}} = 38,000$ K hot subdwarf star.

the exact formation mechanism responsible for the very existence of He-rich subdwarfs in ω Cen, only propositions accounting for the correlation observed in Figure 5.11 can be accepted.

5.4.3 Spectroscopic masses

Given the fundamental data available in Table 5.1, we thought it worthwhile to attempt deriving a mass distribution that would characterize our sample of stars. In view of the expected large uncertainty associated with each individual determination, this was done more with a statistical point of view in mind. At the outset, we disposed of Hubble Telescope Advanced Camera for Surveys (ACS) or 2.2 m MPG/ESO telescope Wide Field Imager (WFI) photometry giving apparent B magnitudes for all of the 38 stars in our sample. Using the

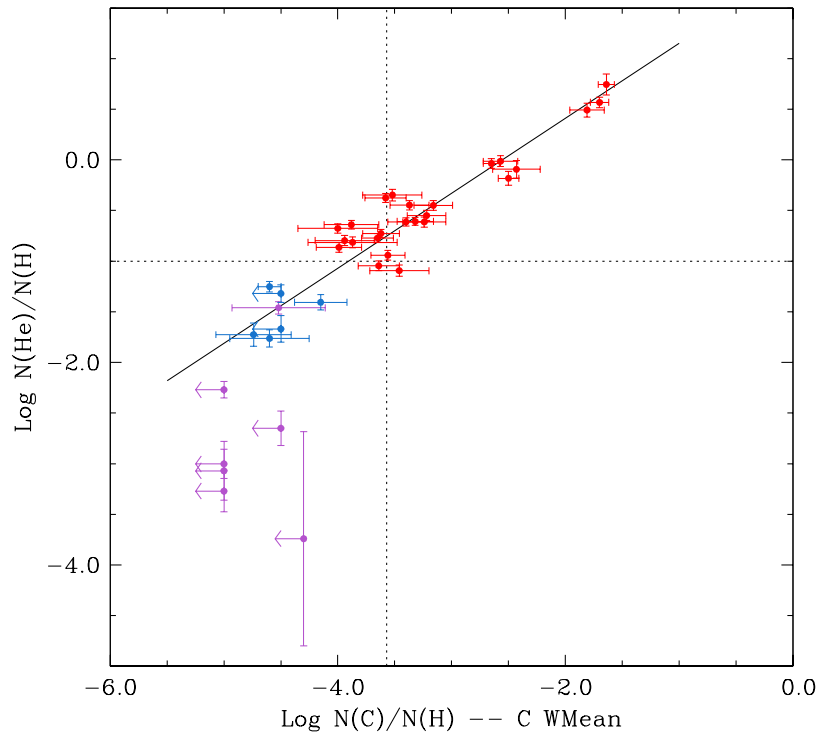


FIGURE 5.11 – Helium abundance versus the mean carbon abundance, still using the same color coding as in Fig. 5.8. Upper limits on the carbon abundance deduced in eight stars are indicated by arrows instead of errorbars. This diagram shows an obvious relation between the abundances of the two elements, which is illustrated by the linear regression (black solid line) made with the 30 stars for which a carbon abundance was obtained. Dotted lines indicate the solar helium and carbon abundances.

distance modulus of ω Cen derived in Calamida et al. (2005) and Bono et al. (2008), $B - M_B = 13.70$, a reddening index of $E(B - V) = 0.11$ from Calamida et al. (2005), and a standard Seaton relation, $A_V = 3.20E(B - V)$, we first computed the absolute magnitude M_B of each target object. The results are reported in the fifth column of Table 5.1.

In a second step, we calculated the theoretical value of M_B from a synthetic spectrum characterizing each entry in Table 5.1, assuming a given mass (hence a radius, given the surface gravity). This was repeated for several values of the mass, and parabolic interpolation was then used to infer the mass of the model with a theoretical absolute B magnitude that would match the observed value. In this way, we derived the mass estimates listed in the last column of Table 5.1.

It is immediately apparent that there is something wrong here, with several mass estimates that are way too low to be reconciled with the idea that most of our hot subdwarfs are helium core or post-helium core burning stars. While the six hottest stars in our sample, the hot H-rich sdO's, show a reasonable mean mass of $0.456 M_\odot$, the rest of the sample, taken as a whole, shows an unacceptably low mean mass value of $0.329 M_\odot$, below the minimum mass for helium burning. Interestingly, this problem with spectroscopically-inferred masses for HB and EHB stars in ω Cen has been encountered and discussed at some length in Moni Bidin et al. (2011). The problem seems to affect only that cluster in particular, hence we suspect that the photometric parameters of the system might be at fault.

In this spirit, we redid the exercise, using photometric parameters that would push in the “correct” direction. Specifically, we used a new distance modulus of $B - M_B = 13.88$ (from the estimate of 13.75 ± 0.13 mentioned in Moni Bidin et al. 2011), and a new value of the reddening index $E(B - V) = 0.13$ (from the estimate of 0.12 ± 0.01 again given in Moni Bidin et al. 2011). In this way, we obtained a new mass distribution for the subsample of the first 32 stars listed in Table 5.1. This mass distribution is shown by the solid curve in Figure 5.12 and is the result of simply adding together individual gaussians defined by an individual value of the mass and its uncertainty (with the underlying minimal assumption that these uncertainties behave as normal errors). Each gaussian has been normalized such that its surface area is the same for each star, thus ensuring the same weight in the addition procedure. The mass

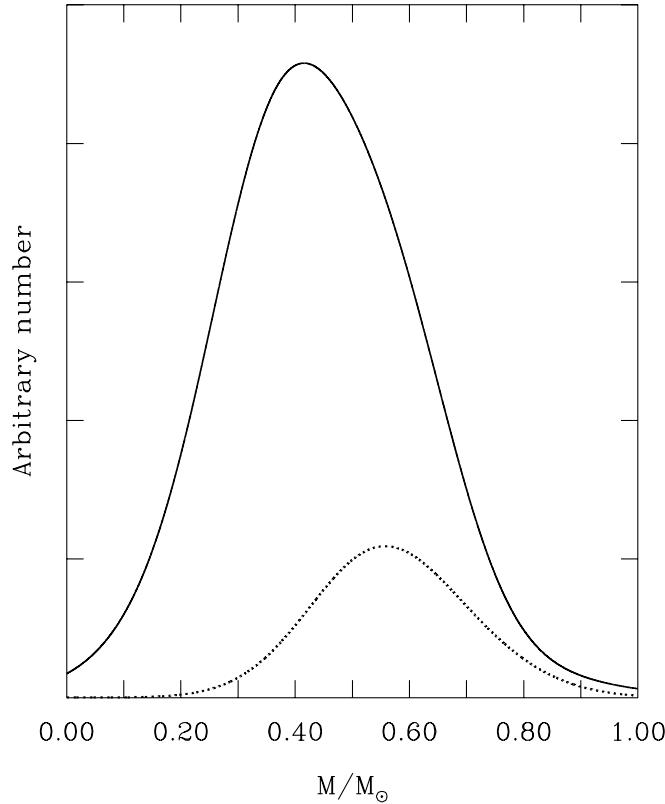


FIGURE 5.12 – Mass distribution of the 32 coolest objects in our sample (solid curve) and equivalent for the subsample of the 6 hottest stars (dotted curve) showing a systematic difference. In both cases, the photometric parameters of the ω Cen cluster have been chosen as extreme values.

distribution represented by the solid curve is characterized by a mean value of $0.441 M_{\odot}$, a median value of $0.437 M_{\odot}$, and a range of values from 0.272 to $0.614 M_{\odot}$ containing 68.3% of the stars in the sample. Given the large uncertainties (reflected by a rather large width in the distribution), we now find that the results are coherent with the idea that the targets are hot subdwarf stars indeed.

Repeating the procedure with Group 3 stars treated as a whole, (the 6 hottest stars in our sample), we find the distribution illustrated by the dotted curve in Figure 5.12. This distribution is formally characterized by a mean value of $0.572 M_{\odot}$, a median value of $0.568 M_{\odot}$, and a range of values from 0.434 to $0.710 M_{\odot}$ containing 68.3% of the stars in the sample. While these numbers are still formally acceptable, they are uncomfortably high, especially if one believes that these hot sdO stars are post-EHB objects and, therefore, should have a similar mean mass as the EHB stars themselves. We now suspect that our estimates of T_{eff} on the basis of optical spectroscopy alone become increasingly unreliable for temperatures

above $\sim 40,000$ K when using models of the kind we employed in this study (Latour et al., in preparation). For instance, $60,000$ K ($80,000$ K) hot subdwarfs may have their effective temperatures underestimated by as much as $10,000$ K ($20,000$ K). Redoing again the exercise with all of the temperatures increased by $10,000$ K leads to a new mass distribution that is now compatible with the solid curve in Figure 5.12. We thus suggest that the mass difference between the two subsamples is not intrinsic, but may be best explained by the temperature scale problem alluded to just above.

5.5 Discussion

The underlying explanations of the different characteristics and properties of the stars in our sample are likely to be found in their formation scenario. So the natural question arising here is: how were these stars formed? As mentioned in the introductory section, this question is unfortunately not a simple one. The evolutionary status of the helium-poor stars in our sample (Group 1 and 3) is somehow the easier to pin down; their characteristics are consistent with them being typical EHB stars (Group 1) and hotter evolved post-EHB stars (Group 3). Let us remember that canonical evolution identifies them as being the progeny of red giant stars that undergo a very important mass loss before their helium flash, leaving behind an helium core burning star almost stripped of all its hydrogen envelope.

A complication appears with the helium-enriched stars, whose existence cannot be explained by canonical evolution. The favorite scenario to explain their presence, as blue hook stars in globular clusters and as He-sdO (and He-sdB) in the field, is the hot helium flash. As mentioned above, in a typical hot flasher event, deep mixing occurs between the helium burning core and the hydrogen-rich envelope, thus consuming most of the hydrogen and leaving behind an atmosphere composed of approximately 96% helium by mass but also enriched in carbon, around 3 to 4% by mass (Brown et al. 2001; Cassisi et al. 2003). Among the stars we analyzed, only the three most helium-rich ones have a mass fraction of helium higher than 90%, but with at most a mass fraction of carbon of 1.5%. These three stars could possibly fit within the framework of a late flash event, but the bulk of our Group 2 stars, with their substantially lower abundance of helium, does not fit very well. An “intermediate” type of flash

mixing was proposed and studied by Lanz et al. (2004) and Miller Bertolami et al. (2008), which they called shallow mixing (compared to the deep mixing case). The mixing between the inner and outer part of the star is not as complete during a shallow mixing event; only the outer part of the core is being mixed with the envelope. The temperatures in the outer regions of the core are not hot enough to sustain the burning of hydrogen, so this element is only diluted among the helium and carbon-rich material dredged up from the core. The amount of remaining hydrogen in the envelope is thus higher in a shallow mixing case. The predicted amount of hydrogen left in the atmosphere by this mechanism varies from 50% to less than 10%, depending on the parameters of the evolutionary sequence, while the amount of carbon is between 4% and 1% (Lanz et al. 2004; Miller Bertolami et al. 2008).

If we compare these predictions with our abundances, we find that the shallow mixing mechanism could possibly explain the hydrogen-to-helium ratio, though the amount of carbon we have, less than 1%, is significantly less than what is predicted. The drawback with this idea, that the bulk of our Group 2 stars could be the result of a hot flash with shallow mixing, is that this scenario is not the usual outcome of a hot flasher event, but happens only for a small range of model parameters. This, combined with the fact that this phenomenon is more likely to occur in metal-rich stars (like those in the field), casts serious doubts on the possibility that this mechanism could have produced the majority of our helium-rich stars. Miller Bertolami et al. (2008) explored the possibility that diffusion in the atmosphere might be important while the star is settling down on the EHB, after its helium flash. They concluded that in the absence of stellar winds a helium-rich subdwarf could turn into a helium-deficient one before it settles onto the EHB. But remembering that the “post hot flasher” stars reach the EHB while contracting, thus their surface gravity increases with time, it would be difficult to explain the fact that our most helium-enriched stars are also among the most compact of our Group 2 objects (see Fig. 5.5). The relation found between the carbon abundance and the helium one (Figure 5.11), which is also observed in the field stars (Németh et al. 2012), might be a consequence of the delayed helium flash. Since a late hot flasher star experiences deep mixing that brings to the surface helium and carbon, maybe that depending on how deep the convection zone (thus the mixing) reaches into the helium core, more or less helium

and carbon will be brought to the surface. Alternatively, and this is our preferred view, this relation could also be interpreted as the signature of diffusion effects, with carbon sinking faster than helium in an increasingly hydrogen-enriched atmosphere. Hence, it would seem that the He-rich star puzzle is far from being deciphered.

Another fact that retains our attention and that we found worth discussing is the difference in temperature at which the helium-rich subdwarfs are found in the field versus those found in globular clusters. As shown in Figure 5.6, the majority of the helium-rich stars in ω Cen is found between 35,000 K and 40,000 K, while the field ones bunch together mainly between 40,000 K and 50,000 K according to Figure 5.7. This latter result is moreover supported by Stroeer et al. (2007) and Németh et al. (2012) who found the same temperature range for the field He-sdO stars included in their studies, whereas Moehler et al. (2004; 2011) found their globular clusters analogs to be definitely cooler in ω Cen and NGC 2808. With all those studies converging toward the same result, the temperature difference cannot be an artefact due to the analysis method or the observations used. It must be regarded, in fact, as a sound result. This temperature offset rather suggests a more fundamental difference in the formation process. In this regard, the first possibility that comes to mind is a difference due to the metallicity of the population: while the majority of the EHB stars in ω Cen comes from metal-poor progenitors, most of the field population has a higher metallicity. The effect of the metallicity on the effective temperature at which the stars reach the EHB has not been discussed in a lot of work⁶; for globular clusters is it more convenient to study the evolutionary tracks in a color-magnitude diagram. Still, the study of Miller Bertolami et al. (2008), being more centered on the field subdwarfs, shows some evolutionary tracks for models having different metallicity in a $\log g - T_{\text{eff}}$ diagram. Finding a difference in the temperature at which these tracks are found while descending on the EHB is not very obvious and moreover the path of the tracks also depends on the mass of the star. Therefore, we cannot really draw firm conclusions on this point.

In this last section, we tentatively tried to address some outstanding issues coming out of our study using available information that could be found in literature. If the general idea of

⁶Note that our own estimates of the $0.47 M_{\odot}$ EHB's in Figure 5.6 and Figure 5.7 suggest that decreasing the metallicity from $Z = 0.02$ to zero leads only to a modest blue shift in temperature.

how the stars of our sample can exist, with the principal characteristics they have, could be drawn, many important details still remains unexplained, in spite of the important amount of work done on the subject in the last decade. In conclusion, our spectroscopic analysis of ω Cen EHB stars has led to three main results, each one raising its own issue.

1. Most of the helium-rich stars have a helium abundance lower than 80% by mass, which is less than what is predicted by theoretical hot-flasher models. Why do these stars still have such a relatively large amount of hydrogen?
2. A majority of helium-rich stars in ω Cen clusters between 35,000 K and 40,000 K while the helium-rich sdO stars in the field are found between 40,000 K and 50,000 K. Why are the temperatures of ω Cen helium-rich stars significantly lower than their field counterparts?
3. The carbon abundance in the stars analyzed is well correlated with the helium abundance. What is the origin and exact nature of this relationship?

This work was supported in part by the NSERC Canada through a doctoral fellowship awarded to Marilyn Latour and through a research grant awarded to Gilles Fontaine. The latter also acknowledges the contribution of the Canada Research Chair Program.

5.6 References

- Ahmad, A. & Jeffery, C. S. 2003, *A&A*, 402, 335
- Anderson, J. 1997, PhD thesis, University of California at Berkeley
- Bedin, L. R., Piotto, G., Anderson, J., Cassisi, S., King, I. R., Momany, Y., & Carraro, G. 2004, *ApJ*, 605, L125
- Bono, G., Stetson, P. B., Sanna, N., Piersimoni, A., Freyhammer, L. M., Bouzid, Y., Buonanno, R., Calamida, A., Caputo, F., Corsi, C. E., Di Cecco, A., Dall’Ora, M., Ferraro, I., Iannicola, G., Monelli, M., Nonino, M., Pulone, L., Sterken, C., Storm, J., Tuvikene, T., & Walker, A. R. 2008, *ApJ*, 686, L87
- Brown, T. M., Landsman, W. B., Randall, S. K., Sweigart, A. V., & Lanz, T. 2013, *ApJ*, 777, L22
- Brown, T. M., Sweigart, A. V., Lanz, T., Landsman, W. B., & Hubeny, I. 2001, *ApJ*, 562, 368
- Brown, T. M., Sweigart, A. V., Lanz, T., Smith, E., Landsman, W. B., & Hubeny, I. 2010, *ApJ*, 718, 1332
- Busso, G., Cassisi, S., Piotto, G., Castellani, M., Romaniello, M., Catelan, M., Djorgovski, S. G., Recio Blanco, A., Renzini, A., Rich, M. R., Sweigart, A. V., & Zoccali, M. 2007, *A&A*, 474, 105
- Calamida, A., Stetson, P. B., Bono, G., Freyhammer, L. M., Grundahl, F., Hilker, M., Andersen, M. I., Buonanno, R., Cassisi, S., Corsi, C. E., Dall’Ora, M., Del Principe, M., Ferraro, I., Monelli, M., Munteanu, A., Nonino, M., Piersimoni, A. M., Pietrinferni, A., Pulone, L., & Richtler, T. 2005, *ApJ*, 634, L69
- Cassisi, S., Schlattl, H., Salaris, M., & Weiss, A. 2003, *ApJ*, 582, L43
- Castellani, M. & Castellani, V. 1993, *ApJ*, 407, 649
- Castellani, V., Calamida, A., Bono, G., Stetson, P. B., Freyhammer, L. M., Degl’Innocenti, S., Moroni, P. P., Monelli, M., Corsi, C. E., Nonino, M., Buonanno, R., Caputo, F., Castellani, M., Dall’Ora, M., Del Principe, M., Ferraro, I., Iannicola, G., Piersimoni, A. M., Pulone, L., & Vuerli, C. 2007, *ApJ*, 663, 1021

- D'Antona, F., Bellazzini, M., Caloi, V., Pecci, F. F., Galleti, S., & Rood, R. T. 2005, *ApJ*, 631, 868
- D'Antona, F., Caloi, V., Montalbán, J., Ventura, P., & Gratton, R. 2002, *A&A*, 395, 69
- D'Cruz, N. L., Dorman, B., Rood, R. T., & O'Connell, R. W. 1996, *ApJ*, 466, 359
- D'Cruz, N. L., O'Connell, R. W., Rood, R. T., Whitney, J. H., Dorman, B., Landsman, W. B., Hill, R. S., Stecher, T. P., & Bohlin, R. C. 2000, *ApJ*, 530, 352
- Dorman, B., Rood, R. T., & O'Connell, R. W. 1993, *ApJ*, 419, 596
- Dreizler, S. 1993, *A&A*, 273, 212
- Fontaine, G., Brassard, P., Charpinet, S., Green, E. M., Randall, S. K., & Van Grootel, V. 2012, *A&A*, 539, A12
- Fontaine, G. & Chayer, P. 1997, in *The Third Conference on Faint Blue Stars*, ed. A. G. D. Philip, J. Liebert, R. Saffer, & D. S. Hayes, 169
- Fontaine, G., Green, E. M., Brassard, P., Latour, M., & Chayer, P. 2014, in *Astronomical Society of the Pacific Conference Series*, Vol. 481, 6th Meeting on Hot Subdwarf Stars and Related Objects, ed. V. Van Grootel, E. M. Green, G. Fontaine, & S. Charpinet, 83
- Green, E. M., Fontaine, G., Hyde, E. A., For, B.-Q., & Chayer, P. 2008, in *Astronomical Society of the Pacific Conference Series*, Vol. 392, Hot Subdwarf Stars and Related Objects, ed. U. Heber, C. S. Jeffery, & R. Napiwotzki, 75
- Haas, S., Dreizler, S., Heber, U., Jeffery, S., & Werner, K. 1996, *A&A*, 311, 669
- Heber, U. 2009, *ARA&A*, 47, 211
- Hu, H., Tout, C. A., Glebbeek, E., & Dupret, M.-A. 2011, *ArXiv e-prints*
- Johnson, C. B., Green, E. M., Wallace, S., O'Malley, C. J., Amaya, H., Biddle, L., & Fontaine, G. 2013, *ArXiv e-prints*
- Kilkenny, D., Koen, C., O'Donoghue, D., & Stobie, R. S. 1997, *MNRAS*, 285, 640
- Lanz, T., Brown, T. M., Sweigart, A. V., Hubeny, I., & Landsman, W. B. 2004, *ApJ*, 602, 342
- Lanz, T. & Hubeny, I. 2003, *ApJS*, 146, 417

- . 2007, *ApJS*, 169, 83
- Latour, M., Fontaine, G., Brassard, P., Green, E. M., Chayer, P., & Randall, S. K. 2011, *ApJ*, 733, 100
- Miller Bertolami, M. M., Althaus, L. G., Unglaub, K., & Weiss, A. 2008, *A&A*, 491, 253
- Moehler, S., Dreizler, S., Lanz, T., Bono, G., Sweigart, A. V., Calamida, A., Monelli, M., & Nonino, M. 2007, *A&A*, 475, L5
- Moehler, S., Dreizler, S., Lanz, T., Bono, G., Sweigart, A. V., Calamida, A., & Nonino, M. 2011, *A&A*, 526, A136
- Moehler, S., Sweigart, A. V., Landsman, W. B., & Dreizler, S. 2002, *A&A*, 395, 37
- Moehler, S., Sweigart, A. V., Landsman, W. B., Hammer, N. J., & Dreizler, S. 2004, *A&A*, 415, 313
- Moni Bidin, C., Villanova, S., Piotto, G., Moehler, S., Cassisi, S., & Momany, Y. 2012, *A&A*, 547, A109
- Moni Bidin, C., Villanova, S., Piotto, G., Moehler, S., & D'Antona, F. 2011, *ApJ*, 738, L10
- Németh, P., Kawka, A., & Vennes, S. 2012, *MNRAS*, 427, 2180
- Piotto, G., Villanova, S., Bedin, L. R., Gratton, R., Cassisi, S., Momany, Y., Recio-Blanco, A., Lucatello, S., Anderson, J., King, I. R., Pietrinferni, A., & Carraro, G. 2005, *ApJ*, 621, 777
- Randall, S. K., Calamida, A., & Bono, G. 2009, *A&A*, 494, 1053
- Randall, S. K., Calamida, A., Fontaine, G., Bono, G., & Brassard, P. 2011, *ApJ*, 737, L27
- Randall, S. K., Calamida, A., Fontaine, G., Green, E. M., Monelli, M., Alonso, M. L., Catelan, M., Bono, G., Dhillon, V. S., & Marsh, T. R. 2013, in *European Physical Journal Web of Conferences*, Vol. 43, *European Physical Journal Web of Conferences*, 4006
- Randall, S. K., Fontaine, G., Calamida, A., Brassard, P., Chayer, P., Alonso, M. L., Catelan, M., Bono, G., Green, E. M., Dhillon, V. S., & Marsh, T. R. 2012, in *Astronomical Society of the Pacific Conference Series*, Vol. 452, *Fifth Meeting on Hot Subdwarf Stars and Related Objects*, ed. D. Kilkeny, C. S. Jeffery, & C. Koen, 241

Saffer, R. A., Bergeron, P., Koester, D., & Liebert, J. 1994, ApJ, 432, 351

Saio, H. & Jeffery, C. S. 2000, MNRAS, 313, 671

Stroeer, A., Heber, U., Lisker, T., Napiwotzki, R., Dreizler, S., Christlieb, N., & Reimers, D.
2007, A&A, 462, 269

Unglaub, K. 2008, A&A, 486, 923

Chapitre 6

Conclusion

6.1 BD+28°4211 et le problème des raies de Balmer

Notre projet d'analyse de BD+28°4211 s'est bâti autour de l'idée lancée par Werner (1996) que l'ajout de métaux dans les modèles d'atmosphères HETL peut résoudre le problème des raies de Balmer, permettant alors de reproduire correctement le spectre visible d'étoiles très chaudes. Nous avons toutefois vite constaté qu'un ajustement de paramètres sur les raies visibles de BD+28°4211 n'était pas possible, même avec nos modèles HETL incluant des métaux en abondance solaire. Étant donné son statut d'étoile standard et sa brillance plutôt élevée, BD+28°4211 a été amplement observée dans l'UV par le satellite *FUSE* ainsi qu'avec le spectrographe *STIS* à bord du télescope spatial Hubble. Les données obtenues par ces deux instruments sont d'une qualité exceptionnelle et n'avaient pas été exploitées dans le but de modéliser l'atmosphère de l'étoile. C'est pourquoi elle nous est apparue comme une candidate parfaite pour s'attaquer au problème des raies de Balmer.

Nous avons donc décidé dans un premier temps de faire une analyse auto-cohérente des spectres UV afin de détailler la composition chimique de l'atmosphère de l'étoile. Notre méthodologie a été cohérente au sens où les abondances des éléments métalliques analysés étaient inclus directement dans les modèles d'atmosphères lors des procédures d'ajustement. De cette façon, nous avons déterminé les abondances de onze éléments métalliques différents présents dans l'atmosphère de l'étoile. L'équilibre d'ionisation de ces éléments (comme le fer) nous a

aussi permis de bien contraindre sa température effective ($T_{\text{eff}} = 82\,000\text{ K} \pm 5000\text{ K}$) confirmant ainsi les résultats obtenus dans le passé (Napiwotzki 1993; Dreizler & Werner 1993). Les raies métalliques examinées étaient moins sensibles à la gravité de surface qu'à la température. Celle-ci n'a donc pu être contrainte très précisément mais la valeur de $\log g$ attribuée dans le passé à l'étoile, de 6.2 dex, nous a semblé très raisonnable. BD+28°4211 est une étoile relativement proche de nous et sa parallaxe, évaluée par *Hipparcos*, la place entre 81 et 106 pc (van Leeuwen 2007). Grâce aux mesures précises de la magnitude de l'étoile (Landolt & Uomoto 2007), il a été possible d'estimer la distance spectroscopique de celle-ci, pour différentes combinaisons de masses et gravités de surface. Les résultats de cet exercice ont montré que pour un $\log g = 6.2$, une masse significativement plus faible que la valeur canonique ($0.45 M_{\odot}$) est nécessaire pour faire concorder la distance mesurée et la distance spectroscopique. Pour obtenir un accord impliquant une masse canonique, la gravité de surface de l'étoile doit être plus élevée ($\log g \gtrsim 6.4$ dex).

Ayant obtenus ces résultats à l'aide des données UV, nous avons pu passer à la seconde étape de notre projet, soit l'analyse du spectre optique de BD+28°4211. Notre objectif était d'arriver à reproduire correctement celui-ci, qui, rappelons-le, présente un fort problème des raies de Balmer, de façon à pouvoir obtenir les paramètres atmosphériques de l'étoile et une bonne reproduction de son spectre optique lors d'un ajustement simultané des raies de Balmer et d'hélium. Tout ceci dans le but de trouver une façon de déterminer avec une meilleure précision les paramètres atmosphériques d'étoiles chaudes en général (sous-naines et naines blanches) en utilisant uniquement des données optiques. Généralement, des spectres UV sont essentiels pour s'assurer de la température effective de telles étoiles, ce qui s'avère assez contraignant puisque ce type d'observations, effectuées de l'espace, sont beaucoup plus difficiles à obtenir que des observations visibles faites au sol. Nous avons confirmé nos résultats préliminaires montrant que le spectre de BD+28°4211 ne peut être reproduit par nos modèles d'atmosphères incluant les huit éléments les plus présents dans l'atmosphère de l'étoile (outre l'hydrogène et l'hélium) à leur abondance mesurée. De plus, les résultats d'une procédure d'ajustement avec ces modèles donnent une température trop faible par environ 10 000 K. Ce qui nous a finalement permis de reproduire correctement le spectre de l'étoile, tout en obtenant

les bons paramètres lors d'un ajustement, a été d'augmenter l'abondance des métaux dans nos modèles à des valeurs dix fois solaires. De cette façon nous avons obtenu des températures près de 82 000 K mais une gravité de surface aux alentours de 6.5 dex en ajustant nos différents spectres observés. Ceci n'est pas totalement sans précédent et quelques études ont montré par le passé que des modèles ETL enrichis en métaux permettent de mieux reproduire les spectres de certaines étoiles dans le régime sdOB (O'Toole & Heber 2006; Geier et al. 2007). Nous avons exploité les données d'archives du KOA dans lesquelles nous avons trouvé d'excellents spectres à haute résolution ($\Delta\lambda \sim 0.1 \text{ \AA}$) de BD+28°4211. Avec ces observations nous avons pu voir en détail comment les raies spectrales obtenues avec nos modèles enrichis en métaux se comparent aux raies observées. Ces comparaisons, effectuées pour les raies suivantes: He II $\lambda\lambda 4686, 5412$, H β , H α and H γ montrent un très bon accord entre les observations et nos modèles. Nous avons aussi pu remarquer que la plupart de ces raies sont très peu sensibles à des variations de gravité de surface entre 6.2 et 6.6 dex. Nous avons donc décidé de réviser à la hausse la valeur du $\log g$ de l'étoile pour 6.5 dex, conséquemment aux résultats de nos procédures d'ajustements, tout en considérant qu'une telle valeur de $\log g$ permet d'accorder la distance spectroscopique avec celle observée de BD+28°4211 en assumant une masse de $0.45 M_{\odot}$.

Nous proposons donc comme solution, pour permettre l'obtention de paramètres atmosphériques plus fiables et une meilleure reproduction des raies observées, d'utiliser des modèles d'atmosphères (HETL) enrichis en métaux pour l'analyse des spectres optiques d'étoiles chaudes (sdO et naines blanches). L'analyse de spectres UV est bien sûr une solution optimale mais dans les nombreux cas où de telles données ne sont pas disponibles, notre méthode devrait s'avérer une bonne alternative. Dans le cas de BD+28°4211 une abondance dix fois solaire nous a donné d'excellent résultats mais il pourrait en être différent pour des étoiles ayant des températures plus faibles. Puisque le problème des raies de Balmer est aussi présent dans des étoiles plus froides que BD+28°4211 (40 000 - 60 000 K), il serait utile de refaire des analyses similaires pour des sdO plus froides.

6.2 Feige 48, sdB pulsante

Le Chapitre 4, portant sur Feige 48, s'inscrit dans une série de travaux qui viseront ultimement à faire une étude astérosismologique complète de l'étoile. Une campagne d'observations photométriques a été en cours durant plusieurs mois, permettant de collecter des données exceptionnelles; une quinzaine de modes g et une trentaine de modes p ont été détectés dans l'étoile (Fontaine et al. 2013). Il s'agit là de données précieuses qui permettront de raffiner le modèle sismique optimal de l'étoile, qui jusqu'à présent a été obtenu en utilisant uniquement 4 modes de pulsations (Van Grootel et al. 2008; Charpinet et al. 2005). De plus, les modes g détectés devraient permettre de sonder les paramètres structuraux du coeur de l'étoile. Notre travail sur cette étoile a été de s'assurer d'une détermination la plus précise possible de ses paramètres fondamentaux, T_{eff} , $\log g$ et $\log N(\text{He})/N(\text{H})$, dont les deux premiers sont des paramètres importants d'un modèle sismique. Puisque les solutions sismiques sont souvent dégénérées (plusieurs combinaisons de paramètres peuvent reproduire les périodes observées, voir Van Grootel et al. 2008 pour le cas de Feige 48), ce sont les paramètres obtenus par la spectroscopie qui permettent de trancher entre les différentes possibilités.

Pour faire l'analyse de cette étoile particulière, nous avons construit une grille de modèles d'atmosphères HETL en y incluant les huit espèces atomiques (autres que l'hydrogène et l'hélium) les plus abondantes dans l'atmosphère de l'étoile. Pour ce faire nous avons mis ensemble les résultats de quatre analyses d'abondances effectuées par le passé. Nous avons ainsi pu inclure dans nos modèles les abondances moyennes des éléments dominants dans l'atmosphère de Feige 48. Les paramètres atmosphériques obtenus à l'aide de cette grille de modèles permettent une excellente reproduction des raies de Balmer et d'hélium I présentes dans nos différents spectres observés. Ces paramètres sont en accord avec ceux obtenus lors d'études précédentes, basées sur des modèles d'atmosphères différents. Ceci assure, de un, que les paramètres de l'étoile sont bien cernés, de deux, que ces valeurs dépendent peu du type de modèles utilisés. Nous avons vérifié les effets qu'ont les métaux dans nos modèles HETL en comparant les modèles d'une grille sans métaux avec ceux de notre grille ayant une métallicité représentative de celle de Feige 48. Effectivement les changements perceptibles sur les raies de Balmer et d'hélium utilisées lors d'une procédure d'ajustement sont très faibles dans un

modèle ayant les paramètres de Feige 48, mais deviennent plus importants à des températures effectives plus élevées. Puisque nous avons à notre disposition des spectres observés de bonne qualité (haut rapport signal-sur-bruit) ayant différentes résolutions et couvertures en longueurs d'onde, nous avons porté attention aux effets systématiques que pourraient avoir ces caractéristiques observationnelles sur les paramètres déterminés. Ce qui a surtout retenu notre attention sont les valeurs systématiquement plus élevées de températures effectives obtenues avec notre spectre ayant la résolution la plus basse (8,7 Å). Cette différence n'est pas énorme (~ 500 K) mais demeure présente même lorsque l'intervalle de longueur d'onde utilisé lors de la procédure d'ajustement est changé (donc les différentes raies comparées). Étant donné l'excellente qualité de notre spectre à 1.0 Å de résolution, de nombreuses raies métalliques y sont bien définies (même si elles sont faibles) et en ajustant légèrement les abondances initialement incluses dans notre grille de modèle, nous arrivons à très bien reproduire les raies présentes dans les observations.

6.3 Les sous-naines chaudes de ω Centauri et le puzzle des étoiles riches en hélium

L'idée de mesurer les abondances de carbone dans les étoiles EHB de ω Centauri est arrivée de façon quelque peu fortuite. Les spectres de ces étoiles ont été obtenus dans le but de caractériser observationnellement la zone d'instabilité des sous-naines pulsantes de l'amas. C'est-à-dire déterminer la ou les régions, dans le diagramme $\log g - T_{\text{eff}}$, où se trouvent les étoiles pulsantes ainsi que les endroits où les étoiles sont constantes. Les résultats préliminaires de cette étude ont été présentés dans Randall et al. (2012) et une version plus complète, incluant les étoiles de notre échantillon, est en préparation (Randall et al.). Lors d'une première analyse spectroscopique des étoiles de ω Cen, nous avons remarqué que les raies de carbone présentes dans les spectres étaient relativement fortes dans les étoiles ayant beaucoup d'hélium et plus faibles dans les étoiles contenant moins d'hélium. La présence de raies de carbone dans les étoiles riches en hélium n'est pas suprenante en soi, étant donné les résultats de Stroeger et al. (2007), qui ont observé du carbone dans la majorité des sdO riches en hélium de leur

échantillon. C'est plutôt la corrélation apparente entre la force des raies de carbone et d'hélium qui nous a poussé à en faire une analyse plus approfondie.

La première étape de notre analyse était de déterminer les paramètres fondamentaux ($\log g$, T_{eff} et $\log N(\text{He})/N(\text{H})$) des étoiles. Pour ce faire, nous avons construit une grille de modèles d'atmosphères incluant du C, N, O en quantité solaire. Les étoiles de ω Cen couvrent une région assez vaste dans l'espace des paramètres et une grille comprenant 1428 modèles a été nécessaire pour couvrir cette région, cette grille a nécessité un temps de calcul considérable, même en utilisant les 320 processeurs de CALYS. L'inclusion de fer dans nos modèles aurait facilement triplé le temps de calcul sans ajouter d'effets importants, c'est pourquoi nous nous en sommes tenus aux C, N, O. Une fois les paramètres des 38 étoiles déterminés, ceux-ci ont été utilisés pour construire 38 séries de six ou sept modèles (une série pour chaque étoile) incluant différentes abondances de carbone. Ces modèles ont été utilisés afin de déterminer l'abondance de carbone pour chaque étoile. C'est alors que nous avons confirmé la forte corrélation positive entre les abondances de carbone et d'hélium dans les étoiles de notre échantillon (principalement celles riches en hélium, qui constituent près du 2/3 de l'échantillon). C'est la première fois qu'une telle relation est observée dans les sous-naines d'un amas globulaire. Une relation similaire, bien que montrant plus de dispersion dans les abondances, a récemment été notée par Németh et al. (2012) dans son échantillon de sous-naines du champ. Cette relation a forcément à voir avec les processus de diffusion (turbulence, faible vent stellaire, tri gravitationnel) à l'oeuvre dans l'atmosphère de l'étoile et pourrait permettre de contraindre les paramètres possibles d'un vent stellaire ou de la turbulence. Sans la présence d'un phénomène venant contrecarrer les effets du tri gravitationnel, le carbone et l'hélium couleraient rapidement sous l'atmosphère de l'étoile et très peu d'étoiles semblables aux étoiles riches en hélium (et enrichies en carbone pour la plupart) de notre échantillon seraient visibles ; leur atmosphère deviendrait rapidement riche en hydrogène. La position de ces étoiles dans le diagramme $\log g - T_{\text{eff}}$ est intrigante quand on considère les prédictions théoriques et l'emplacement, dans le même diagramme, des étoiles équivalentes du champ. Les étoiles riches en hélium de ω Cen se trouvent majoritairement entre 35 et 40 kK alors qu'elles sont systématiquement plus chaudes dans le champ ($T_{\text{eff}} \gtrsim 40$ kK). Le modèle de formation

expliquant l'existence de sous-naines riches en hélium est celui du flash tardif, évoqué à la Section 1.2.1. Les séquences évolutives prévoient que les étoiles ainsi formées passeront la majeure partie de leur vie (lors du brûlage d'hélium) près de la ZAHEMS (voir Figure 5.6). On devrait donc trouver une accumulation de ces étoiles dans cette région, ce qui n'est pas le cas dans ω Cen. La disposition des étoiles riches en hélium dans ω Cen, mais aussi dans le champ, demeure donc quelque peu mystérieuse, tout comme l'origine de la différence de température entre cette même population dans l'amas et dans le champ. Pour l'instant, il semble que de nouvelles études théoriques de séquences évolutives soient nécessaires pour éclaircir la situation.

Pour en revenir aux sdO pulsantes découvertes dans ω Cen, l'étude présentée dans Randall et al. (2012) n'a pas trouvé de signes d'instabilités (indiquant des pulsations) dans la région $\log g - T_{\text{eff}}$ où se trouvent les sdO pulsantes. Ceci est plutôt intrigant puisque les pulsations observées dans les sdB et la sdO pulsantes du champ sont facilement prédites par les modèles présentés dans leur article. L'une des explications possible serait que les sdO pulsantes de ω Cen sont en réalité plus chaudes que 50 000 K. Étant donné les conclusions tirées au Chapitre 3 et la distribution de masse présentée à la section 5.4.3, cette hypothèse semble très réaliste et permettrait d'expliquer la variabilité des étoiles puisque les modèles à plus de 56 000 K montrent des instabilités. Dans le but d'élucider un peu cette question, nous tenterons d'obtenir des observations UV pour trois des cinq pulsateurs de l'amas, dont l'étoile polluée qui n'a pas été incluse dans notre échantillon. Les spectres UV nous permettraient de déterminer avec plus de précision, on l'espère, la température effective des étoiles, tout en fournissant des indications supplémentaires sur les abondances métalliques de leur atmosphère.

Bibliographie

- Ahmad, A. & Jeffery, C. S. 2006, *Baltic Astronomy*, 15, 139
- Auer, L. H. & Mihalas, D. 1969, *ApJ*, 156, 681
- Baran, A. S., Kawaler, S. D., Reed, M. D., Quint, A. C., O'Toole, S. J., Østensen, R. H., Telting, J. H., Silvotti, R., Charpinet, S., Christensen-Dalsgaard, J., Still, M., Hall, J. R., & Uddin, K. 2011, *MNRAS*, 414, 2871
- Bear, E. & Soker, N. 2012, *ApJ*, 749, L14
- Brown, T. M., Ferguson, H. C., Davidsen, A. F., & Dorman, B. 1997, *ApJ*, 482, 685
- Brown, T. M., Sweigart, A. V., Lanz, T., Landsman, W. B., & Hubeny, I. 2001, *ApJ*, 562, 368
- Cassisi, S., Schlattl, H., Salaris, M., & Weiss, A. 2003, *ApJ*, 582, L43
- Castellani, M. & Castellani, V. 1993, *ApJ*, 407, 649
- Charpinet, S., Fontaine, G., Brassard, P., Billères, M., Green, E. M., & Chayer, P. 2005, *A&A*, 443, 251
- Charpinet, S., Fontaine, G., Brassard, P., & Dorman, B. 1996, *ApJ*, 471, L103
- Charpinet, S., Fontaine, G., Brassard, P., Green, E. M., Van Grootel, V., Randall, S. K., Silvotti, R., Baran, A. S., Østensen, R. H., Kawaler, S. D., & Telting, J. H. 2011, *Nature*, 480, 496
- D'Cruz, N. L., Dorman, B., Rood, R. T., & O'Connell, R. W. 1996, *ApJ*, 466, 359
- D'Cruz, N. L., O'Connell, R. W., Rood, R. T., Whitney, J. H., Dorman, B., Landsman, W. B., Hill, R. S., Stecher, T. P., & Bohlin, R. C. 2000, *ApJ*, 530, 352

- Dorman, B., Rood, R. T., & O'Connell, R. W. 1993, *ApJ*, 419, 596
- Dreizler, S. & Werner, K. 1993, *A&A*, 278, 199
- Fontaine, G., Brassard, P., Charpinet, S., Green, E. M., Randall, S. K., & Van Grootel, V. 2012, *A&A*, 539, A12
- Fontaine, G., Brassard, P., Green, E. M., Chayer, P., Charpinet, S., Andersen, M., & Portouw, J. 2008, *A&A*, 486, L39
- Fontaine, G., Green, E. M., Charpinet, S., Latour, M., Randall, S. K., Van Grootel, V., & Brassard, P. 2013, *ArXiv e-prints*
- Geier, S. & Heber, U. 2012, *A&A*, 543, A149
- Geier, S., Nesslinger, S., Heber, U., Przybilla, N., Napiwotzki, R., & Kudritzki, R.-P. 2007, *A&A*, 464, 299
- Green, E. M., Fontaine, G., Reed, M. D., Callera, K., Seitzzahl, I. R., White, B. A., Hyde, E. A., Østensen, R., Cordes, O., Brassard, P., Falter, S., Jeffery, E. J., Dreizler, S., Schuh, S. L., Giovanni, M., Edelmann, H., Rigby, J., & Bronowska, A. 2003, *ApJ*, 583, L31
- Green, E. M., Guvenen, B., O'Malley, C. J., O'Connell, C. J., Baringer, B. P., Villareal, A. S., Carleton, T. M., Fontaine, G., Brassard, P., & Charpinet, S. 2011, *ApJ*, 734, 59
- Haas, S., Dreizler, S., Heber, U., Jeffery, S., & Werner, K. 1996, *A&A*, 311, 669
- Han, Z., Podsiadlowski, P., Maxted, P. F. L., & Marsh, T. R. 2003, *MNRAS*, 341, 669
- Han, Z., Podsiadlowski, P., Maxted, P. F. L., Marsh, T. R., & Ivanova, N. 2002, *MNRAS*, 336, 449
- Heber, U. 2009, *ARA&A*, 47, 211
- Heber, U., Kudritzki, R. P., Caloi, V., Castellani, V., & Danziger, J. 1986, *A&A*, 162, 171
- Herbig, G. H. 1999, *PASP*, 111, 1144
- Hirsch, H. A., Heber, U., & O'Toole, S. J. 2008, in *Astronomical Society of the Pacific Conference Series*, Vol. 392, *Hot Subdwarf Stars and Related Objects*, ed. U. Heber, C. S. Jeffery, & R. Napiwotzki, 131
- Hubeny, I. & Lanz, T. 1992, *A&A*, 262, 501

—. 1995, *ApJ*, 439, 875

Johnson, C. B., Green, E. M., Wallace, S., O'Malley, C. J., Amaya, H., Biddle, L., & Fontaine, G. 2013, ArXiv e-prints

Kilkenny, D., Koen, C., O'Donoghue, D., & Stobie, R. S. 1997, *MNRAS*, 285, 640

Landolt, A. U. & Uomoto, A. K. 2007, *AJ*, 133, 768

Lanz, T., Brown, T. M., Sweigart, A. V., Hubeny, I., & Landsman, W. B. 2004, *ApJ*, 602, 342

Lanz, T. & Hubeny, I. 1995, *ApJ*, 439, 905

Lanz, T., Hubeny, I., & Heap, S. R. 1997, *ApJ*, 485, 843

Latour, M., Fontaine, G., Brassard, P., Green, E. M., Chayer, P., & Randall, S. K. 2011, *ApJ*, 733, 100

Liebert, J., Saffer, R. A., & Green, E. M. 1994, *AJ*, 107, 1408

Maxted, P. f. L., Heber, U., Marsh, T. R., & North, R. C. 2001, *MNRAS*, 326, 1391

Mihalas, D. 1978, *Stellar Atmospheres*, 2nd ed. (W. H. Freeman & Company)

Mihalas, D. & Auer, L. H. 1970, *ApJ*, 160, 1161

Napiwotzki, R. 1992, in *Lecture Notes in Physics*, Berlin Springer Verlag, Vol. 401, *The Atmospheres of Early-Type Stars*, ed. U. Heber & C. S. Jeffery, 310–+

Napiwotzki, R. 1993, *Acta Astronomica*, 43, 343

—. 1997, *A&A*, 322, 256

Napiwotzki, R., Karl, C. A., Lisker, T., Heber, U., Christlieb, N., Reimers, D., Nelemans, G., & Homeier, D. 2004, *Ap&SS*, 291, 321

Napiwotzki, R. & Rauch, T. 1994, *A&A*, 285, 603

Németh, P., Kawka, A., & Vennes, S. 2012, *MNRAS*, 427, 2180

O'Toole, S. J. & Heber, U. 2006, *A&A*, 452, 579

Passy, J.-C., Mac Low, M.-M., & De Marco, O. 2012, *ApJ*, 759, L30

Randall, S. K., Calamida, A., & Bono, G. 2010, *Ap&SS*, 329, 55

- Randall, S. K., Calamida, A., Fontaine, G., Bono, G., & Brassard, P. 2011, *ApJ*, 737, L27+
- Randall, S. K., Fontaine, G., Calamida, A., Brassard, P., Chayer, P., Alonso, M. L., Catelan, M., Bono, G., Green, E. M., Dhillon, V. S., & Marsh, T. R. 2012, in *Astronomical Society of the Pacific Conference Series*, Vol. 452, *Fifth Meeting on Hot Subdwarf Stars and Related Objects*, ed. D. Kilkenney, C. S. Jeffery, & C. Koen, 241
- Rauch, T., Ziegler, M., Werner, K., Kruk, J. W., Oliveira, C. M., Vande Putte, D., Mignani, R. P., & Kerber, F. 2007, *A&A*, 470, 317
- Rodríguez-López, C., Ulla, A., & Garrido, R. 2007, *MNRAS*, 379, 1123
- Stark, M. A. & Wade, R. A. 2003, *AJ*, 126, 1455
- Stroeer, A., Heber, U., Lisker, T., Napiwotzki, R., Dreizler, S., Christlieb, N., & Reimers, D. 2007, *A&A*, 462, 269
- Van Grootel, V., Charpinet, S., Fontaine, G., & Brassard, P. 2008, *A&A*, 483, 875
- Van Grootel, V., Charpinet, S., Fontaine, G., Brassard, P., Green, E. M., Randall, S. K., Silvotti, R., Østensen, R. H., Kjeldsen, H., Christensen-Dalsgaard, J., Borucki, W. J., & Koch, D. 2010, *ApJ*, 718, L97
- van Leeuwen, F. 2007, *A&A*, 474, 653
- Werner, K. 1996, *ApJ*, 457, L39
- Whitney, J. H., O'Connell, R. W., Rood, R. T., Dorman, B., Landsman, W. B., Cheng, K.-P., Bohlin, R. C., Hintzen, P. M. N., Roberts, M. S., Smith, A. M., Smith, E. P., & Stecher, T. P. 1994, *AJ*, 108, 1350
- Woudt, P. A., Kilkenney, D., Zietsman, E., Warner, B., Loaring, N. S., Copley, C., Kniazev, A., Väisänen, P., Still, M., Stobie, R. S., Burgh, E. B., Nordsieck, K. H., Percival, J. W., O'Donoghue, D., & Buckley, D. A. H. 2006, *MNRAS*, 371, 1497